To the Graduate Council:

I am submitting herewith a dissertation written by Daryl Allen Smith entitled "Elucidating the Growth Mechanisms of Electron Beam Induced Deposition via a Three Dimensional, Monte-Carlo Based Simulation." I have examined the final electronic copy of this dissertation for form and content and recommend that it be accepted in partial fulfillment of the requirements for the degree of Doctor of Philosophy, with a major in Materials Science and Engineering.

Philip D. Rack
Major Professor

We have read this dissertation and
recommend its acceptance:

David C. Joy

Bin Hu

Claudia J. Rawn

Accepted for the Council

Carolyn Hodges
Vice Provost and Dean of the
Graduate School

(Original signatures are on file with official student records.)

Elucidating the Growth Mechanisms of Electron Beam Induced Deposition via a Three Dimensional, Monte-Carlo Based Simulation

A Dissertation

Presented for the

Doctor of Philosophy

Degree

The University of Tennessee, Knoxville

Daryl Allen Smith

May 2007

Dedication

This dissertation is dedicated to my loving parents, Mona and Ed Smith, whose selfless support and encouragement during the course of my graduate study allowed me to accomplish the seemingly impossible. I've never been more proud to be your son. I also wish to dedicate this work to my Godparents, Harold and Becky McReynolds, who helped raise me as if I were their own and have also been a tremendous source of encouragement. I love you guys so much. To the rest of my family who have supported me and my crazy notion to go back to school to get my PhD… thank you from the bottom of my heart. In addition, I want to dedicate this to Matt and Marcedes Long, as well as their entire family, who have been behind my efforts from the beginning and have become lifelong friends. I bet you're as glad as I am that this is done! This work is also dedicated to my advisor and my friend, Dr. Philip Rack, who patiently nourished my mind and spirit along my journey. You have changed my life forever… thank you. A special thank-you and dedication is also due to Dr. Ron Nutt, who so generously provided me a scholarship on behalf of his late son Randall. Your philanthropy is more inspiring than you'll ever know… thank you so much, Ron. Finally, I would like to thank my late grandfather, Roger Isbell, for instilling his wisdom of life and engineering to me from an early age. His memory continues to inspire me to want to benefit science and mankind. I think I get it now, Papaw.

Acknowledgements

First and foremost, I would like to thank my mentor, Dr. Jason Fowlkes, whose friendship and knowledge were an invaluable source of inspiration during my research. I would also like to thank Dr. Steven Randolph for his assistance with Dr. Fowlkes in laying the groundwork for my research and providing the spark of genius that led to the conclusion of this work. It is my sincere hope that their vision will continue to propagate research projects well into the future. I would like to thank the past and present members of our research group with whom I've worked with over the years, Dr. Yuepeng Deng, Dr. Seung-Ik Jun, Ryan Rucker, Jung-Won Park, Jon Peak, Matt Lassiter, Se Yeoul Kwon, and Yingfeng Guan, along with all members of Dr. David C. Joy's research group. For your help and support I am greatly appreciative. I also would like to thank my committee members for their time and effort they invested in me: Dr. David Joy, Dr. Bin Hu, Dr. Philip Rack, and Dr. Claudia Rawn. For Sandy Maples and Carla Lawrence in the MSE office, thank you for all your assistance over the years! You two are the backbone of our department. Finally, a special thank you is due to Dr. Ted Liang of Intel, who has generously funded my research and continues to enrich this University through other collaborative research projects.

Abstract

The rapid and precise direct-write growth of nanoscale features by electron-beam-induced deposition (EBID) and etching (EBIE) requires the optimization of the growth parameters to maintain nanoscale feature dimensions. The tremendous and complex EBID parameter space includes the precursor gas pressure, the primary electron beam energy, the electron beam current, surface diffusion rates of adsorbed precursor species, thermal effects on desorption, and the cascade of electron species produced by elastic and inelastic scattering processes. These variables determine the feature growth velocity and the size of the structure through a series of complex, coupled nonlinear interactions. A dynamic computer simulation based on Monte-Carlo calculation sequences was created to aide in the interpretation of experimental observations by simulating experimental EBID growth conditions for a nanoscale stationary and scanned electron beam with properties characteristic of a conventional SEM.

In this dissertation, initially the Monte Carlo EBID simulation details are presented. Subsequently, four specific case studies are simulated. The details of the mechanisms and electron types responsible for vertical and lateral growth are presented. Initially, EBID growth was compared in a reaction rate limited regime at different beam energies (1keV versus 5keV). This yielded lower growth rates at higher energy due to a combination of variables, including a lower dissociation cross section and a decreased secondary electron coefficient. Second, reaction rate versus mass transport limited growth of tungsten from a WF6 precursor was studied, and the lateral broadening associated with mass transport limited growth was elucidated. Third, a study was performed to determine

the effects of precursor surface diffusion on pillar growth rates and morphology. The changes were attributed to a shift in the otherwise mass transport limited growth with no surface diffusion to a pseudo reaction rate limited growth when the surface diffusion coefficient was sufficiently high. Fourth, two different materials were simulated and compared: tungsten from WF6, and SiO2 from $Si(OC_2H_5)_4$. The different growth rates and pillar morphology correlated to the different dissociation cross sections, secondary electron yields, and the electron range, respectively.

Sample applications of the simulation are provided, including rastered depositions, via filling, and duplication of "volcano-like" structures.

Table of Contents

Chapter 1-- Introduction.....1

1.1 The Nanotechnology Revolution 1

1.2 History and Application of EBID 6

1.3 EBID In Depth 10

1.4 Studies of EBID Mechanics 16

1.5 EBID modeling 21

Chapter 2-- Simulation Description.....29

2.1 Introduction to Monte Carlo Methodology 29

2.2 Electron-Solid Interactions 30

2.3 Discretizing the System 36

2.4 The Plural Scattering Model 39

2.5 Secondary Electrons 47

2.6 Backscattered and Secondary Electron Yields 60

2.7 Dissociation Cross Section 65

2.8 Gas Dynamics 73

2.9 Pressure Simulation 95

Chapter 3-- Simulation Results 104

3.1 Overview 104

3.2 General Simulation Output 107

3.3 Beam Energy Study 110

3.4 Mass Transport Limited EBID vs. Reaction Rate Limited Growth Study 125

3.5 Surface Diffusion Effects Study 131

3.6 Tungsten vs. SiO_x Study 138

Chapter 4-- Applications.....152

4.1 Raster Simulations 152

4.2 Via Filling 163

4.3 The Volcano Effect 173

Chapter 5-- Conclusions.....182

References.....184

Appendices.....192

Appendix A: Simulation Inputs 193

Appendix B: Simulation Flowchart 195

Appendix D: Inputs and Outputs from Energy Study 198

Appendix E: Inputs and Outputs from MTL vs. RRL Study 201

Appendix F: Inputs and Outputs from Surface Diffusion Study 203

Appendix G: Inputs and Outputs from TEOS Study 206

Appendix H: Raster Run Results 212

Appendix I: Via Simulation Results 216

Appendix J: Volcano Run Results 220

Vita 222

List of Figures

Figure 1-1: Moore's Law[3] 2

Figure 1-2: Limitations of Photolithography.[5] 4

Figure 1-3: Illustration of the EBID Process[6,7]. 5

Figure 1-4: FE Device Fabricated by EBID.[32] 9

Figure 1-5: EBID System Schematics.[6,46] 11

Figure 1-6: Beam diameter as a function of convergence angle.[55] 13

Figure 1-7: WF_6 and TEOS precursor properties. 15

Figure 1-8: Base broadening as function of time.[77] 19

Figure 1-9: Tungsten pillars grown under various pressures.[86] 22

Figure 1-10: Silvis-Cividjian *et al.* 2D Monte Carlo model of EBID.[78] 25

Figure 1-11: 3D Cartesian coordinates from the Fowlkes model.[88] 27

Figure 2-1: Illustration of electron-solid interactions.[101] 31

Figure 2-2: Illustration of Interaction Volume.[102,103] 33

Figure 2-3: Designations of electron type. 35

Figure 2-4: 3D Discretized Matrix. 37

Figure 2-5: Beam profile types. 40

Figure 2-6: Bethe range as function of beam energy. 43

Figure 2-7: Electron Scattering Geometry.[46] 45

Figure 2-8: Example Monte Carlo. 46

Figure 2-9: Monte Carlo Trajectory Example. 48

Figure 2-10: Inelastic Mean Free Path 52

Figure 2-11: SE generation[106] 54

Figure 2-12: SE Cascade generation[93] 55

Figure 2-13: Comparison of SE emission spectra[105] 57

Figure 2-14: SE^{I} and SE^{II} Generation.[124] 59

Figure 2-15: Illustration of beam current components. 62

Figure 2-16: Universal Law Plot for Tungsten SE Yield.[109] 64

Figure 2-17: Simulated BSE and SE Emissions for Tungsten. 66

Figure 2-18: Dissociation cross-section for WF_6.[132] 70

Figure 2-19: Dissociation cross section with SE and BSE emission spectra. 72

Figure 2-20: Surface Mesh for Gas Tracking. 75

Figure 2-21: Energy Barrier for Adsorption/Desorption. 77

Figure 2-22: $d\theta/dt$ compared to simulated results. 82

Figure 2-23: Six-directional Scan Illustration. 85

Figure 2-24: Independent Surface Diffusion Tests. 87

Figure 2-25: Repulsive Surface Diffusion Tests. 88

Figure 2-26: 18-Directional Surface Diffusion Scan Illustration. 90

Figure 2-27: Diagonal search pattern in center tier. 91

Figure 2-28: Vertical diagonal search directions for surface diffusion 93

Figure 2-29: Surface diffusion search algorithm comparisons. 94

Figure 2-30: Comparison of $d\theta/dt$ to Utke/Reimer model. 96

Figure 2-31: Hitachi S-4300SE VPSEM EBID System 97

Figure 2-32: Nozzle Geometry 99

Figure 2-33: Example output from pressure simulation. 102

Figure 3-1: Electron to Gas Flux Ratio for Reaction-Rate Limited Conditions. 111

Figure 3-2: Calculation of mean gas to electron flux ratios for varying pressure. 113

Figure 3-3: 5keV Pillar grown to 166nm tall. 115

Figure 3-4: 1keV Pillar grown to ~167nm tall. 116

Figure 3-5: SE and BSE emission spectra. 118

Figure 3-6: SE and BSE Yields as a function of Pillar Height 121

Figure 3-7: Sampled deposition events by electron type (1keV vs. 5keV) 122

Figure 3-8: Normalized Pillar Profiles at 1keV and 5keV 124

Figure 3-9: Mass transport limited pillar at 1keV. 128

Figure 3-10: Normalized comparison of MTL and RRL pillars. 129

Figure 3-11: Sampled deposition events from 1keV MTL pillar. 130

Figure 3-12: Surface Diffusion Sampled Deposition Plots 134

Figure 3-13: Deposition rates, surface diffusion study. 136

Figure 3-14: Surface coverage as function of # electrons 137

Figure 3-15: TEOS and WF_6 Cross Sections 142

Figure 3-16: Cross-sections through 1keV MTL pillars from WF_6 and TEOS. 144

Figure 3-17: Example Monte Carlo simulations of 100 electrons in W and SiO_2. 146

Figure 3-18: Top curvature heights of tungsten (a-c) and SiO_2 pillars (d-e). 147

Figure 3-19: Comparison of conical caps from tungsten and SiO_2 pillars. 148

Figure 3-20: SiO_2 pillar simulation results. 149

Figure 3-21: Surface coverage and pillar height of TEOS Runs 5 and 6. 151

Figure 4-1: Illustration of Raster Technique. 153

Figure 4-2: Pixel Spacing. 156

Figure 4-3: Raster Run 1 Results. 158

Figure 4-4: Raster Run 2 Results. 159

Figure 4-5: Raster Run 3 Results. 160

Figure 4-6: Time Profiles and Deposition Events for Raster Runs 1-3. 161

Figure 4-7: Raster Run 4 Results. 162

Figure 4-8: Examples of via filling techniques. 166

Figure 4-9: Via Run Setup. 168

Figure 4-10: Gas Gradient in vias. 169

Figure 4-11: Via Monte Carlo Illustration. 170

Figure 4-12: Via Run 1 Results. 171

Figure 4-13: Via Run 2 Results. 172

Figure 4-14: Via Run 3 Results. 174

Figure 4-15: Via Run 4 Results. 175

Figure 4-16: Volcano structures grown at UTK by J. Kim.[162] 176

Figure 4-17: Volcano Run 1 Results. 178

Figure 4-18: Gas surrounding volcano periphery. 179

Figure 4-19: Volcano Run 2 Results. 180

Chapter 1--Introduction

1.1 The Nanotechnology Revolution

The semiconductor industry today is a trillion dollar market that accounts for almost 8 percent of the total global economic activity.[1] In 1958, Jack Kilby and Robert Noyce independently invented the integrated circuit[2] and revolutionized the world of technology. Since then, the drive for electronics to become miniaturized and faster has created a vast number of fabrication techniques which are aimed at mass-producing the current technology and delivering it to the end user.

Since the dawn of the computer, users have demanded faster and smaller devices for more computational power. To achieve this end, the trend in lithography has been to make the pattern size smaller and smaller, thus achieving more transistors on a computer chip which can run faster and cooler than previous generations. Gordon Moore postulated in 1965 (four years after the first planar integrated circuit was discovered) that this trend would follow an exponential growth, whereby the number of transistors on a computer chip would double every eighteen months (see Figure 1-1).[3,4]

Indeed, this trend has been followed almost exactly! Intel's latest Central Processing Unit (CPU) devices planned to be fabricated on the 45-nm node have 410 million transistors on a single chip. Their manufacturing process is constantly looking for new ways to extend the physical barriers of lithography, such as using Extreme Ultra Violet (EUV) and X-ray lithography. There is however a theoretical limit as to how small these processes can make the millions of transistors. It was first thought that

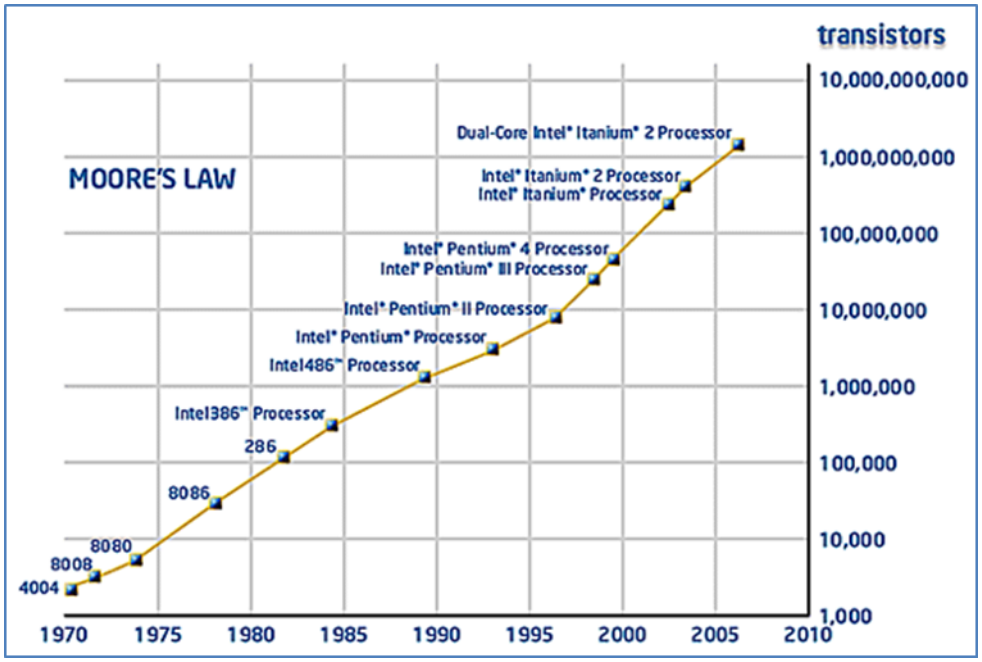


Figure 1-1: Moore's Law[3]

Processing power, measured in millions of instructions per second (MIPS), has steadily risen because of increased transistor counts. Gordon Moore predicted in 1965 that the number of transistors on a chip would double about every two years.[3]

100nm resolution would limit this process, but new materials and procedures have enabled Intel to launch 45nm sized components. It is clear, however, that further improvements to current technology are getting harder to derive, and more expensive to implement. Ultimately, a better solution is needed to create solid state devices well below the limits of traditional lithography. Experiments with X-ray lithography, Ion Beam lithography, and Electron-Beam Lithography are currently ongoing in an attempt to achieve that goal. In fact, in order for Moore's Law to be followed, new developments in nanometer-sized fabrication *must* be developed. It is estimated that somewhere around year 2010, the demand for smaller and faster microprocessors will surpass what can be manufactured due to physical limitations of traditional lithography (see Figure 1-2).[5]

This demand has created a lucrative market in the field of nanotechnology which seeks to solve this problem and pave the way for advances in miniaturization technology. At the forefront of this highly competitive arena is the process known as Electron-Beam Induced Deposition (EBID). EBID is basically a process whereby an electron source (such as a SEM, i.e. a scanning electron microscope) is used to modify an adsorbed molecular species on a substrate surface such that it deposits material or reacts with the substrate to etch it away. The adsorbed species is referred to as the precursor, and can be in a liquid, solid, or gas phase. Usually, the precursor is introduced to the substrate in gaseous form, since the process takes place in a low pressure environment.

An illustration of the EBID process is shown in Figure 1-3. Here the precursor is a molecule of metallic product and volatile by-product, which dissociate under the electron beam to form the metallic deposit. The volatile product then desorbs from the surface and

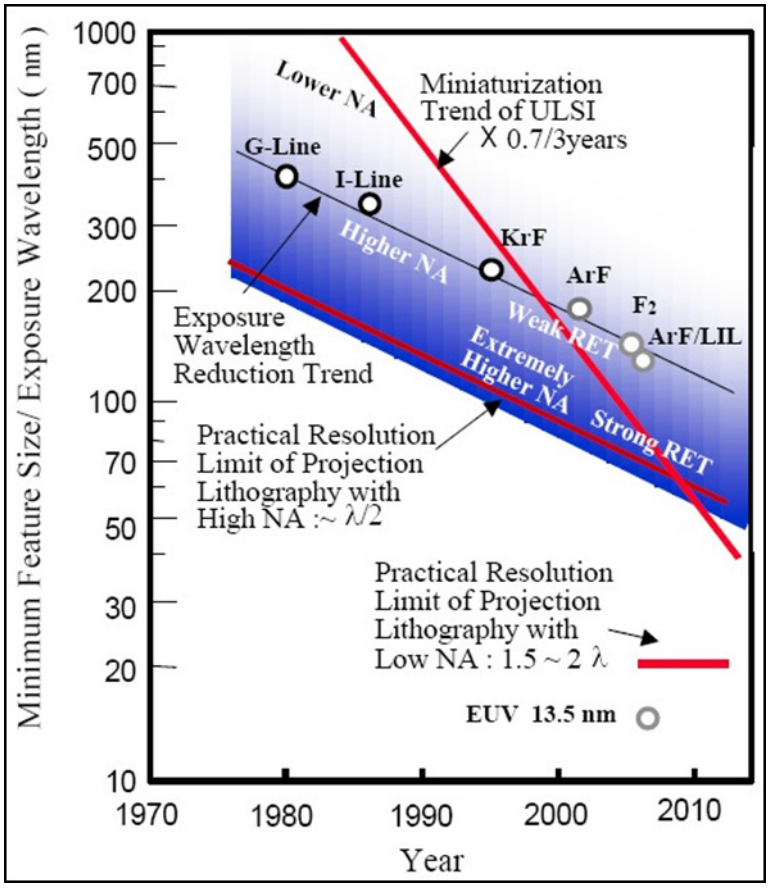


Figure 1-2: Limitations of Photolithography.[5]

The demand for smaller devices is approaching the physical limits of photolithography. Sometime during the next decade, new methods of fabricating devices with the necessary minimum feature sizes must be developed.

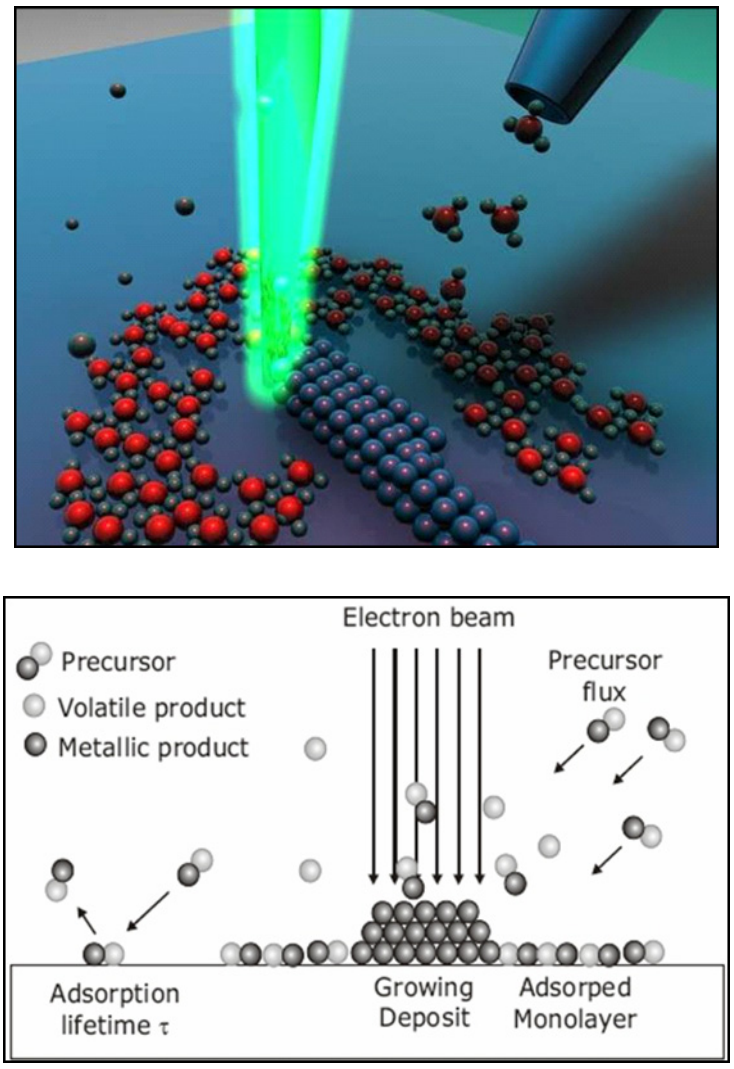


Figure 1-3: Illustration of the EBID Process[6,7].

A precursor containing the desired species to be deposited is adsorbed onto the substrate, where it is irradiated by an electron beam and dissociated into the deposit material and by-products (which are evacuated out of the system).

diffuses away from the substrate and is removed through the vacuum system. Though the process of EBID is understood on a macroscopic level, the fundamental electron-solid interactions that compose the EBID process are still being explored. A thorough analysis of this process is necessary in order to maximize the performance and resolution of EBID so that it can be effectively used in industry to contribute to the nanotechnology revolution that is on the horizon. Leading this research field, the University of Tennessee in collaboration with Oak Ridge National Laboratories and Intel, Inc. is actively exploring to resolve some of the mysteries surrounding EBID. This research is a necessary step in this direction, and can be utilized by the vast amount of EBID applications both inside and outside the semiconductor industry, such as lithography mask and chip repair, and nanoscale device prototyping of new biological, electronic, optoelectronic, magnetic, or nanomechanical devices.

1.2 History and Application of EBID

As with most scientific breakthroughs, EBID was not purposefully developed. Rather, it was discovered as a nuisance of electron microscopy. It was found as far back as the 1930's where an electron beam was found to coat the surface of an object with a carbonaceous substance.[8,9] Hart *et al*. stated circa 1970 that an unwanted side effect of electron microscopy was "carbon staining", which was a result of the electron beam interacting with an adsorbed layer of hydrocarbons on the sample surface being examined[10]. They concluded that by controlling the substrate temperature, this contamination could be minimized by minimizing the adsorbed carbonaceous gas and controlling the surface diffusion. Broers *et al.*[11] are credited with the first patterns (8-nm-wide metal lines) grown for use as an etching mask by EBID. Some of the early uses of

EBID were patterning superconductors[12] and fabricating oxidation resistant coatings for gas turbine airfoil shapes.[13]

With advances in resolution and electron-beam focusing equipment, the possibility of high-resolution nanofabrication via EBID has recently come of interest. Since electrons have a much shorter wavelength than light, it should be theoretically possible to fabricate structures by EBID that are much smaller than can be imaged via traditional optical lithography. One key work toward obtaining this goal was performed by Silvis-Cividjian *et al*. who deposited ~10-nm carbon nanowires and dots using a C_2H_5 precursor in a STEM.[14] Other work using different precursor materials created other similar structures via EBID, including nickel[15], cobalt[16], platinum[17], rhodium[18], gold[19], and tungsten[20,21]. Early application of these structures were used for metal interconnects between electrode pads and carbon nanotubes (CNT)[22] and single-walled carbon nanotubes (SWNT).[23] More complex 2D and 3D structures have also been fabricated by EBID as well. Utke *et al.* examined deposition of vertical structures from horizontal fibers which were grown in free space by a slow, linear scan of an electron beam. [24] Pattern generators have also been utilized to create complex 3D features, such as leaning nanofibers by Koops *et al.*[25,26] and mesh patterns by Ueda *et al*.[27]

One nanostructure which can be fabricated by EBID that has a number of practical uses is the nanopillar. These structures are created by dwelling an electron beam in one location in order to grow a high-aspect ratio pillar. These have been made from many types of materials such as cobalt[16], carbon[18,28], and tungsten[29]. The geometry of these nanopillars makes them ideal for nanoscale vertical-cathodes[30,31] and field emission devices. Murkami *et al.*, for example, demonstrated Fowler-Nordheim FE

behavior from a platinum nanofiber deposited by EBID (Figure 1-4).[32] Platinum nanopillars have also been used to create FE cathodes for planar microtriode arrays.[33] These nanopillars can be fabricated with super-sharp tips at the top in order to enhance emission, such as the sub-7-nm radii tips fabricated by Koops *et al.*[34] Nanopillars have also been grown on scanning probe tips for improving resolution in devices such as SPM's[35]. These FE devices can be produced by EBID in a massively parallel array, which is used in applications such as the Digital Electrostatic Electron Beam Array Lithography (DEAL).[36-38] This device is designed for Electron-Beam Lithography (EBL) using multiple electron beam sources[38] as opposed to just one source in traditional EBL. EBID has also been used to modify optical elements on near field scanning probes[39].

One of the main commercial applications that EBIE and EBID have impacted is in the area of lithography mask and chip repair. Studies on repairing EUV masks with EBID rather than standard FIB processing[40] have shown significant improvements, such as no ion implantation, no deleterious transmission loss, and better feature selectivity while minimizing surrounding structure damage[41-43]. The resolution of this tool has been shown to be suited for the 90nm and 65nm nodes, as well as the 45nm node[44]. While sub-10nm structures have been fabricated by EBID for a long time, recently 1nm resolution was demonstrated[45]. This could make electron beam induced processing a possible next generation lithography technique if appropriate resist schemes can be developed. For a complete review of electron beam induced processing see Randolph *et al*.[46]

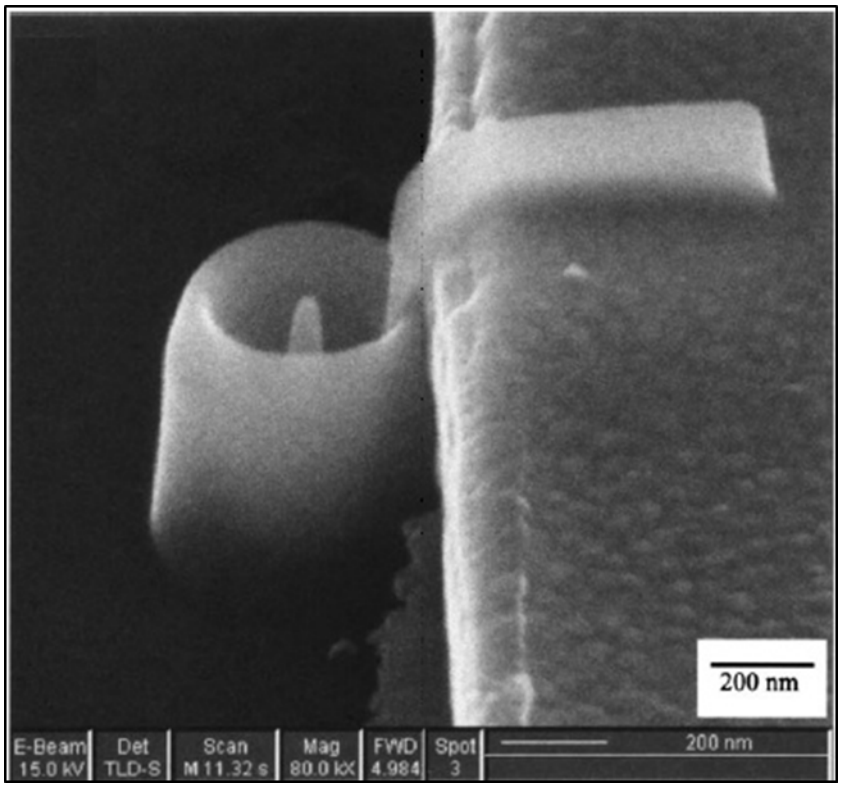


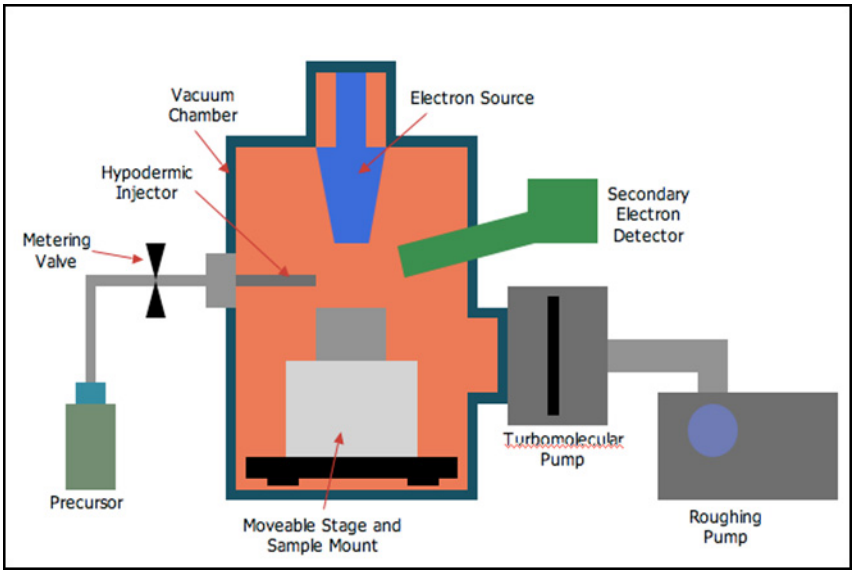
Figure 1-4: FE Device Fabricated by EBID.[32]

Murakami *et al.* demonstrated the fabrication of a Pt emitter within a Pt ring-shaped gate via EBID in 2004. FIB could not be used due to Ga contamination and damage.

Typically, EBID uses traditional electron-beam sources such as thermal and field emitters to generate the electron beam that induces deposition at the substrate. Other electron sources have been explored, however, with varying results. Multi-walled carbon nanotubes have been demonstrated to transfer electrons to a substrate by Dong *et al*.[47] Here, a CNT was applied to the tip of an atomic-force microscope (AFM) cantilever so that it could perform carbon deposition by EBID on a silicon substrate. Arai *et al*. also used this method to deposit tungsten by EBID from CNT's that were functionalized with ruthenium dioxide nanoparticles.[48]

1.3 EBID In Depth

The process of EBID has been performed using a variety of tools. Some of the existing devices which have been modified to facilitate EBID include the scanning electron microscope (SEM)[49], scanning tunneling microscope (STM)[15], scanning transmission electron microscope (STEM)[14], and transmission electron microscope (TEM).[50] These systems are already set up to deliver a dose of electrons to a substrate in a vacuum environment. All that is necessary to allow for EBID is the introduction of a precursor gas into the localized area where electrons interact with the substrate so as to initiate the EBID reaction (see Figure 1-5). This is achieved by utilizing a precursor injection system that allows the operator to control the dose of precursor species at the local site where deposition occurs. This gas injection controls the localized gas pressure and is critical to maintain the integrity in reproducibility of the EBID process. Since most systems have their own complex and unique method of incorporating the precursor gas



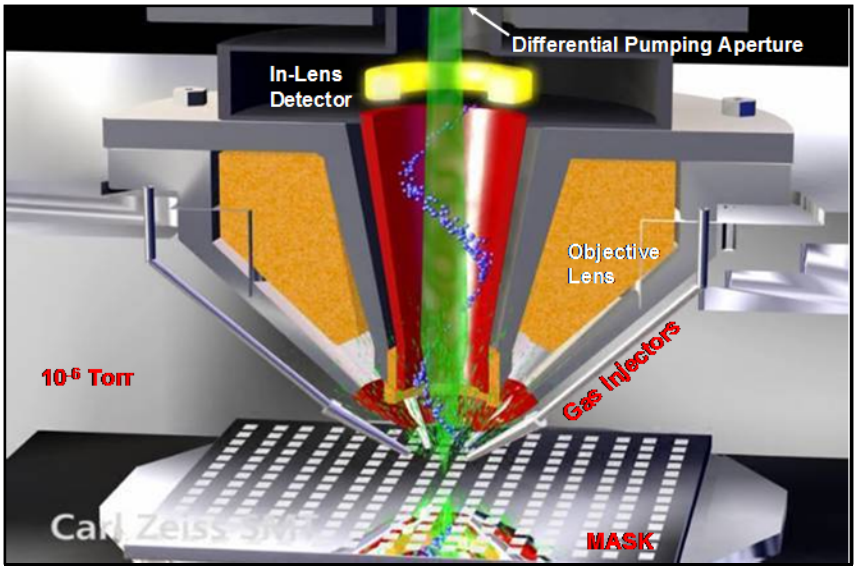


Figure 1-5: EBID System Schematics.[6,46]

The EBID system is essentially a SEM with a vapor injection system attached. Multiple injectors can also be used as shown in the lower illustration.

into the electron-beam interaction site, a standard method of calculating this parameter is not available. Various methods of precursor injection have been proposed[51], such as a computer-controlled model by Koops *et al.*[52] For research in this dissertation, precise geometric measurements and flow rate calculations were employed.

Once the precursor has been successfully adsorbed onto the substrate, the electron source that allows for the dissociation of the precursor must be controlled in a precise manner. Current SEM's are capable of applying electrons via a static (i.e. focused "spot") mode, as well as by a line and raster scan mode which dynamically moves the electron beam one- or two-dimensionally across the substrate surface. The advantage of rasterizing the beam in this fashion is that larger areas can be affected by EBID at the expense of longer deposition times. Pattern generators have been employed to further enhance this concept by forming a specific EBID pattern on the substrate surface in a method resembling Electron-Beam Lithography (EBL).[25,27]

The system where EBID will take place must be optimized prior to deposition in order to obtain the highest quality results. Selection of the electron source, whether thermal or field emission, for example, relates to the minimum attainable spot size of the electron beam. Schottky field emission cathodes make an excellent EBID source because of their low noise and small spot size[53]. Ensuring a small spot diameter will lead to improved resolution of the EBID process. Other factors, such as spherical aberration, chromatic aberration, source size limit, and diffraction contribute to the beam size, as shown in Figure 1-6. Liu *et al., for example* demonstrated how changing the focus of the electron beam results in broadening of deposited tungsten lines.[54]

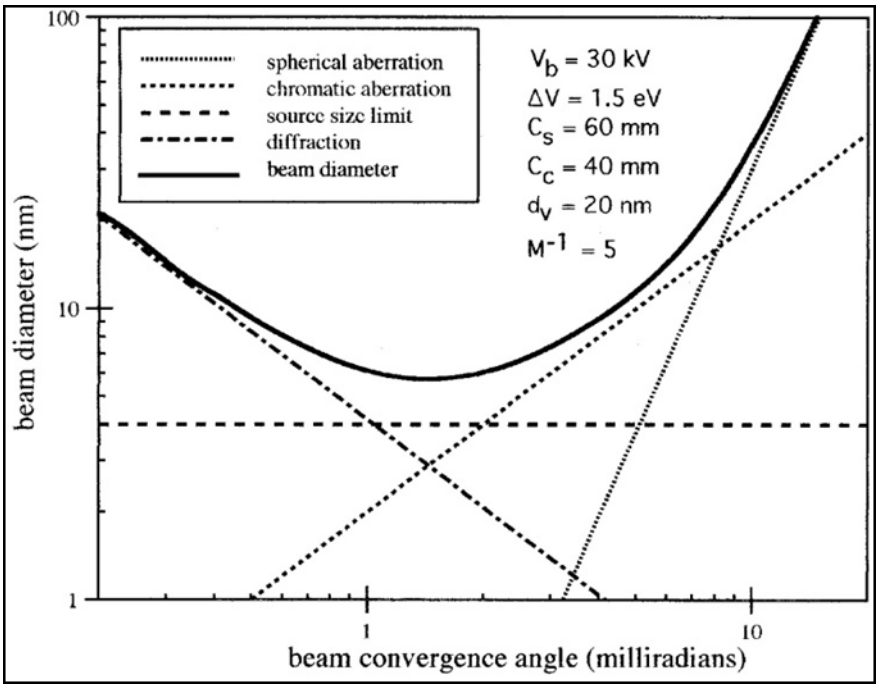
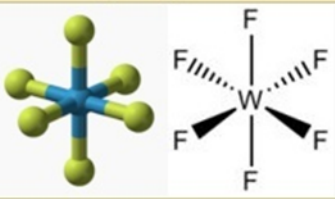


Figure 1-6: Beam diameter as a function of convergence angle.[55]

Illustration of various factors which affect the beam spot size and therefore resolution in a scanning electron microscope.

Selection of the precursor for EBID will determine the type of deposit generated by the process. There are several chemical species which are currently being investigated in the semiconductor industry. The important qualities of the precursor are: 1) it must decompose under an electron beam to form the required deposit, 2) the by-products must be inert and gaseous in nature so they can diffuse away from the deposition site, and 3) the vapor pressure of the precursor must be such that it is the desired phase in the low-vacuum environment where EBID is taking place. Furthermore, contaminants in the precursor must be minimized, such as hydrocarbons and water vapor.

Many metals have been deposited by EBID, such as chromium[49], rhodium[56], iron[57], cobalt[16], platinum[58], copper[24], palladium[59], aluminum[60], molybdenum[61], osmium[62], nickel[15], rhenium[63], and ruthenium[62]. Non-metals such as semiconductors, insulators and oxides can also be deposited by EBID. Examples of these include gallium arsenide[64], gallium nitride[50], silicon[65], silicon nitride[66], silicon oxide (SiO_x)[67], and titanium oxide (TiO_x)[68]. The most well studied precursor gases involve the deposition of tungsten, either from tungsten hexacarbonyl, $W(CO)_6$[69] or tungsten (VI) hexafluoride, WF_6.[49] See Figure 1-7 for a brief summary of these two precursors. For the purposes of the experiments in this dissertation, WF_6 was chosen because the lack of carbon in its chemical composition produces a more homogenous deposit of tungsten metal.[70] The second precursor used for this work was tetra-ethyl-ortho-silicate (TEOS) which decomposes to SiOx under an electron beam.

Tungsten(VI) fluoride	
	
General	
Systematic name	Tungsten(VI) fluoride
Other names	Tungsten hexafluoride
Molecular formula	WF_6
Molar mass	297.83 g/mol
Appearance	Colorless gas.
CAS number	[7783-82-6]
Properties	
Density and phase	13.1 g/L^{-1}, gas.
Solubility in water	Hydrolyzes.
Melting point	2.3°C (275.45 K)
Boiling point	17.1°C (290.25 K)
Structure	
Molecular shape	Octahedral
Dipole moment	0 D
Hazards	
MSDS	External MSDS
Main hazards	Corrosive, highly toxic.
NFPA 704	
Flash point	Non-flammable.

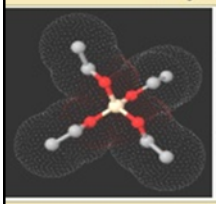
Tetraethyl Orthosilicate	
	
General	
Systematic name	Tetraethyl Orthosilicate
Other names	TEOS
Molecular formula	(C2H5O)4Si
Molar mass	208.33 g/mol
Appearance	Colorless liquid
CAS number	78-10-4
Properties	
Density and phase	0.94 g/cm3
Solubility in water	Decomposes
Melting point	-86C
Boiling point	169C
Structure	
Molecular shape	see above
Dipole moment	
Hazards	
MSDS	External MSDS
Main hazards	Flammable, highly toxic
NFPA 704	
Flash point	39C

Figure 1-7: WF_6 and TEOS precursor properties.

Various properties of two main precursor gasses used in this work.

1.4 Studies of EBID Mechanics

As scanning electron microscope technology improved over the last decade, the possibility of utilizing EBID as a method of direct write or maskless nanoscale fabrication became feasible.[71] The theoretical understanding of the EBID process, however, was significantly lacking as compared to older technologies such as physical and chemical vapor deposition. These processes can be used with a high degree of confidence in reproducibility because of the extensive research which has been performed in studying their mechanisms of deposition. Within the last 5 years, those who have been working closely with EBID have been actively performing experiments with the hopes of understanding the underlying mechanics of this process. This research will ultimately allow EBID to be utilized more efficiently in industry, as the level of control and predictability of the process will be significantly increased.

As a first-order approach to understanding the EBID process, researchers have attempted *in-situ* studies, which are real-time measurements of the process. These data have resulted in a better knowledge of how input parameters affect the EBID result, thus allowing for more predictability and reproducibility of experiments. Rack *et al.* studied the gradual compositional changes during growth of tungsten on germanium by EBID[72]. To monitor how the chemical composition of the deposit evolved over time, *in-situ* measurements by Energy Dispersive X-ray Spectrometry (EDS) were taken over various deposition times. Bret *et al.* monitored electron current during deposition, which was found to drop at a characteristic rate and saturate at a plateau.[73] These measurements were then correlated to the deposit geometry, composition, and precursor supply.

Perentes *et al.* proposed an optical *in-situ* technique for monitoring the thickness of transparent materials during EBID.[74] A laser was confocused in the plane of the sample which allowed for monitoring changes in reflection intensity during EBID growth. This provided information as to the growth rate and changes in composition during growth. Though quantitative in nature, these experiments only attempted to show correlation between measured values and observed phenomena. A detailed understanding of the underlying processes which are responsible for these behaviors was still lacking.

Of primary importance to nanotechnology is the minimum attainable feature size using EBID. The control variables which ultimately affect resolution in the EBID process are complex and numerous. In addition, predicting electron-solid interactions and gas dynamics make designing experiments to predict the optimum parameters for high resolution a difficult task. One of the EBID parameters which have been studied for its effect upon resolution is the beam energy. In general, higher energies have resulted in smaller spot sizes[75], which indicates that high energy electron beams can make smaller EBID deposits. Very high energy depositions (200keV) of tungsten produced dots of approximately 3.5nm in diameter in one experiment[76], and as small as 1nm when using an ESTEM[45]. These features are indeed small, but unfortunately are not suited for many applications. The attempt to grow these small features into pillars, for example results in broadening of the features because of the complex-interplay between pillar morphology and the electron-solid interactions.

Electron-solid interaction influences the growth of EBID and is a complicated interaction that includes elastic and inelastic electron-solid scattering, secondary electron generation, material properties, and depends strongly on the substrate surface topography.

To better understand resolution limits and fundamental mechanisms associated with EBID, experimental studies have been carried out to elucidate the specific type of electron responsible for inducing the deposition process.[77,78] Kohlmann – von Platen *et al*. deposited tungsten pillars by electron beam stimulated dissociation of $W(CO)_6$ precursor gas with the aim of determining the resolution limiting parameter.[77] They concluded that secondary electrons generated in the deposited pillar by the primary beam controlled the width of the deposited pillar. Controlled experimental pillar growth and a model based on geometrical principles were proposed. It was suggested that secondary electrons controlled the diameter of the pillar over the entire growth time cycle; the Gaussian nature of the beam coupled with the enhanced emission of secondary electrons from the steep slope of the pillar, which overlaps the edge of the beam, causes the continual broadening of the pillar base even after the scattered volume within the pillar no longer reaches down to the pillar base.[77] A plot of base broadening as a function of time from this study is shown in Figure 1-8. Hiroshima *et al*. deposited W wires from the EBID of WF_6 precursor[79] by a beam raster process. In this study, the lateral growth rate dependence on the rastered beam speed was compared to the SE exit angle from wire edge surfaces. A linear, flexible string array of nodes simulated the evolving cross section. The results showed the lateral resolution of the lines were consistent with the mechanism proposed by Kohlmann-von Platen *et al.*[77]

Backscattered electrons (BSE) have also been cited as the possible source of inducing deposition at the flanks of emerging deposits[69]. Koops *et al*. indicated that BSE induced deposition at the flanks limits the aspect ratio achievable by an electron–beam

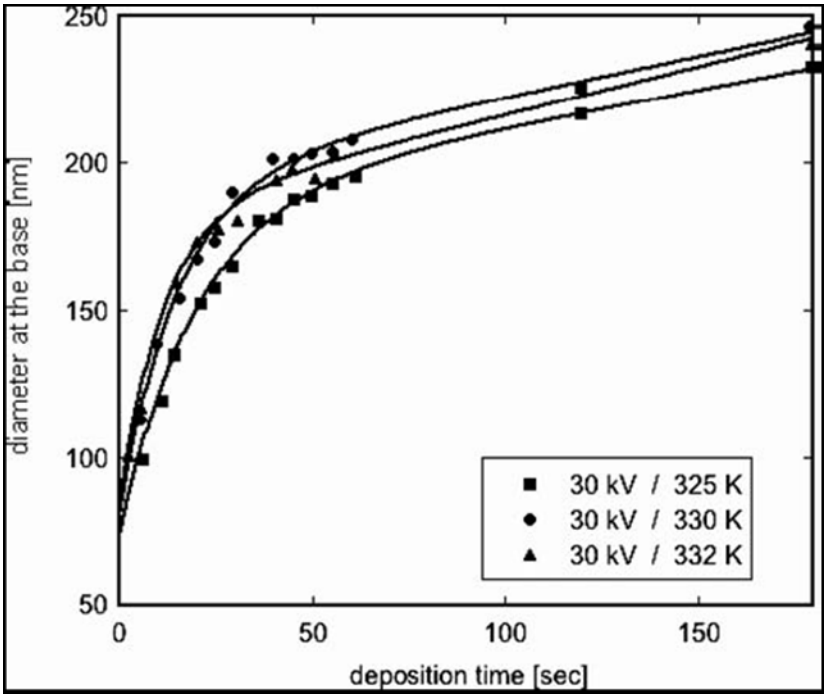


Figure 1-8: Base broadening as function of time.[77]

A curve representing the observed base broadening as a function of time as occurs during EBID fiber deposition.

stimulated growth process.[69] Fujita *et al.* also found a similar result, with the addition that forward scattered electrons (FSE's) as well as secondary electrons (SE's) emitted from the flanks of the growing nanopillars will affect the pillar morphology.[80] Self supporting nanowires have been fabricated which exhibit impressive aspect ratios by rastering the beam from the edge of a substrate specimen[27,54,80,81]. In this growth configuration the electron interaction with the growing feature is minimized yielding sub–20 nm wires.[27,54,80,81]

The temperature profiles of structures grown by EBID have also been studied recently. Randolph *et al*. simulated the temperature profile in EBID nanowires and performed temperature dependent growth studies to show that the EBID process was limited by mass transport as opposed to reaction rate limited growth.[82] This proposes an interesting question as to how the mass-transport limited (MTL) growth affects pillar morphology as opposed to reaction-rate limited (RRL) growth. This parameter can be affected by pressure variations at the deposit site as well as by controlling the substrate temperature. Clearly more research is required in this area.

When performing EBID depositions, the amount of material deposited for a given time is a critical piece of information which should be known prior to performing the experiment. If EBID is to be adopted for commercial use, not only must its resolution be minimized, but the speed of the process must be optimized. To this end, the growth rate of EBID has been studied with an attempt to determine limiting factors which will improve the usefulness of the process. Hübner *et al.* observed the effect of pixel time on the growth of platinum nanostructures using a solid precursor (CpPtMe3)[83]. Intuitively, shorter beam times yielded smaller structures. Kohlmann-von Platen *et al*. examined the

electron scan rate during rastered deposition on EBID growth.[84] It was reported that short pixel dwell times, coupled with long frame refresh loop-times allowed for the precursor to be replenished between pixel passes. This yielded an optimization of the growth rate for the rastered growth. As with most experiments of this nature, however, the results were only applicable to a particular system of inputs such as beam energy, current, and precursor pressure. Changing one or more of these variables makes such growth rate predictions more qualitative rather than quantitative. In addition, directionality of the scan affects the EBID growth rate. This has to do primarily with gas flow dynamics and beam location relative to the precursor injection site. In work by Bret *et al.,* higher growth rates were observed as the beam traveled toward the injection needle.[85] Similarly, Choi *et al.* showed how directly changing precursor pressure directly affects the growth rate of tungsten and SiO_x nanopillars[86] (See Figure 1-9 for an example SEM photomicrograph of these pillars).

1.5 EBID modeling

As previously mentioned, the complex interplay between input variables for the EBID process, electron-solid interactions, and gas dynamics make it very difficult to accurately understand the physical phenomena taking place during deposition. One parameter can be studied in detail, however changing other system parameters may conversely affect the previous trend. Attempts to model this complex system using computer algorithms are therefore of primary importance to understanding EBID. Several models have been proposed, each focusing on specific properties of the EBID process.

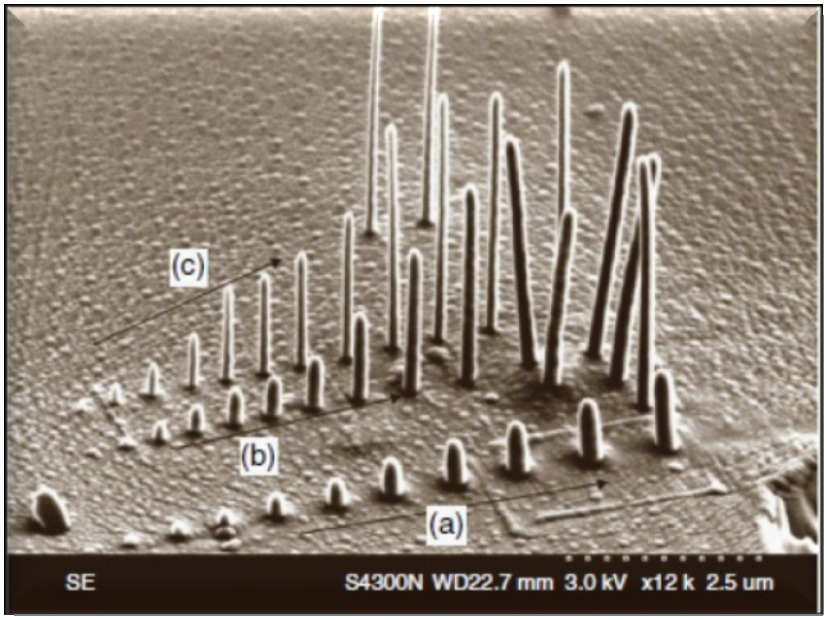


Figure 1-9: Tungsten pillars grown under various pressures.[86]

Growths with WF6 precursor gas at various pressures. (a) 1×10^{-6} Pa, (b) 3×10^{-6} Pa, and (c) 8×10^{-6} Pa.

The first EBID simulation was developed by Silvis-Cividjian *et al*., and used a 2D dynamic profile simulator to follow pillar growth as a function of time for high-energy (200keV) electron beams.[78] Their first generation simulation utilized Joy's Monte Carlo algorithm to model the electron-solid interactions.[87] Their model utilized assumed rotational symmetry to generate a two-dimensional "slice" through a statically grown pillar. It neglects the deposition effects of primary electrons (PE's), backscattered electrons (BSE's) and forward-scattered electrons (FSE's) because these energies are much higher than the energy of the secondary electrons (SE's) which they attribute as the primary contributors of pillar growth. One of the key elements of any EBID simulation is the determination of the probability for precursor dissociation based on electron energy. This "dissociation cross section" is not readily available in literature typically; therefore it must be approximated by the simulation. The cross section used by Silvis-Cividjian *et al.* "grossly underestimates the probability of high energy dissociation events".[88] As a first approximation, however, this model does a good job in illustrating the importance of SE dissociation on lateral broadening of nanopillars. The elastic scattering of electrons within the substrate foil or growing nanopillar was neglected, which ultimately underestimated growth morphology. SE generation was handled in two ways: the initial development of the slice was performed using existing flat-surface SE data. Once a structure had developed, the Chung and Everhart[89] "straight line approximation model" (SLA) for SE generation was used for simplicity in calculations. To generate a dissociation event, the SE's simply accumulate at each discretized spatial coordinate until the accumulated energy exceeds that of the precursor's molecular dissociation threshold

energy. At that time, a new atom is formed from the dissociation event. Figure 1-10 shows example output from this simulation. They reported that this "ultimate resolution case" fit the 20nm full width half maximum (FWHM) measure for experimentally grown pillars using a STEM with a sub-1-nm beam diameter.

Further investigation by Silvis-Cividjian *et al.* into the high energy EBID model[90] proposed other models for SE contribution to EBID. First, the "direct model" which assumes that SE's are generated isotropically only though excitations of the target conduction electrons. Second, the "fast-secondary model" that is not isotropic and generates SE's at large angles to the beam direction.[91] Third is the "dielectric function model" proposed by Ding and Shimizu[92] which calculates inelastic scattering in terms of the dielectric function of the target. An enhancement to the SLA model was suggested by incorporating SE cascades proposed by Koshikawa and Shimizu.[93] The model they used for their simulation was Joy's "fast electron model" which was the most computationally friendly. This model attempted to determine growth analytically by combining spatial and energetic information from the Monte Carlo simulation and the electron-impact dissociation cross section of the precursor (again, underestimated at high energies), then convolving this result with a Gaussian distribution profile of the PE's. One of the key elements of this model is their attempt to simulate delocalized inelastic scattering. This is a difficult procedure due to the unknown parameters associated with delocalization; therefore it is often approximated with simple methods. The "classical approach" utilizes a maximum impact parameter[94], *b,* also known as the Bohr cut-off radius. This method is generally accepted to overestimate the delocalization. The "semi-classical approach" treats the electron as a point charge and describes the delocalization quantum

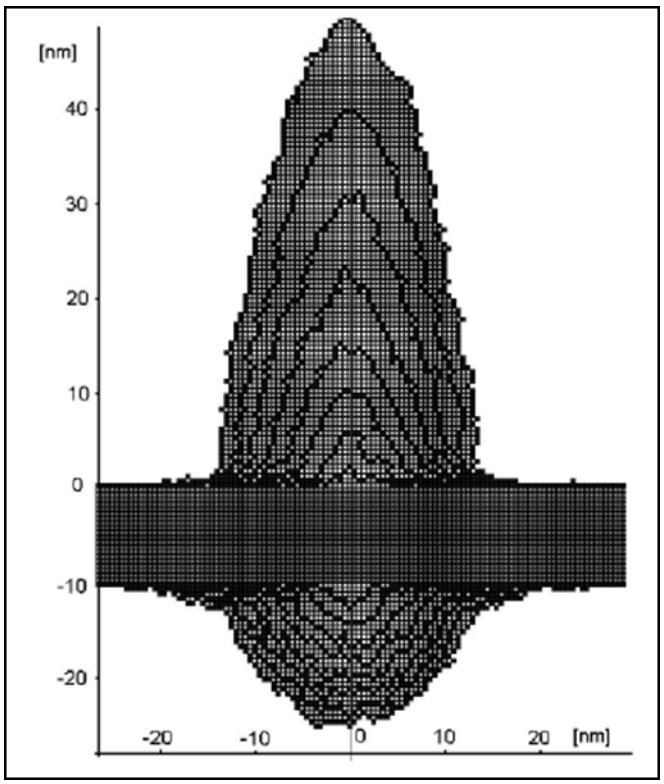


Figure 1-10: Silvis-Cividjian *et al.* 2D Monte Carlo model of EBID.[78]

A sequence of simulated profiles of a contamination tip grown by a 200-keV, zero diameter, electron beam on a 10-nm carbon foil, in steps of 9000 PE, starting at 3000 PE.

mechanically[95]. Ultimately, it was concluded that delocalized SE emission does not significantly limit the resolution of EBID when high-energy (i.e. >100keV) irradiation is employed.

Fowlkes, *et al.* developed Monte Carlo algorithms in three-dimensional Cartesian coordinates (see Figure 1-11) using similar models for SE generation, but with the added benefit of tracking PE's, BSE's and FSE's.[88] A more thorough approach to determining the dissociation cross section was examined and applied to the WF_6 precursor. The results focused on lower beam energies (5-20keV) and demonstrated how the combination of all electron types contribute to deposition and pillar broadening. Interestingly, Fowlkes found that the high flux of PE's can contribute more to pillar deposition than SE's. Thus, they can overcome the expected lateral broadening at these low energies and high-aspect ratio structures can still be produced. The Fowlkes model took the first steps toward approximating gas dynamics by approximating surface coverage due to precursor flux, which was updated after every incident electron. This model does not incorporate a 3D surface diffusion dynamics algorithm, so only gas adsorbed from the gas phase is considered.

Liu *et al*. generated a dynamic Monte Carlo simulation that accurately predicted the shape and profile of W pillars deposited at E_o = 20 and 200 keV.[96-98] Their model applied to substrate foils, and incorporated similar algorithms as the Fowlkes model for Monte Carlo modeling of the PE's, BSE's, FSE's, and SE's. Gas dynamics were not incorporated into the simulation. Comparing growth of deposits above and below a foil, the effect of gas dynamics could be subtracted in order to produce experimentally

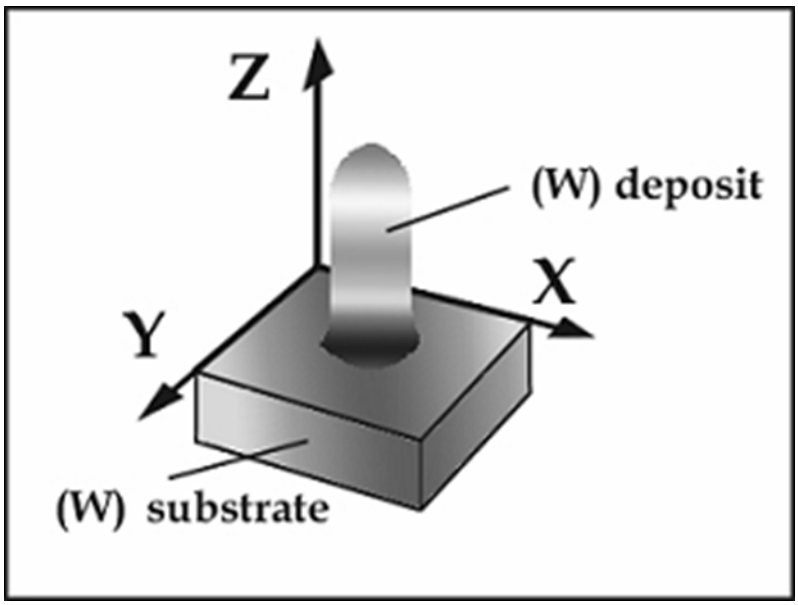


Figure 1-11: 3D Cartesian coordinates from the Fowlkes model.[88]

Illustration of the 3D Fowlkes model's Cartesian coordinate planes established for modeling EBID.

verifiable quantitative results. Therefore the practicality of the simulator is limited to these conditions which are not applicable to most EBID applications.

To date, a comprehensive, 3D model for EBID which incorporates all of the above features including the ability to simulate 3D surface diffusion of the precursor has yet to be established. It is therefore the goal of this work to present a comprehensive model that is non-system dependent such that experiments may be simulated in the static or raster scanned condition. The Fowlkes model was chosen as a basis for the comprehensive model, and has been significantly modified as described in the following sections.

Chapter 2-- Simulation Description

2.1 Introduction to Monte Carlo Methodology

The term "Monte Carlo" refers to a method of solving physical or mathematical systems by stochastic or nondeterministic methods whereby random numbers are passed through repetitive algorithms with the intention of modeling statistical behavior through large numbers of computations. The nature of this process is useful when studying systems that have a large number of variables, especially complex systems involving interdependent variables that are very difficult to solve numerically or analytically. Monte Carlo methods have been employed in various fields for solving these difficult systems, from physics to quantum chromodymanics.[99]

The process of EBID certainly falls into the category of a system with many complex variables that cannot be completely solved in an analytical or numerical fashion. In order to develop a thorough model of EBID, a means to simulate the complex electron-solid interactions which occur as the deposition progresses needed to be used. Monte Carlo methods have been employed for modeling these interactions since personal computers became available to the general public. One of the first analyses of electron-solid interactions using the Monte Carlo method was by M. Green in 1963.[100] Since then, the algorithms have been constantly improved by Ding, Hovington, Joy, Kotera, Murata, Reimer, Shimizu, Silvis-Cividjian, Ziegler, etc.

The EBID simulation developed by Fowlkes, *et al*. utilized a combination of algorithms employed by several authors, in order to achieve a basic model and identify methods for improvement. This simulation was used as a basis for this research, and developed further to obtain the most robust simulation of its type to date. There are

roughly three parts to the simulation which will be discussed: the Monte Carlo model, the dissociation cross-section, and the gas-solid dynamics.

2.2 Electron-Solid Interactions

Before beginning to describe how the Monte Carlo model is used as part of this simulation, it is important to describe how the system behaves in terms of electron-solid interactions. When an electron beam impinges on a solid, the propagation of the beam does not occur in a straightforward manner. Within a few atomic planes of the solid, the electrons will begin to interact with the specimen and alter course, while simultaneously generating a cascade of events that very quickly become almost impossible to quantify.

When electrons interact with the solid due to atomic charge differences between the negatively charged electron and the positive nuclei in the solid, the electron's path is changed but the change in its kinetic energy is negligible. This is called an *elastic* scattering event, as the electron is thought of elastically recovering its energy from the modification of its trajectory. Other events in which the electron's path and energy are modified are known as *inelastic* scattering events. These events include removing a solid electron from its orbit (i.e. ionization) which in turn can generate x-rays and Auger electrons, colliding with a solid electron in order to generate another free-moving electron (called a "secondary electron", or SE for short), and interacting with the solid lattice to create phonons. There are other physical interactions which could also cause inelastic scattering, but are relatively small compared to these main types of events. See Figure 2-1 for an illustration of the various types of electron-solid interactions.

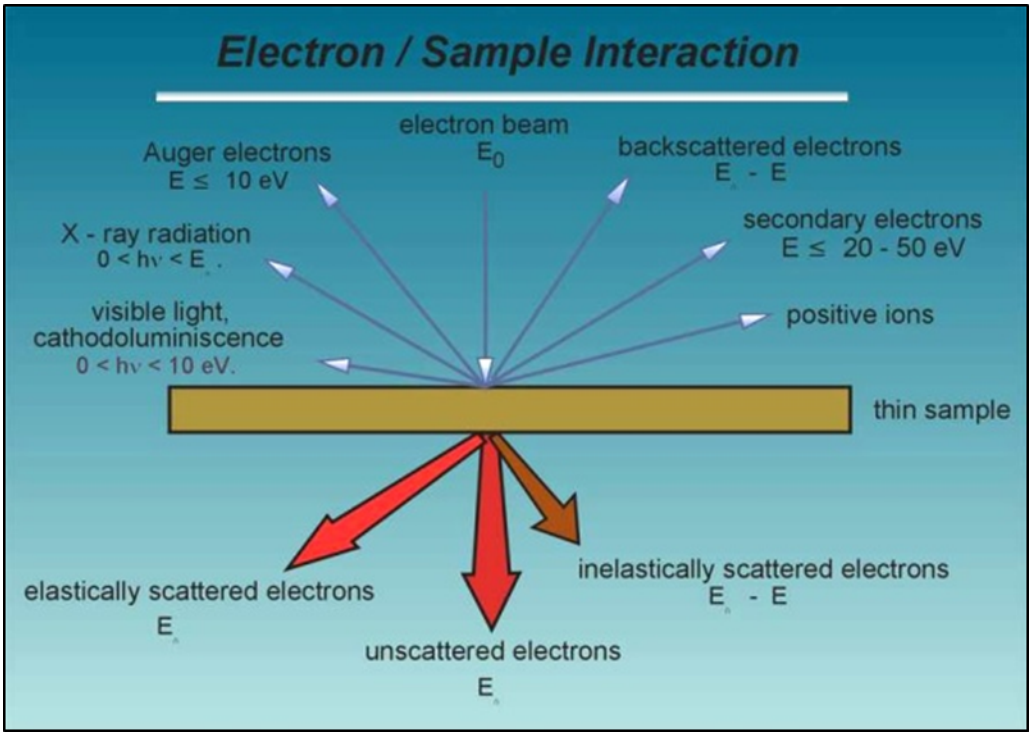


Figure 2-1: Illustration of electron-solid interactions.[101]

Some of the many consequences of electron bombardment of a solid surface.

Electrons which penetrate a sample generally are confined to what is called the "interaction volume". This 3D space is the area where the previously mentioned electron-solid interactions take place. The size of the volume is dependent upon several factors, such as the material's properties, beam energy, etc. The concept of the interaction volume is important to those studying the ultimate resolution of EBID because this volume can be much larger than the beam diameter. The shape of the interaction volume is typically depicted as tear-drop shaped as shown in Figure 2-2[102]. Experiments have been performed to visualize this region, such as cross-linking and etching PMMA at various beam currents to reveal the volume shape (Figure 2-2)[103].

The interaction volume can be thought of in terms of electron propagation through the solid. Initially, the electrons have higher energy upon entering the sample, and thus inelastic scattering predominates the neck region near the surface. As the electrons lose energy, elastic scattering allows the lateral spread of the volume. The penetration along the beam axis is greater in lower atomic number materials due to the larger mean free path. The penetration depth can also be increased by increasing the beam energy. As the penetration depth increases, so does the lateral broadening. Therefore the tear-drop shape is maintained regardless of beam energy, but its overall size changes.

When an electron enters a sample, it is designated as a "primary electron" or PE for short, because it originated from the electron beam source and not as one of the sample's electrons. After an electron travels some distance subsequent to a scattering event, it can be scattered again, and so on until the electron obtains thermal equilibrium

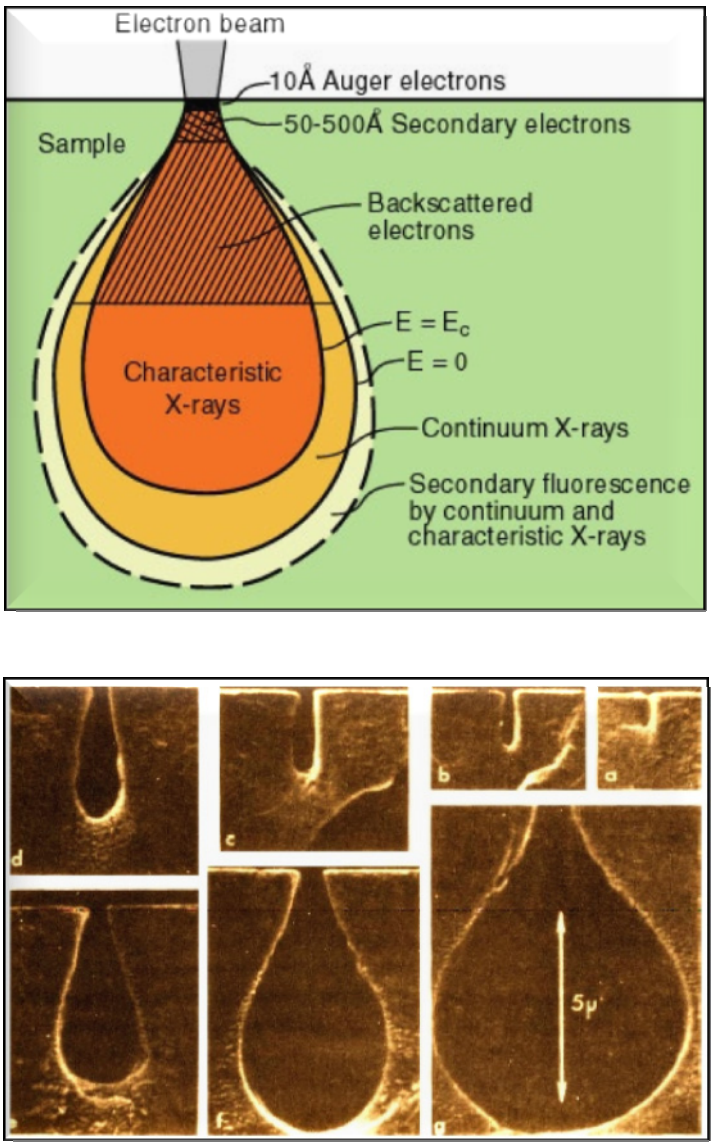


Figure 2-2: Illustration of Interaction Volume.[102,103]

The electron interaction volume was shown in PMMA by maintaining a constant electron dose but progressively increasing etch time (from a to g as indicated) to reveal successively lower energy damage amounts.[103]

with the solid or escapes the solid by overcoming the "escape potential" of the solid. This value is classically defined as the sum of the Fermi energy, E_f and the material's work function. If a primary electron leaves the sample, it is traditionally referred to as a "backscattered electron" or BSE for short, since its interactions have modified its course enough to exit the plane it entered. When dealing with the 3D environment of EBID, it is interesting and useful to designate these as BSE's if their trajectories are truly opposite to the direction of the incident electron beam. That is, if the beam is traveling in the *negative z* Cartesian coordinate direction, and the PE escapes in a direction such that it is traveling in the *positive z* direction, it is designated as a BSE. If, however, the PE exits the solid but continues to travel in the *negative z* direction (for instance, if it exits a pillar of material deposited on the surface, or if it travels through a thin foil), it is referred to as a "forward scattered electron", or FSE for short. If the energy of the electron is less than the escape potential, or if it is on a shallow angle of approach to the solid/vacuum interface (i.e. less than a "critical escape angle"), it will simply be reflected back into the solid and continue along a trajectory until it reaches thermal equilibrium.

The above listed electron types can all contribute to EBID, as shown in Figure 2-3. Note that the secondary electrons in this figure have been further described as type I or II, which will be clarified later in this description. Other emissions due to electron irradiation whose ability to dissociate precursor are negligible are not tracked by the system. The benefit of Monte Carlo modeling is that *all* emissions and sources of energy loss for the primary electrons as they are scattered in a solid do not have to be quantified. In fact, the large number of variables involved would make this task intractable.

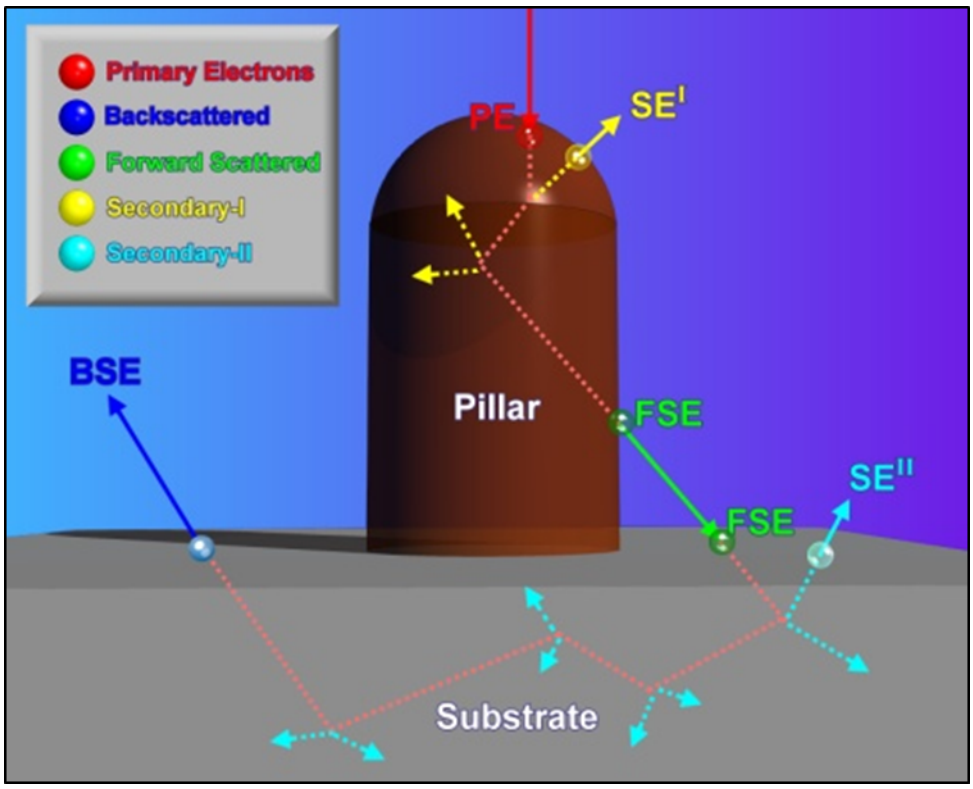


Figure 2-3: Designations of electron type.

The types of electrons which can contribute to EBID are shown in this illustration: Primary electrons (PE), backscattered electrons (BSE), forward scattered electrons (FSE), and secondary electrons (SE), which are further identified as type I or II.

Fortunately, there are simple methods of estimating energy loss and scattered trajectories which have been shown to accurately simulate electron paths in solids by statistically averaging many trajectories. These methods have been compared to experimental data by several authors, including Joy[104], Kotera[105], Ding and Shimizu[106], Wen-Zhi Li[107], and many others. While Monte Carlo modeling is not an exact recreation of experimental data, it does provide a "sensible approximation to experimental reality" according to Joy.[91]

2.3 Discretizing the System

In order to create a 3D environment for the simulation, a discretized matrix is created that forms the electron beam-gas-substrate interaction area (Figure 2-4) for the purpose of tracking gas adsorption, desorption, and electron stimulated deposition on a per unit basis. The surface surrounding and containing the circular shaped primary beam entry point is broken up into a series of 3D "voxels" of size $\Delta x \times \Delta y \times \Delta z$. These voxels are contained within a boundary region of $l \times w \times h$ where l is the length of one side of the area measured along the x-axis and w is the width of the typically square boundary in the direction of the y-axis (Figure 2-4). The height of this matrix is initially set to typically ~1nm, and expands as the growing structure requires. For a typical simulation, the variables l and w are typically chosen to be on the order of the size of the interaction volume diameter, so that most of the BSE deposition events can be registered. Any electron which crosses the $l \times w \times h$ matrix boundary is discarded. An optimum boundary region size exists per experiment, as a function of time, due to the competitive nature of

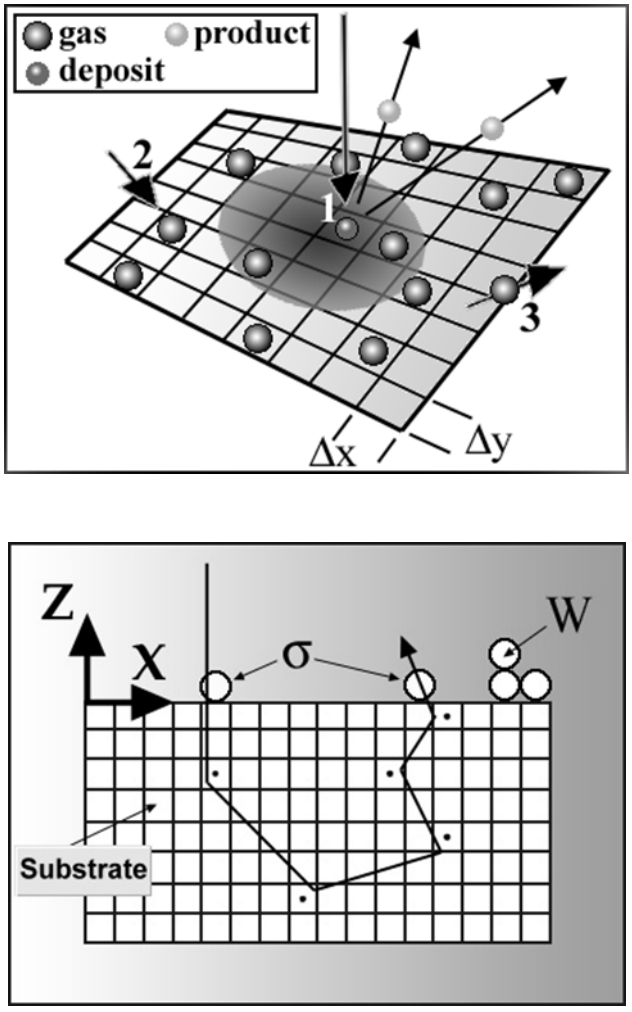


Figure 2-4: 3D Discretized Matrix.

The simulation is discretized into voxels that are $\Delta x \times \Delta y \times \Delta z$ in size. Illustrated above are the various processes that can occur on the surface over the course of a simulation: 1) electron stimulated deposition, 2) absorption, and 3) desorption. The circular electron beam is represented in the top illustration as the shaded region; the shading profile within the circular region illustrates the Gaussian nature of the beam intensity.

computing time and the resolution of collected data. If the matrix size is chosen to be too large, the computation time increases significantly, but if too small an area is chosen important information may be excluded from the boundary region. Electrons below the matrix (which is taken to be the substrate interface at z=0) are tracked regardless of their spatial coordinates. If these electrons are backscattered beyond the matrix boundaries, their emission is counted, but they cannot count toward deposition.

The voxel size $\Delta x \times \Delta y$ is chosen to contain 1 atom per voxel based on the value of S_p (the average atomic surface density) for a perfectly polycrystalline material,

$$\Delta x, \Delta y = \left(\frac{1}{S_\rho} \right)^{\frac{1}{2}} \qquad \mathbf{1}$$

where Δx and Δy represent the voxel edge length. For a simulated system using a WF_6 precursor, one tungsten atom was calculated to occupy an area of $\Delta x = 0.250$ nm by $\Delta y = 0.250$ nm. Note that this value is calculated for the atom or molecule size which is being *deposited*, since it will compose the bulk of the matrix. It is completely independent of the substrate material, since the scattering in the substrate (below the discretized matrix) does not need to be tracked on a per-voxel basis. The precursor molecule may be larger than the deposited atom, as in the case of the W-WF_6 system; however this discrepancy is accounted for by the code as described later in the "gas dynamics" section of this paper.

In static, or "spot mode" depositions, the electron beam is stationary and centered at the origin (x = 0 nm, y = 0 nm), and projected in the negative z direction. At present, the simulation can be set to simulate a Gaussian-like beam profile (typical of most SEM emitters), or a cylindrical (or "square profile") beam which has a uniform beam density across its diameter. In either case, the radius or full-width-half-max (FWHM) of the beam

is input to the simulation, and the beam profile is projected upon the x-y plane. For the Gaussian-like distribution, the intensity is represented by the following equation:

$$i_B = \int_0^{2\pi} \int_0^{\infty} i_{\max} e^{-\frac{r^2}{R^2}} \theta dr d\theta \qquad \mathbf{2}$$

where r and θ are the position coordinates and R = FWHM of the current distribution. Electron irradiation is treated in a Monte Carlo fashion but weighted to the current distribution expression in Equation 2 (Figure 2-5). For the cylindrical beam profile, the voxels contained within the circle formed by the beam radius are randomly chosen for radiation, such that the intensity profile is constant over a statistically large number of electrons (Figure 2-5).

2.4 The Plural Scattering Model

Estimating the electron-solid interactions by the Monte Carlo method involves making several thousand calculations for *each electron* that enters the sample, tracking their positions, and tracking the positions of any secondary electrons generated by the primary electron. With so many computations, it is easy to see how quickly a large simulation can be slowed by the complex computations involved. A first-order approach to Monte Carlo modeling of electron-solid interactions was described by Joy in 1991 called the "single scattering model".[87] The physics behind this model made two assumptions in order to determine the path of an electron through a solid. First, the changes in trajectory (i.e. scattering angle) of an electron are *only* due to elastic events. Joy neglects small changes in trajectory due to inelastic events, and therefore greatly

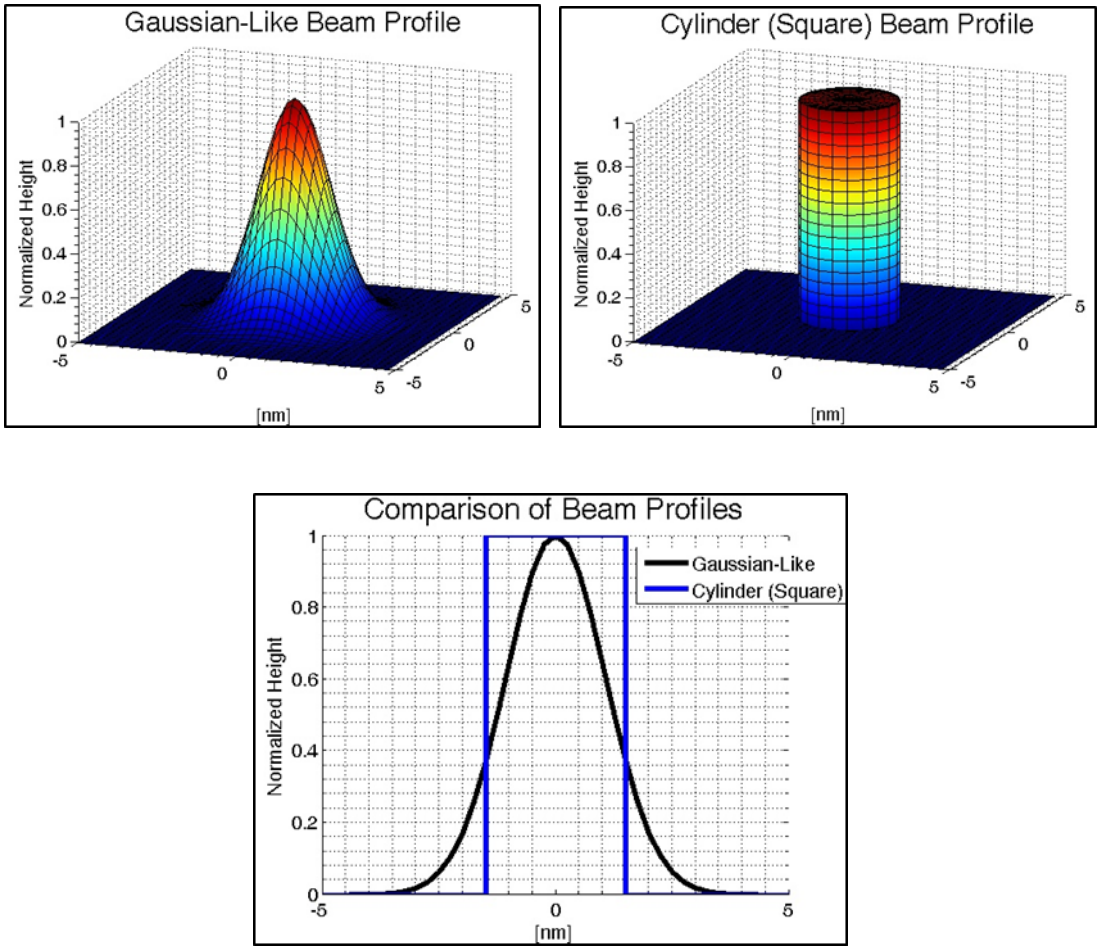


Figure 2-5: Beam profile types.

Illustration of Gaussian-Like beam profile (top left) and cylinder (or square) profile. 5 million electrons were simulated to generate these normalized intensity distributions. The lower illustration is a cross-section through each type showing their relative shapes. The beam radius for both profiles was 1.5nm.

simplifies the number of calculations for each electron. The second assumption is that the electron loses energy continuously along its path at a rate determined by the material's "stopping power". This allows for all energy losses due to inelastic events to be accounted for using only one variable.

The single scattering model is a very accurate method of approximating the electron path through a solid, but very computationally intensive. A more popular model of simulating electron-solid interactions is called the "plural scattering model" which was first described by Curgenven and Duncumb in 1971[108] and later modified by Joy in 1995[91]. This model uses the same physical assumptions as the single scattering model, except that it only calculates the effect of a set number of scattering events in a solid, as opposed to all of them before coming to rest. Most of the equations which follow are taken from Joy's 1995 text on the subject[91], with exceptions noted.

The electron energy loss term used to simulate the energy loss due to inelastic events (dE/dS) is given by the Luo and Joy [109,110] modified Bethe expression:

$$\frac{dE}{dS} = -78500\frac{\rho Z}{AE}\log\left(\frac{1.166*(E+0.85*J)}{J}\right) \qquad \textbf{3}$$

where ρ is the material density, Z is the atomic number, A is the atomic weight, E is the electron energy, and J is the mean ionization potential. The expression is applicable down to primary electron beam energies of 100 eV and has units of [keV/cm]. The mean ionization potential J [keV] represents the average energy loss per unit distance due to the host of inelastic energy loss pathways mentioned previously, and is given by:

$$\mathrm{J} = \left(9.76Z + \frac{58.5}{Z^{0.19}}\right)\times 10^{-3} \qquad \textbf{4}$$

The Bethe range (R_B) [cm] is the total length the electron travels in the sample if the electron fails to escape from the sample. According to the plural scattering method, this range is divided into segments, and a new trajectory is calculated per segment to account for elastic scattering. The Bethe range expression

$$R_B = \int_0^E -\left(\frac{dE}{dS}\right)^{-1} dE \qquad \textbf{5}$$

is integrated numerically to solve for R_B, and this range is divided into 50 segments[109] giving 50 computational steps per incident electron. This number was taken as a compromise between accuracy and computing time by Joy[91] and can easily be increased in the code as computing speeds improve in the years to come. Figure 2-6 shows the Bethe range calculated for SiO_2, Germanium, and Tungsten as a function of beam energy. The energy at each computational step E_n is also numerically evaluated using Equation 6:

$$E_n = E_{n-1} - \int_{51}\left(\frac{dE}{dS}\right)dS, \;\; E_1 = E_o, \;\; E_{51} = 0 \qquad \textbf{6}$$

where E_o is the incident beam energy and E_{51} is set to zero to force the electron to complete energy loss after a distance R_B is traveled.

Elastic scattering controls the trajectory change the electron experiences with each of 50 set scattering events. The azimuthal scattering angle ψ is chosen completely at random as follows:

$$\psi = 2\pi \cdot rand \qquad \textbf{7}$$

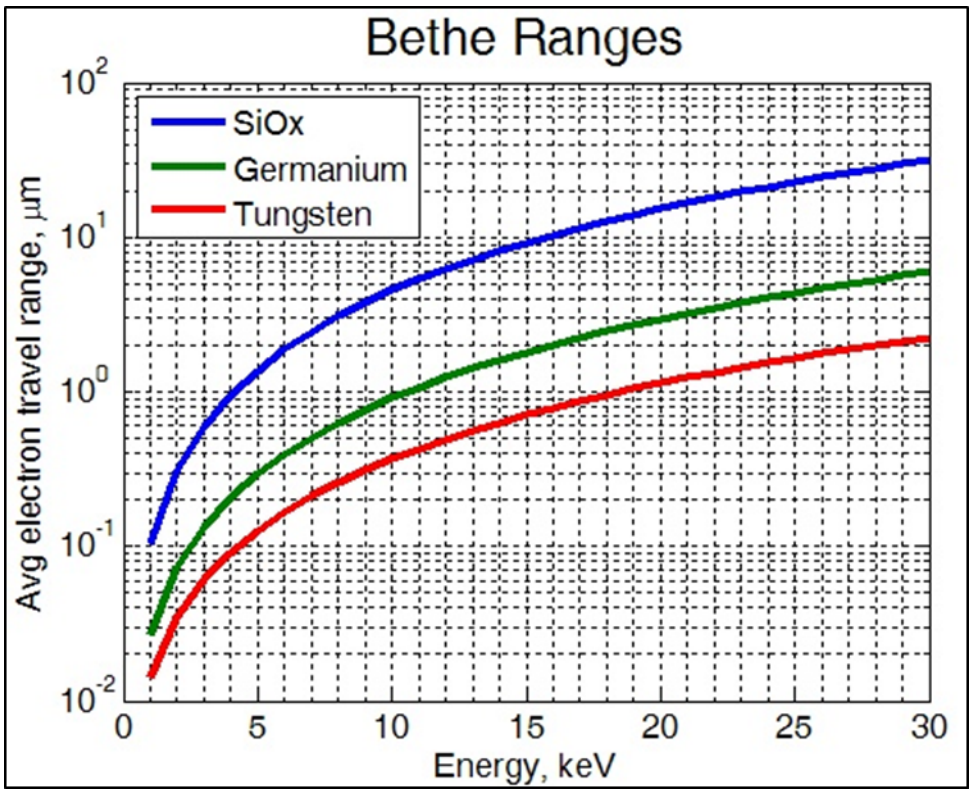


Figure 2-6: Bethe range as function of beam energy.

Bethe ranges calculated by the simulation for various materials. The Bethe Range expression which uses the modified stopping power equation by Joy and Luo[109,110] is integrated using a trapezoidal numerical integration technique.

and the angle ϕ the electron is scattered from its previous trajectory is a function of the electron's current energy value and the host material's atomic number:

$$\phi = 2\tan^{-1}\left\{\left(\tan\frac{\phi_o}{2}\right)\left(\frac{E_o}{E}\right)\left(\frac{1}{\sqrt{rand}}-1\right)\right\} \quad \textbf{8}$$

where tan (ϕ_o/2) is calculated by Joy's approach [109] combining approaches of several authors:[111,112]

$$\phi_o = 2\tan^{-1}\left\{0.016697 + 0.55108E^{0.1382-\frac{0.9211}{\sqrt{Z}}}C - 0.96777\left(E^{0.1382-\frac{0.9211}{\sqrt{Z}}}C\right)^2 + 1.8846\left(E^{0.1382-\frac{0.9211}{\sqrt{Z}}}C\right)^3\right\} \quad \textbf{9}$$

and

$$C = 0.1904 - 0.2235\ln Z + 0.1292(\ln Z)^2 - 0.01491(\ln Z)^3 . \quad \textbf{10}$$

See Figure 2-7 for an illustration of this geometry.

These equations form the core of the simulation's Monte Carlo model for the primary electron path through the system. See Figure 2-8 for example simulations of 1 and 5 keV electrons in a tungsten substrate. It is important to note that the simulation checks each scattering step to determine the material present. If the electron travels into a different material, the trajectories and energy lost is re-calculated based on that material's stopping power. This allows for multiple materials to be used in the simulation, for example depositing one material onto a substrate of a different material. Another possibility would be a pre-existing structure composed of multiple layers of material which would be modified by EBID. It was the intent from the creation of this simulation

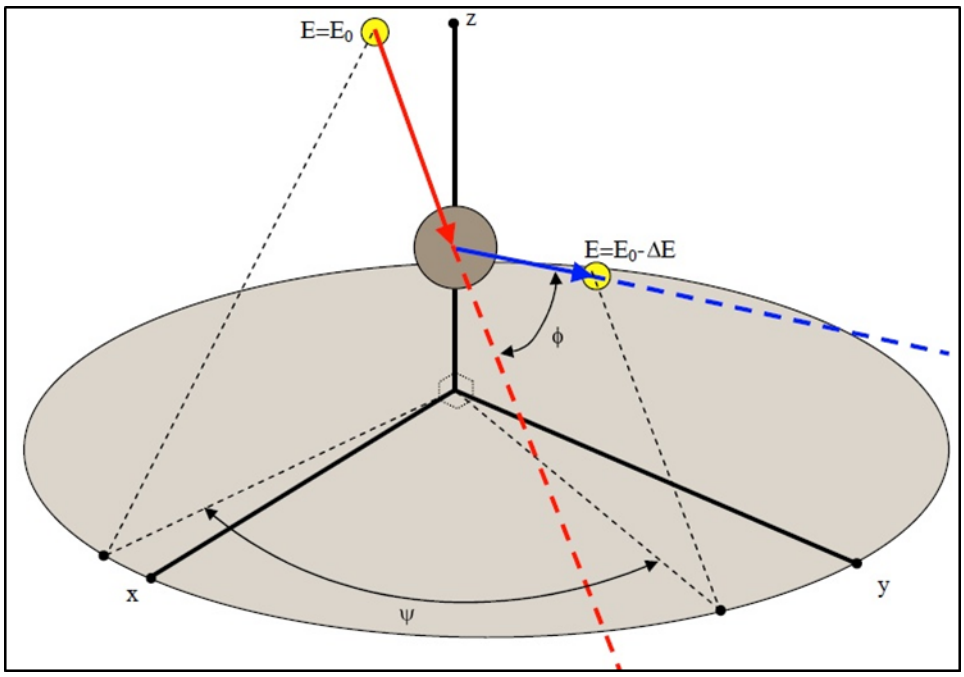


Figure 2-7: Electron Scattering Geometry.[46]

In this illustration, the electron undergoes a scattering event where its energy is decreased by the quantity ΔE, and its trajectory is modified by the azimuth angle (Ψ) and scattering angle (Φ).

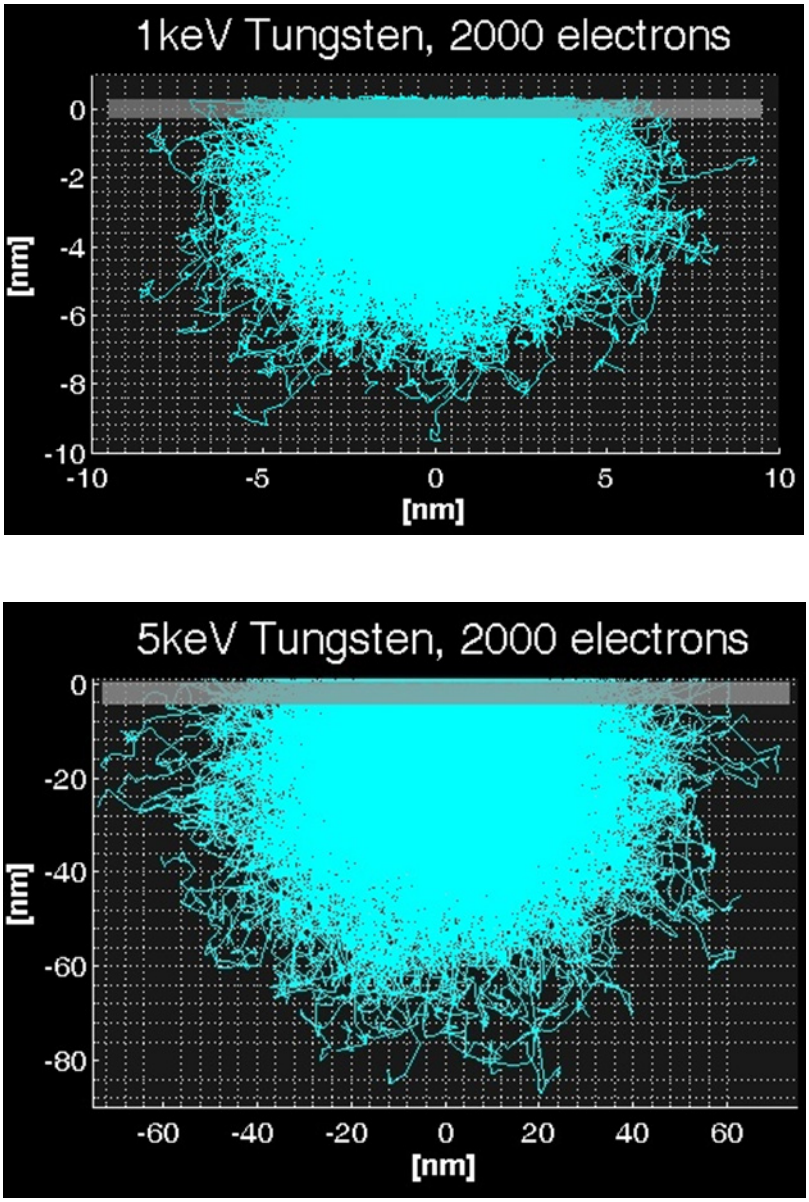


Figure 2-8: Example Monte Carlo.

Simulated Monte Carlo in tungsten, 1keV (top) and 5keV (bottom).

to utilize complex 3D-environments rather than a radially-symmetrical dependence developed by previous authors. This is but one unique feature of this simulation which enhances its usefulness.

Figure 2-9 shows an electron which has exited a structure and is propagating through vacuum until it enters the substrate. In this example, deposition has occurred at the exit point and the re-entry point of the electron, as well as the first entry point where the primary electron first encountered the solid.

2.5 Secondary Electrons

Secondary electrons (SE's) are generated by inelastic scattering events in the solid by the primary electron. During this interaction, some of the energy of the primary electron is transferred to a free electron in the solid. This results in a "cascade" of other secondary electrons generated from this initial secondary electron. Attempts to model SE generation have been thoroughly explored, resulting in a very detailed process to accurately account for these events.

Initially, Chung and Everhart used an exponential decay law with quantum theory to calculate the form of the SE energy distribution[89,113,114]. The simulation of secondary electrons using Monte Carlo techniques was first proposed by Koshikawa and Shimizu[93] in 1974, where the cascade of secondary electrons was generated by the PE traveling in a straight line. Thus, SE's from backscattered electrons were neglected. A more thorough analysis of SE generation would take into account their generation from PE's and BSE's with free and valence electrons, as well as from the contribution of Plasmon decay. These

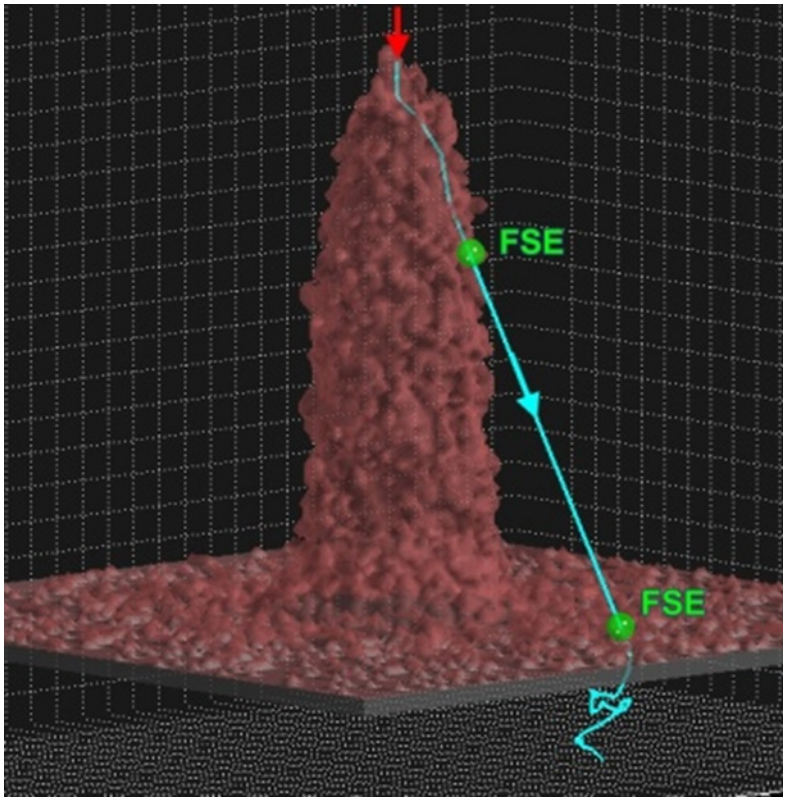


Figure 2-9: Monte Carlo Trajectory Example.

Simulation of an electron trajectory entering a feature (red arrow), exiting the structure, propagating through vacuum and re-entering the solid. Since the trajectory is in the *negative z* direction (i.e. toward the substrate), it is classified as a Forward Scattered Electron (FSE). The green spheres indicate possible FSE dissociation sites.

processes are difficult to model, as the parameters required for each are known for few materials. Instead, a "fast secondary model" for SE generation was proposed by Murata *et al.* in 1981[115], and greatly simplifies the process by only taking into account "knock-on" collisions with free electrons. Joy adopted this model in 1984[116], which more accurately modeled SE's from the PE's, BSE's, and other SE's. Limitations in computing power did not examine SE's below 200eV, however. Secondaries of energy <200eV were simply assumed to escape according to an exponential decay law. Ding and Shimizu[117]proposed a theoretical model based on the dielectric function which took into account the contribution of valence electrons to inelastic scattering processes. Luo and Joy proposed a hybrid model for SE simulation by combining the exponential decay and cascade process[118], but it was still restricted to low energy secondary electrons. In fact, most of the work up to this point only dealt with low energy SE's (i.e. "slow electrons"), neglecting SE's which could be generated at higher energies with the use of higher beam energy. Kotera in 1989[105,119] and Luo and Joy in 1990[120] updated this model to include these "fast electrons" (>100eV), which utilized Rutherford cross sections for the fast electrons. (Lower energies tend to scatter SE's spherically, according to Koshikawa and Shimizu[93]). Specifically, Joy used the fast secondary electron model without tertiary electrons considered, which resulted in SE spatial distributions in the middle of the ranges presented by other authors.[116] Kotera used a hybrid model that included the Koshikawa and Shimizu cascade only for slow electrons, while fast electrons are treated by single scattering. Auger and plasmon contributions to SE generation were later incorporated into this model by Kotera in 1990,[121] however the differences in results from Joy's model were almost negligible.

The secondary electron model for this simulation is a modified version of Joy and Kotera's interpretation of the equations. For brevity, the derivation of these equations will not be discussed here; rather references will be listed so the reader may consult the literature for more information and details.

Since the majority of work was planned to be on "bulk" samples, it was not deemed necessary to waste computing time on SE's which would probably not emerge from the sample surface. Therefore, secondary electron generation is only calculated within the substrate at depths up to $z < 5\lambda$ below the solid surface, where λ is the inelastic mean free path (IMFP, the mean distance between inelastic scattering events) of the secondary electron in the specific material and is typically in the range of 0.5-3 nm depending on the electron energy. Literature (i.e. experimentally determined) values for the IMFP were used in the simulation if available. For example, the IMFP of electrons in tungsten is calculated for energies > 50eV by use of the Tanuma-Powell-Penn (TPP-2M) equation[122]:

$$\lambda(\text{Å}) = \frac{E}{E_p^2\left[\beta \ln(\gamma E) - (C/E) + (D/E^2)\right]} \qquad \textbf{11}$$

where β=-0.10+0.944/(E_p^2+ E_g^2)0.5+0.069ρ0.1, γ=0.191 ρ-0.5, C=1.97-0.91U, D=53.4-20.8U, U=N$v\rho$/M = E_p^2/829.4, ρ is the density (g cm-3), Nv is the number of valence electrons per atom, M is the atomic weight, E_g is the band gap energy (eV) for nonconductors.

For energies <50eV, the mean free path was estimated by fitting a polynomial to the known IMFP curves for Au and Cu[106], which are similarly shaped but shifted in energy

relative to tungsten. A shift was applied to make the calculation continuous for tungsten over the entire energy range of interest, such that the simulation picks which equation set to use for IMFP calculations based on the instantaneous energy of the electron. The combined IMFP curves are shown in Figure 2-10. Note that traditionally, SE's are defined as those electrons emerging from the surface with an energy <50eV. Higher energy SE's are counted as BSE's by most detectors. This simulation, however, makes no such distinction, which is why the TPP-2M equation is used to calculate the IMFP for SE's with energies >50eV.

The number of secondary electrons produced per scattering step n_{SE} is assumed to be inversely proportional to the energy required to generate a secondary electron ε and proportional to the energy difference of the scattering electron at the previous scattering step and the energy at the new scattering event.

$$n_{SE} = \frac{(E_{n-1} - E_n)}{\varepsilon} \qquad \textbf{12}$$

By using Equation 12 it is assumed that the secondary electrons are emitted in an isotropic fashion from their point of origin and the mean free path of the electron is used as an attenuation length and hence, the probability of secondary electron escape from the substrate falls off as an exponential term from the point of origin of the secondary electron.

An energy amount is ascribed to each generation event of secondary electrons as opposed to ascribing a discrete energy to each secondary. A fast secondary electron is

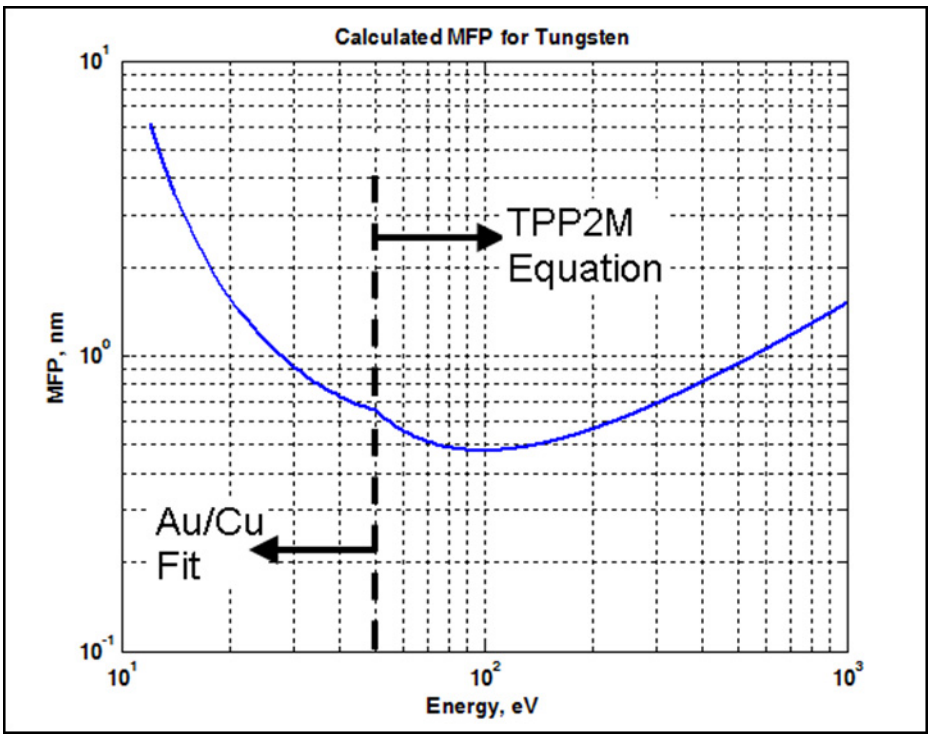


Figure 2-10: Inelastic Mean Free Path

Inelastic Mean free path calculation showing the Tanuma-Powell-Penn (TPP-2M) equation above 50eV, and a polynomial fit to the Au-Cu MFP curve below 50eV.

generated from the primary electron at each scattering point as proposed by Koshikawa and Shimizu[93] and later used by Kotera[119] by choosing a random number to represent:

$$rand = \frac{\int_{Ec}^{E} S(E)dE}{\int_{E_C}^{E_P} S(E)dE} \qquad \textbf{13}$$

where E is the energy of the secondary electrons, E_C is the surface potential barrier (sum of the Fermi energy and work function), and E_P is the energy of the primary electron that excites the secondary electron (Figure 2-11). This allows the energy to be calculated as follows:

$$E = \left(\frac{R_E E_F - A E_C}{R_E - A} \right) \qquad \textbf{14}$$

where $A=\frac{E_P - E_F}{E_P - E_C}$. Creation of the slow SE is assumed to be spherically symmetric[121] therefore the scattering and azimuth angles are randomly selected between 0° and 360°.

This slow SE then travels in the direction determined by the random trajectory described above, and its path length is the IMFP calculated based on its material and energy. This slow SE then initiates a cascade of other slow SE's which are also taken from Kotera[105]. The initial SE generates two SE's (provided its energy is high enough) as shown in Figure 2-12. The first SE has an energy value (originally theorized by Wolff in 1954[123]) given by:

$$E' = E\sqrt{rand} \qquad \textbf{15}$$

where E is the energy of the SE that creates this cascade and *rand* is a random number.

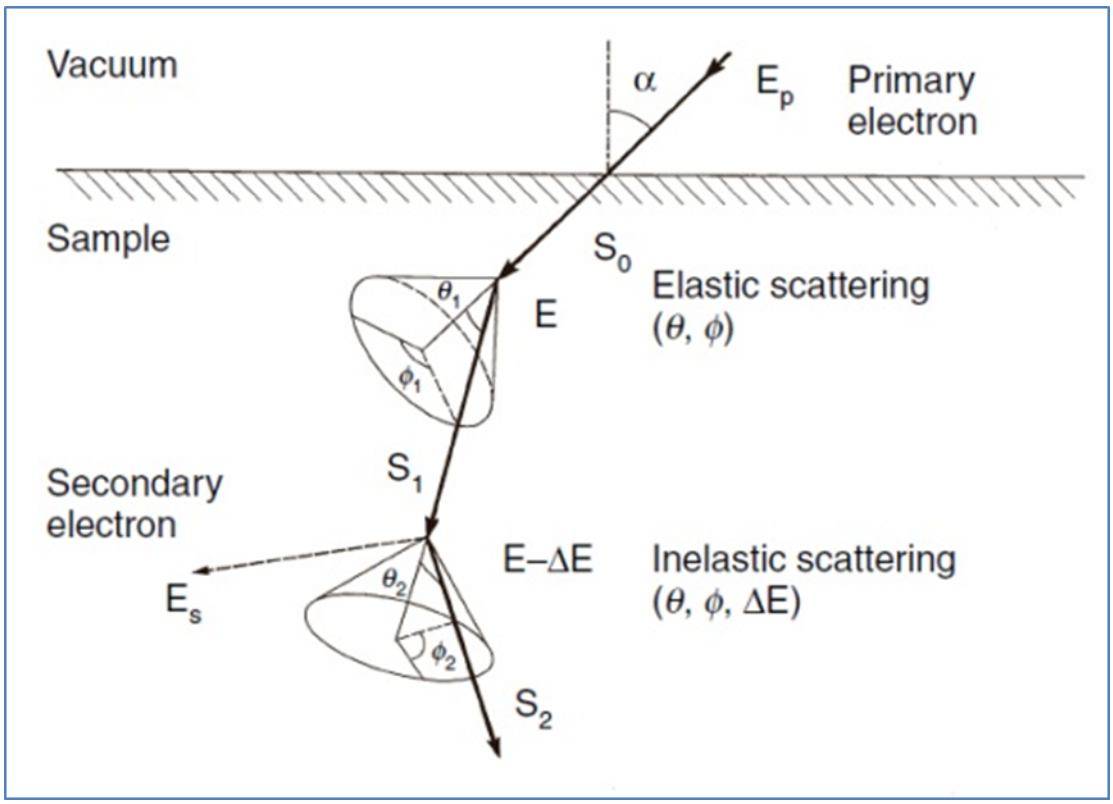


Figure 2-11: SE generation[106]

Schematic model of SE generation by Ding and Shimizu. The scattering angles and distances involved in the SE generation event by a PE are calculated based on inelastic scattering equations.

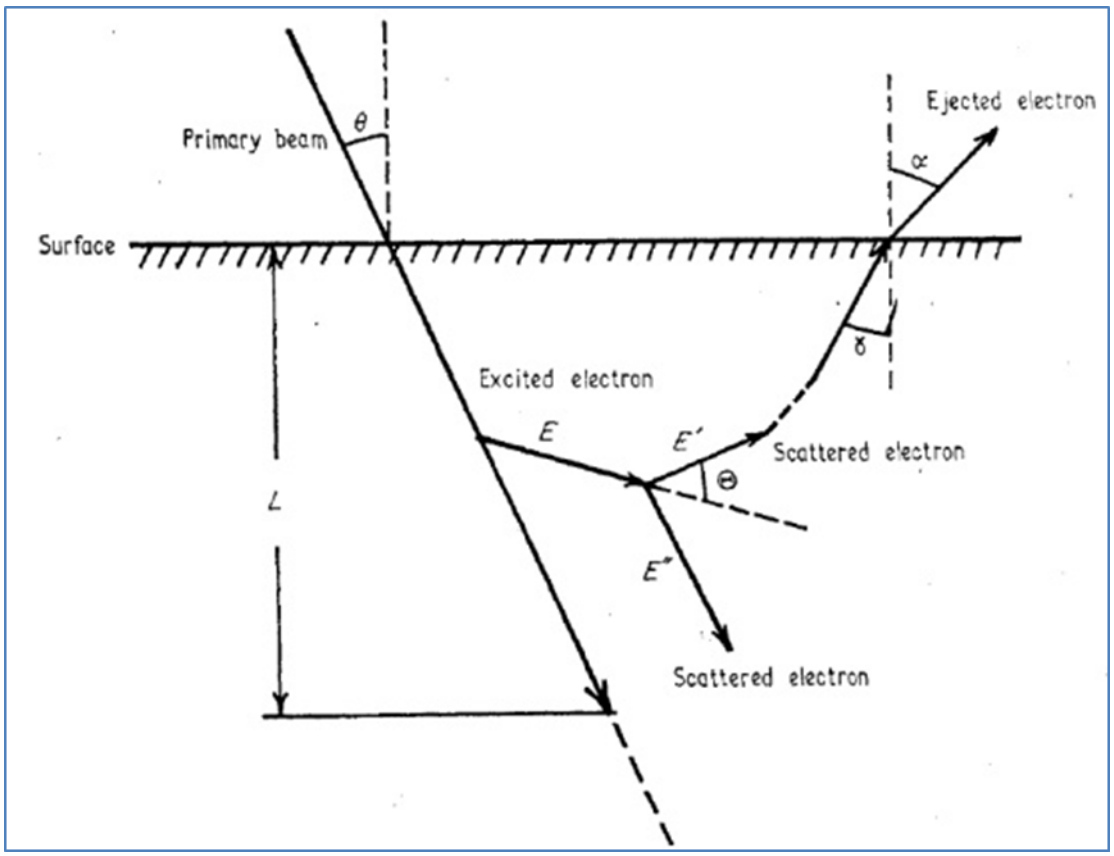


Figure 2-12: SE Cascade generation[93]

Model of the SE cascade process, proposed by Koshikawa and Shimizu in 1974.

The scattering angle θ can then be obtained from the relation $E'=E\cos^2(\theta)$. The second SE is then given the energy:

$$E'' = E\sin^2(\theta) \qquad \textbf{16}$$

and is randomly assigned a scattering angle. In order to preserve spherical symmetry, the previous SE's azimuth angle is simply incremented by 180°. The distance traveled by each cascade SE was taken to be the IMFP which is calculated based on the electron's new energy as described above. The cascade continues until the SE's escape the surface of the material, or their energies are too low to escape the material (at which point they are neglected).

The escape probability P of the secondary electrons depends on the material's Fermi energy, work function, and the electron's energy, as described by Joy and Luo[120]. It is derived from the maximum allowable value of the escape angle and the normal component of momentum, and yields the total reflectance probability as follows:

$$P(E) = 1 - \sqrt{\frac{E_F + \Phi}{E}} \qquad \textbf{17}$$

The result of applying this probability is a reduction in emission at the lower energy portion of the emission spectrum, which has been shown by Kotera[105] and others to nearly reproduce what is observed experimentally (see Figure 2-13).

Like Joy's model, tertiary SE generation from the PE knock-on event is neglected in order to save computing time. All SE's involved in the cascade model are treated as slow secondary electrons, governed by Equations 15 and 16 above. For a more rigorous

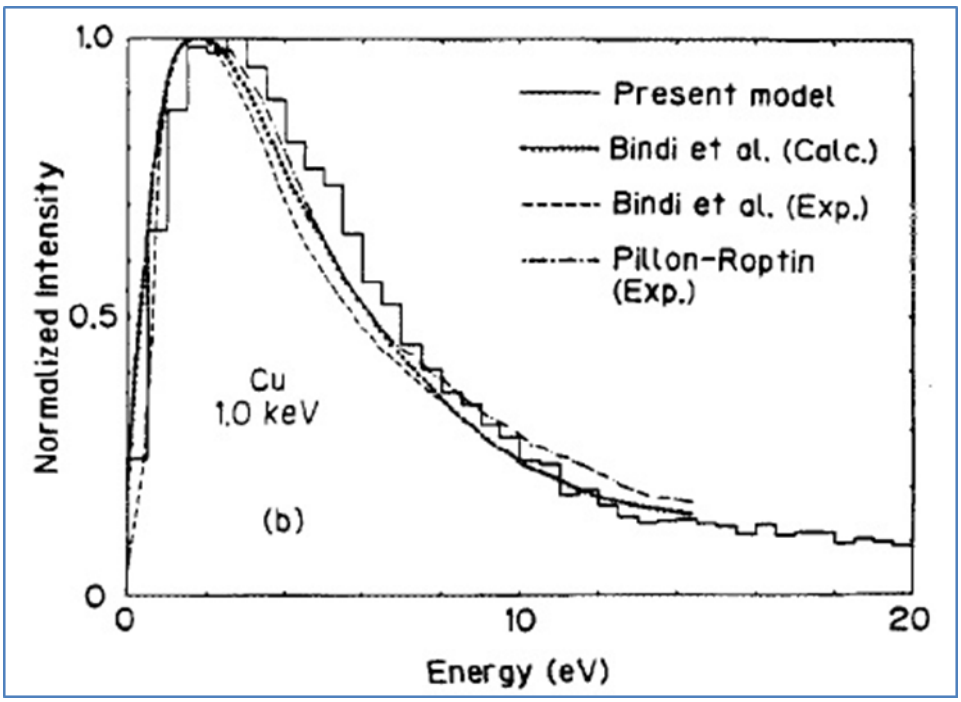


Figure 2-13: Comparison of SE emission spectra[105]

Example of the Kotera model's accuracy compared to other works. Here, the SE process in Cu is modeled at 1keV. Energy and angular distributions were shown to have good agreement with results from other authors.

treatment of SE's, each should have its energy tested to see if it is a fast or slow SE. Fast SE's should be computed using a single scattering model which accounts for elastic and inelastic scattering. Deviations from experimental values of SE generation are observed at high energy values due to this approximation.

It is often useful to discriminate the SE's which are generated by the PE upon entry into the solid (defined as type I, or SE^{I}) from those that are generated by BSE's or FSE's before exiting the sample (type II, or SE^{II}) as shown in Figure 2-14. The simplest way to discern the SE^{I} events from the SE^{II}'s is to examine which of the 50 scattering steps initiates the SE generation. In this simulation, a value is calculated which represents the "cut-off" scattering step after which all SE's will be classified as SE^{II}'s. Determining this value involves solving two problems. First, when using the plural scattering Monte Carlo method, the first scattering event of the incident primary electron in the sample may take place at depths sufficiently deep such that at high electron energies, roughly > 5 keV, secondary electrons created have a low probability of escaping from the first scattering depth due to their very short mean free paths. To avoid this problem, the first electron trajectory along the initial penetration into the substrate between the 1st and 2nd scattering events is discretized such that SE^{I} generation takes place at a random increment along this first trajectory. The second problem to solve is to determine how many subsequent scattering events will be counted as SE^{I} generation sites. This value is called the SE^{I} Boost term, calculated as follows:

$$SE^{I}\,Boost(mat'l) = ceil\left[\frac{\lambda\left(mat'l, E_o\right)}{Step\left(mat'l\right)}\right] \qquad \textbf{18}$$

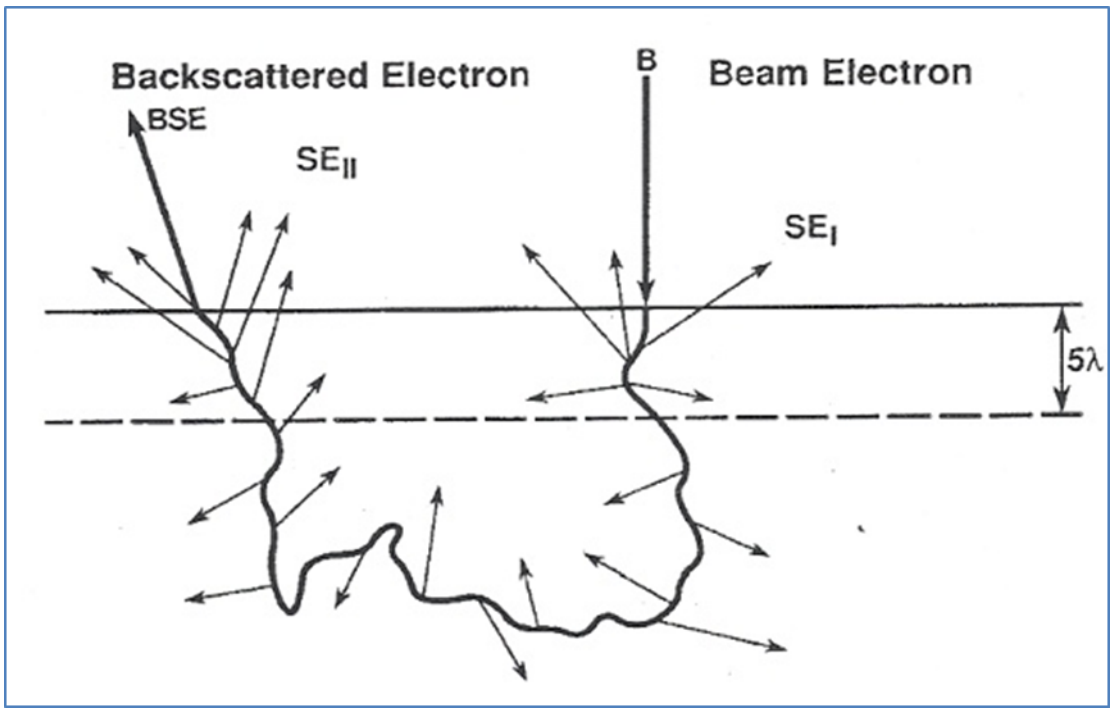


Figure 2-14: SE^{I} and SE^{II} Generation.[124]

Illustration of SE^{I} vs. SE^{II} generation events. For this simulation, a cut-off scattering event was calculated to determine which could generate SE^{I}'s and which would generate SE^{II}'s. This is because EBID generates complex 3D structures which rise above the bulk specimen.

where "ceil" is the rounded up integer value of the ratio of the mean free path and the Plural scattering step size (which is defined as $1/50^{th}$ of the Bethe Range). Note that this boost term is material and energy dependent and calculated based on the inelastic mean free path at the incident energy. Thus at lower energies in a dense material, this can have a value of 5 or 6 (as is the case of 1keV tungsten). Higher energies return a lower boost term because of deeper penetration. A typical boost term for 5keV tungsten is 2. A higher boost term will increase the number of SE^{I} events, while decreasing SE^{II}'s. In Figure 2-3, the first two scattering events generate SE^{I} events, and all subsequent events are SE^{II}. In this case, the SE^{I} *Boost* would be equal to 2.

2.6 Backscattered and Secondary Electron Yields

One of the ways to verify accuracy of the Monte Carlo simulation is to examine the backscattered (η) and secondary electron (δ) yield. The secondary electron coefficient δ is the result of the sum of two components namely the contribution from SE^{I}'s (δ_1) and SE^{II}'s (δ_2):

$$\delta = \delta_1 + \eta\delta_2 \qquad \textbf{19}$$

δ is defined simply as i_{SE} / i_b, the secondary electron current divided by the incident beam current.

$$\delta = \frac{i_{SE}}{i_b} = \frac{i_{SE_I} + i_{SE_{II}}}{i_b} = \frac{i_{SE_I}}{i_b} + \frac{i_{SE_{II}}}{i_b} \cdot \frac{\eta}{\eta} = \left[\frac{i_{SE_I}}{i_b}\right]_{\delta_1} + \left[\frac{i_{SE_{II}}}{\eta i_b}\right]_{\delta_2} \cdot \eta \qquad \textbf{20}$$

By algebraic manipulation, the individual expressions for both δ_1 and δ_2 are derived in Equation 20 where δ_1 is the ratio of the SE_I current to the incident beam current and δ_{II} is the ratio of the SE_{II} current to the backscattered electron current.

Applying Kirchoff's current law to an electron irradiated specimen yields an expression including current signals from all three electron species. Figure 2-15 shows a schematic diagram of the current flow in an electron-irradiated sample. The Kirchoff current balance from Figure 2-15 is written in the form

$$i_b^{PE} = \frac{i_s}{\left[1-(\eta+\delta)\right]},\ \ i_{out}^{BSE} = \eta i_b^{PE},\ \ i_{out}^{SE} = \delta i_b^{PE} \qquad \textbf{21}$$

where i^{BSE} an i^{SE} are the backscattered and secondary electron currents, respectively, and i_b is written as the dependent variable because η and δ are material dependent properties. Practically, i_s is measured during experiments and if η and δ are known experimentally for the specific beam energy, i_b may be calculated. Alternatively, a faraday cup can be used to directly measure i_b.

The relative efficiency of backscattered electrons that can produce secondary electrons (i.e. SE^{II}'s) is called β, the beta coefficient. It is defined as:

$$\beta = \frac{SE2}{\eta SE1} \qquad \textbf{22}$$

where SE1 and SE2 are the number of SE^{I} and SE^{II} electrons leaving the surface, respectively. It typically has values between 2 and 7, and can be compared to values measured experimentally, such as those reported in Luo and Joy[120], Drescher *et al.*[125] and others. It is used in this simulation merely as a sanity check to ensure the yield ratios are properly balanced.

For this simulation, the secondary electron yields were of particular importance, therefore small adjustments to the yield can be performed by the simulation which will

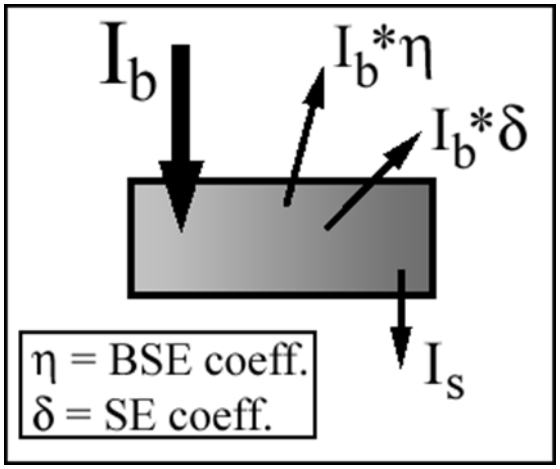


Figure 2-15: Illustration of beam current components.

Illustration of how the beam current i_b is divided into the sample current (i_s) and emitted current from backscattered electrons ($i_b*\eta$) and secondary electrons ($i_b*\delta$).

artificially increase or decrease the SE generation in order to further enhance accuracy when comparing the total SE yield to experimental results. Simple empirical simulations that incorporate experimental results to "calibrate" SE emission have also accurately predicted the energy profiles of emitted SE's [120,126]. Stark et al. for example used Monte Carlo simulations to qualitatively predict the feature size produced by the EBID of palladium acetate [59]. To obtain accurate SE yields for calibration, a "universal law for SE yield" was taken from Lin and Joy's database of SE yield data [109] with the necessary inputs taken from the most recent publication of the CRC Handbook of Chemistry and Physics [127]. The target SE yield (δ) for Tungsten at 1keV was calculated by this method to be 1.3 SE's per PE. See Figure 2-16 for the Universal Law plot for tungsten.

Two input factors were adjusted so that the SE yield from the flat substrate (i.e. no EBID - only electron-solid Monte Carlo) would match that of the experimental yield. The first factor was called "*SEfactor*", which is a number between 0 and 1 that serves as a general regulator for SE generation. At each scattering step, a random number is compared to the value of *SEfactor*, and if that random number is less than *SEfactor*, SE generation takes place. By this method, the user can throttle SE generation from 100% to 85% by changing *SEfactor* from 1.0 to 0.85. The second factor is "*cascades*", which controls the number of possible SE cascade events generated from each SE. Typically, this value is set between 1 and 4 and will saturate the yield at higher values (due to the fact that SE's lose energy along the cascade and eventually will not have enough energy to escape). By changing these two factors (*SEfactor*=0.85, *cascades*=1), the secondary

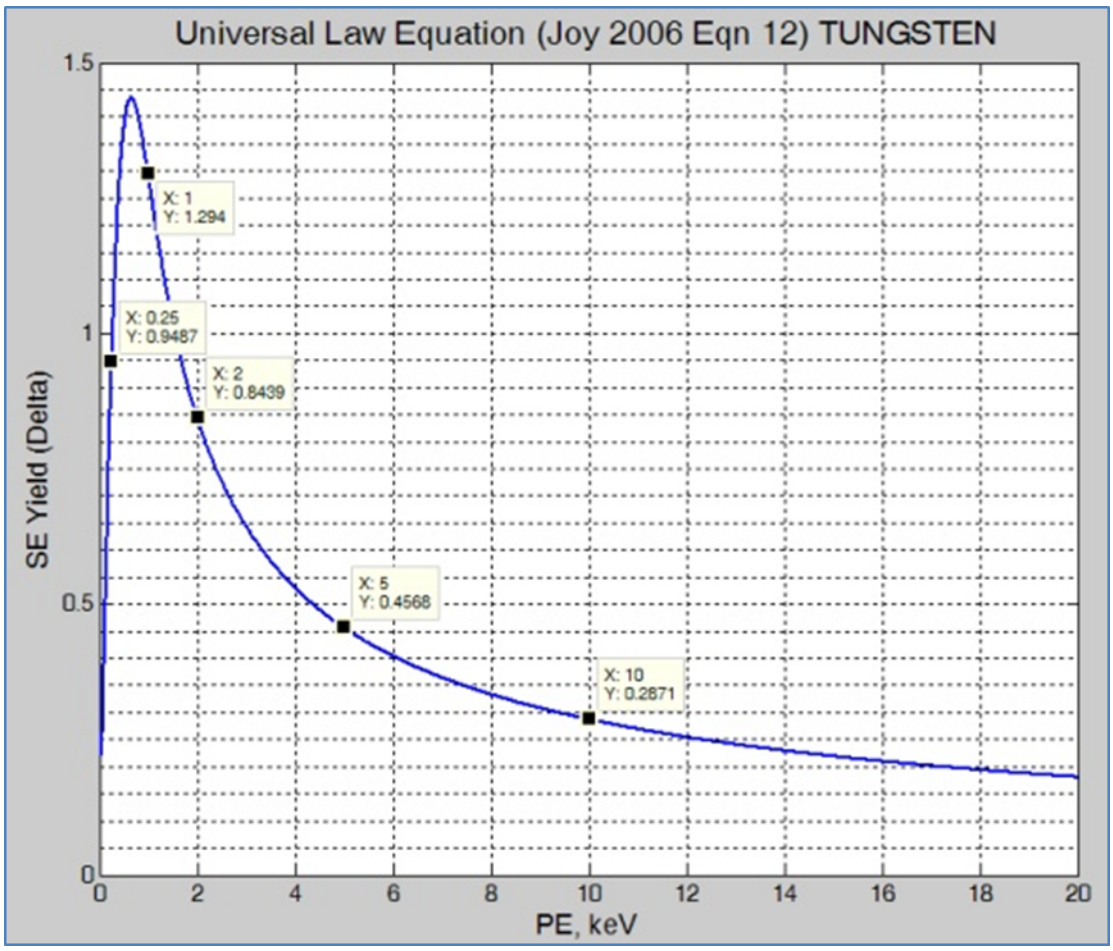


Figure 2-16: Universal Law Plot for Tungsten SE Yield.[109]

The Universal Law was used to get the best approximation for SE Yield of the materials involved in this simulation.

yield of tungsten at 1keV is 1.3, which is similar to what is observed experimentally and calculated by the universal law.

BSE yields are automatically calculated by the simulation via the Hunger-Küchler-Love-Cox-Scott (HKLCS) model from within Joy's Monte Carlo algorithm.[91] The simulation tallies the emitted backscattered electrons and compares the BSE/PE ratio to the calculated value in order to verify accuracy of the model. For example, the experimental and calculated values of η are both 0.43 for tungsten at 1keV.

Example SE and BSE emissions are plotted as a function of emission energy in Figure 2-17. These spectra were obtained by simulating 100,000 electrons on a tungsten substrate at 1keV. Note that the SE yield reaches a maximum around 50eV, but decreases with decreasing energy. Without the reflection term in Equation 17, the SE emissions would continue to increase as the energy decreased. Since the reflection term decreases the emitted SE's of very low energy, a maximum in the SE emission spectra is observed around 50eV. Experimental BSE and SE yields from tungsten at 1keV are also shown in Figure 2-17 for comparison purposes.

2.7 Dissociation Cross Section

The probability, Q, of electron-induced molecular dissociation per incident primary electron is governed by the following analytical expression that represents a macroscopic estimation of the probability

$$Q_{analytical} = \frac{\theta \cdot S_{\rho}}{n_{PE}} \cdot \int_{E_i}^{E_f} n_x(x,E) \cdot \sigma(E) dE \qquad \textbf{23}$$

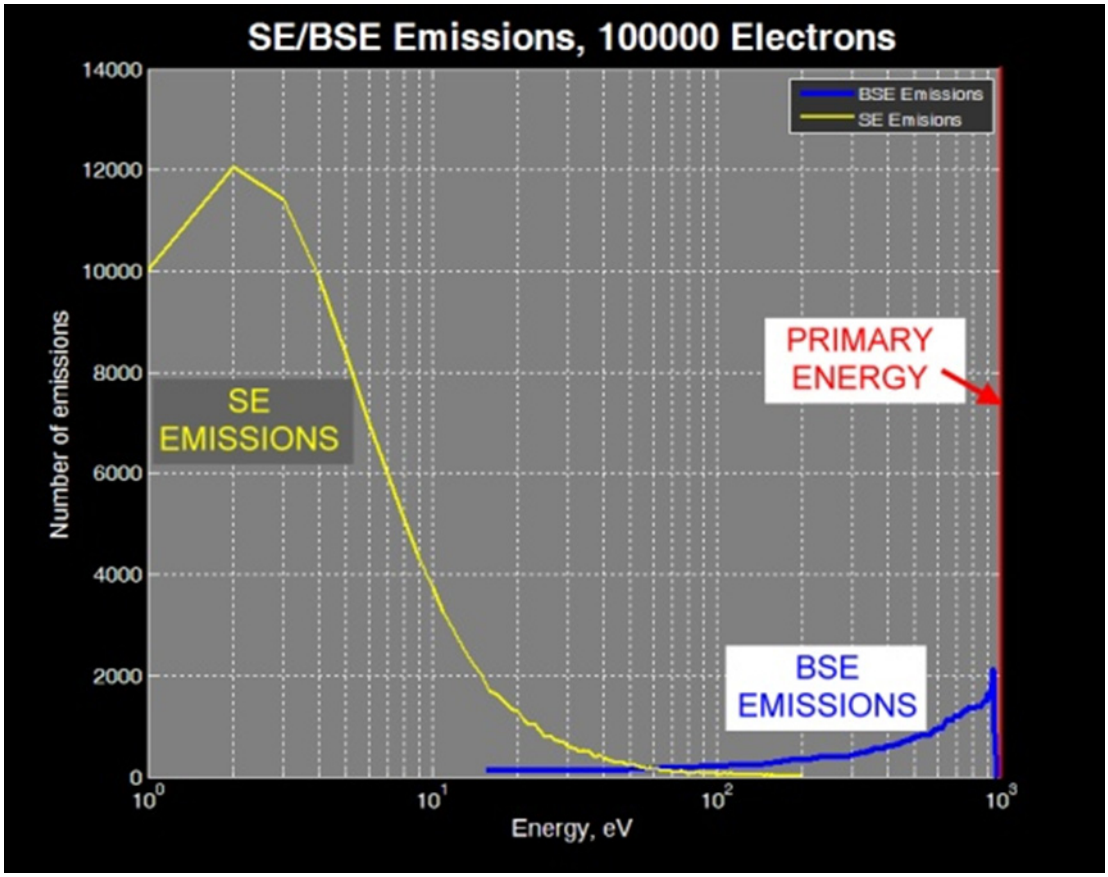


Figure 2-17: Simulated BSE and SE Emissions for Tungsten.

where $n_x(E)$ is the electron energy distribution of the particular electron species and where x = SE, BSE, FSE, or PE, $\sigma(E)$ is the dissociation cross-section for the precursor gas species and θ is the percentage surface coverage of adsorbed precursor molecules and S_ρ is the atomic surface density.

The probability of precursor dissociation is governed by the electron dissociation cross-section assuming that the growth is caused by an electron induced dissociation process rather than a thermal process. Dissociation is most probable in regions where the electron energy distribution significantly overlaps the dissociation cross–section.

For many precursors, the dissociation cross-section is not known. This is due to the difficulty in accurately measuring the dissociation events. Educated approximations must therefore be made in order to have a realistic model. For example, the dissociation cross-section of WF_6 is unavailable based on extensive literature searches. The available data from literature sources applies predominantly to simple gases such as H_2 and N_2[128] and carbon based species such as C_xH_y[129]. Experiments to determine the ionization cross–section are far easier to perform. Therefore, the total ionization cross–section for WF_6 gas was used in our EBID predictor in place of the unavailable dissociation cross–section with minor modifications applied to the ionization cross–section making it more applicable for describing dissociation events. It is well documented that the *shape* of the ionization and dissociation cross–section curves are similar[130,131]. For most molecules the dissociation cross–section has a *lower threshold energy* and typically has a *higher maximum value* versus the ionization cross–section. The total ionization cross–section for tungsten was modified by shifting the threshold ionization energy to E = 5.7 eV (from 15 eV) which is the W-F bond energy. Additionally the cross–section at low energies

$12eV \leq E \leq 100eV$ was increased because dissociation events are more probable than ionization events in this energy regime. To do this, a scaling procedure was applied over this low energy range based on the ratio of the dissociation cross–section to the ionization cross–section for the hydrocarbon species C_2H_5 for which both cross–sections are known; the methodology is described in detail below, as originally related by Fowlkes *et al.*[132]

The total ionization cross-section of WF_6, as a function of energy ($\sigma(E)$) was determined by Basner *et al.*[133] and Kwitnewski *et al.*[134]. Fowlkes *et al.*[132] used a fitting algorithm to obtain an equation of the form:

$$\sigma(\mathrm{E}) = \left(\mathrm{A}_1\left(1-\frac{1}{E}\right) + \mathrm{A}_2\left(1-\frac{1}{E}\right)^2 + \mathrm{A}_3\left(\frac{\log E}{E}\right) + \mathrm{A}_4 \log E \right)\frac{1}{E} \qquad \textbf{24}$$

where the A_x's represent constants and E is the electron energy[135,136]. Mathematica® applied a least-squares fit to a linear combination of input functions and approximated the data. The resultant equation was derived from the binary-encounter-Bethe model[137] which combines the Mott cross-section and the high temperature behavior of the Bethe cross section.

The total ionization cross-section was subsequently modified to approximate the dissociation cross-section for WF_6. Silvis–Cividjian[138] simulated the deposition of carbon at high beam energies (E_o > 20 keV) using the estimated dissociation cross–section for C_2H_5 from Alman *et al.*[130] A scaling procedure was applied based on the ratio of dissociation cross–section for C_2H_5 ($\sigma_{d,C2H5}$) and the ionization cross–section for C_2H_5 ($\sigma_{i,C2H5}$).

$$\sigma_{d,WF_6} = \left[\frac{\sigma_{d,C_2H_5}}{\sigma_{i,C_2H_5}}\right]\cdot\sigma_{i,WF_6}, \quad \text{for } \frac{\sigma_{d,C_2H_5}}{\sigma_{i,C_2H_5}} \geq 1 \qquad \textbf{25}$$

$$\sigma_{d,WF_6} = \sigma_{i,WF_6}, \text{for } \frac{\sigma_{d,C_2H_5}}{\sigma_{i,C_2H_5}} < 1. \qquad \textbf{26}$$

Molecular dissociation occurs preferentially at low energies (E < 100 eV) relative to ionization for most molecules and Equation 25 modifies the ionization cross–section to account for this. Figure 2-18 shows a plot of the ionization total cross–section for WF_6 shown superimposed with the modified dissociation cross–section, and the dissociation and ionization cross–sections for C_2H_5 from Alman *et al.*[130] and used by Silvis–Cividjian *et al.*[78] For electron energies E > 100 eV the modified dissociation cross–section and ionization total cross–section were assumed to be equivalent. This was done based on the fact that the dissociation cross–section in Alman, *et al.*[130] for C_2H_5 decreases in magnitude too steeply beyond 25 eV. For example, the dissociation cross-section decreases *10 orders of magnitude* from E = 120 eV to E = 1900 eV based on the functionality applied by Alman *et al.*[130]. This is a severe underestimation of the dissociation probability at high energy and is related to the fitting procedure used by Alman, *et al.*[130] as they were interested primarily in the accuracy of fit at low energies. In the case of CF_4, the measured dissociation cross-section at E = 600 eV is only one half of the value of the maximum at E = 100 eV[139], which illustrates that there is less severe drop in dissociation cross-section with energy relative to what is used in Silvis–Cividjian *et al.* The curve fitting described in Alman, *et al.*[130] applied to CH_3 and CH_2 data[129] were fit for

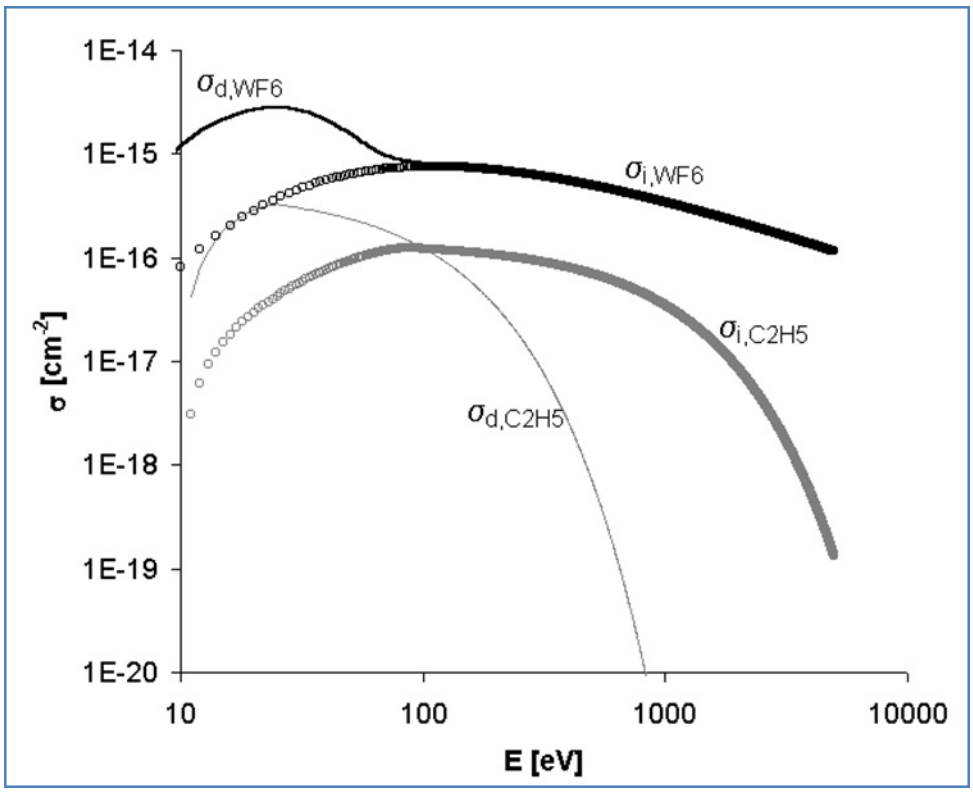


Figure 2-18: Dissociation cross-section for WF_6.[132]

The approximate dissociation cross-section for WF_6 gas (log σ vs. log E) estimated from the experimental determined ionization cross-section for WF_6[133,134] and the estimated dissociation and ionization cross–sections for C_2H_5 based on extrapolations from experimental data on CH_x species[130].

the energy range of 0 - 100 eV, which makes them impractical for use at high energies. Moreover, Alman *et al*. extrapolated the cross-sections for C_xH_y species from CH_y data due to the difficulties associated with collecting dissociation cross-section experimental data for heavier hydrocarbon species. Hence, the probability of dissociation at high energies was thought to be strongly underestimated by extrapolating the data from Alman, *et al.*[130] and therefore it was assumed that the total ionization cross-section was a reasonable approximation of the dissociation cross-section at E > 100 eV. Fowlkes speculated that ionization events could also induce deposition via exchange processes, because when the SE yield is < 1 the near surface region should be negatively charged.

Figure 2-19 shows the approximated dissociation cross-section up to an electron energy of 5 keV. Also shown in Figure 2-19 is a representative secondary electron (SE) and BSE distribution for tungsten at 5 keV that was generated by a Monte-Carlo scattering based simulation.

In this discretized simulation, the gas coverage is indexed on a per voxel basis so the probability for gas dissociation is modified with the following equation:

$$Q = \frac{\sigma(E) * S_{FCC}}{A_m} \qquad \textbf{27}$$

where S_{FCC} is the FCC planar density and A_m is the molecular cross-sectional area of the particular precursor gas. The estimation was made that one WF_6 may adsorb per voxel. This may represent an overestimation of the surface coverage since a WF_6 molecule has a cross-sectional area larger than the voxel size; therefore the adjustment to the dissociation probability shown in Equation 27 was made to account for the discrepancy.

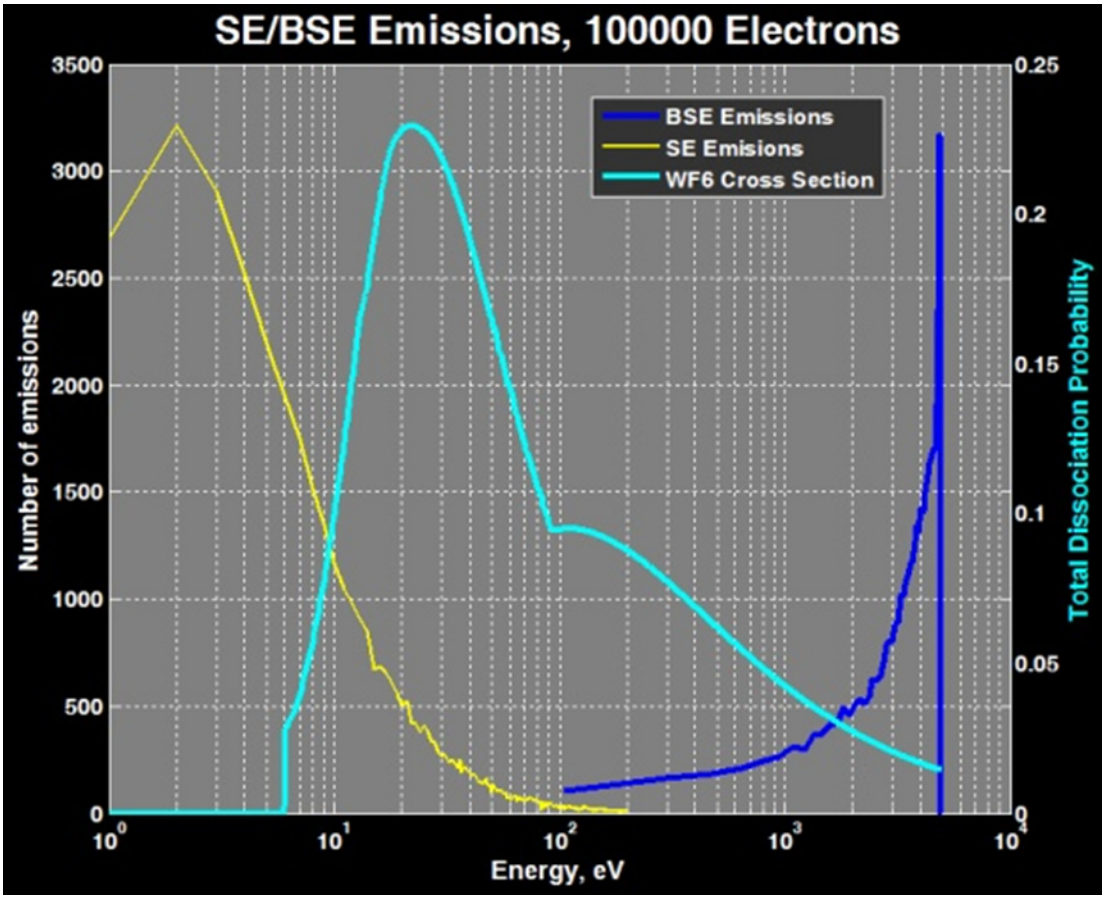


Figure 2-19: Dissociation cross section with SE and BSE emission spectra.

The secondary (SE) and backscattered (BSE) energy distributions from a flat tungsten substrate derived by a Monte Carlo simulation of 100,000 electrons at 5keV superimposed with the approximated WF_6 dissociation cross–section. Note that the cross-section is given in terms of total probability for dissociation (right *y* axis).

The probability of precursor dissociation is governed by the electron dissociation cross-section assuming that the growth is caused by an electron induced dissociation process rather than a thermal process. Any time an electron traverses the material/vacuum interface, the voxel in which it is traversed is tested to see if a precursor gas species is adsorbed at that site. If a precursor atom is adsorbed there, the following expression is used to determine if dissociation takes place by using a random number generator:

IF rand < Q, AND gas present: Deposit Material.

where *rand* is a random number between 0 and 1, and Q is the total dissociation cross section probability taken from Equation 27. If this expression is satisfied, deposition occurs and the discretized 3D matrix is incremented at that voxel.

2.8 Gas Dynamics

Up to this point, the parts of the simulation described above fit together as follows: the system boundaries are discretized into a 3D matrix which sits atop a substrate at z=0 in Cartesian coordinates. Electrons are simulated either in a Gaussian-like or cylindrical profile upon the substrate, and Monte Carlo tracking of the electron energy and position proceeds according to the algorithms described by Joy's plural scattering model. Secondary electrons are generated via Kotera's hybrid model, and tests for dissociation are made whenever an electron of sufficient energy crosses a solid-vacuum interface in the presence of a gas molecule based on the modified WF_6 cross-section. The remainder of this section will discuss how the gas molecules arrive and diffuse via these locations by various methods which are critical to the EBID process. *This is a unique feature of this simulation which has not yet been examined in this field of*

research.

When testing a voxel for the presence of gas, a first-order approximation would be to simply assign a concentration value to that location based on its position in space relative to the simulation boundaries and the electron beam. This method would rely heavily on radial symmetry in the system, and was not conducive to the development of a robust, 3D model which can simulate complex structures. It was therefore decided that the gas-solid dynamics would be controlled by an independent, discretized surface mesh of gas sites which would wrap around any 3D surfaces within the bounds of the simulation (Figure 2-20). Within this mesh, molecules could arrive by adsorption from precursor gas flux, desorb from the surface with a prescribed residence time, and move by surface diffusion controlled by a realistic diffusion coefficient that can be input to the simulation. All of these gas sites (empty or filled) are stored in an array within the simulation.

An initial percentage of surface coverage, θ_i, is input to the simulation to describe initial conditions on the surface. It has a value of 0 to 1, where a value of 0 indicates that no gas is initially present, and a value of 1 indicates that there is a complete monolayer of coverage. The initial surface can be a flat substrate, or a complex 3D surface which is input to the simulation. All possible gas adsorption sites are located on such a surface by scanning the solid for the vacuum/solid interface in all three Cartesian coordinate directions.

In order to model the gas adsorption onto the surface of the substrate, a number of assumptions were made. First, adsorption can be physical or chemical in nature[140].

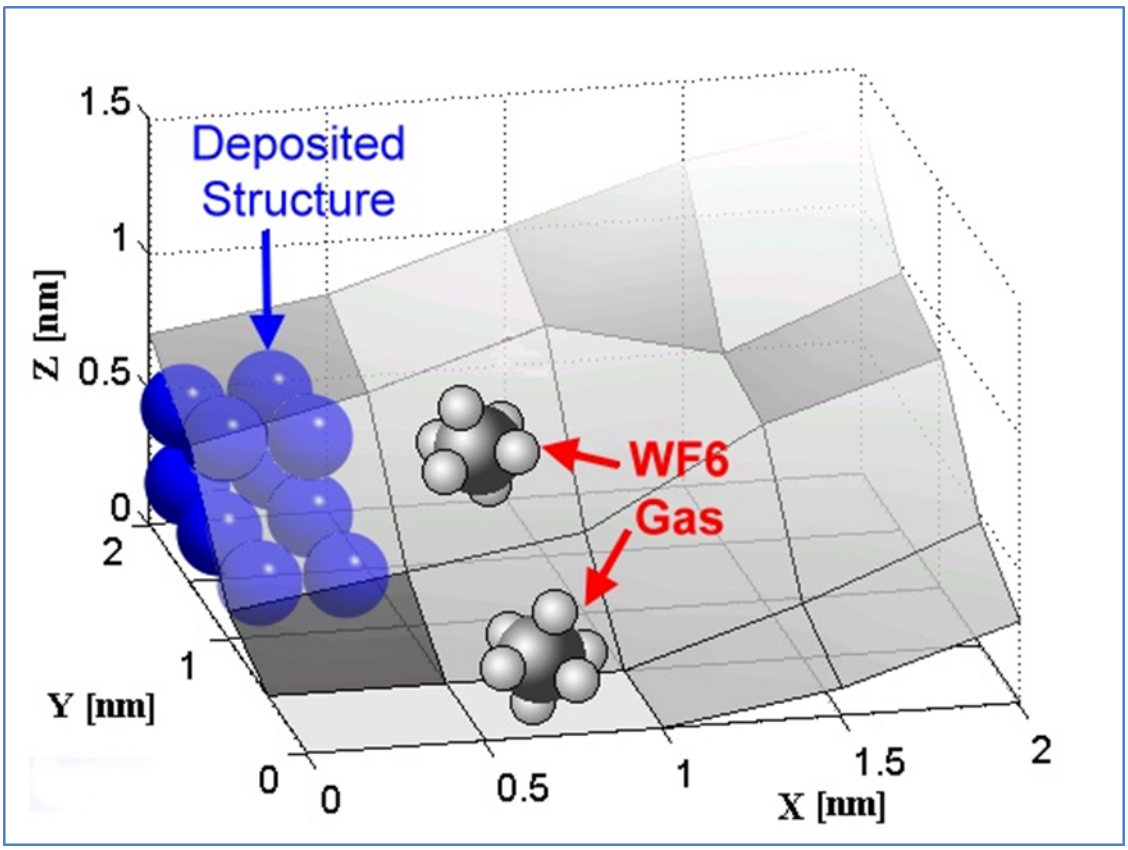


Figure 2-20: Surface Mesh for Gas Tracking.

Surrounding the deposited structure (blue) is a surface mesh of discretized voxels that contain the precursor gas site locations.

Molecules that approach a surface will experience an attractive force as they near the surface, and eventually repelled by the surface if they get too close. The result is a minimum in the potential energy (called the "energy well") where the molecule is held close to the surface (See Figure 2-21). Molecules then bond to the surface by either weak van der Waals forces or by stronger chemical forces, such as covalent bonding, hydrogen bonding, or metallic bonding. If they are bonded weakly, they are said to be "physisorbed" onto the surface. Chemically bonded molecules are called "chemisorbed".

Several models of adsorption have been proposed, each with varying degrees of accuracy and complexity. The Langmuir isotherm model was chosen to represent the method of precursor adsorption due to its ease of use and applicability to the EBID environment. It is based on the Absolute Rate Theory (ART) of gas kinetics, and was used as a first-order approximation for quantitatively predicting surface adsorption of molecules throughout most of the 20th century[141]. This model makes the following assumptions for adsorption:

- All gas adsorption locations on the surface are equivalent and independent of flux directionality;
- The substrate surface is homogenous;
- Gas molecules are assigned a finite residence time (τ_a) upon adsorption to an available gas site, but do not adsorb (or "self-sputter") if a gas molecule is already present;
- There can never be more than one layer (i.e. "monolayer") of gas molecules on the surface; and

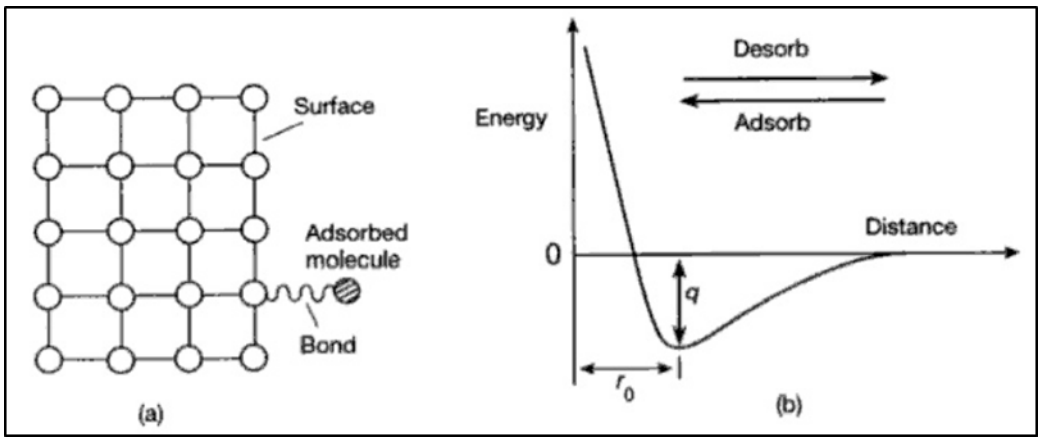


Figure 2-21: Energy Barrier for Adsorption/Desorption.

The energy barrier for adsorption/desorption is designated q, and changes as the molecule approaches the surface. The minimum energy acts as a "well" where the particle is held during the residence time.

- The heat of adsorption of all molecules is the same to any site.[142]

The Langmuir isotherm is derived from the kinetic theory of gasses and describes the change in theta per change in time as a difference in the rates of adsorption and desorption. A semi-empirical model for this behavior is typically described by equations like:[143]

$$\frac{d\theta}{dt} = R_a - R_d = K_a p(1-\theta)^s e^{\frac{-\varepsilon_a}{kT}} - K_d p(\theta)^s e^{\frac{-\varepsilon_d}{kT}} \qquad \textbf{28}$$

where θ is the fractional amount of surface coverage, R_a and R_d are the rates of adsorption and desorption (respectively), K_a and K_d are constants, ε_a and ε_d are the activation energies of adsorption and desorption (respectively), *s* is the number of adsorption sites involved in an elementary adsorption/desorption process (reaction), R is the universal gas constant, T is the absolute temperature, and *p* is the adsorbate pressure. In the case *s* =1, at the equilibrium when (dθ/dt) = 0, Eq. 28 yields the Langmuir isotherm equation:

$$\theta^{(e)}(p,T) = \frac{Kp^{(e)}e^{\frac{\varepsilon}{kT}}}{1+Kp^{(e)}e^{\frac{\varepsilon}{kT}}} \qquad \textbf{29}$$

where $K = K_a/K_d$ and $\varepsilon = (\varepsilon_d - \varepsilon_a)$, and where the superscript (e) refers to equilibrium.

The Monte Carlo approach to simulating this isotherm involves utilizing the same principles that describe the Langmuir isotherm. This is carried out in two separate stages for adsorption and then desorption. After each electron completes its trajectory, the simulation first checks for gas adsorption of new gas molecules from the precursor flux. This term is calculated from the local pressure at the substrate surface using the equation derived from classical kinetic theory [144]:

$$\frac{\Gamma_{gas}}{N_A}(\text{moles/cm}^2\text{-s}) = \frac{P}{\sqrt{2\pi MRT}} \quad \textbf{30}$$

where N_A is Avogadro's number, M is the molecular weight of the precursor, R is the Universal Gas Constant, T is the temperature of the gas, and P is the local pressure.

The number of gas molecules that are randomly deposited on the surface changes as the structure grows, since the surface area increases while gas flux is constant. The equation that determines the number of gas molecules deposited (N_{gas}) is as follows:

$$N_{gas} = \Gamma_{gas} * N_{sites} * \Delta x^2 * t \quad \textbf{31}$$

where N_{sites} is the number of total gas surface sites on the structure within the simulation bounds, Δx is the voxel spacing dimension, and t is the time between electrons (based on the prescribed beam current). Note that the quantity $N_{sites} * \Delta x^2$ represents the approximate instantaneous surface area of the structure. When a gas molecule is adsorbed, a random time between 0 and the mean residence time (τ_a) is assigned to the molecule. This also applies to gas molecules adsorbed in the initial gas layer coverage (θ_i) described earlier.

The desorption of gas is then handled by incrementing the instantaneous residence time of each gas molecule by the elapsed time between electrons (τ_e), which is based on the input beam current (i_{beam}) as follows:

$$\tau_e = \frac{1.6\text{e-}10}{i_{beam}} \quad \textbf{32}$$

Once the residence time of a gas molecule exceeds the mean residence time (τ_a), the molecule is removed. The mean residence time (also referred to as the desorption time) can be written as:

$$\tau_a = \upsilon^{-1} e^{\frac{q}{kT}} \quad \textbf{33}$$

where ν is an effective surface vibration frequency of molecules (~10^{13} s^{-1}),[145] q is the activation energy for adsorption (Figure 2-21), k is Boltzmann's constant, and T is temperature in Kelvin. Equation 33 shows that when molecules are physisorbed, their energy barrier is small; therefore they have a short residence time. Chemisorbed species can remain resident for weeks. See Table 1 for values of τ_a for various values of q at 295°K. For convenience, all precursor gasses were assumed to be bound with a mean residence time of 1.0s (exact values were difficult to find in literature).

The combination of the adsorption and desorption algorithms satisfactorily approximate the Langmuir isotherm as shown in Figure 2-22. Note that the analytical expression described by the first part of the Christy model[147] and later explained by Utke *et al.*[148] and Reimer[149] with regard to EBID is used to show this relationship as follows:

$$\frac{d\theta}{dt} = \alpha_i J(1-\theta) - \frac{n}{\tau_a} \quad \textbf{34}$$

where J is the gas flux, n is the number of adsorbed molecules, and α_i is the "sticking coefficient". Molecules impinging on a surface cannot be adsorbed either physically or chemically unless they lose their energy during their collision with the substrate. The amount of energy lost has to be enough so that the incident molecules can be trapped within an energy well as previously described.[150] Thus, the amount of adsorbed molecules is the incident flux multiplied by the sticking coefficient (which is given a number between 0 and 1). The sticking coefficient is typically a function of temperature,

Table 1: Values of τ for various *q* at 295 K.[146]

q(eV)	*τ*
0.2	3e-10 s
0.4	1 μs
0.6	20 ms
0.9	400 s
1.1	1.2e6 s (=2 weeks)

This table shows physisorbed molecules (i.e. small energy barriers for desorption) have a much shorter residence time than chemisorbed molecules.

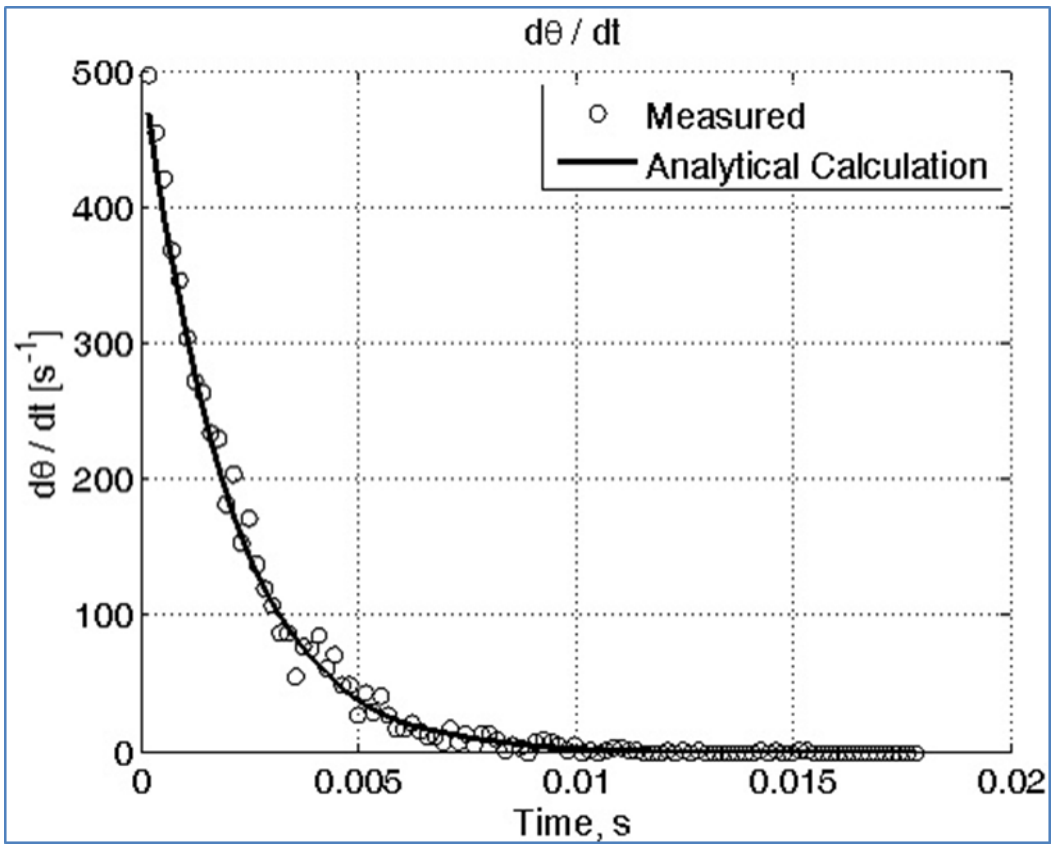


Figure 2-22: dθ/dt compared to simulated results.

The analytical expression for change in surface coverage due to adsorption and desorption was plotted against the simulated (i.e. "Measured") values.

surface roughness, surface imperfections, the incident particles' velocities, etc. For the results demonstrated here, the sticking coefficient is taken as unity unless stated elsewhere.

In order to make the simulation computationally efficient, a test is made after every electron to determine if the simulation is operating in "reaction-rate limited" conditions (or, "RRL" for short). In this regime, the amount of gas adsorbing greatly exceeds that which is being removed by desorption and dissociation. If at any time, the following condition is true:

$$\frac{\text{gas adsorbed - gas desorbed}}{\text{number of gas sites}} > 1 \qquad \textbf{35}$$

then the simulation is in reaction rate limited conditions. Additionally, if the following is true:

$$\text{(gas adsorbed) - (gas desorbed) - } \frac{\text{number of deposition events}}{\text{number of electrons run}} > 2 \qquad \textbf{36}$$

then RRL conditions can be assumed (Note that the gas adsorbed and desorbed is per electron in these equations). When this is the case, the algorithms for adsorption and desorption are bypassed and all gas sites are filled with gas between each simulated electron. The assumption is made that once the simulation crosses into RRL conditions, it never reverts to the previous case. Details of mass-transport limited vs. reaction-rate limited growth will be discussed later in this dissertation.

The simulation has the option for two sources of gas. The first is deposited from the precursor flux as previously described. The second is a constant source of gas which is diffused in from the simulation boundary. Typically, EBID occurs on a very small area,

and the gas covered region is much larger. It follows, therefore, that as gas is consumed from within the small area of the beam interaction region, a concentration gradient will form that will diffuse gas from the boundary inward toward the beam spot. The simulation would see this as a constant source of gas at the boundary (θ_b=1.0). The effects of the addition of this extra source of gas in addition to precursor flux will be demonstrated later.

During EBID, material deposited increases the surface area of the simulation, including the number of gas sites. When the dissociation of a gas molecule creates a newly deposited atom, new gas sites are created around this atom. These sites are added to the surface mesh which tracks the gas sites, assuming they are adjacent to the solid surface. Six directions are sampled surrounding the new deposit, as shown in Figure 2-23. These six directions are composed of the positive and negative directions in each of the three Cartesian coordinate axes surrounding the newly deposited atom. The diagonals are not searched because these are not directly adjacent to the discretized solid structure.

After the gas adsorption and desorption algorithms are run, the simulation updates the position of each gas molecule by a 3D surface diffusion algorithm. Possible adsorption sites are tracked and updated after deposition events, and gas molecules move along vacant sites by random walk motion, as described by Einstein in 1906.[151] The gas molecules are treated as ideal in that no two gas molecules can occupy the same site; therefore motion is restricted to empty sites. The number of gas jumps is determined by the surface diffusion coefficient, time for gas to move (dependant on the beam current),

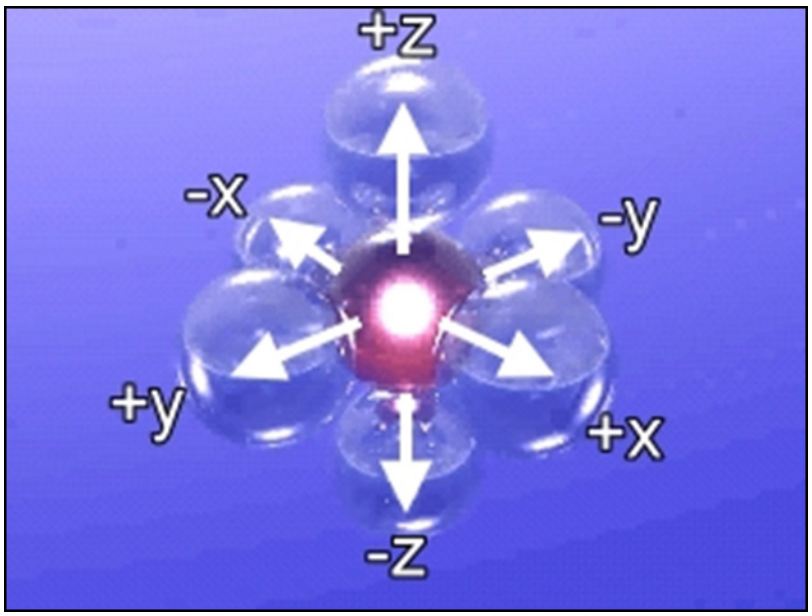


Figure 2-23: Six-directional Scan Illustration

The directions which are searched following a deposition event (purple) are shown as clear bubbles. There are two directions in each of the three Cartesian coordinate axes.

and the discrete voxel separation distance. Fractional jumps are also tallied so that the overall gas motion is accurate. Since a 3D system is employed, the number of jumps per electron is based on the expression for root mean square displacement via Brownian motion. It is calculated by the expression:

$$jumps = \frac{\sqrt{4D_{surf}\tau_e}}{\Delta x^2} \qquad \textbf{37}$$

where D_{surf} is the surface diffusion coefficient, τ_e is the elapsed time per electron, and Δx is the voxel separation distance. Note that *t* is inversely proportional to the beam current (i.e. seconds per electron), since gas molecules are updated after every electron trajectory. The constant 4 is used in this equation because despite the 3D environment,

gas molecules are still confined to essentially a 2D surface which wraps around the substrate and the deposited structure[152].

Extensive tests on the diffusion accuracy were performed in order to verify accuracy of the model. Figure 2-24 shows an example test which was performed. 2,000 independent gas molecules were allowed to diffuse from a spot-source on the substrate at a jump rate of one voxel per electron (D_{surf}=8.7891e-009 cm^2/s, i_{beam}=0.009nA, Δx=0.25nm per voxel, τ_e=1.7778e-8s, therefore *t*=(2,000*τ_e)=3.555e-5s). The root mean square distance traveled is calculated as $< x_{rms} >= \sqrt{4Dt}$, or 11.2 nm. The measured value (10.4 nm) was close to this value, as shown. Figure 2-25 shows another test, in which 500 electrons were simulated with gas diffusing from the boundary of the simulation (D_{surf}=1.0e-009 cm^2/s, i_{beam}=0.009nA, Δx=0.25nm per voxel, τ_e=1.7778e-8s, therefore

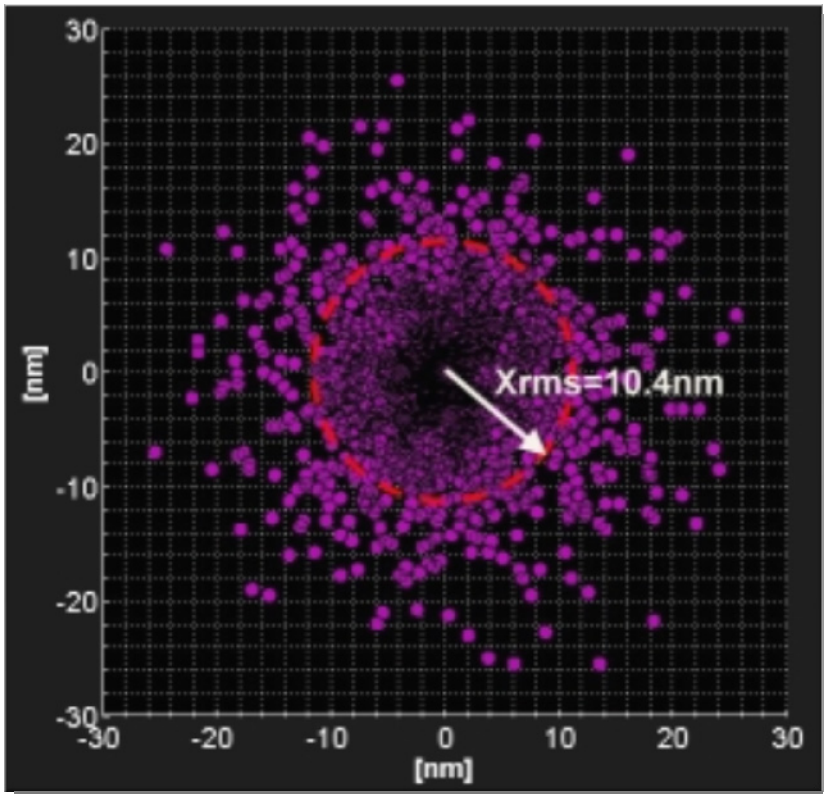


Figure 2-24: Independent Surface Diffusion Tests.

Independent random walk surface diffusion yielded $<x_{rms}>$ values comparable to predicted values.

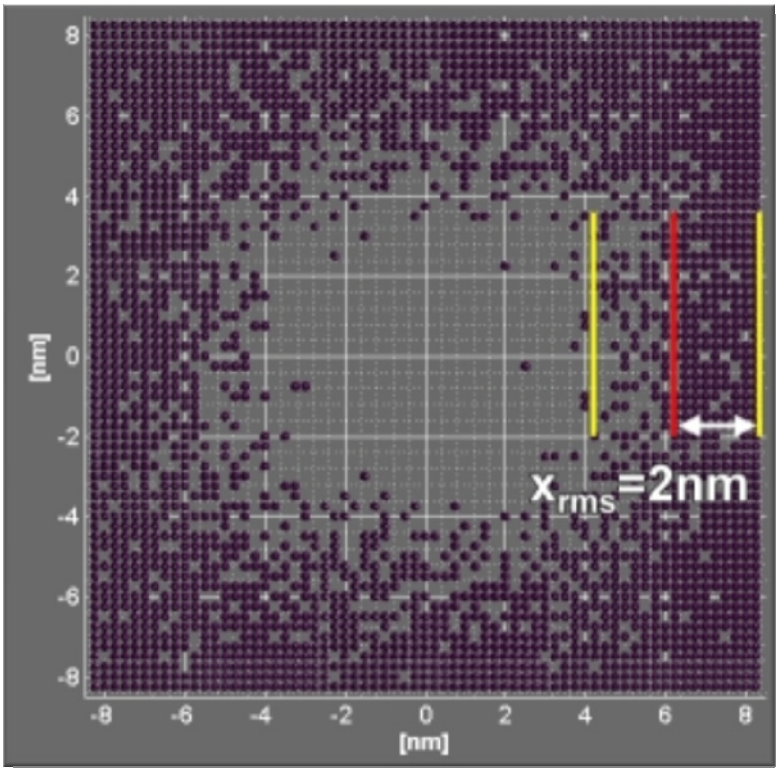


Figure 2-25: Repulsive Surface Diffusion Tests.

Repulsive surface diffusion from the boundary of the simulation. Calculated $\langle x_{rms} \rangle$ was 1.9nm, which is indicated as diffusion from the boundary to the red line. Gas molecules have diffused well past twice this value, indicating that the rate of diffusion is slightly increased, as expected.

t=(500*τ_e)=8.886e-6s). The <x_{rms}> was calculated to be 1.9 nm, and the mean distance traveled can be seen to be somewhat greater than this value. The algorithm for surface diffusion is similar to a repulsive-type of gas interaction, because gas cannot diffuse into occupied gas sites. This type of diffusion was shown by Bowler and Hood to increase the diffusion rate in Monte Carlo simulations of gas diffusion from a boundary source[153]. This is because the concentration of particles near the edge of the simulation acts as a wall and hinders the migration of the particles farther back in the pack. This is referred to as a "site blocking effect". As the particles move into a more diffuse area, the root mean square displacement becomes approximately that expected from random walk motion.

In order to accurately model "true-3D" surface diffusion, the available gas sites surrounding each gas molecule are sampled at random in order to locate an acceptable jump location. Since gas molecules cannot jump into vacuum (unless desorbing), they must move into an empty gas site that is adjacent to the solid surface. In three dimensions, there are 18 directions which are adjacent to any gas molecule which are scanned for an available jump site. Figure 2-26 shows an illustration of the 18 directions that are searched for an adjacent gas site during surface diffusion. There are three tiers surrounding a gas molecule: top, middle, and bottom. The top and bottom tiers have 5 directions which are searched, and the middle has 8. The reason for this configuration is to allow gas molecules to climb around and on top of the 3D structure. The 8 directions which are searched in the middle tier are shown in Figure 2-27. Here, the diagonals are included in the search pattern so that adjacent sites in the corners of a 3D structure can be

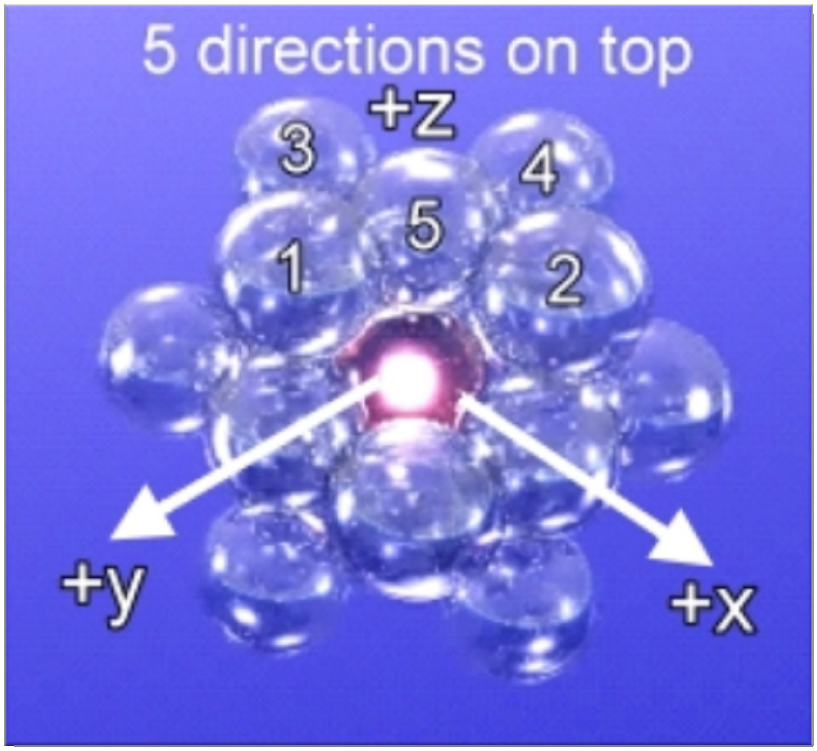


Figure 2-26: 18-Directional Surface Diffusion Scan Illustration.

The 18 directions which are scanned during surface diffusion are composed of three levels: 5 sites on top, 8 in the middle, and 5 sites on the bottom. The five sites on the top of the gas molecule are shown in this illustration for clarity. Note that the site numbered "5" is in the +z direction.

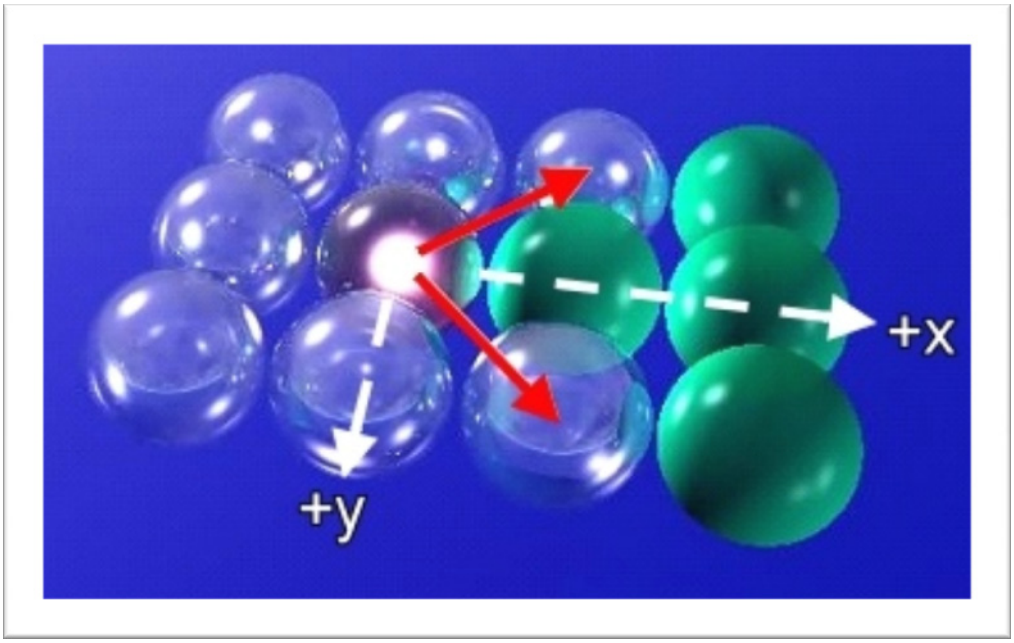


Figure 2-27: Diagonal search pattern in center tier.

Gas molecules (purple orb) need to be able to search diagonally (red arrows) to find adjacent gas sites in corners of the 3D structure (shown as green spheres). The middle tier search pattern is composed of 8 directions, as indicated by the clear bubbles. Note that one of the search directions in the (+x) direction is occupied by a solid atom.

located. Inclusion of the vertical diagonals in the search pattern ensures that the gas molecules can "climb on top of" the existing 3D structure, as shown in Figure 2-28. Utilizing this algorithm for identifying possible adjacent gas sites allows gas molecules to "crawl" across the surface at a rate determined by the diffusion coefficient.

Initially, a six-directional scan similar to that shown in Figure 2-23 was used for surface diffusion in an earlier version of this simulation. The 18-directional scan allowed for a more complete model to be obtained, however, as shown in Figure 2-29. Here, 25,000 electrons of 1keV energy were simulated in a WF_6-W system with a relatively high surface diffusion coefficient of 1.0e-8 cm^2/s. After the simulation, the pillar structure had a surface coverage of 68% when the 6-directional scan was utilized, and a coverage of 99% with the 18-directional scan. Additionally, the pillar in the 18-directional simulation grew more than 3 times taller because of the greater availability of precursor gas in the beam vicinity. Clearly, the 18-directional approach is satisfactory for simulating true 3D surface diffusion.

The kinetics that describe the gas coverage on a complete system (i.e. one that involves adsorption, desorption, dissociation, and surface diffusion) have been modeled by several authors, such as Utke *et al.*[148] and Reimer[149]. The Reimer model essentially modifies Equation 34 to include two new terms: one that describes the loss of gas due to dissociation, and one that includes gas flux diffusing from the surrounding surface:

$$\frac{d\theta}{dt} = \alpha_i J(1-\theta) - \frac{n}{\tau_a} - \theta\sigma f + D_{surf}\nabla^2\theta \qquad \textbf{38}$$

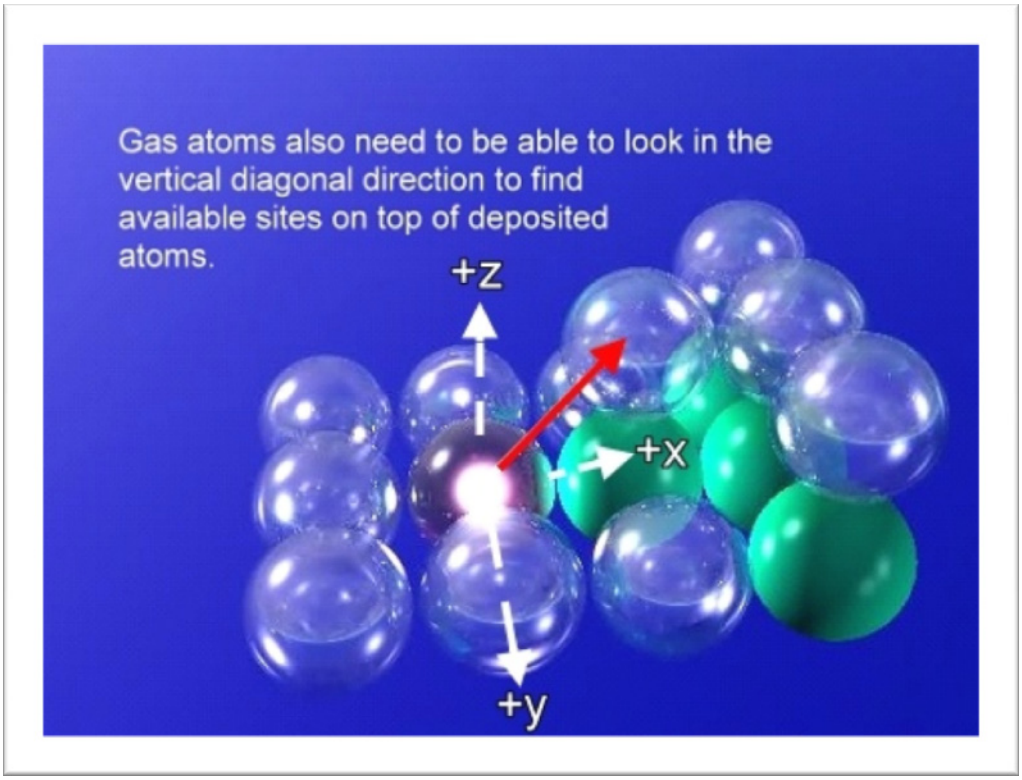


Figure 2-28: Vertical diagonal search directions for surface diffusion

True 3D surface diffusion requires the gas molecules (shown as the purple orb above) to be able to "climb on top of" the 3D structure (green spheres). Therefore vertical diagonal directions are searched for available gas sites (clear bubbles) as shown in the above illustration. The red arrow indicates a vertical diagonal direction that lies in the (xz) plane.

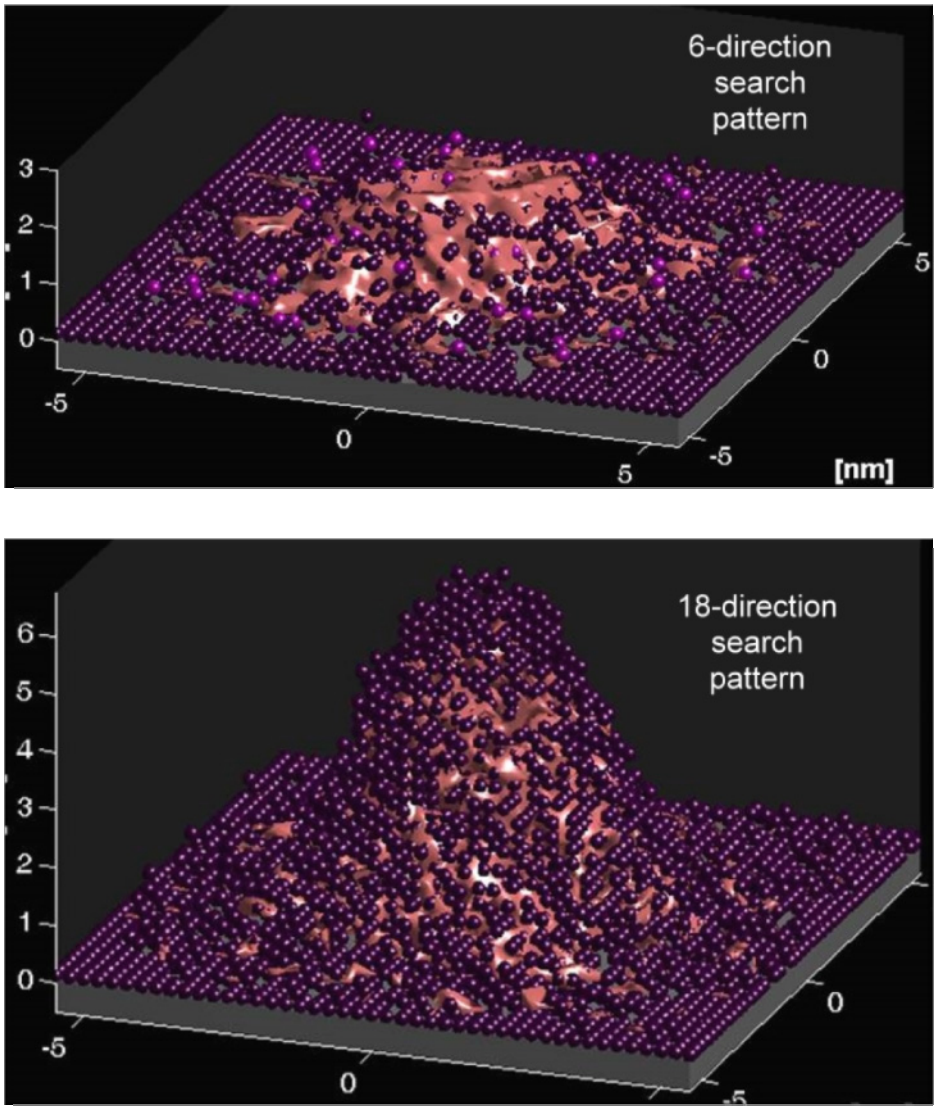


Figure 2-29: Surface diffusion search algorithm comparisons.

A comparison of a pillar structure grown with the original 6-direction surface diffusion scan algorithm (top) vs. the 18-directional scan algorithm (bottom). The 18-directional scan allowed the gas (purple spheres) to climb over the complex surface in a true-3D fashion.

where f is the electron flux, and σ is the dissociation cross section. This analytical expression has been compared to $d\theta/dt$ from simulations as shown in Figure 2-30.

The inclusion of all of these algorithms makes a complete 3D simulation of the EBID process. For a list of all necessary inputs to the simulation, see Appendix A. A detailed flowchart of the simulation is shown in Appendix B. Example outputs from the simulation will be given in Chapter 3.

2.9 Pressure Simulation

When attempting to compare experimental to simulated results, it is necessary to know several variables relating to the system under investigation. Some parameters, such as beam energy and current, are easily identified because they are physical adjustment settings on most EBID devices or easily measured. The beam current, for example, can be measured by using a Faraday cup to completely capture the electron beam. The stage current, which can be measured with an ammeter, is then equal to the beam current. Other parameters, such as the local gas pressure in the area of EBID, are not implicitly known and cannot be easily measured. For this particular input parameter, a pressure simulation is often employed to estimate the local pressure in the beam vicinity.

A model of an EBID system's local gas pressure can only be obtained if specific parameters relating to the system are known, such as geometry, effective pumping speed of the vacuum system, precursor input configuration, etc. For most of the EBID experiments in this dissertation whose parameters were used for simulation input, a modified Hitachi S-4300SE/N variable pressure SEM was utilized (Figure 2-31). This

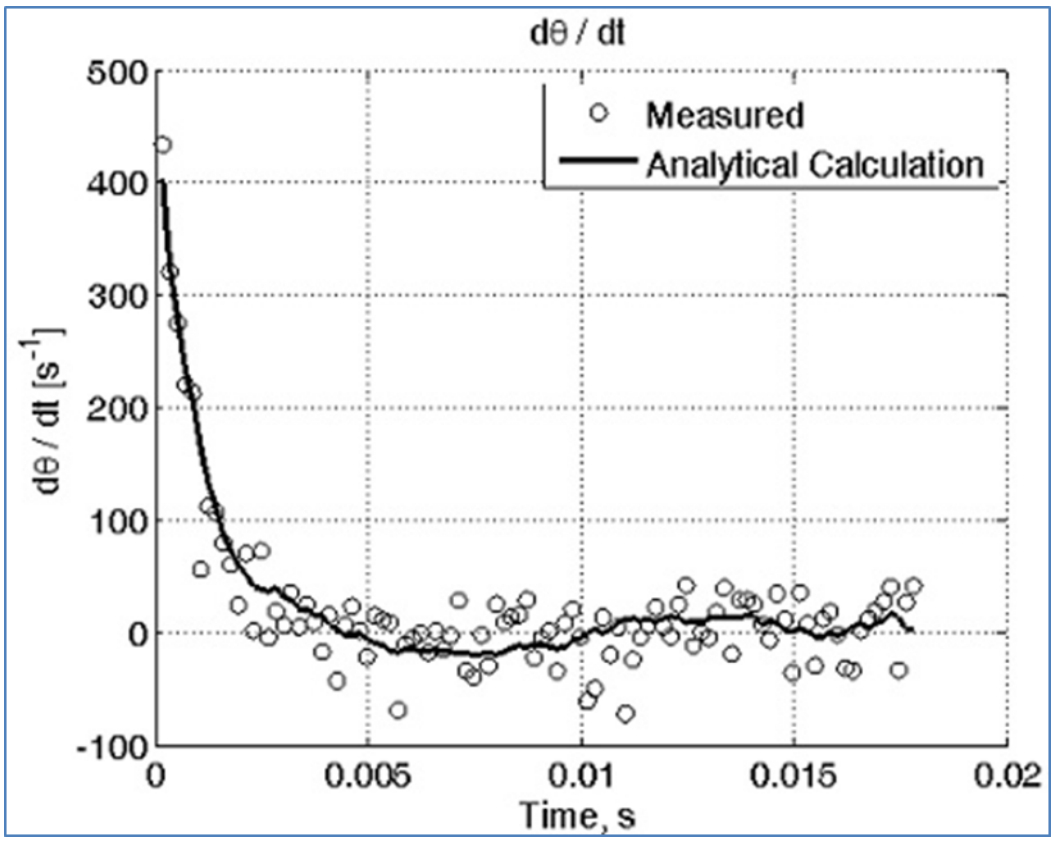


Figure 2-30: Comparison of dθ/dt to Utke/Reimer model.

The analytical expression in Equation 38 was plotted against the simulated (i.e. "Measured") results to show good agreement with the Utke/Reimer model.

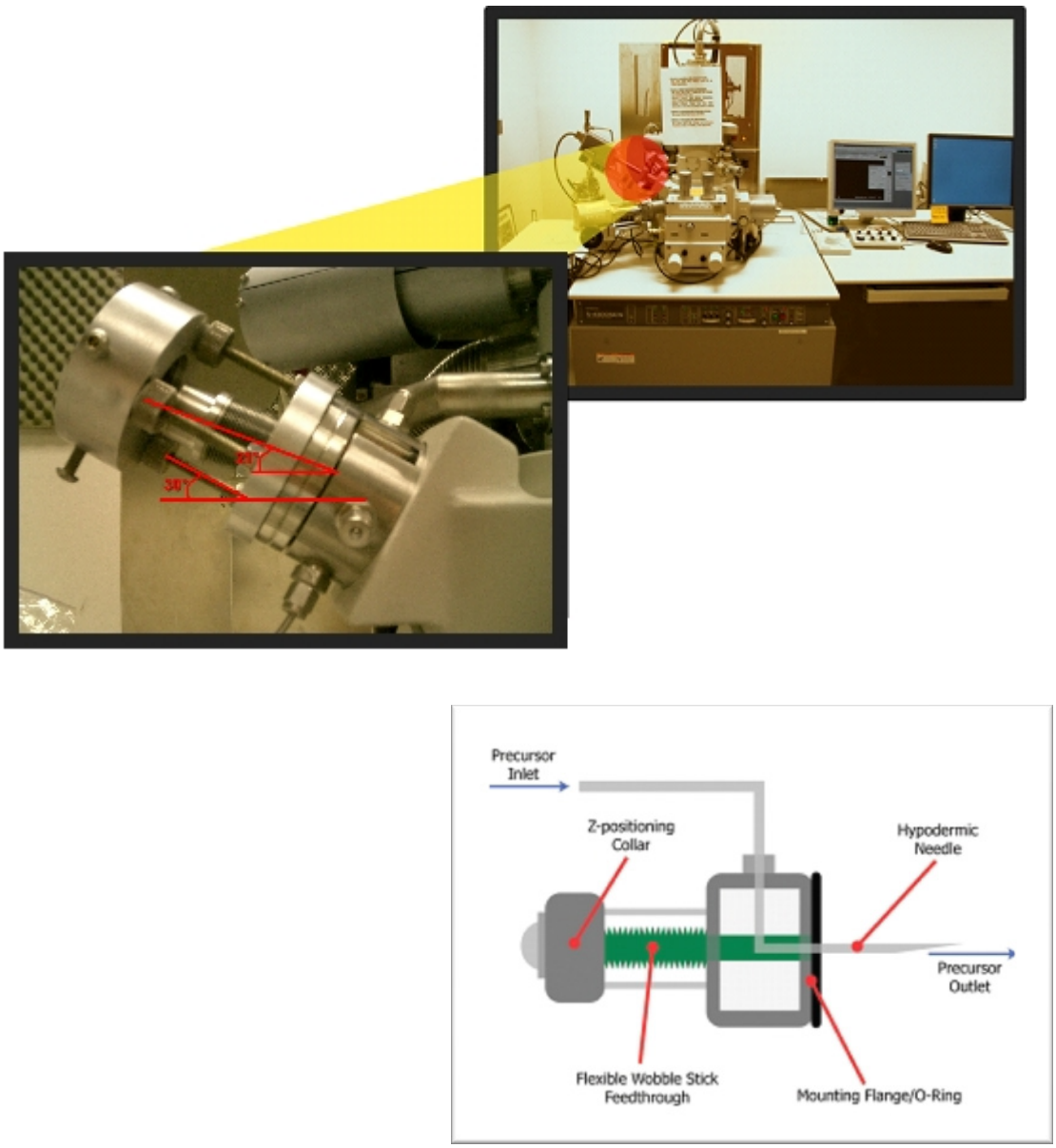


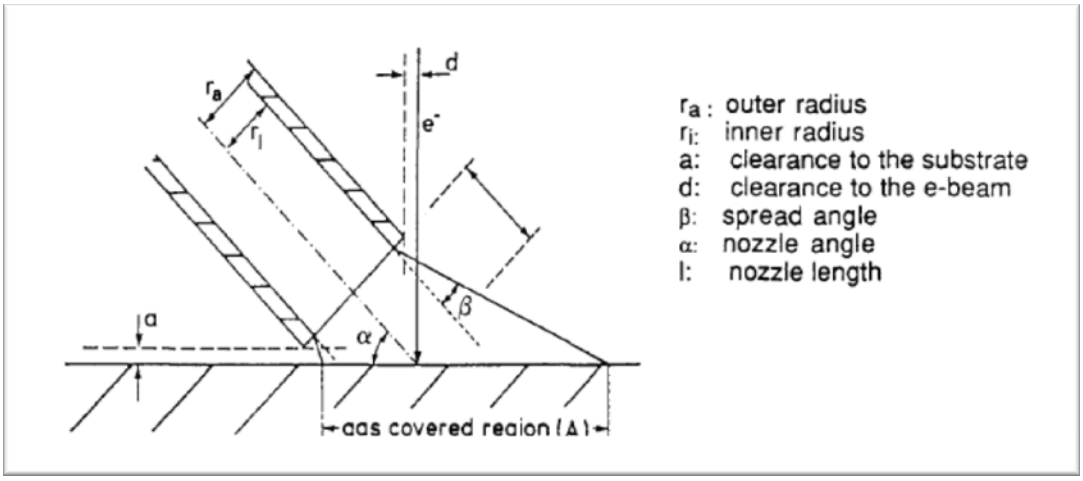
Figure 2-31: Hitachi S-4300SE VPSEM EBID System

The EBID system used at The University of Tennessee, Knoxville which has been modified with a vapor injection system (middle photo). A schematic of the vapor injection system is shown in the lower photograph.

system was equipped with a vapor injection system to facilitate EBID experiments. The vapor injection system consisted of a three-dimensional wobble stick fitted with a hypodermic needle.

In order to estimate the local gas pressure, two key pieces of information must be obtained: the gas coverage area, and the gas throughput of the system. To solve this problem, equations were found in literature that analytically estimate the average gas coverage area based on the nozzle shape and size, tilt angle, gas spread angle, and height above the surface of the sample. Some of the geometrical measurements required by the pressure simulation are shown in Figure 2-31 and Figure 2-32. The angle of the hypodermic needle is measured from the photograph in Figure 2-31. In this case, the wobble stick is aligned such that the hypodermic needle makes a 21° angle with the substrate surface. The hypodermic needle geometry is known, and the distance above the substrate can be measured by varying the working distance between the needle and the substrate.

The program uses two forms of input for calculating the throughput of the system. First, the flow rate of precursor gas in standard cubic centimeters per minute (SCCM) is input. Alternatively, one can determine the flow rate noting the pressure rise in the system. The flow rate is a function of the pressure-rise, the volume of the chamber, and the effective pumping speed (S_{eff}) of the chamber. To find the approximate gas spot area and associated pressures, the gas molecular weight and temperature is required. Table 2 summarizes the variables and units of used in the analytical simulation.



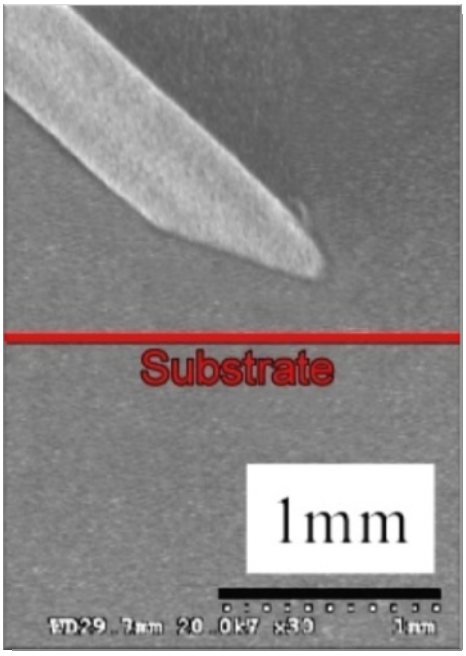


Figure 2-32: Nozzle Geometry

Illustration of nozzle geometry necessary for input into pressure simulation (top).[154] A SEM photomicrograph of the hypodermic needle used for vapor injection at the University of Tennessee is shown in the lower photograph. Its orientation with regard to the substrate is indicated.

Table 2: Pressure Simulation Inputs.

Variable	Units	Notes
EITHER: Flow rate of precursor gas, OR: Ion Gauge Pressure and Effective pumping speed	SCCM; Torr and l/s	If MFC used, SCCM of input gas can be used. Otherwise, ion gauge pressure and effective pumping speed of the system can be used.
Precursor Temperature	°K	Defaults to 300°K for room temperature
Precursor Mol. Weight	g/mol	-
Geometry Factors:		(see diagram in Figure 2-32)
Outer nozzle radius	μm	Measured to bottom of nozzle
Inner nozzle radius	μm	Taken from hypodermic needle catalog
Substrate clearance	μm	(or nozzle height above substrate)
Nozzle tilt angle	Degrees	Typically 45° or 90°. Measured at 21° for UT's system
Gas spread angle	Degrees	This is the half angle, typically 37.5°

Once all of the inputs are known, the program will determine the molecular flux at the beam spot and the area covered by the gas. From this, the local pressure at the substrate can be obtained. If the precursor flow rate (SCCM) is input to the simulation, the system pressure (P_{sys}, Torr) will be output for comparison to the reading from the EBID system's ion gauge. In addition to the local and system pressures, trends can be shown such as:

- Covered area as a function of nozzle vertical clearance
- Molecular flux as a function of temperature
- Pressure as a function of temperature, or height, or other geometry variables such as tilt angle and gas spread angle.

An example of output from the pressure simulation is shown in Figure 2-33. This shows the effect of nozzle height and spread angle on local gas pressure at the EBID site. A summary of the effects of input variables on the primary outputs is shown in Table 3. For related equations used by the simulation, see Kohlmann *et al.*[154] and Maissel[155].

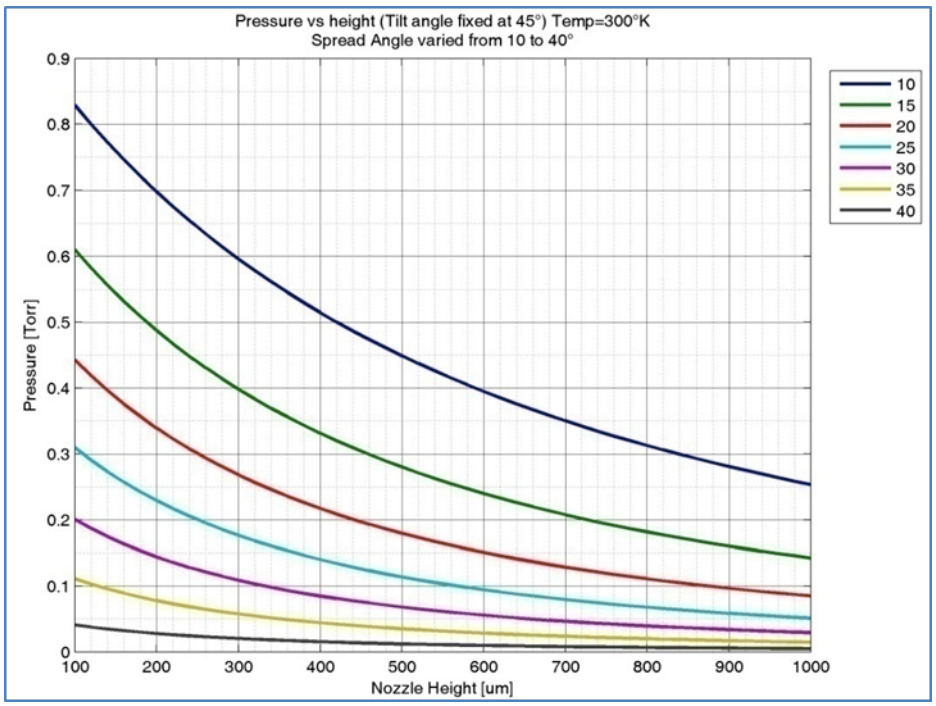


Figure 2-33: Example output from pressure simulation.

This output shows the effect of nozzle height and spread angle on the local pressure at the EBID site.

Table 3: Input/Output Summary from Pressure Simulation.

EFFECT OF INCREASING:	Area	Flux	Pressure
Nozzle Diameter	Increases	Decreases	Decreases
Nozzle Height	Increases	Decreases	Decreases
Tilt Angle	Decreases	Increases	Increases
Spread Angle	Increases	Decreases	Decreases

Chapter 3--Simulation Results

3.1 Overview

Once the series of tests were completed to verify the integrity of the simulation with respect to the equations derived from literature and the physics involved, a series of simulations to examine the fundamental EBID process were performed. Because the EBID process is such a complex interaction of many parameters, predicting the effects of changing primary input variables is often difficult and unwieldy. The simulation has the unique ability to combine all of these parameters to produce viable results, however, which can explain many of the observations studied experimentally since the inception of EBID. This chapter will discuss four specific simulation studies that were performed to validate the simulation and ultimately elucidate some of the important and subtle aspects of electron beam induced deposition.

Four sets of simulations were performed. These were selected to study the effects of altering four of the main input parameters for the EBID process. These parameters were beam energy (E_o), beam current, gas pressure, and material (i.e. precursor gas and substrate choice). These parameters are easily controlled by the EBID operator- and made the most sense for a baseline verification of the simulation. However, to fully understand the underlying process mechanisms, a number of "secondary parameters" were also altered in these experiments. These secondary parameters are input variables which the simulation uses to change the physics involved, but are not able to be controlled necessarily by the EBID operator in an actual experiment. Some of these secondary parameters include:

- The mean desorption time of gas molecules,

- The surface diffusion coefficient of the precursor, and
- The initial state of the gas coverage prior to EBID deposition (i.e. monolayer coverage vs. no coverage).

Other secondary parameters exist, such as beam radius and profile, substrate temperature, and sticking coefficient, which were not examined for this dissertation but could easily be investigated by the simulation. Indeed, the possibility for exploration of a number of input variables exists for future study. This makes the simulation invaluable because it provides insight into changing parameters which might not be altered in the experimental environment.

The overall results for each of these studies are the changes in pillar morphology and growth patterns which can be observed qualitatively and quantitatively through the simulation output. Trends already commonly known to experimentalists will justify the simulation's accuracy, while deviations from the norm will reveal opportunities for closer examination. In all of these cases, many of the parameters have been held constant in order for cross-comparison between simulations.

The parameters chosen for these studies are based on working knowledge of EBID systems currently in use, as well as our own modified Hitachi SEM/EBID system. For instance, the beam diameter is set to 3nm (in a Gaussian-like distribution) which represents a typical spot size in a typical system. Clearly, as was previously discussed and shown in Figure 1-6, this parameter can easily change depending on the components of the system.

The materials involved include tungsten, which is deposited from tungsten

hexafluoride gas (WF_6), and silica (SiO_2) which is deposited from tetraethyl -orthosilicate (TEOS) vapor. These have been well studied by researchers, particularly at the University of Tennessee, and therefore made excellent choices for materials to include in this study. One item to note is that the simulation has the ability to use multiple materials; for example different pre-cursor/substrate materials such as depositing tungsten on germanium, or SiOx on silicon. In an effort to minimize complexity, which improves the actual time it takes to run these simulations, only single-material systems have been employed for study in this dissertation. For instance, the WF_6 precursor (which deposits tungsten) was deposited onto a tungsten substrate, and TEOS (which deposits SiO_2) was deposited on a SiO_2 substrate. Furthermore, the exact stoichiometry of TEOS deposits varies, therefore the exact material properties of this deposit are unknown. The properties of SiO_x are, however, close enough to the properties of SiO_2 (whose properties are well known). Therefore, all input parameters into the simulation with regard to SiO_x are based on the properties of SiO_2. Clearly, the results from these simulations will not duplicate all experimental results due to these assumptions. The goal of this work is rather to show trends and behaviors when major properties are altered, rather than scrutinize the quantitative results in comparison to experimentally obtained values. This is the reason that this simulation is not referred to herein as a "model". Many more variables and improvements need to be implemented into this program before such a claim can be made, including the general acceptance by the scientific community that a Monte Carlo approach to this problem is a viable method for obtaining these results. See Appendix C for a list of the material properties for tungsten and SiO_2 which were used for the simulations mentioned in this dissertation.

The four studies which were performed are identified as follows:

1. Beam Energy Study,
2. Mass-Transport vs. Reaction-Rate Limited Growth,
3. Surface Diffusion Effects, and
4. Material comparison (tungsten vs. SiO_x).

Each of these will be thoroughly described in their applicable sections.

3.2 General Simulation Output

The simulation has several outputs which are used for studying the results. Firstly, the structures grown are displayed in 3D format with spheres representing each deposited atom. Deposited atoms are color coded to aid the identification of the electron type which initiated the dissociation event (red=PE, green=FSE, blue=BSE, yellow=SE^I, and cyan=SE^{II}). This is illustrated in Figure 2-3. As previously described, the simulation is 3D in nature, therefore comprised of a myriad of cubic units, called "voxels". The term "pixel" is generally assigned to 2D environments, and will be used in this dissertation to describe rastered movements of electron-beams on a sample surface (e.g. "*the pixel dwell time", etc.*). The voxel size was determined from the surface density (which is inherently 2D) of the deposited species (see Equation 1) and then extended to 3D by adding the *z* dimension. For simplicity, a simple cubic deposition lattice was utilized for all simulations.

Due to the nature of how Monte Carlo simulations track electron locations through the system, it is possible to perform a quantitative analysis of the deposition events so that each type of deposition event (PE, BSE, FSE, SE^I, SE^{II}) can be can be

compared. These data are displayed in a number of ways. First, the number of deposited species of each can be reported. This can be compared to the number of electrons simulated, for example, to give an approximation to "deposition efficiency," which is simply the number of deposited atoms per incident electron. The percentages of deposition from these values can be calculated for each electron type, in order to illustrate which type of electron contributed the most to structure growth.

This data is better represented by showing the evolution of these quantities as a function of time, number of electrons, or even pillar height, so that transient behavior can be investigated. The information can be displayed cumulatively, as the simulation progresses, or by sampling the output at set increments of time or number of electrons. This type of plot yields more information, because it can display "cross-over" trends where one type of electron becomes prevalent over another, or "saturation levels" where depositions of a particular electron type reach a steady-state condition. Each of these types of behavior has some physical significance in the development of the structure, which cannot always be gleaned from studying EBID growth experimentally. When data is displayed in this fashion, it is often reported on a "per-electron" basis because sample size can change from one simulation to the next, which makes comparison difficult.

BSE and SE emissions are also tracked by the simulation, and histograms as a function of electron energy or radius can be generated. This provides the BSE and SE yield data which changes as the surface topology changes. Like the deposition events, this data can be simply tabulated or plotted as a function of time/electrons ran. The simulation has the unique ability to measure SE or BSE emission because its origin is known. Detectors utilized in SEM's, however, discern electron type by issuing a "cut-

off" level of energy so these classifications can be made. SE's, for example, are typically measured up to 50eV, despite the fact that high-energy SE emissions exist. A BSE detector cannot discern a high-energy SE from a regular BSE, however, therefore these high energy SE's are just added into the BSE yield coefficient. It was debated whether to make this simulation count the SE's and BSE's as a SEM detector might, in order to accurately compare simulated yields to experimental yields. Ultimately, the *true* SE/BSE emission yields were decided to be reported, in lieu of these comparisons. Fortunately, this had minimal impact on the results because the number of high energy SE's were relatively insignificant compared to the amount of low-energy SE's emitted from samples when comparisons of these two methods were examined.

Other statistics such as deposition rate, pillar height, gas coverage, and simulation surface area can be output both cumulatively or sampled at varying intervals throughout the simulation. Pillar shape is of particular interest, therefore the progression of this output is plotted in a number of ways. Firstly, the size of the pillar is reported in terms of height and width. A common term for the height/width quotient is the "aspect ratio", which gives a quantitative idea as to if a pillar is relatively "thin" or "thick". Of somewhat more importance, however, the temporal progression of pillar morphology is also output by this simulation. 2D traces of the pillar shape as a function of time reveal how the shape changes during growth, as well as how the rate changes (as illustrated by differences in separation of each chronological stratum).

Following this dissertation will be appendices which give the tabularized data for each simulation. For interpretations of this data, please see the text in the applicable section.

3.3 Beam Energy Study

The first study performed involved tungsten pillars grown under reaction-rate limited conditions at 1keV and 5keV electron energies. These simulations were run to 2 million electrons each, in order to determine the effects of changing beam energy on pillar growth and morphology. The center of the Gaussian-like beam (3nm diameter) was held in a static location, which is referred to as "spot-mode" deposition to differentiate it from a rastered beam.

Reaction-rate limited (RRL) growth is a regime where the flux of gas molecules is much greater than the flux of electrons at the substrate surface. These conditions can be obtained by altering many of the system parameters, most notably the gas pressure and beam current. In order to be assured of RRL growth, these parameters were input such that the gas flux was three orders of magnitude larger than the electron flux (i.e. $\Gamma_{gas} \approx 1000 * \Gamma_{electrons}$). To obtain the necessary flux ratio, a local pressure of 7 Torr and a beam current of 0.009pA were used. This current gives an approximate electron flux (with a 3nm diameter beam) of $8x10^{17}$ electrons/cm^2-s. A local pressure of 7 Torr corresponds to a molecular flux of approximately $8x10^{20}$ molecules/cm^2-s, assuming ideal gas behavior. Figure 3-1 shows a simulation of these conditions that calculates the flux ratio for a Gaussian-like electron beam. Near the center of the beam, the flux of gas is about 1000 times the flux of electrons.

Since the amount of gas molecules will therefore be overly abundant when compared to the amount of electrons available to create a dissociation event, the growth behavior is said to be limited by the electron dissociation reaction, and not the gas

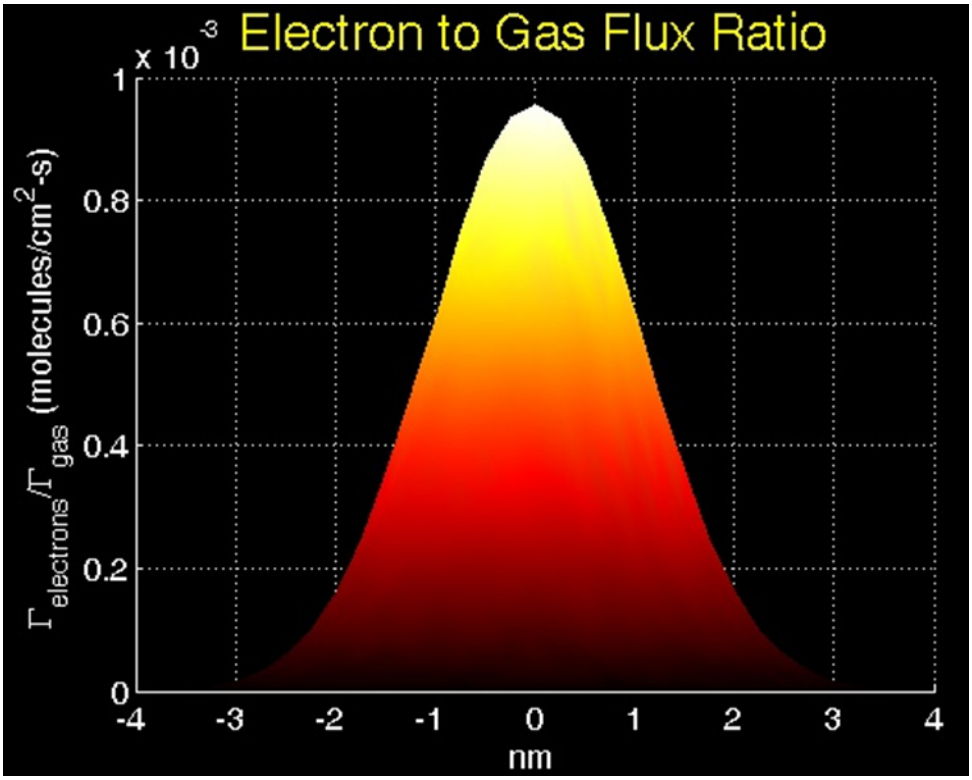


Figure 3-1: Electron to Gas Flux Ratio for Reaction-Rate Limited Conditions.

Examination of the ratio of electron flux to gas flux for a Gaussian-like beam of 3nm diameter. At the beam center, there are about 1000 more gas molecules than electrons, indicating reaction-rate limited conditions.

delivery. Under these conditions, all of the gas sites covering a surface are typically filled between incident electrons (i.e. a saturated surface). When in this regime, surface diffusion and other gas dynamics routines are not necessary. In fact, the code detects the flux ratio and disables these algorithms as previously discussed in Section 2.8. The flux ratios as a function of local pressure for several beam currents has been calculated and plotted in Figure 3-2.

Once the input conditions were calculated, the simulations were ran to examine the effect of beam energy on pillar morphology. For a summary of the inputs and outputs for this simulation, please see Table 4. A complete listing of inputs and outputs for this study is in Appendix D.

Figure 3-3 shows the 5keV pillar in a 3D view as well as a 2D time-evolution plot. The time progression plot gives a qualitative look at the vertical growth rate, which as expected is linear for the RRL regime. The pillar grew to a height of 168 nm tall with a width of 5.4nm, giving an aspect ratio of approximately 31:1. Also shown in Figure 3-3 is the tip region which has an 11nm cone atop the otherwise cylindrical pillar.

The 1keV RRL pillar was grown under the same conditions as the 5keV pillar, yet reached a height of 446 nm tall with a width of 5.8nm, giving an aspect ratio of approximately 77:1. The 1keV RRL pillar is shown in Figure 3-4. In order for a logical comparison between the two pillars, the 1keV pillar was examined after 750k electrons in order to compare it to the 5keV pillar at 2 million electrons because both had a height of ~168nm at these increments.

When comparing the 1keV and 5keV pillars grown in RRL conditions, it was

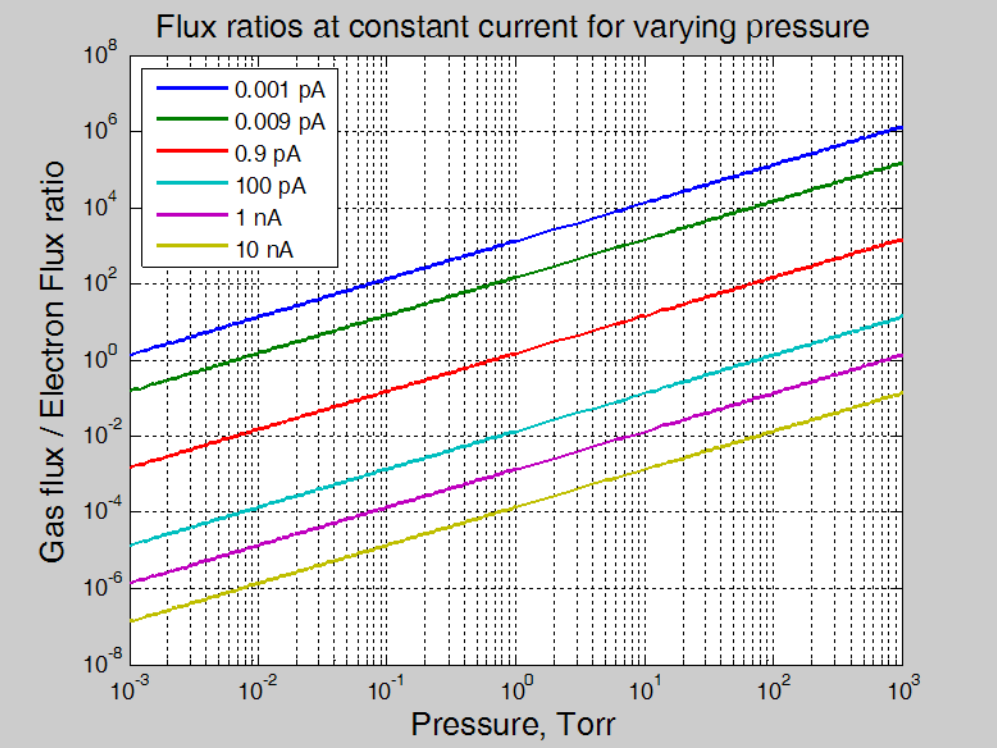


Figure 3-2: Calculation of mean gas to electron flux ratios for varying pressure.

These curves represent how the gas to electron flux ratios vary as a function of local pressure for several beam currents.

Table 4: Energy Study Run Summary

Run	Energy	MTL/ RRL	Other	# e-	Height, nm	Width, nm	SE Yield	BSE Yield
				(SE/BSE Emissions Tests)				
-	1keV	N/A	No Gas	2 M	0	0	1.3	0.41
-	5keV	N/A	No Gas	2 M	0	0	0.44	0.46
				Energy Study				
1	5keV	RRL	No ML	2 M	168.25	5.4	0.56	0.95
2	1keV	RRL	No ML	2 M	446.25	5.8	1.3	0.96
2a*	1keV	RRL	No ML	750k	167.25	5.3	1.3	0.94

Energy Study Depositions

Run	PE	FSE	BSE	SE^{I}	SE^{II}	Total Depositions	Deposit Efficiency
1	29.5k	60.8k	2.6k	69.4k	22.2k	184.5k	9.2%
2	88.4k	175.1k	32.8k	110.7k	84.4k	491.4k	24.6%
2a*	33.2k	65.2k	12.9k	41.7k	32.7k	185.7k	24.8%

* Run 2 was examined at various locations to compare to other runs at similar heights. "Run 2" is the full 2 million electrons and grew to a height of 446nm.

"Run 2a" is at 750k electrons (167nm tall) which can be compared to "Run 1" (that grew to 168 nm at 2M electrons) for the energy study (1keV vs. 5keV).

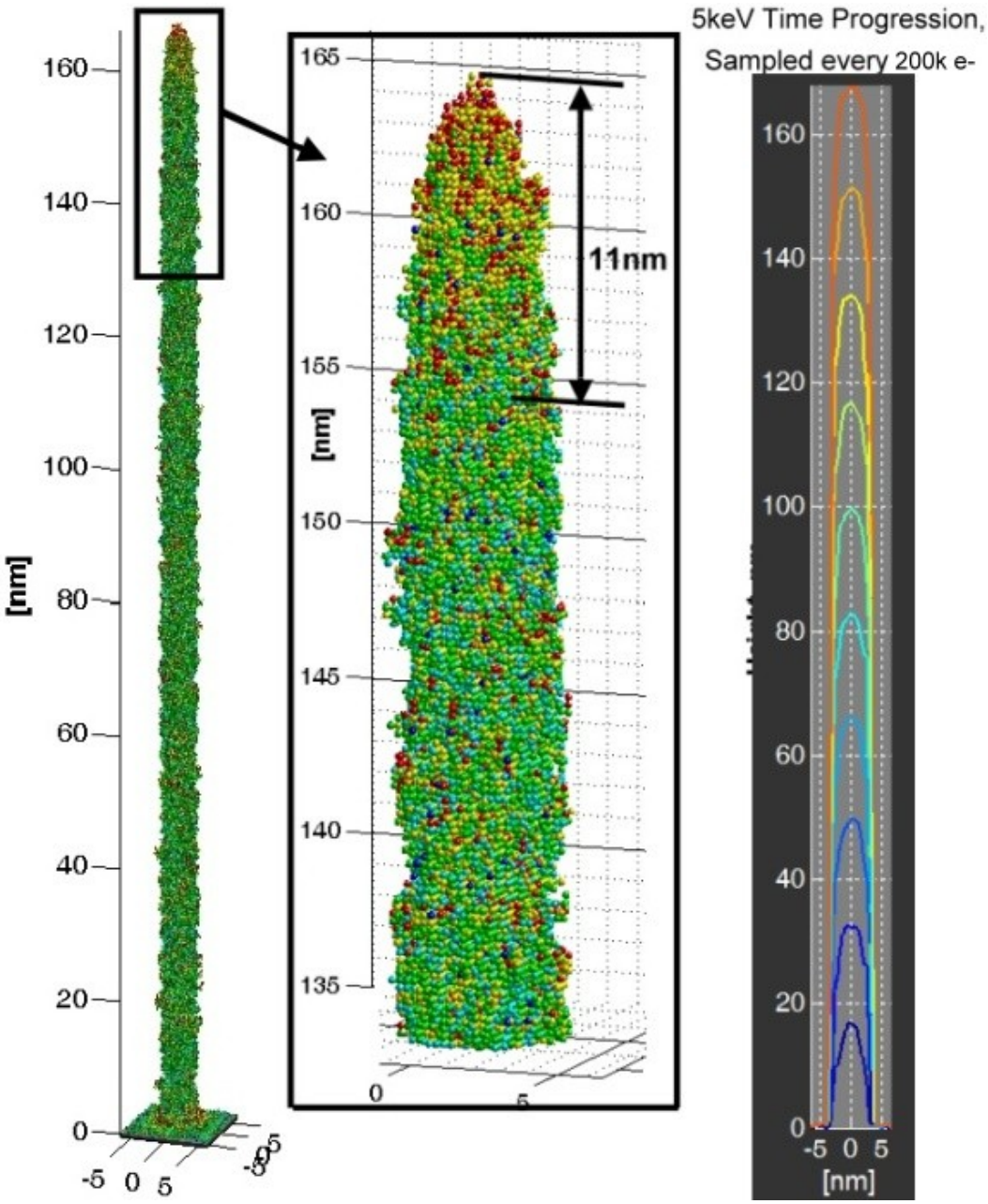


Figure 3-3: 5keV Pillar grown to 166nm tall.

Tungsten pillar grown on tungsten at E_o=5kev. This was simulated under RRL conditions to a height of 168 nm after 2 million electrons. The top of the pillar is a conical cap that measured approximately 11nm atop an otherwise cylindrical body. Also shown is a 2D cross-sectional view through the pillar showing the progression of the pillar growth divided into 10 increments of 200,000 electrons each.

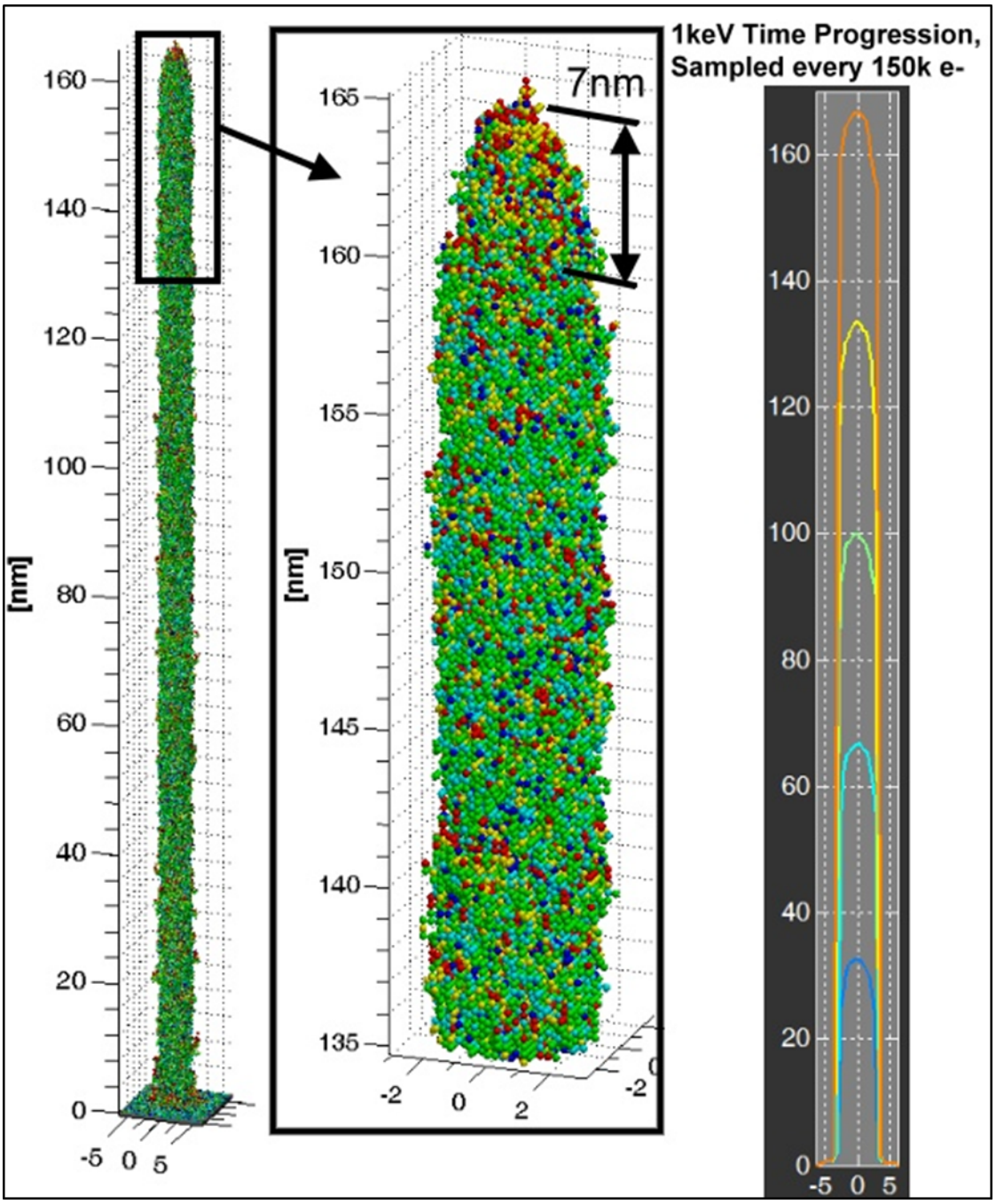
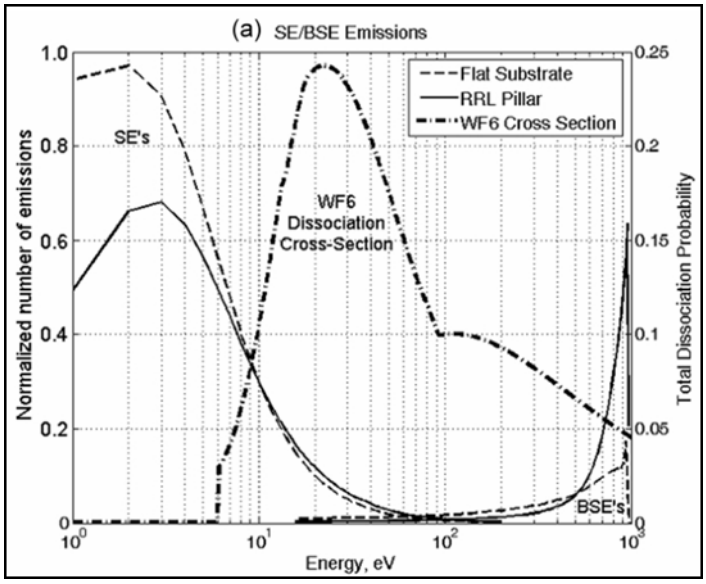


Figure 3-4: 1keV Pillar grown to ~167nm tall.

RRL tungsten pillar at E_o=1kev. The pillar was grown to 446nm tall at 2M electrons, but shown after 750k electrons at a height of 167nm (for comparison purposes). The conical cap was measured to be 7nm tall.

observed that the as the beam energy increased, the pillar growth rate declined (446nm tall for 1keV vs. 168nm tall at 5keV). This is due to a combination of several factors, which is difficult to separate experimentally. The statistical data obtained by this simulation, however, elucidates the different contributions to the deposition rate change. To understand this, first the primary electron energy and the SE and BSE emissions from the simulation are compared to the total WF6 cross section. When one compares the dissociation cross section at the two primary energies (0.0442 at 1keV and 0.0148 at 5keV) the ratio at 1keV/5keV is ~ 3:1. This compares almost exactly to the simulated ratio of PE deposition events for 1keV/5keV ~3.

Figure 3-5 shows the normalized SE/BSE emission spectrum for the 1keV pillar as well as the baseline spectrum from a flat substrate. The cumulative SE yield (δ) at 1keV was approximately the same (1.3) for both the flat substrate (2 million electrons) and for a pillar grown to 2 million electrons. However, the emission spectra show a higher number of low-energy SE electrons being emitted from the flat substrate surface. Since electrons are scattered out of the pillar after a small number of scattering events, the SE's tend to be emitted at higher energy (because energy decreases for each scattering step according to the Plural scattering model). Conversely, BSE emission at high energies is significantly higher in the pillar relative to the flat substrate. In addition, the backscattered energy distribution shifts toward higher energy as the electrons escape after only a few energy loss collisions (the BSE yield peaks at 938eV for a flat 1keV substrate and at 955eV for a full grown pillar at 1keV). The cumulative BSE yield (η) for the flat substrate at 1keV was 0.41 (calculated by the HKLCS model to be 0.43), and η was



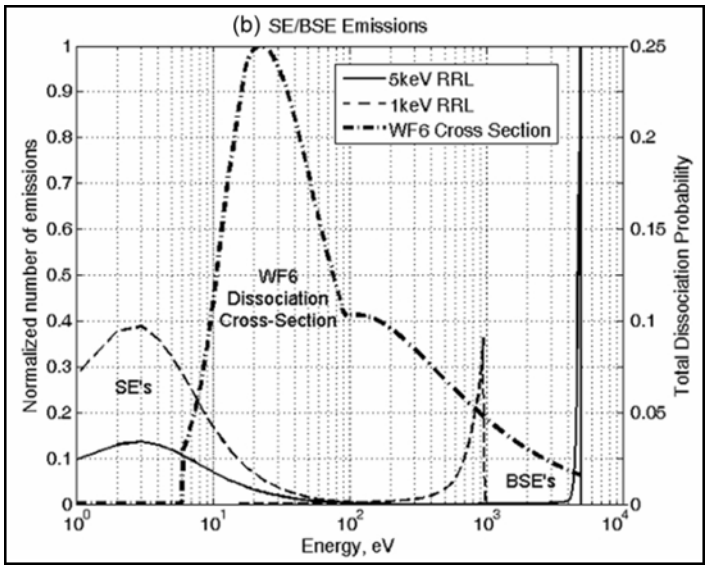


Figure 3-5: SE and BSE emission spectra.

SE and BSE emission spectra as a function of energy. (a) 1keV RRL pillar showing the normalized comparison between the flat substrate emissions and pillar-structure emissions after 2 million electrons. The total dissociation probability as a function of primary beam energy is superimposed on this figure. (b) A comparison of the emissions from 1keV and 5keV pillars grown to the same number of electrons (2 million) with the total dissociation probability curve superimposed.

measured to be 0.95 after growing a pillar to 2 million electrons. The reason the BSE yield approaches 1 is because the BSE counter is incremented any time one of the primary electrons leaves the solid. As the pillar grows, virtually all the primary electrons scatter out of the pillar, thus the BSE yield approaches unity.

Figure 3-5 also shows a normalized comparison of the secondary and backscattered electron spectra from the 1keV and 5keV pillars at the same number of electrons (2 million). The main item of note from Figure 3-5 is the fact that the BSE emission curve for the 1keV pillar overlaps the total dissociation probability curve of WF_6 at a higher probability (.025-.075) than the 5keV emissions (which overlap the probability curve in the 0.01-0.02 range). Thus, the probability for dissociation of the 1keV BSE is more than double that for BSE emitted electrons at 5keV. Since both the 1keV and 5keV pillars have approximately the same BSE yield (~0.95), this qualitatively explains one of the reasons for higher growth in the 1keV pillar after the same number of simulated primary electrons. Note that the 5keV emissions were more concentrated at higher energies due to fewer scattering events, which explains why the normalized peak is higher and narrower.

Another observation is that the SE yields are higher at lower primary electron energy and decline as 1/E at higher energies[109]. Since the energy spectra of the SE's are comparable for both 1keV and 5keV, the amount of deposition at each primary energy is directly dependent on the yield. The SE yield after growing the pillar to 167 nm tall was 1.3 at 1keV but only 0.6 at 5keV. This is similar to experimentally observed yields.[156] The combination of these factors resulted in a 25% deposit efficiency at 1keV as opposed to a 9% efficiency at 5keV under similar reaction rate limited growth conditions.

Figure 3-6 shows how the yields change as the pillars grow. This figure shows the sampled yield as a function of pillar height for the 1keV RRL pillar (a) and the 5keV RRL pillar (b). The sampled yields are calculated at each increment of 10,000 (a) and 30,000 (b) electrons. The BSE yields increase slowly as the pillar grows before reaching a steady state value. The SE^{I} yield increases slowly, but the SE^{II} yields peak at 0.9 before dropping to a steady state value of about 0.6. This is due to the temporary increase in surface area during initial formation of the pillar, since the electron interaction volume is still in the substrate and the SE^{II}'s can emit over an enlarged area. Once the pillar grows beyond the effective stopping range (where the electron interaction volume is encapsulated within the pillar), the SE^{II} emissions fall to a lower steady state value. A similar but less pronounced phenomena is seen in the 5keV pillar as well (Figure 3-6). Note that the steady state values for the sampled yields are different than the cumulative yields reported in Table 4 and Appendix D.

One of the primary purposes for this simulation is to answer one of the prevailing questions regarding the EBID process: which electrons are primarily responsible for the pillar growth? Figure 3-7 shows the total sampled deposition events during the initial stages of the 1keV and 5keV pillars. The electron type contributing most to the growth of the 1keV pillar was the FSE's; however the SE^{I}'s contributed the most in the 5keV pillar. The pillar growth reaches steady state very quickly because of the RRL conditions. Note in the 1keV pillar that the combined effect of the BSE's and FSE's contributes more to deposition than the SE^{I}s and SE^{II}s combined (by about 11%). At 5 keV, however, the SE^{I}s and SE^{II}s are responsible for 50% more growth than the BSE's + FSE's.

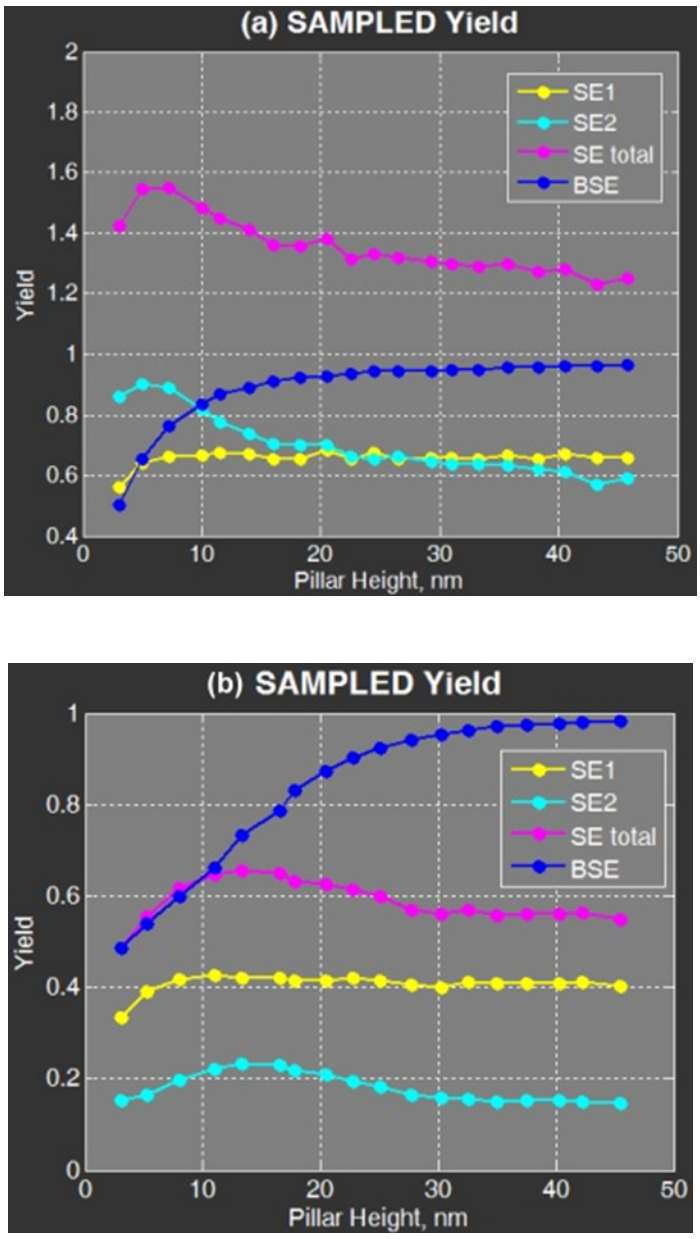


Figure 3-6: SE and BSE Yields as a function of Pillar Height

Sampled SE and BSE yields as a function of pillar height in the (a) 1keV RRL pillar and (b) the 5keV RRL pillar. Only the first stages of the pillar development (<45nm tall) are plotted. The 1keV samples were taken every 10,000 electrons, while the 5keV samples were taken every 30,000 electrons. Yields were normalized to each sample size.

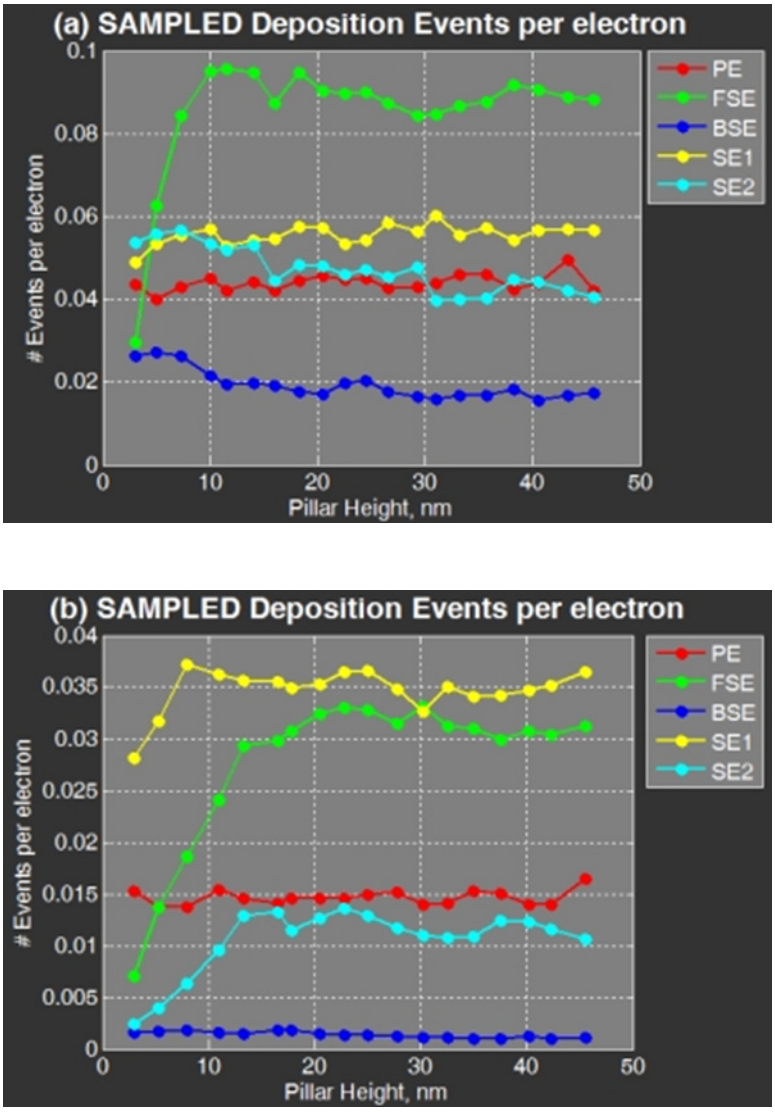


Figure 3-7: Sampled deposition events by electron type (1keV vs. 5keV)

Deposition events based on electron type as a function of pillar height in the (a) 1keV RRL pillar and (b) the 5keV RRL pillar. Only the first stages of the pillar development (<45nm tall) are plotted. The 1keV sample size was 10,000 electrons, while the 5keV sample size was 50,000 electrons. The number of events was normalized to the sample size.

As the pillar grows, the interaction volume is eventually contained within the dense tungsten pillar, and only forward scattered electrons reach the substrate after traversing the vacuum. At this point the deposition rate becomes approximately steady state. At 1keV, this steady state behavior occurs at ~7nm, and at about ~20nm in the 5keV pillar. As a validity check for the simulation, the pillar height where saturation occurs (particularly the FSE's) should be related to the "effective" Bethe range (the distance the electron travels before exiting the pillar) dictated by the material, beam energy, and pillar size. An estimate of the effective Bethe range was made at 1keV and 5keV by calculating the average number of scattering events that occur before the primary electron leaves the pillar, multiplied by the scattering distance per step. This was calculated for tungsten to be ~3.5nm for 1keV and ~11.1nm for 5keV electrons. The saturation height was approximately twice this value for both energies.

The pillar shape was found to be similar at both primary beam energies; at 168nm tall, the width was ~5.5nm (both at 1keV and 5keV). It was determined that a balance between the vertical growth rate and the number of emitted electrons causes this effect. See Figure 3-8 for a comparison of the pillar profiles for both pillars taken at a sampled height of 50nm each (22k electrons at 1keV and 60k electrons as 5keV). Initially, it was suspected that the large magnitude of SE^{II} emission from the pillar sidewalls and to a lesser degree the forward and backscattered electrons at low energy would promote significant lateral growth at the pillar sidewalls. This would in turn result in wider pillars grown at lower energies. However, the vertical growth rate is higher at low beam energies and the electron range is lower; hence the time for lateral growth is limited at

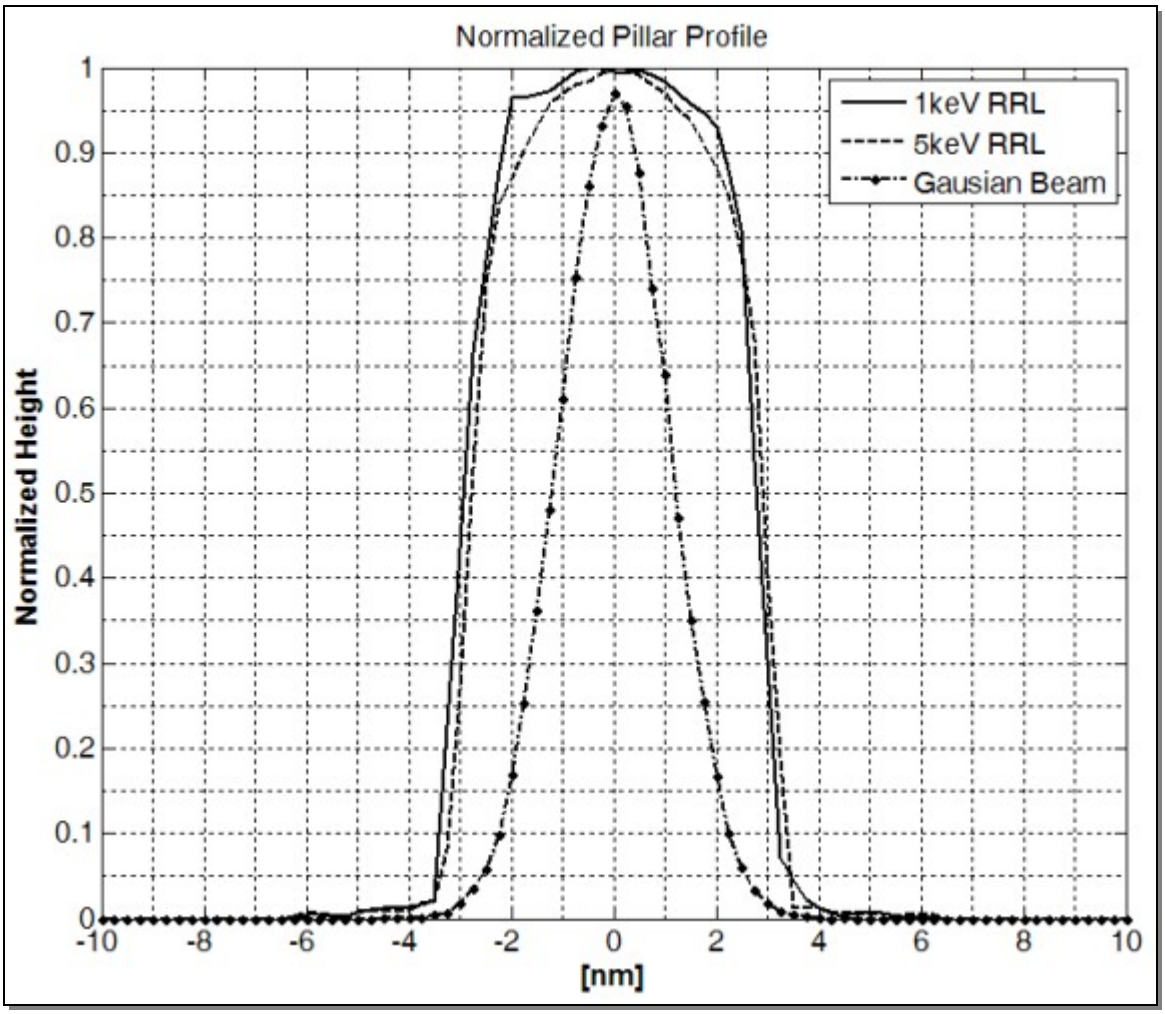


Figure 3-8: Normalized Pillar Profiles at 1keV and 5keV

The 1keV and 5keV pillars were sampled at heights of 50nm (22k electrons at 1keV and 60k electrons at 5keV). Their profiles show no difference in lateral resolution.

low beam energies because the electron interaction volume "rises" through the pillar faster. *Thus, the surprising result was obtained that vertical pillar growth rates are faster at lower energies without a loss in lateral resolution*. At E_o = 5keV the vertical growth rate was less than half of that at 1keV, yet at this higher energy the number of SE^{II}'s and BSE's emitted from the pillar was reduced and thus lateral pillar growth was lower. This is very significant result in the context of EBID as a nanoscale feature repair tool where lateral resolution is important with regards to cross contamination and fast growth times are attractive from a throughput perspective.

Another morphological difference between the pillar grown at 1keV and that grown at 5keV is that the shapes of the "cone" atop the pillars are different. At 1keV, this cone has a height of about 7 nm, and at 5keV the cone was measured to be about 11 nm tall (Figure 3-3). Both of these correlate to the saturated growth described above and is described in more detail by Choi *et al*.[86]

3.4 Mass Transport Limited EBID vs. Reaction Rate Limited Growth Study

The same conditions which formed the 1keV RRL pillar described above were used to simulate another pillar, except that the beam current was increased to 9pA and the pressure lowered to 7mTorr. This has the effect of creating a mass-transport limited (MTL) operating regime because the ratio of electrons to available gas molecules is high ($\Gamma_{electron}$= 1000*Γ_{gas}). Table 5 summarizes the input and output for the reaction rate limited growth versus the mass transport limited growth. For a complete list of inputs and outputs from this simulation, see Appendix E.

The MTL pillar was grown to 2 million electrons like the 5keV RRL pillar shown

Table 5: MTL vs. RRL Study Run Summary

Run	Energy	MTL/ RRL	Other	# e-	Height, nm	Width, nm	SE Yield	BSE Yield
2b*	1keV	RRL	No ML	50k	11.5	4.8	1.5	0.72
3	1keV	MTL	No ML	2M	11.5	9.7	1.6	0.63

MTL vs. RRL Study Depositions

Run	PE	FSE	BSE	SE^{I}	SE^{II}	Total Depositions	Deposit Efficiency
2b*	2.1k	3.7k	1.2k	2.7k	2.7k	12.4k	25%
3	2.9k	14.2k	8.3k	4.8k	16.8k	47.1k	2.4%

* Run 2b is the same as "Run 2" (see Table 4), but at 50k electrons (11.5nm tall) which can be compared to "Run 3" that grew to 11.5 nm tall at 2M electrons for the MTL vs. RRL study.

in Figure 3-3. In the 1keV MTL case, however, the pillar only grew to a height of ~12 nm tall (Figure 3-9). The significant morphological difference is the lateral broadening which is observed under MTL conditions. The width of the MTL pillar is 9.7nm wide, which is almost twice the width of the RRL pillar grown to the same height. A normalized comparison of the pillar shapes at a height of 12nm is shown in Figure 3-10 (also included is the Gaussian electron beam profile).

The individual electron contributors to growth and deposition rate of the MTL and RRL pillars (both grown to 12nm tall) are shown in Figure 3-11. This plot shows that SE^{II}'s contribute the much more to the pillar growth in the MTL condition than in the RRL condition. In fact, the sum of the SE^{I} + SE^{II} depositions account for 44% of all growth in both conditions, however SE^{II}'s contributed more in the MTL pillar than in the RRL pillar (34% of the depositions were SE^{II} in the MTL, whereas only 22% were SE^{II}'s in the RRL condition). These electrons contribute more to the pillar broadening than the SE^{I}'s because they can emerge from any part of the surface (not just near the cone apex).

In the MTL pillar, the SE^{II}'s initially dominate the growth; however the FSE's steadily increase. As the pillar grows to a height where the interaction volume is encompassed within the pillar, the FSE's and SE^{II}'s start to saturate and reach a steady-state. This behavior is observed early on in the RRL pillar (around 50,000 electrons), however, because of the lower deposition efficiency, the FSE's don't begin to saturate until about 1.6M electrons in the MTL pillar. Accordingly, this is at about the same height as the RRL pillar saturation point (~10 nm). *This is an indication that saturation and steady-state growth are dependent upon the electron stopping power, which is the same in both*

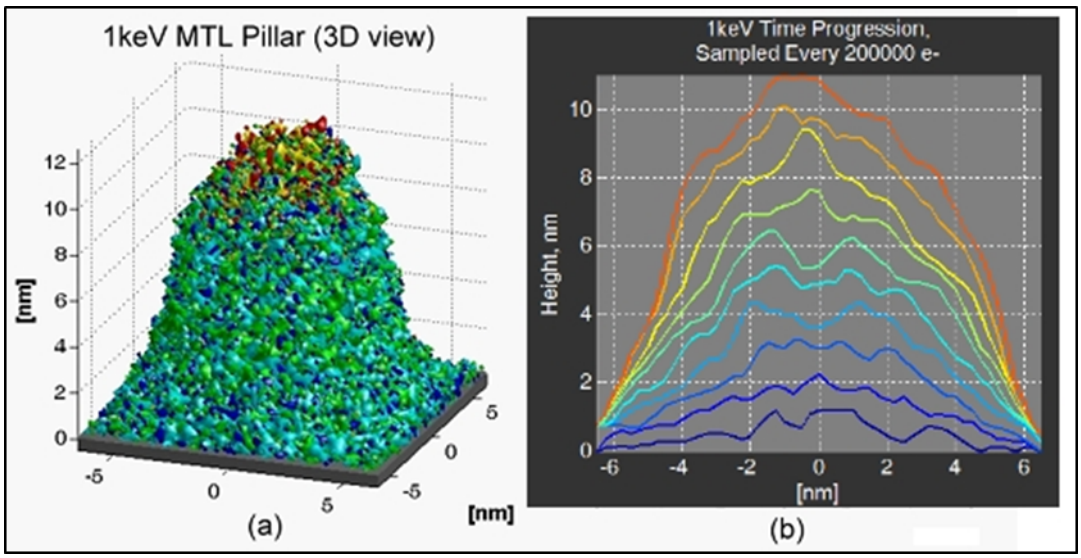


Figure 3-9: Mass transport limited pillar at 1keV.

(a) Mass-transport limited pillar (Run 3) with no initial monolayer. (b) The time-evolution of this pillar in 200,000 electron increments.

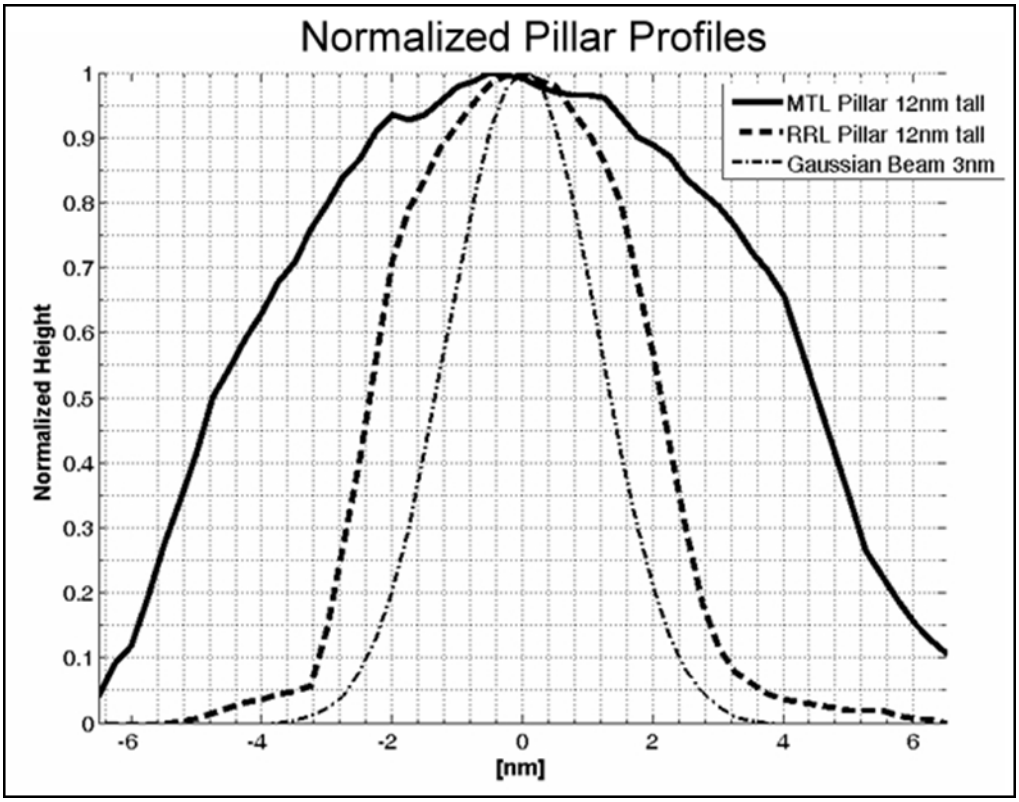


Figure 3-10: Normalized comparison of MTL and RRL pillars.

Normalized comparison of the MTL pillar shape, RRL pillar shape, and Gaussian beam profiles. These profiles were taken from the 1keV MTL and RRL pillars at the same height (11.5nm). 100,000 random Gaussian samples of a 3nm diameter beam were superimposed on the substrate surface to show the beam profile.

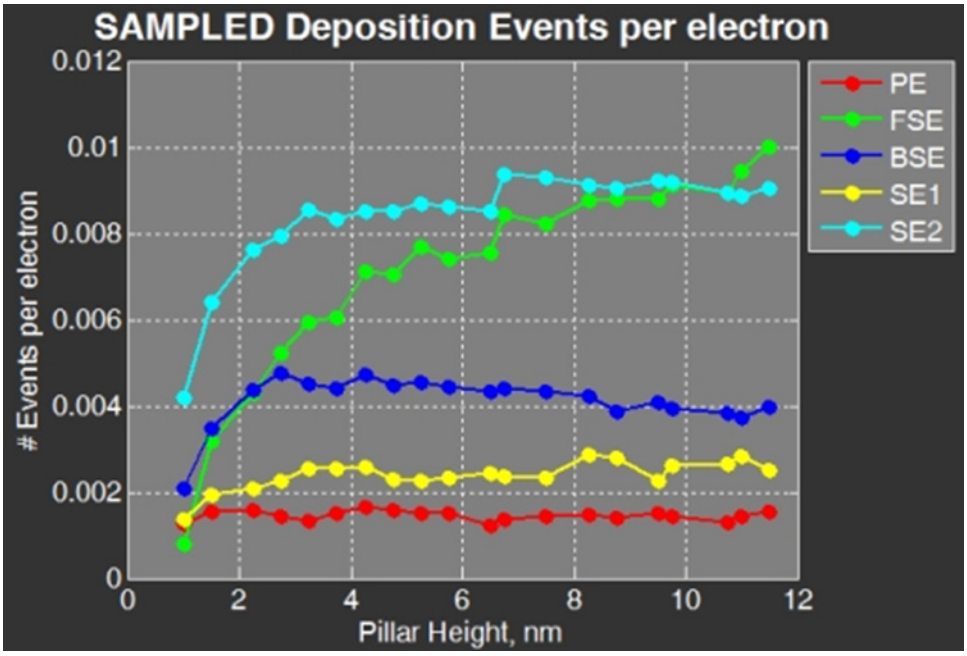


Figure 3-11: Sampled deposition events from 1keV MTL pillar.

Deposition events based on electron type as a function of pillar height in the 1keV MTL pillar, grown to 2 million electrons. The sample size was 100,000 electrons, and the number of events was normalized per electron.

simulations. The MTL regime causes the pillar to broaden more relative to the RRL regime because virtually all the gas molecules that strike the surface in the electron interaction range get deposited. Thus MTL growth is more isotropic.

3.5 Surface Diffusion Effects Study

For this study, four simulations of 2,000,000 electrons were conducted in the MTL ($\Gamma_{electron}$= 1000*Γ_{gas}) regime (E_o = 1 eV, beam current i_b = 0.009 pA, pressure 7mTorr), as listed in Table 6. The full list of inputs and outputs for these simulations is in Appendix F. These simulations were designed to examine the effect of gas/surface interactions on pillar morphology.

The first run is a mass transport limited grown pillar which originated with no gas monolayer present and no gas dynamics on the surface (already shown in Figure 3-9). All growth of this pillar was due to adsorption of gas molecules onto the surface based on the prescribed localized pressure and a desorption time of 1.0 s (common to all simulations). Next, the effect of starting with an initial monolayer (ML) coverage of gas was examined. The third case employed surface diffusion (D=1x10^{-9} cm^2/s) of adsorbed species. This allows the gas particles to migrate on the surface in a true-3D fashion within the bounds of the simulation. Gas species which diffuse to the simulation boundary were reflected back into the simulation. The fourth pillar simulation employed surface diffusion (D=1x10^{-9} cm^2/s) and included a constant source of gas at the boundary perimeter of the simulation. This simulation therefore had two gas sources: the flux from the precursor adsorption, and surface diffusion from the boundary which was constantly replenished after each electron. Note that no initial monolayers were present in these last two simulations.

Table 6: Surface Diffusion Simulation Summary

Run	Energy	MTL/ RRL	Other	# e-	Height, nm	Width, nm	SE Yield	BSE Yield
3	1 keV	MTL	No ML	2M	11.5	9.7	1.6	0.63
4	1 keV	MTL	With ML	2M	13.5	8.9	1.6	0.69
5	1 keV	MTL	Diffusion	2M	62	5.9	1.5	0.88
6	1 keV	MTL	Diff+Boundary	2M	111	6	1.4	0.94

Surface Diffusion Study Depositions

Run	PE	FSE	BSE	SE^{I}	SE^{II}	Total Depositions	Deposit Efficiency
3	2.9k	14.2k	8.3k	4.8k	16.8k	47.1k	2.4%
4	3.1k	16.1k	7.9k	5.3k	16.7k	49.1k	2.5%
5	14.9k	34.1k	8.1k	19.1k	19.9k	96.1k	4.8%
6	26.7k	60.1k	13.4k	33.4k	33.6k	167.2k	8.4%

Note that Run 3 was previously used in the MTL vs. RRL study (Table 5).

Figure 3-12 shows the electron deposition plots and pillar cross sections for the last three simulations (Runs 4, 5, and 6) in the gas dynamics study mentioned above. In all four simulations which were run, the BSE's+FSE's contributed more toward the pillar growth than the SE's (SE^{I} + SE^{II}). The first two simulations both produced approximately the same amount of depositions and pillar morphology except there was ~ one extra monolayer worth of deposition (2,032 more deposition events with the initial monolayer). Initially during the simulation, there is a spike in SE depositions, as shown in the deposition plot for Run 4 (MTL 1keV + ML).

Enabling surface diffusion increased pillar growth as expected, because the previously unused gas that is adsorbed at the periphery of the simulation can diffuse into the beam location where EBID can take place. In fact, twice as many deposits occurred with surface diffusion enabled than without. The morphology also slightly changed as the surface diffusion increased the vertical growth rate and decreased the width as molecules that would otherwise contribute to growth outside of the beam spot could contribute to the vertical growth. The increased pillar height (greater than the effective Bethe range) meant that more FSE's contributed to the deposition. An interesting outcome from the simulation was that SE^{I} depositions accounted for 10% of the depositions without diffusion, but increased to 20% of the total depositions with diffusion enabled. PE deposition events saw a similar increase (from 6% to 16%). This exemplifies the importance of surface diffusion in vertical pillar growth because these events predominantly take place at the top of the pillar.

Providing gas from the boundary of the simulation (Run 6) significantly increased

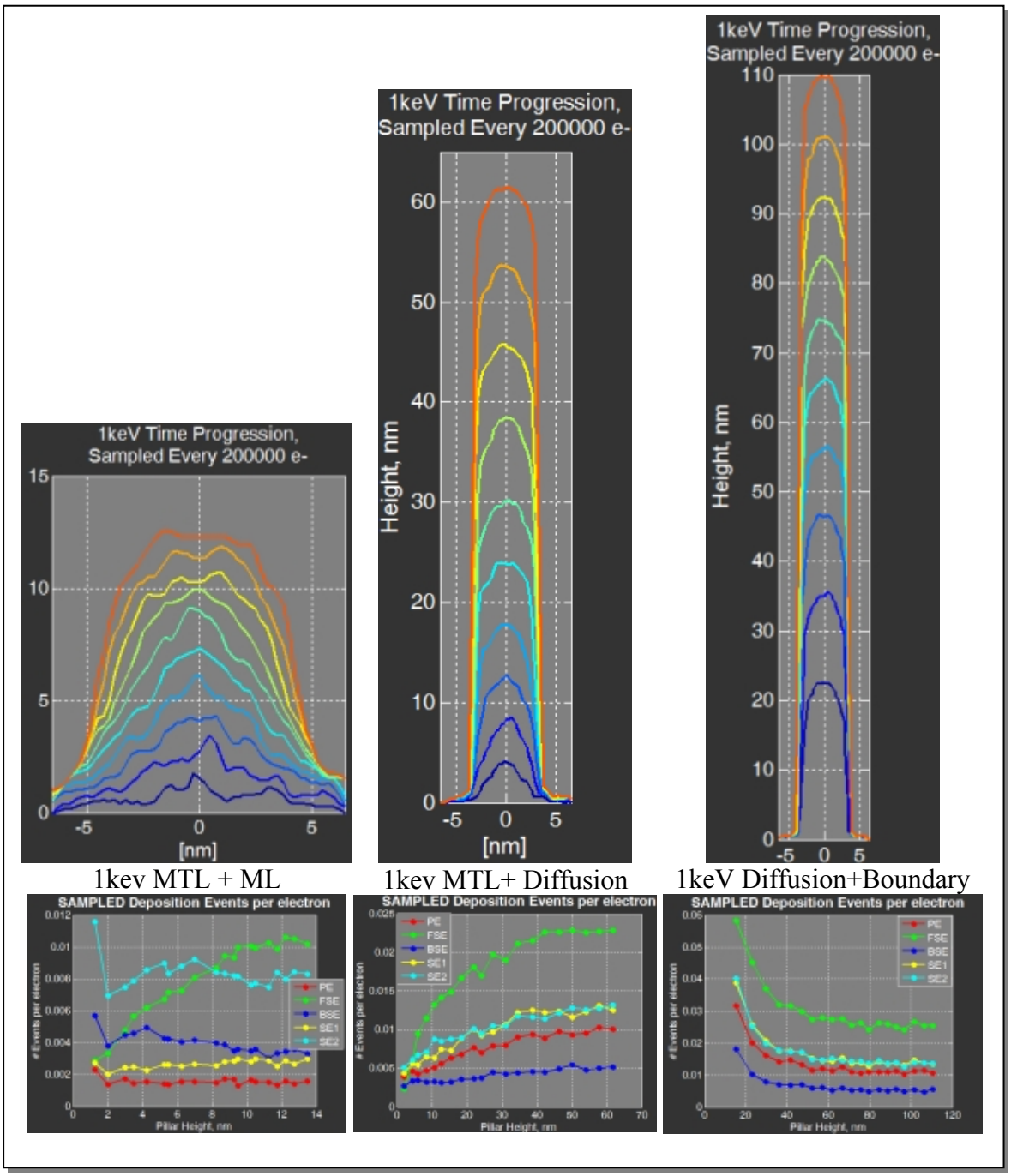


Figure 3-12: Surface Diffusion Sampled Deposition Plots

These plots depict the time-resolved profiles as well as amount of deposition events (per electron) recorded for the tungsten pillars: Run 4 (left), Run 5 (middle) and Run 6 (right).

the deposition rate. The proportions of each deposition event (PE, FSE, BSE, SE^{I}, and SE^{II}) did not change, and the width decreased by 39% when compared to the MTL simulations with no diffusion (Runs 3 and 4).

Plots of the deposition rates versus number of electrons (i.e. time) from the diffusion-enabled runs (Runs 5 and 6) are shown in Figure 3-13. Note that the deposition rates for both simulations saturate at approximately the same value. Run 5 (diffusion only) increases toward a steady-state value and Run 6 decreases towards the same value. For Run 5, initially, only a few gas molecules are adsorbed on the surface, but as the pillar grows, more gas is adsorbed and accumulates on the surface and thus more deposition takes place. The growth rate, visible in the time-resolved cross sections in Figure 3-12, shows that the change in deposition height increases with each time increment. This can be correlated to the surface coverage (θ) which increases as a function of number of electrons (Figure 3-14).

One important thing to note is that the accumulated growth time is less than the prescribed desorption time, therefore any gas that is adsorbed remains on the surface or is consumed by deposition. Initially in Run 5, θ does not increase because the effective deposition region is comparable to the simulation boundary. As gas molecules are adsorbed, they are consumed at a comparable rate. During pillar growth, the effective deposition region becomes a smaller fraction of the total simulation region, therefore more gas molecules are adsorbed relative to the number consumed. To clarify this point, the surface coverage for the top 15 nm of the pillar was plotted as a function of the number of electrons which is also shown in Figure 3-14.

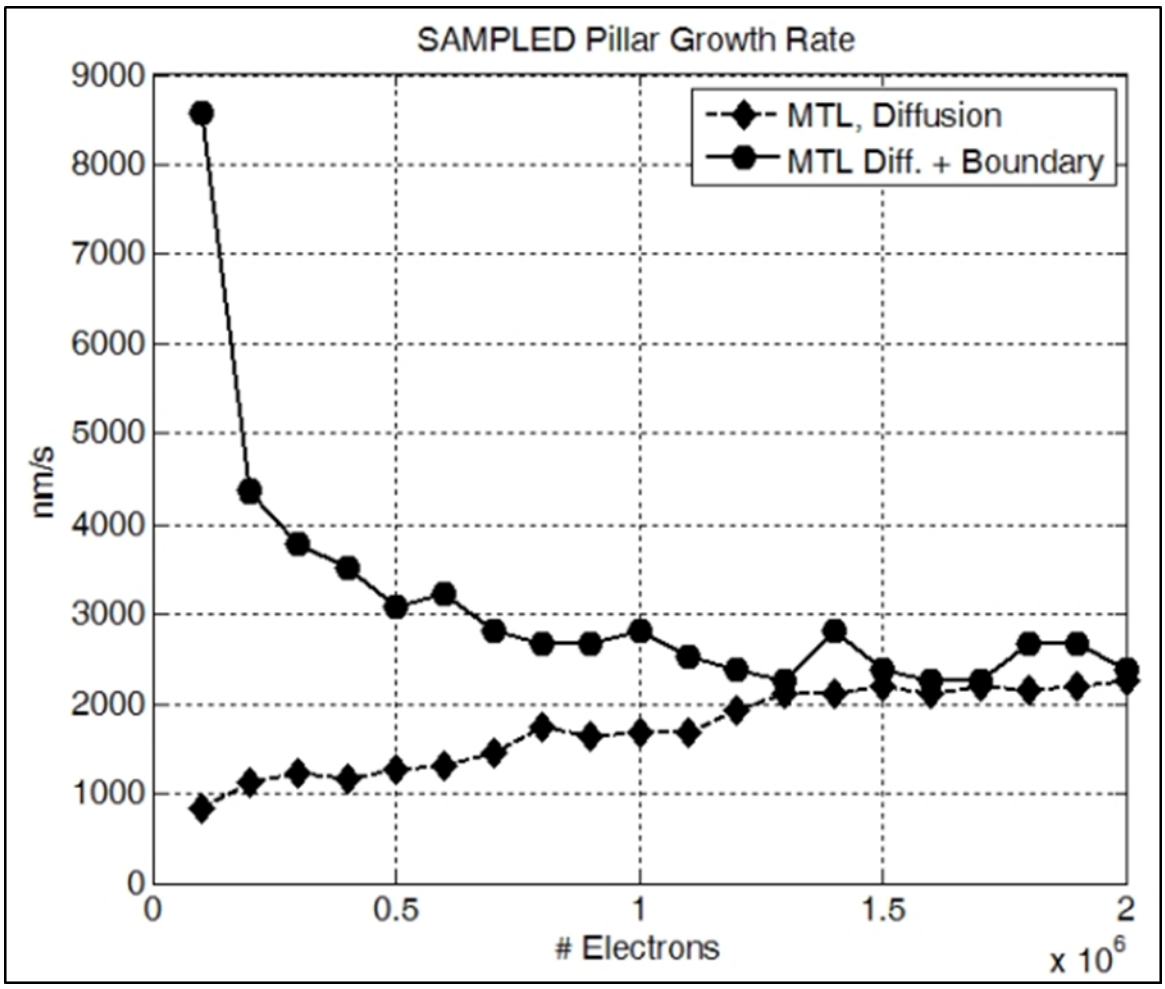


Figure 3-13: Deposition rates, surface diffusion study.

Note that both runs saturate at the same sampled growth rate.

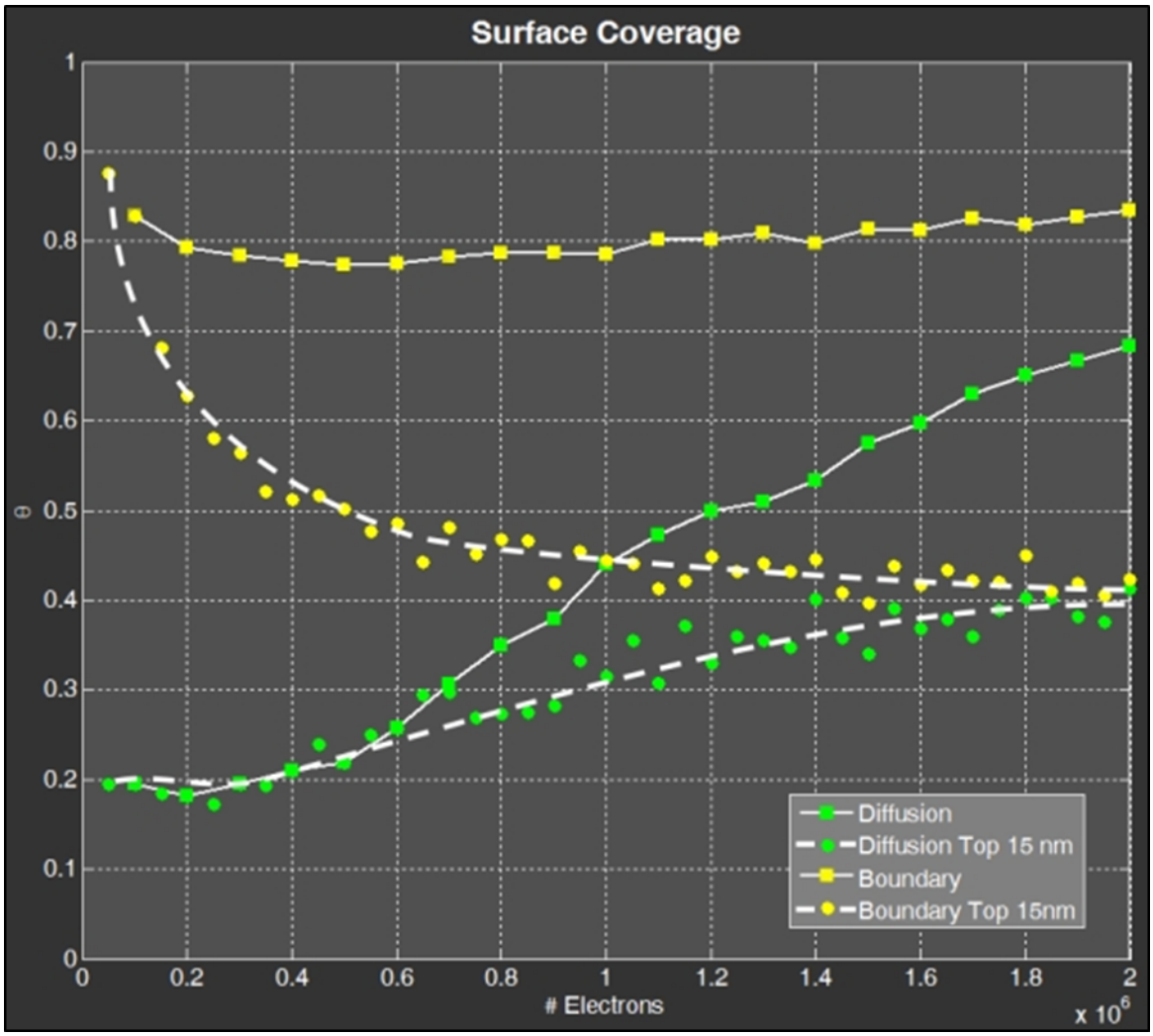


Figure 3-14: Surface coverage as function of # electrons.

The surface coverage from Run 5 ("Diffusion") and Run 6 ("Boundary"), showing the total coverage and the coverage from just the top 15 nm of pillar.

The deposition rate for Run 6 (with the constant boundary source) continuously decreased and eventually saturated to the same steady-state growth rate as Run 5 (Figure 3-13). Figure 3-14 shows the overall surface coverage remains ~ 80%, however. A comparison of the surface coverage near the beam interaction region (top 15 nm) in Figure 3-14 shows that the surface coverage decreases to a saturated value of ~ 40%. Thus for both of these simulations, the steady state growth rate is comparable because the surface coverage in the beam interaction regions both saturate to the same value. While future simulations will be run to demonstrate the interplay of the gas transport parameters (diffusion coefficient, desorption time, etc.) on the EBID growth, suffice it to say that the surface diffusion coefficient used in these simulations has transitioned the otherwise mass transport limited regime into a pseudo-reaction rate limited regime.

3.6 Tungsten vs. SiO_x Study

The fourth study which was performed was designed to illustrate the effects of varying material properties on pillar morphology. It has already been discussed that the electron stopping power, *dE/dS*, is a function of atomic number, atomic weight, density, and electron energy (See Equation 3). Changing the first three of these properties therefore will adjust the distance that electrons travel within a sample, as well as the shape of the interaction volume (see Figure 2-6 which shows the different Bethe Ranges for three different materials). When creating structures on the nanometer scale, altering the stopping distance from a few nanometers to a few micrometers, for example, has a significant impact on the shape of the structure which is formed.

Stopping power is not the only intrinsic property that will affect the simulation, however. The material's Fermi energy and work function also will change any structures

grown by EBID, because those values determine the escape probabilities of electrons (especially secondary electrons) that leave the material's surface. The five intrinsic properties that must be modified for a material change are therefore: atomic number, atomic weight, density, Fermi energy, and work function. These parameters must be input separately for the substrate material, any pre-existing materials existing within the simulation boundaries, as well as the material to be deposited from precursor dissociation. See Appendix C for a list of material properties that were used for these simulations.

Another important factor to consider when changing materials in a simulation is that the secondary electron control variables (*SEfactor* and *cascades*) must be altered slightly in order to match simulation out with experimental values. This is not a very large alteration- for instance, SEfactor is 0.9 in tungsten at 5keV and 1.0 in SiO_2 at5keV. It was noticed that the SE yield in TEOS at 5keV was a little lower than experimental values (0.28 vs. 0.58), which is just a limitation of generating secondary electrons at plural scattering steps with a high Bethe range.

If it is desired to alter the deposited material, the properties of the precursor gas must also be modified (molecular weight, atomic radius, and dissociation cross section). Using the properties of TEOS and SiO_2, the six runs performed for the previous three studies were duplicated, except that SiO_2 was deposited on SiO_2 from the dissociation of TEOS. A summary of these runs is listed in Table 7. A complete list of inputs and outputs from these simulations is give in Appendix G. Note that the dissociation cross section for TEOS was taken from Morgan *et al.*[131]

Table 7: Summary of Runs for Material Comparison

Run	Energy	MTL/ RRL	Other	# e-	Height, nm	Width, nm	SE Yield	BSE Yield
			(Emissions Tests*)					
-	1 keV	N/A	For Emissions	2M	-	-	1.0	0.18
-	5 keV	N/A	For Emissions	2M	-	-	0.28	0.14
			SiO_2 Run Summary					
1	5 keV	RRL	No ML	2M	903	5.9	0.9	0.94
2	1 keV	RRL	No ML	2M	2465	6.3	1.27	0.99
3	1 keV	MTL	No ML	2M	39	17.8	1.81	0.43
4	1 keV	MTL	With ML	2M	41	18.4	1.88	0.47
5	1 keV	MTL	Diffusion	2M	101.5	15.7	1.92	0.79
6	1 keV	MTL	Diff+Boundary	2M	103.7	16.5	1.93	0.85

SiO_2 Depositions

Run	PE	FSE	BSE	SE^I	SE^{II}	Total Depositions	Deposit Efficiency
1	84.7	77.9k	16	102k	122k	387.1k	19.4%
2	261k	621k	6.3k	108k	223k	1.2M	61%
3	7.4k	89.6k	18.1k	11.5k	142k	268.2k	13.4%
4	7.6k	106k	18k	11.2k	149k	291.4k	14.6%
5	19.5k	193k	9k	10k	123k	355.4k	17.8%
6	20.2k	223k	10.7k	10.8k	141k	405.8k	20.3%

*Note: Literature values for SiO_2 SE yields are 1.1 at 1keV and 0.58 for 5keV.
BSE yields were calculated to be 0.18 at 1keV and 0.14 at 5keV.

The total dissociation probabilities for TEOS and WF_6 are shown in Figure 3-15. Note that at 1keV, the probability for dissociating TEOS is about 2.4 times higher than the probability for dissociating WF_6 (0.1042 vs. 0.0442, respectively). This translates into greater deposition efficiency and therefore higher SiO_2 pillars for the same conditions when compared to tungsten.

The reaction-rate limited (RRL) runs in the SiO_2 system grew to a height of 2465nm and 903nm at 2 million electrons for the 1keV and 5keV runs, respectively. Compared to the tungsten system, this was ~5.5X taller for the same conditions. The deposit efficiency scales with the difference in cross section (i.e. 2.4X higher in the TEOS system), therefore the extra height achieved must be due to other causes.The voxel size in the TEOS system is 0.36 x 0.36 x 0.36 nm as compared to 0.25 x 0.25 x 0.25 nm in the WF_6 system, which is a 1.4:1 ratio. In terms of atom stacking, the 1keV TEOS pillar is approximately 6,849 atoms tall whereas the 1keV WF_6 pillar is 1780 atoms tall after the same number of electrons. This is a ratio of ~3.8:1, which comes from the additive combination of the cross-section ratio (2.4:1) and the atomic size ratio (1.4:1). The same calculation can be shown for the 5keV pillar, indicating that the simulation is accurately scaling the results based on the modified cross section and atomic spacing.

Experimentally grown SiO_2 pillars at relatively high pressure showed a similar ratio (~3:1) when comparing TEOS and WF_6 deposited structures.[86] The ratios from the experimentally grown pillars were probably slightly lower because of 1) the lack of a completely RRL environment as simulated (i.e. $\Gamma_{gas}= 1000*\Gamma_e$), and 2) temperature effects when these pillars are grown to a significant height.[82]

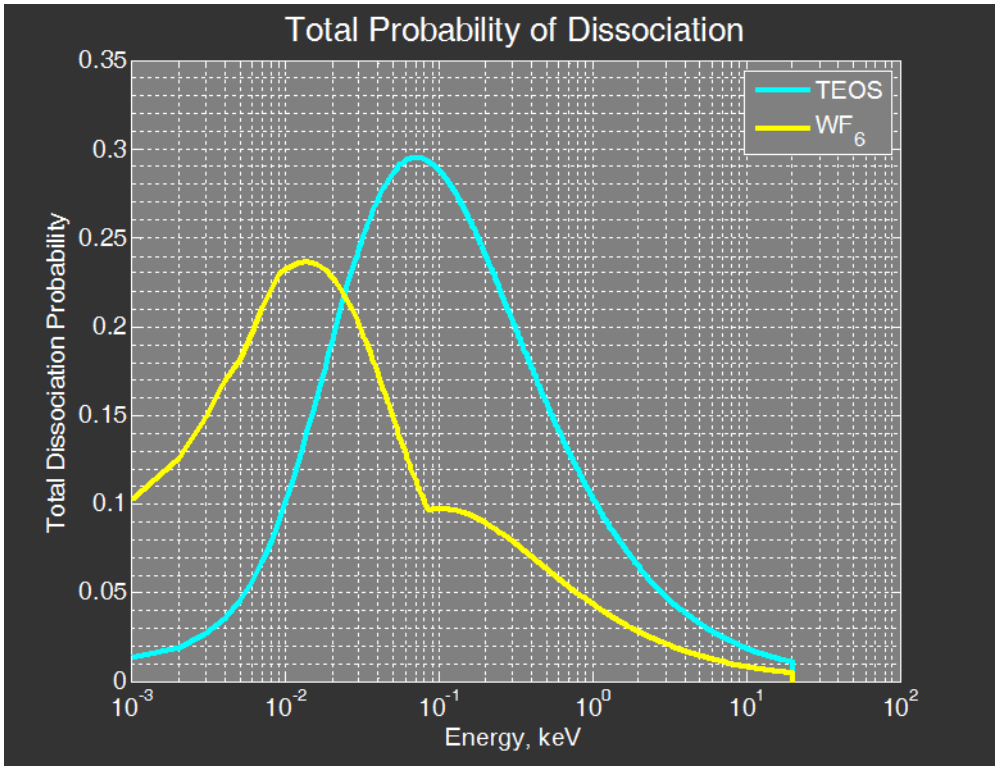


Figure 3-15: TEOS and WF_6 Cross Sections

The probability of dissociation, as taken from Fowlkes *et al*[88]. and Morgan *et al.*[131] for WF_6 and SiO_2, respectively.

The 5keV RRL pillar grown in the TEOS system was the same width as the 1keV RRL pillar in the TEOS system (~6nm). Because a plural scattering model for Monte Carlo trajectories is employed in this simulation, each electron trajectory is divided into 50 steps. At 5keV, SiO_2 has a Bethe Range of 1374.9 nm. With a step size of 50 increments, this is ~27nm per step. Clearly, the electron will likely exit the pillar after the first or second scattering step with such a large step size. This reduces the amount of SE generation, particularly the SE^{II}'s which have been shown to be responsible for lateral broadening.

Experimentally, Choi *et al*. demonstrated that the WF_6 and SiO_2 pillars broadened to a particular width, then maintained that width during the remainder of growth.[86] The same phenomena is observed in the simulated pillars. Furthermore, as pressure was decreased, the experimentally grown pillars exhibited more lateral broadening, particularly in the less dense SiO_2 pillars. This can be seen by comparing the mass-transport-limited (MTL) grown SiO_2 pillar (Run 3) to the tungsten pillar grown under the same MTL conditions. Figure 3-16 shows a side-by-side comparison of the tungsten and SiO_2 pillar cross sections. Note that the tungsten pillar has been grown to the same height as the SiO_2 pillar for comparison purposes. The SiO_2 pillar appears to have a more conical shape while the tungsten pillar is more cylindrical. Comparing the sampled deposition events listed in the lower portion of Figure 3-16, there is significantly more FSE and SE^{II} deposition events than PE+BSE+SE^{I} events in the SiO_2 pillar as compared to the tungsten pillar. Obviously, the FSE and SE^{II} events are responsible for the increased lateral broadening in the SiO_2 pillar.

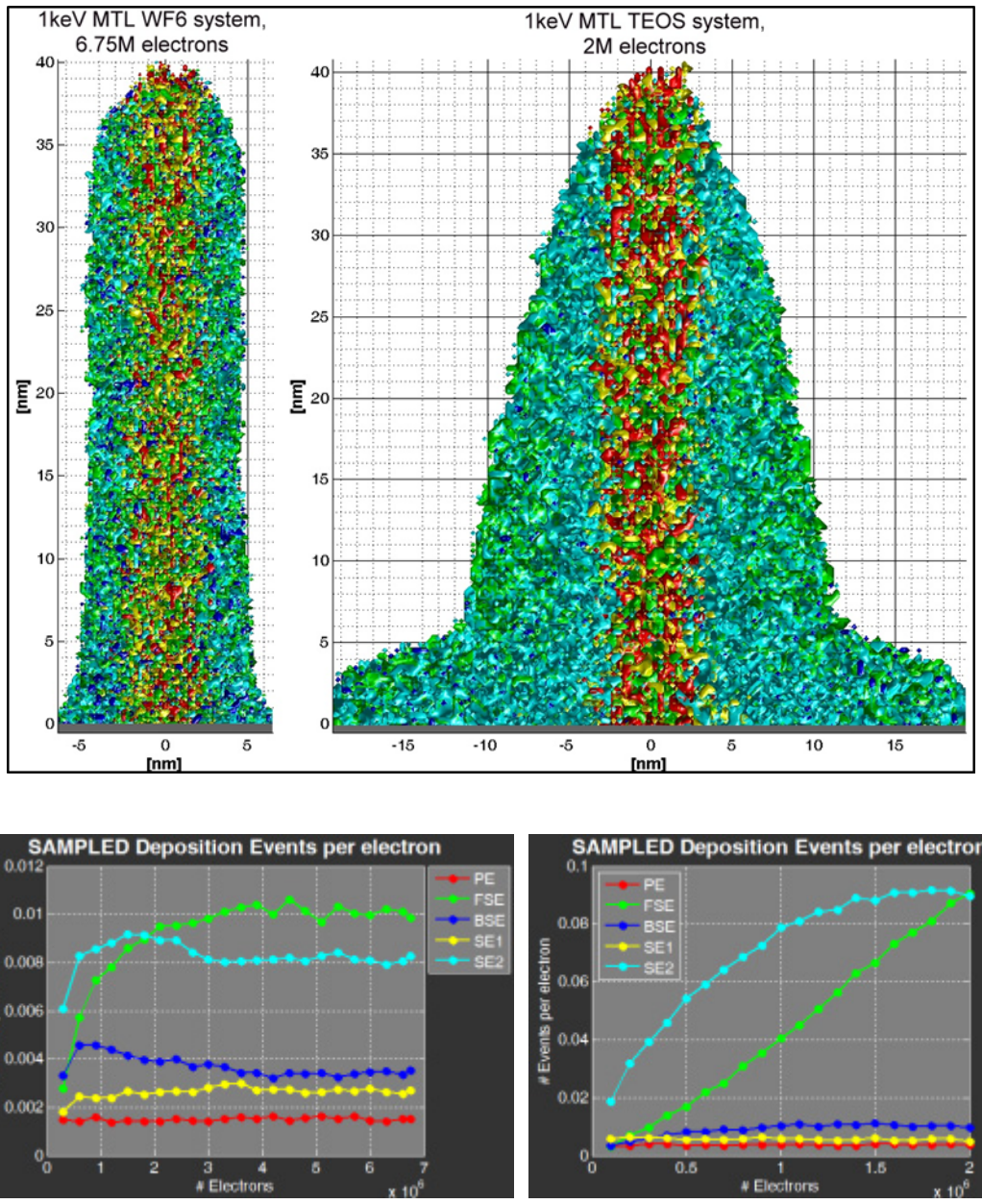


Figure 3-16: Cross-sections through 1keV MTL pillars from WF_6 and TEOS.

The MTL tungsten pillar is shown on the left after 6.75 million electrons, while the MTL SiO_2 pillar (Run 3) is on the right after 2 million electrons. Sampled deposition events from each are shown at the lower left for tungsten, and lower right for SiO_2.

The shapes of the pillars shown in Figure 3-16 are characteristic of the shape of the interaction volume, which takes a more conical appearance in the lower density SiO_2 as compared to tungsten. Figure 3-17 shows how the electron trajectories vary upon entering tungsten vs. SiO_2. The different shapes of the interaction volume have been noted in experimentally grown pillars as well, as shown in Figure 3-18. Note that the conical-shaped caps had a ~0.8 aspect ratio (i.e. height of the cone / width of the cylindrical body) for the experimentally grown tungsten pillars, and a ~1.4 aspect ratio for the experimentally grown SiO_2 pillars. *Thus, the simulation predicted aspects similar to experimental results.*

When surface diffusion was enabled, the SiO_2 pillars grew taller than without diffusion, as observed previously in the tungsten pillar simulations. The conical caps of the diffusion enabled runs (i.e. Run 5) from the tungsten and SiO_2 1keV MTL pillars are shown in Figure 3-19 after 2 million electrons. Note that the aspect ratios of these caps were ~0.8 for the tungsten pillar, and ~1.6 for the SiO_2 pillar. These values align with the experimentally determined values, as mentioned above.

The time-resolved plots of SiO_2 pillar evolution as well as plots of the sampled depositions by electron type are shown in Figure 3-20. Note that the height of Run 6 (with a boundary precursor source) is approximately the same as Run 5 (with only diffusion enabled), unlike the same conditions in the WF_6 system. Recall that the boundary source provided extra gas to the WF_6 simulations, therefore the number of depositions increased when compared to the run with surface diffusion enabled (but no boundary source). The TEOS system, however, has a much higher dissociation cross-

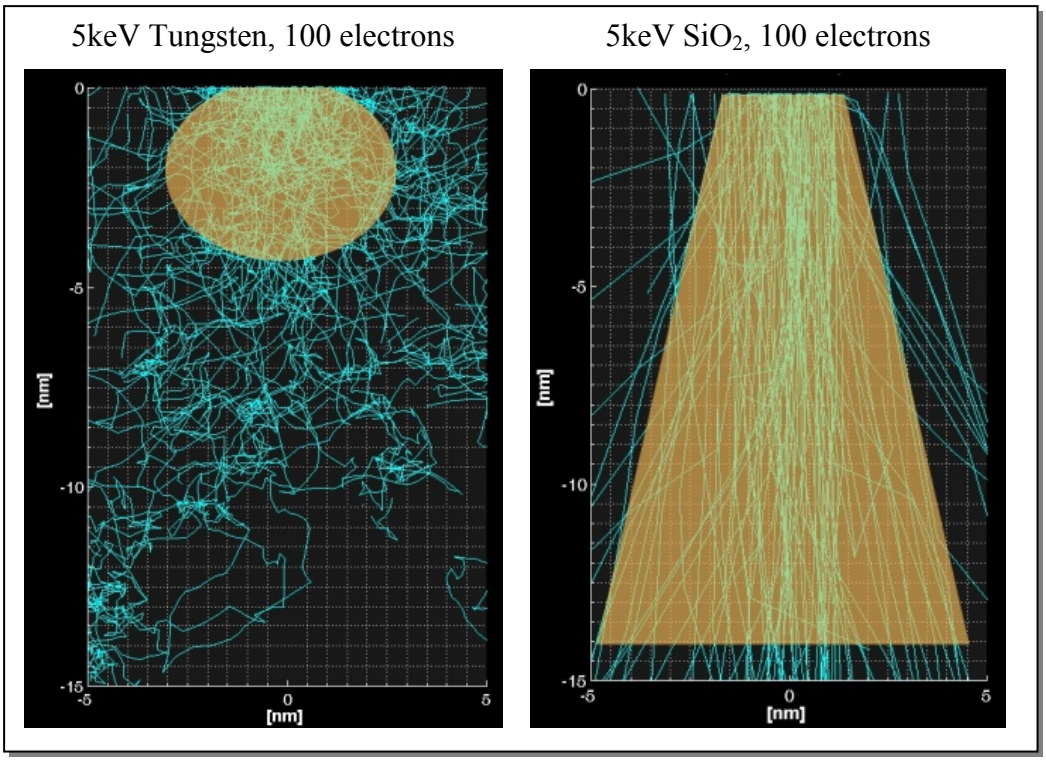


Figure 3-17: Example Monte Carlo simulations of 100 electrons in W and SiO_2.

The properties of tungsten change the shape of the interaction volume (left) when compared to SiO_2 (right). The shaded area illustrates the initial shape of these volumes.

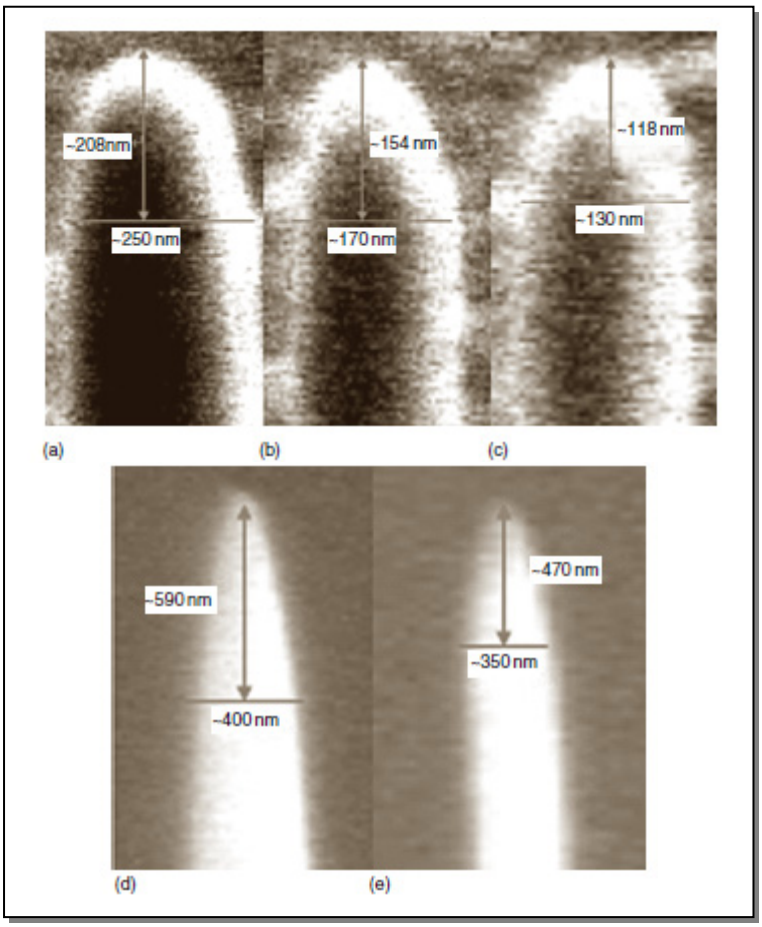


Figure 3-18: Top curvature heights of tungsten (a-c) and SiO_2 pillars (d-e).

Example pillars at (a) $1x10^{-3}$Pa, (b) $3.6x10^{-3}$Pa, and (c) $8x10^{-3}$ Pa for tungsten, and (d) $3.6x10^{-3}$ Pa, and (e) $8x10^{-3}$Pa for SiO_2.[86]

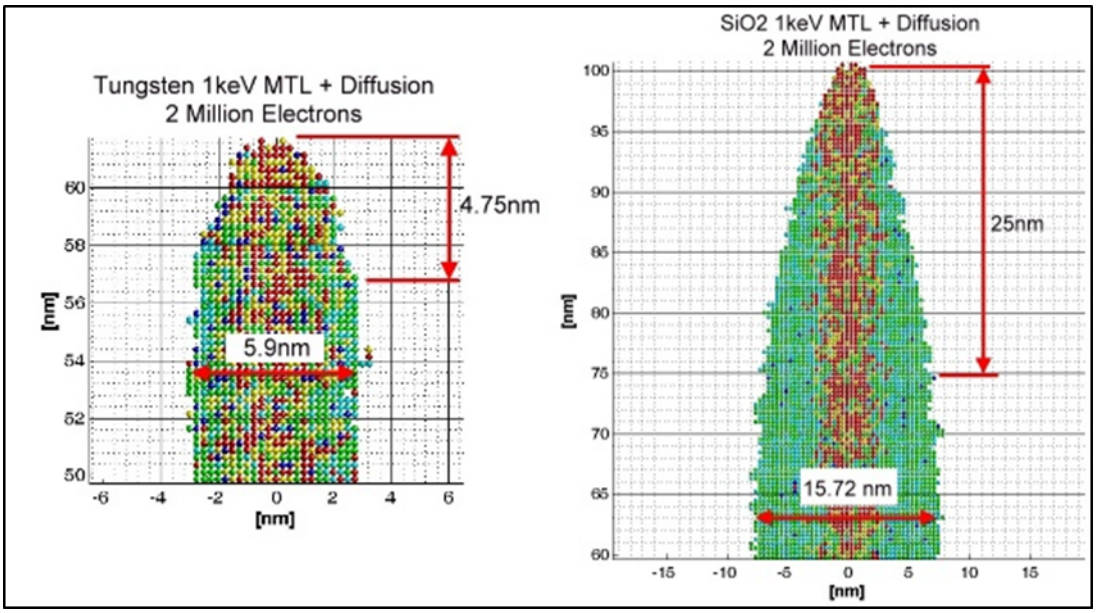


Figure 3-19: Comparison of conical caps from tungsten and SiO_2 pillars.

These pillars were grown under 1keV MTL conditions (Run 5) with surface diffusion enabled ($D=1x10^{-9}$ cm^2/s). The caps are shown in cross-section.

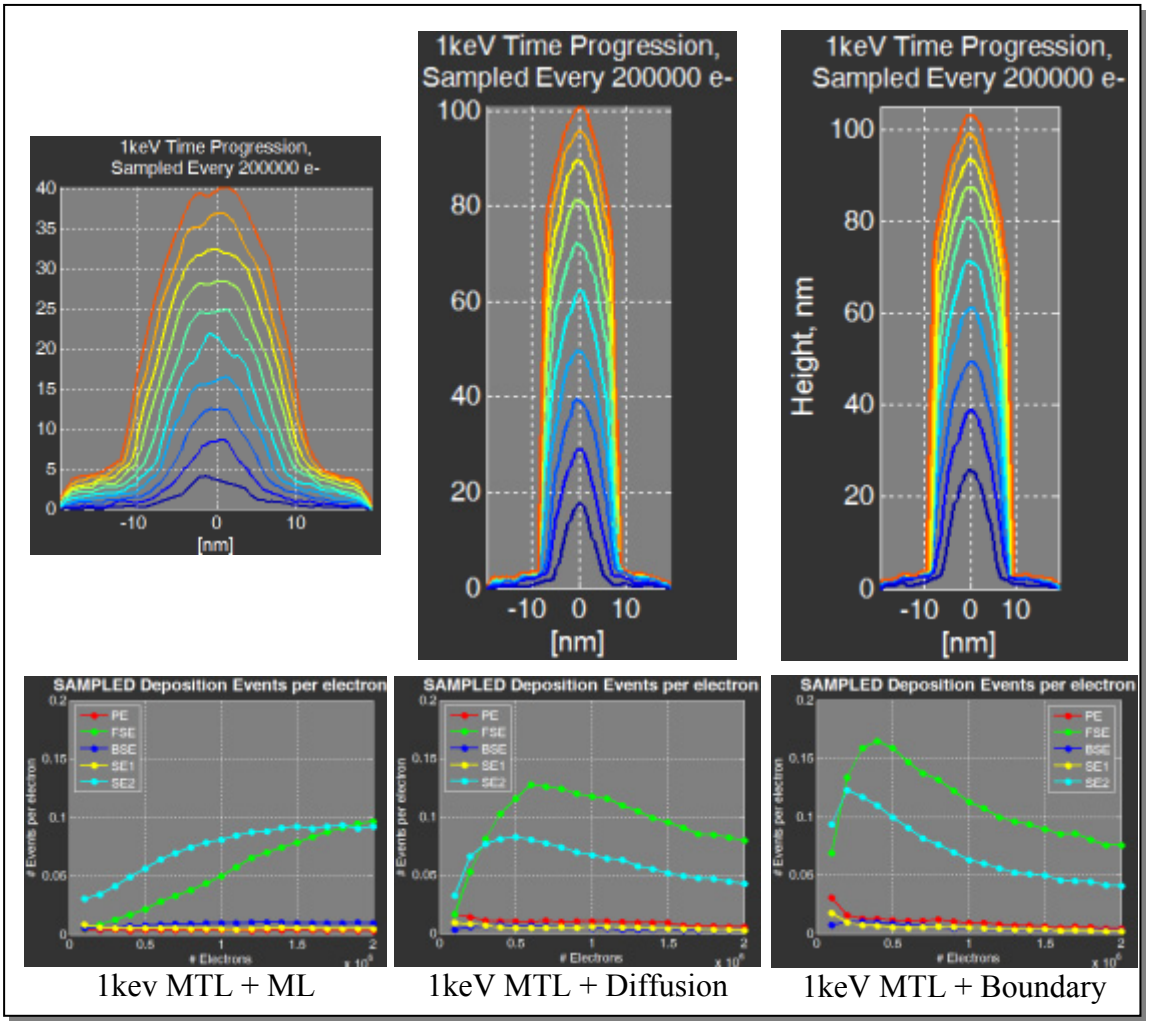


Figure 3-20: SiO_2 pillar simulation results.

These plots depict the time-resolved profiles as well as amount of deposition events (per electron) recorded for the SiO_2 pillars: Run 4 (left), Run 5 (middle) and Run 6 (right).

section, so that more gas is consumed by the forward scattered and SE^{II} electrons than in the WF_6 system. This can be seen by examining the quantitative results.

The width of the boundary source SiO_2 pillar (Run 6) is 16.5nm, which is slightly wider than the Run 5 pillar with no boundary source (15.7nm). Most notably, the extra gas consumption allows for more FSE and SE^{II} deposition events (as seen in Figure 3-20) which is primarily responsible for pillar broadening. The amount of surface coverage of the gas is shown in Figure 3-21 for Runs 5 and 6. Note that with only surface diffusion, there is a slight incubation period until which the surface area of the pillar is large enough to reach a steady state surface coverage of ~0.8. With a boundary source of precursor gas, steady-state behavior is maintained throughout the simulation. The increased gas consumption is evidenced by the declining surface coverage at the top of the pillars (top 15nm). This explains the decreasing number of deposition events shown in the previous figure. Since the boundary source simulation (Run 6) reaches steady state sooner, the pillar height is always a little taller than Run 5, as shown in the lower portion of Figure 3-21. Thus the vertical growth rates are comparable except for early on when the boundary source diffusion makes it to the pillar tip. As the pillar grows, however, the vertical growth rate for the boundary saturates to a comparable value while the lateral growth rate for the boundary source is slightly higher. Eventually both saturate because they have comparable coverage (i.e. the effect of the boundary becomes obsolete).

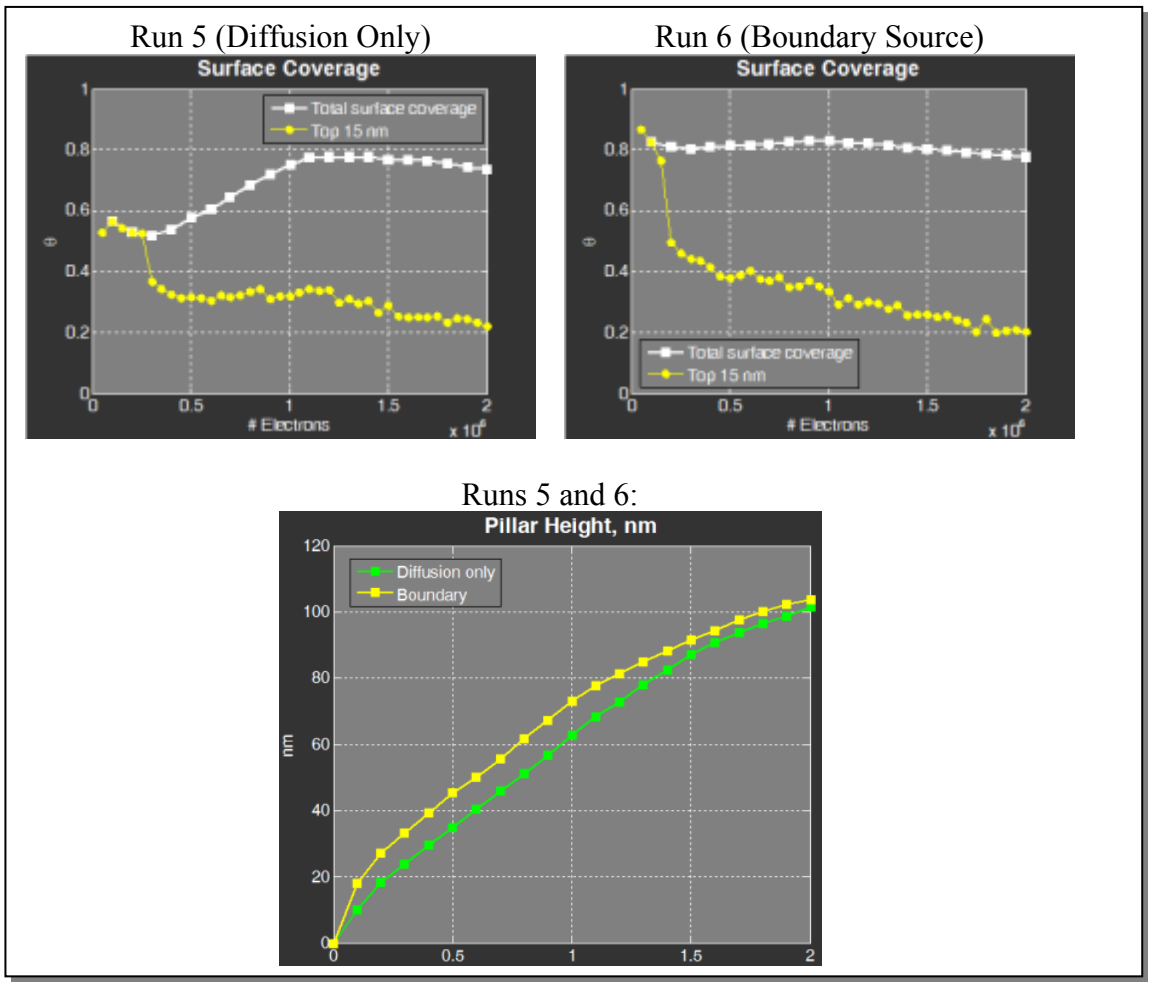


Figure 3-21: Surface coverage and pillar height of TEOS Runs 5 and 6.

The effect of higher gas consumption due to dissociation cross section is evidenced by similar pillar growth in Run 5 and 6.

Chapter 4--Applications

4.1 Raster Simulations

The previous simulations in Chapter 3 dealt with holding an electron beam stationary above a substrate to deposit a 1D structure by EBID. This is referred to as "static" or "spot mode" of electron beam control, which is used primarily for creating nanopillars. Scanning electron microscopes are given the name "scanning", however, because they have the ability to move the electron beam using a system of magnetic "lenses" which control the beam location on the substrate surface. This allows for linear EBID to create traces, for example, in circuits, or 2D rectangles composed of rastered lines to perform EBID on a much larger area.

The basis of rastering an electron beam is simply to perform a spot-mode deposition for a brief period of time (called the "dwell time"), then move the beam a certain distance for the next deposition location (called a "pixel"). This continues in a line until the beam reaches the boundary of the rastered region, at which time it "rests" before starting the next line. This "rest," referred to as "line refresh time" is simply a pause to allow the electronics to catch up before starting another line across the rastered region. After the last line is rastered, there is usually an additional refresh time to allow the electronics to move the beam back to the initial spot of the rastered region. This is referred to as the "frame refresh time" since the 2D group of lines that compose a rectangular region rastered by the beam is called a "frame". Figure 4-1 shows an illustration of this sequence of events.

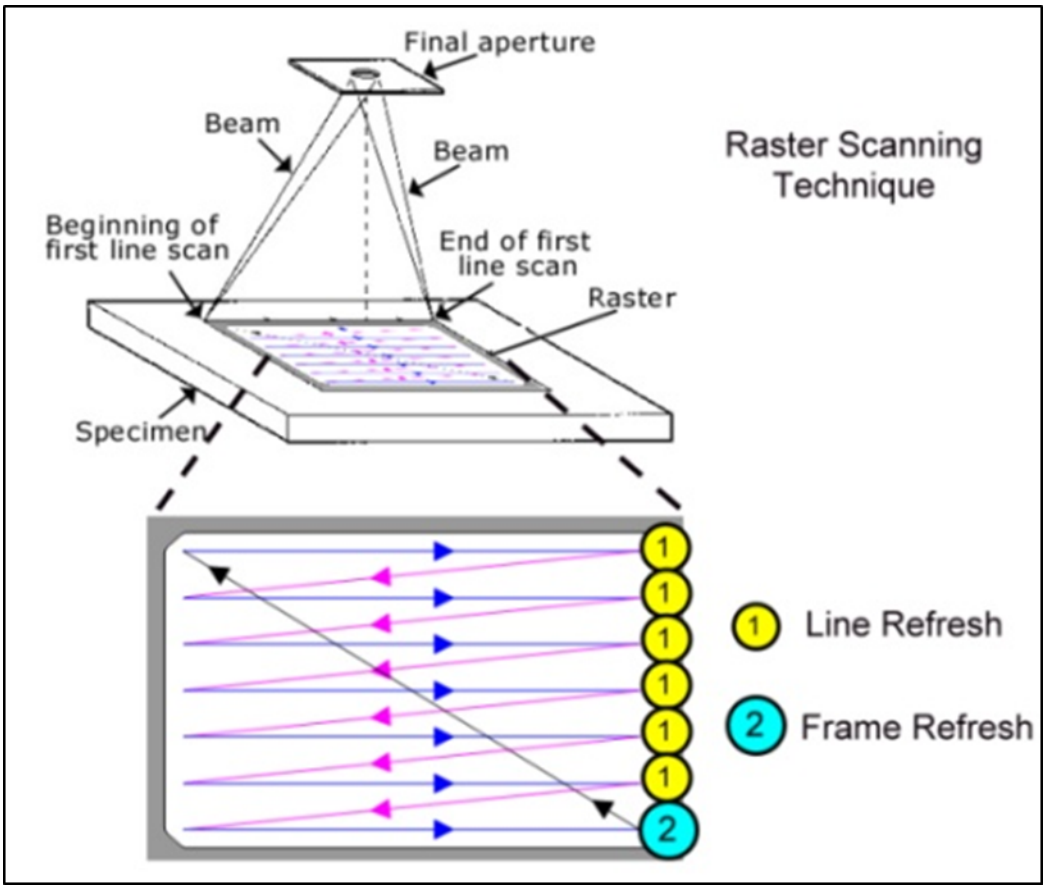


Figure 4-1: Illustration of Raster Technique.

In rastered scanning, the beam travels linearly across the sample, resting for a "line refresh" period of time (1), before continuing on the next line. After the frame is painted, the beam rests for a "frame refresh" time (2) before beginning a new frame.

The pixel spacing is an important feature for this mode of EBID, because it affects the resultant EBID structure as shown in Figure 4-2. Pixels can be spaced in the *x* or *y* dimension by more than one FWHM, overlapping (< 1 FWHM) or adjacent (1 FWHM). The interplay of dwell time, line and frame refresh times, and pixel spacing add further complexity to the EBID simulation when operated in raster mode.

To illustrate the capabilities of the simulation in raster mode operation, four simulations were run as listed in Table 8. These runs were designed to show the effects of two main parameters in raster setup: 1) pixel spacing and 2) frame refresh time. Each run was carried out to ~1 million electrons that were divided into frames consisting of 3x3 pixels with a dwell time of 1 μs. To maintain consistency with previous runs, the same parameters were used as the 1keV MTL WF_6-W system (i_{beam}=9pA, P_{sys}=7mTorr, etc.). These runs were only carried out to 1 million electrons, however. Three pixel orientations were selected: adjacent pixels, overlapping pixels (½ FWHM spacing), and separated pixels (2 FWHM spacing).

The surface diffusion gas dynamics were disabled for these simulations for the purpose of studying frame refresh time. For Runs 1, 2, and 3, the effect of frame refresh time was simulated by applying one monolayer of precursor gas after every frame. This had the effect of simulating a long frame refresh time such that gas could accumulate back on the rastered surface between frames. Run 4 was varied by turning this function off such that gas could only be replenished during the simulation by impingement from the gas flux (which was minimal due to the MTL conditions).

Table 8: Raster Simulation Setup

Run	*Pixel Spacing*	*Dwell Time*	*Line Refresh*	*Frame Refresh*	*Pixels/ Frame*	*# Frames*
1	Adjacent	1 μs	0 s	1 ML	9 (3x3)	1984
2	2 FWHM	1 μs	0 s	1 ML	9 (3x3)	1984
3	½ FWHM	1 μs	0 s	1 ML	9 (3x3)	1984
4	Adjacent	1 μs	0 s	none	9 (3x3)	1984

All runs were operated in MTL conditions (i_{beam}=9pA, P_{sys}=7mTorr, 1keV) on the WF_6-W system.

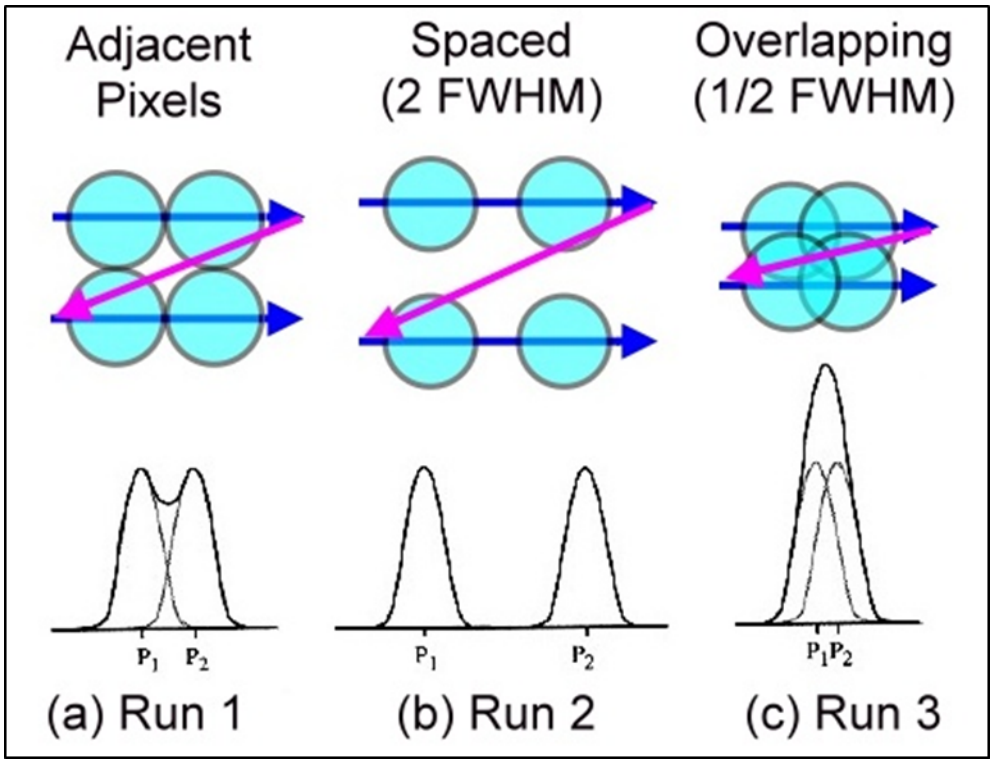


Figure 4-2: Pixel Spacing

Pixel spacing affects EBID structure. Various options are adjacent pixels (a), separation by more than one FWHM (b), and overlapping pixels (c).

The results from Run 1 are shown in Figure 4-3. Orthographic and top-down views are shown as well as a cross section through the [110] plane. Note that the Gaussian-like beam structure has nicely filled in gaps between the diagonally-adjacent pixels. For a complete list of all results of these runs, see Appendix H. Results from Runs 2 and 3 are shown in Figure 4-4 and Figure 4-5, respectively. Note that in Run 2, the spacing of the pixels prevented diagonally spaced pixels from completely filling the voids. The [100] and [010] plane cross sections (not shown) had partially filled gaps due to slightly closer proximity of the pixels in these planes. The overlapped pixels resulted in a taller pillar because of the superposition of the Gaussian beam profiles.

Run 1 grew to 36.5nm high, and 11.8nm wide. Spacing the pixels resulted in Run 2 growing to only 28.3 nm tall, and 17.6nm wide. The overlapped pixels in Run 3 resulted in a 92nm tall pillar that was 8.2nm wide. The time-resolved cross sections (on the [100] plane) and sampled deposition event plots are shown in Figure 4-6. The results follow expected trends. For instance, spaced pixels allow for more combined (BSE+FSE) deposition events than (SE^{I} + SE^{II}) events as compared to the overlapped pixels which had about the same amount of (BSE+FSE) and (SE^{I} + SE^{II}) combined events.

Runs 1 through 3 utilized a method of refreshing the gas coverage on the surface between frames by applying one monolayer of gas at the end of every frame. Run 4 shows the effect of removing this parameter (again analogous to a short frame refresh time). As shown in Figure 4-7, the structure only grew to 5nm tall and 12nm wide. The reduced growth rate reflects the nature of mass transport limited growth when gas is not allowed to refresh the surface during the frame refresh time.

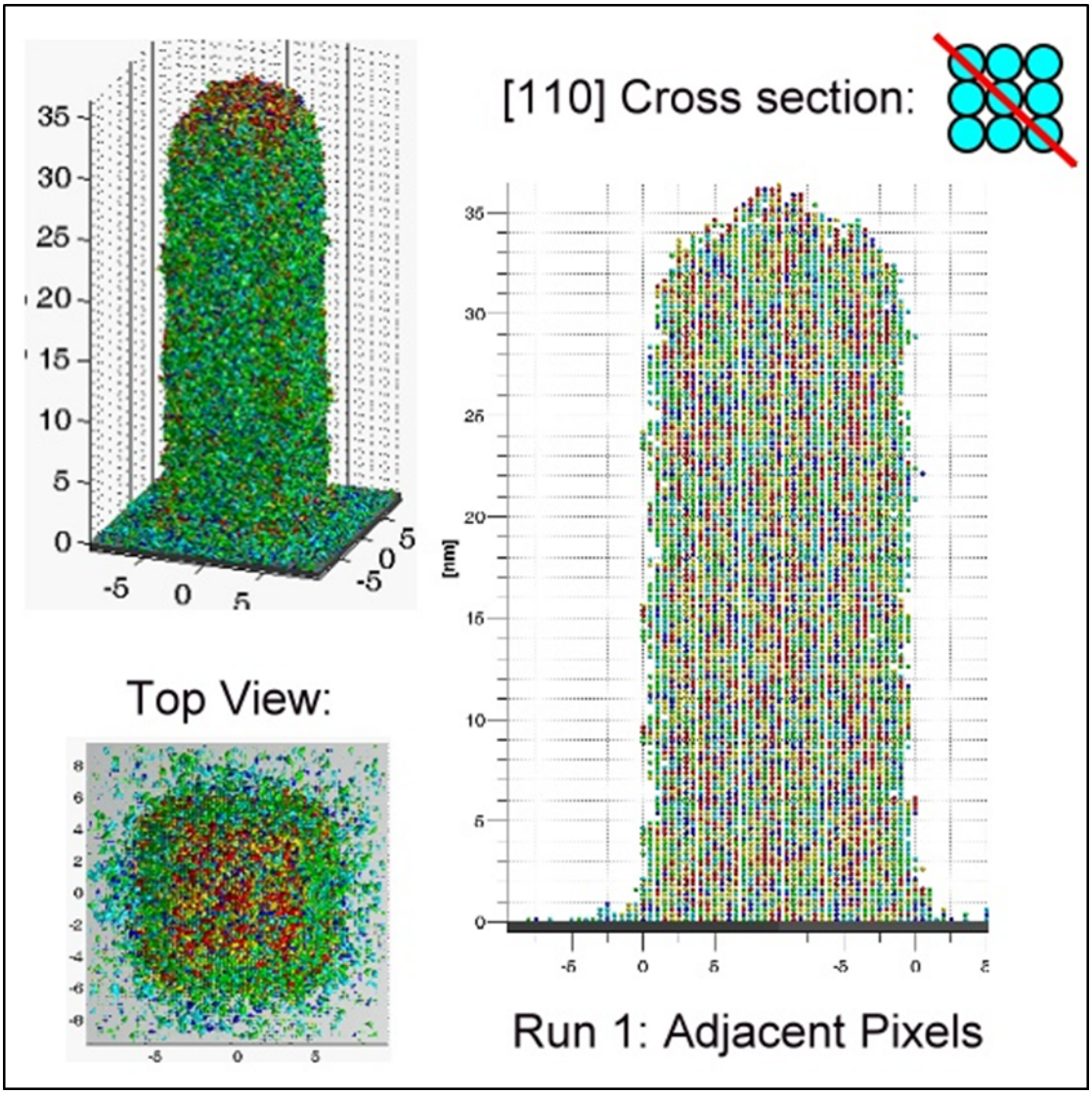


Figure 4-3: Raster Run 1 Results.

Orthographic view (top left), top-down view (bottom left) and [110] slice plane cross section (right) are shown. Pixels were spaced 3nm apart. Beam diameter=3nm. One monolayer of gas was applied between frames.

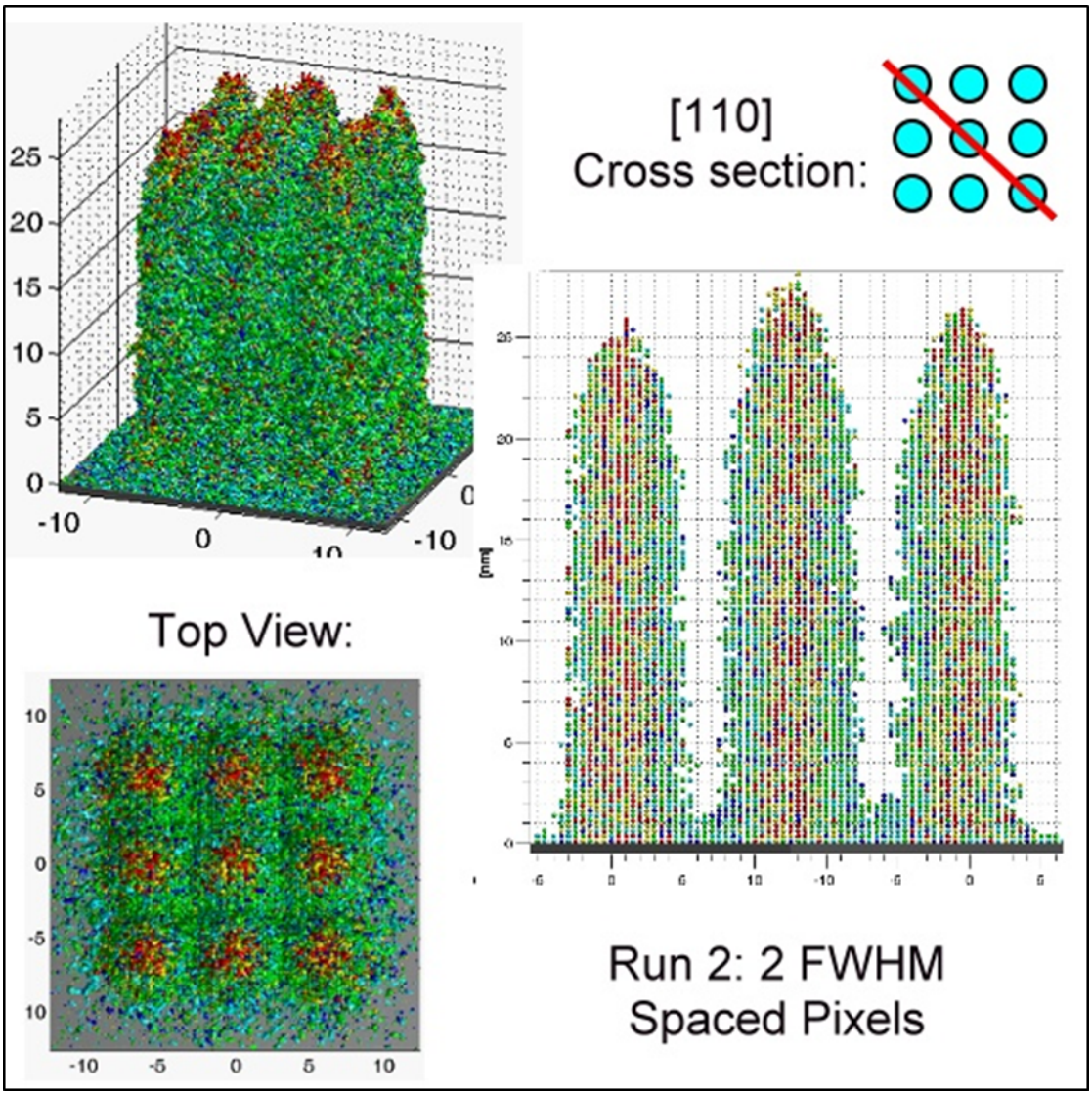


Figure 4-4: Raster Run 2 Results.

Orthographic view (top left), top-down view (bottom left) and [110] slice plane cross section (right) are shown. Pixels were spaced 6 nm apart. Beam diameter=3nm. One monolayer of gas was applied between frames.

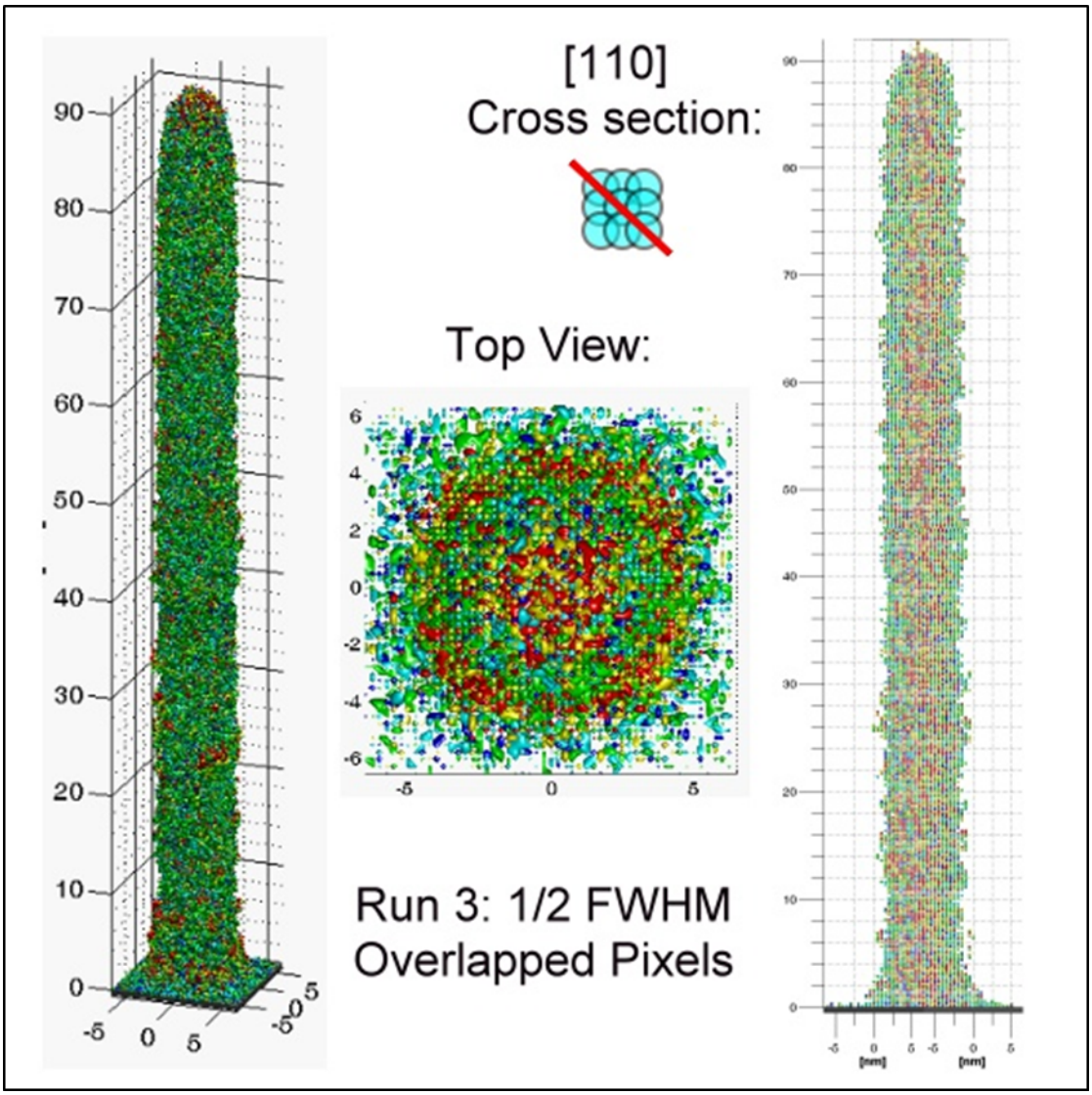


Figure 4-5: Raster Run 3 Results.

Orthographic view (left), top-down view (center) and [110] slice plane cross section (right) are shown. Pixels were spaced 1.5 nm apart. Beam diameter=3nm. One monolayer of gas was applied between frames.

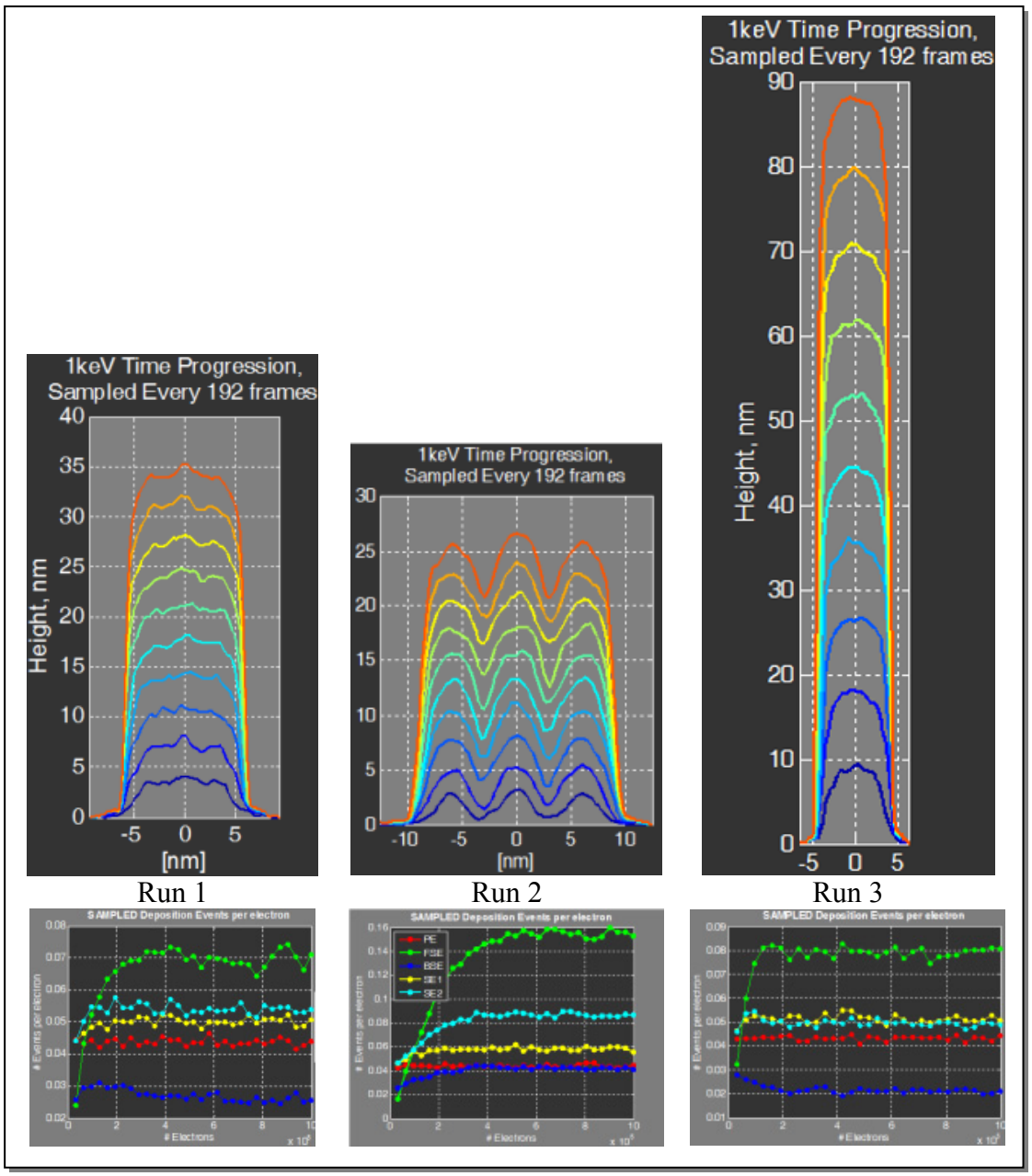


Figure 4-6: Time Profiles and Deposition Events for Raster Runs 1-3.

Cross-sections taken through [100] planes. Sampled deposition events are shown per electron. Sample size ~10k electrons.

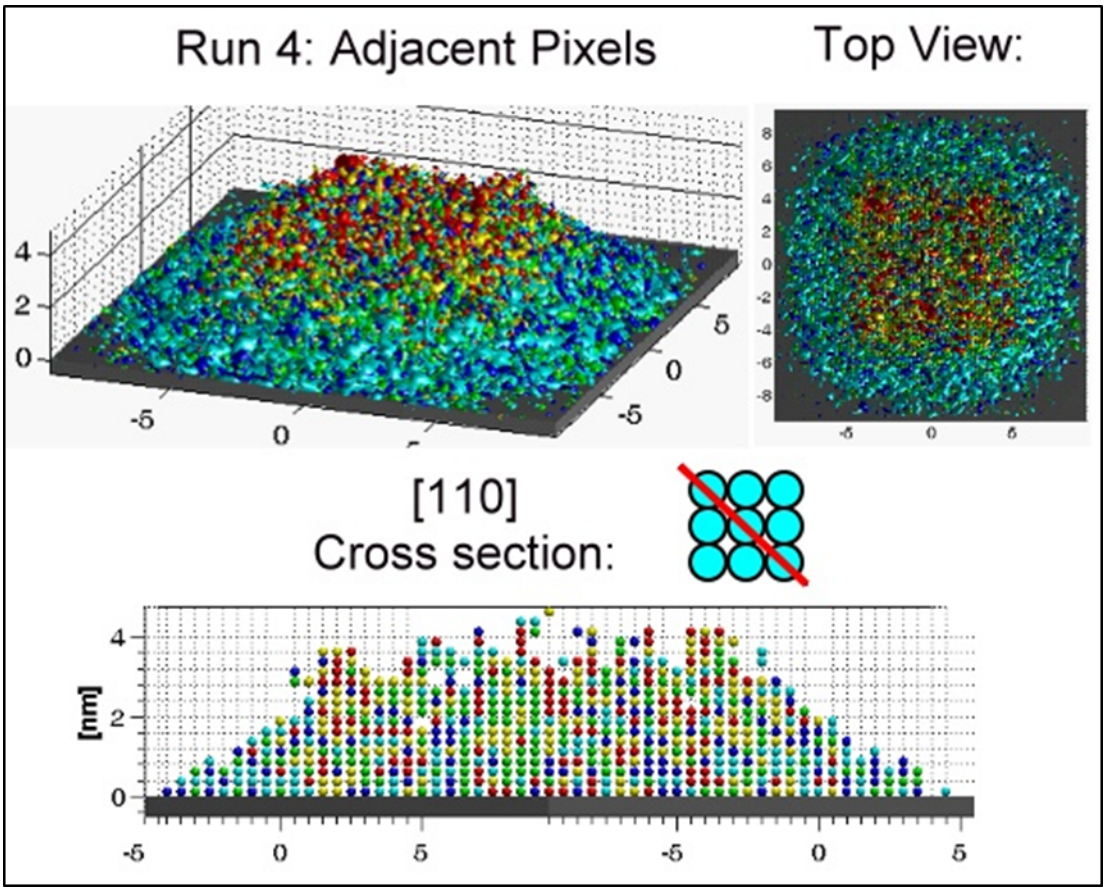


Figure 4-7: Raster Run 4 Results.

Orthographic view (top left), top-down view (top right) and [110] slice plane cross section (bottom) are shown. Pixels were spaced 3 nm apart. Beam diameter=3nm. No gas was applied between frames.

These runs showed that the simulation is capable of reproducing rastered growth, and has the ability to study the effects of several key parameters for this type of beam scanning. Other parameters, such as pixel dwell time, line refresh time, and the effect of surface diffusion on rastered scanning will be examined in the future.

4.2 Via Filling

The process of filling high aspect-ratio voids, or "vias" is of particular significance in VLSI manufacturing and repair. Several techniques have been studied for filling these vias, such as bias sputtering, pulsed laser irradiation, selective CVD, and electroless plating. Wang *et al*.[157] and Shingubara *et al*.[158] demonstrated success at using electroless copper for filling these voids, but this technique often requires planarization due to the conductivity of copper. Similarly, Mei *et al*.[159] showed an approach to nonconformal filling of vias by partially ionized beam (PIB) deposition followed by planarization. This technique is useful only when the beam is normal to the via, eliminating the ease of filling vias near the edge of wafers. Ray *et* al. used tungsten FIB deposition to fill vias milled in SiO_2. Their approach was to confine the beam to a size much smaller than the aperture size in order to minimize SE deposition events near the surface. These events were postulated to cause the vias to "pinch off" during filling. Ray *et al.* found that confining the beam size only was successful at filling vias 0.20μm and larger, however. Other applications of via filling can be seen in preparation of biological specimens, such as the drilling and subsequent filling of vias in Pt coated spores.[160] Figure 4-8 shows some examples of various techniques mentioned above.

The ability of EBID to confine a beam to small areas, coupled with its inherent lack of ion implantation and substrate damage makes it an attractive alternative for filling

vias. The low deposition rates, however, would probably limit the size of the via apertures to 50nm and below.[161] Since the simulation described in this dissertation is built in a true 3D environment, the possibility of starting the simulation with a pre-existing structure allows for the examination of filling vias by EBID.

For this example application, four simulations were run as listed in Table 9. For continuity, the same conditions as raster Run 1 were used: 1keV WF_6-W system, MTL, 9pA, 7mTorr, adjacent pixels, 1 μs dwell time, no surface diffusion or boundary source of gas, monolayer coverage after frame completion, etc. The via was an artificially created structure (from tungsten) that was 20nm deep and had an aperture size of 10x10nm.

Run 1 placed a 3x3 pixel array at the center of the via. Since the beam diameter was 3nm, this meant there was a ~1nm clearance around the rastered area within the via. The Gaussian-like nature of the beam, however, would provide some small amount of overlap at the aperture surface. Run 2 exaggerated this overlap, by utilizing a 4x4 array of adjacent pixels which overlapped the aperture on two sides.

These runs assumed that gas could reach any part of the via during the frame refresh time. Some authors who have studied the phenomena of via pinching have stated that a possibility for the lack of via filling is the inability of gas to reach the lowest points of the via. In order to make a more accurate simulation, the possibility of applying a "gradient" of gas down the sides of the via was implemented. For simplicity, a linear gradient was chosen with a minimum of 20% coverage at the bottom of the via up to 100% coverage at the aperture surface. Run 3 shows the effect of applying this gradient

Table 9: Via Fill Simulations

Run	*Raster size*	*Overlap?*	*Gradient*	*# Electrons per pixel*	*# Frames until closed*
1	3x3	No	None	56	896
2	4x4	Yes	None	56	603
3	3x3	No	Linear	56	912
4	2x2	No	Linear	56	2464

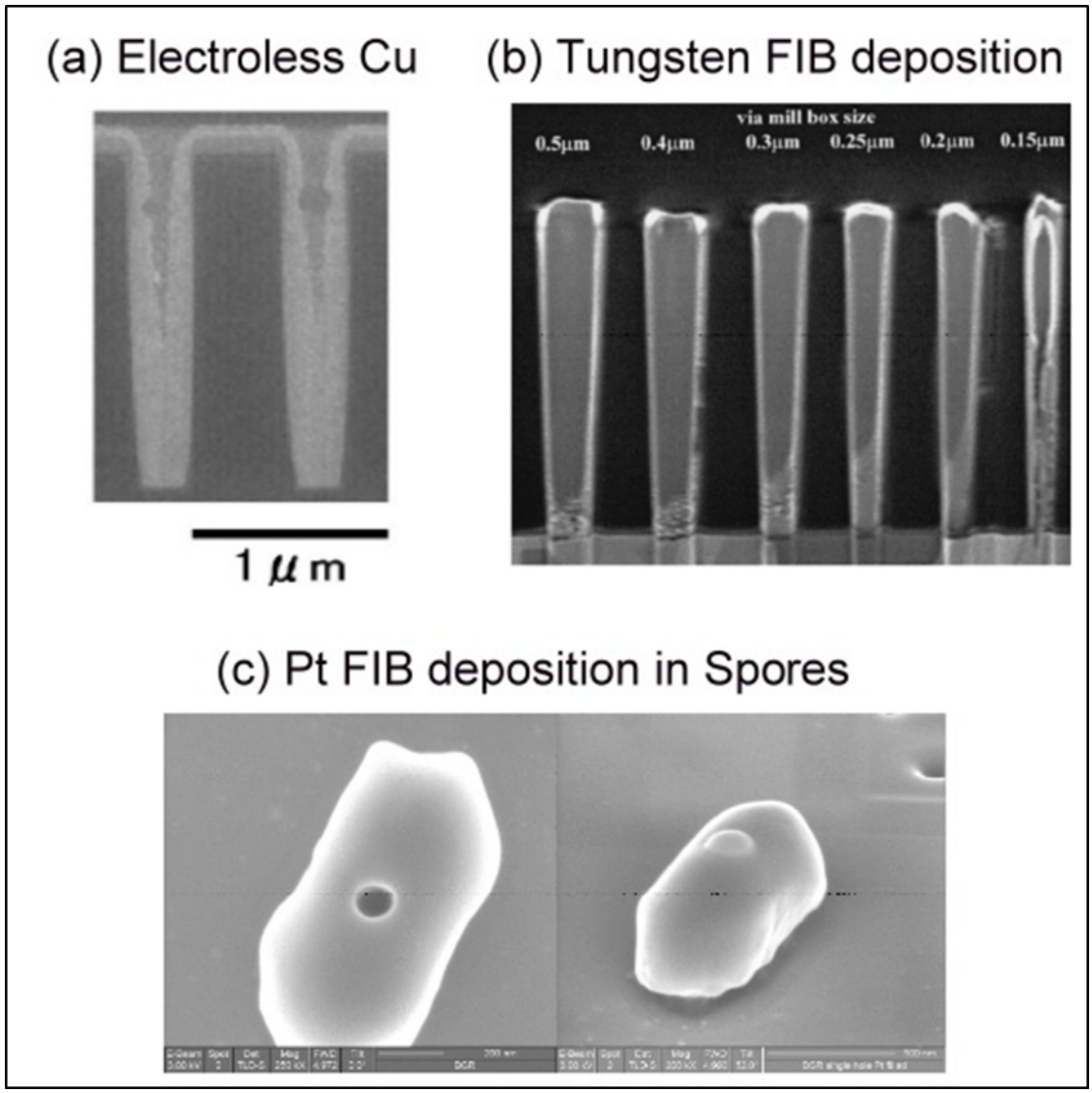


Figure 4-8: Examples of via filling techniques.

Examples of via filling from various authors, including (a) 10 minute electroless Cu plating of 0.31 μm hole by Wang *et al.*[157], (b) tungsten FIB deposition of vias varying in size by Ray, *et al.*[161], and (c) Pt FIB deposition in spores by Wall *et al.*[160].

with the 3x3 pixel array. Run 4 attempts to fill the via more completely with the gradient enabled by using a 2x2 rastered beam array at the center of the 10x10nm via. Figure 4-9 shows illustrations of the four run scenarios, and Figure 4-10 shows an illustration of the gas gradient.

When an electron beam enters a via, depositions are not localized to the bottom where the primary electrons enter the bulk. Backscattered electrons emerge from the bottom of the via as well as the sidewalls, and travel across the vacuum to re-enter on the other side of the via, as shown in Figure 4-11. This is one of the reasons that depositions can occur on the sidewalls. Once the thickness of these sidewall depositions reaches the point that it begins to overlap the Gaussian beam, more depositions occur due to PE and SE^{I} electrons. In fact, the PE's do not even reach the bottom of the via any more. This causes a "pinched-off" effect where a void remains within the via.

The results from attempting to fill a via with a 3x3 rastered beam are shown in Figure 4-12. Here, the 3x3 adjacent pixel array with no gas gradient filled the via almost completely to the top. A small void at the top is seen, due to the via pinching off around frame 896. (Note: there were 56 electrons per pixel at i_{beam}=9pA and 1μs dwell time). For a complete list of all simulation results from the via application runs, please see Appendix I.

The effect of overlapping a pixel on the aperture surface is shown in Figure 4-13. Electron-solid interactions at the corners of the via create additional depositions that cause premature pinch-off. A larger void is found in this via as compared to Run 1.

For Run 3, a linear gas gradient was applied to the same conditions as the 3x3

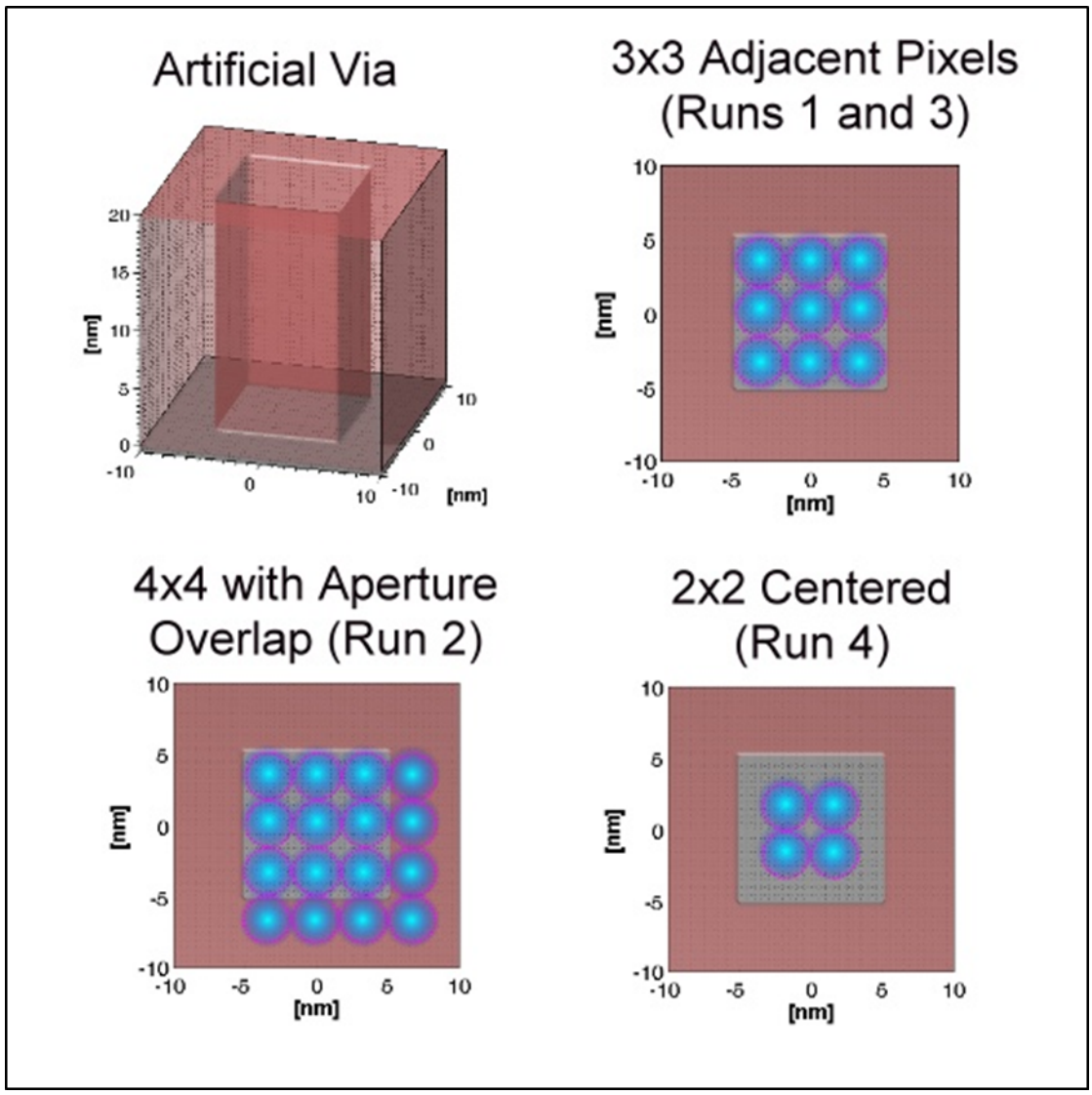


Figure 4-9: Via Run Setup.

Illustration of the pixel array setup for the four runs in the via application simulations.

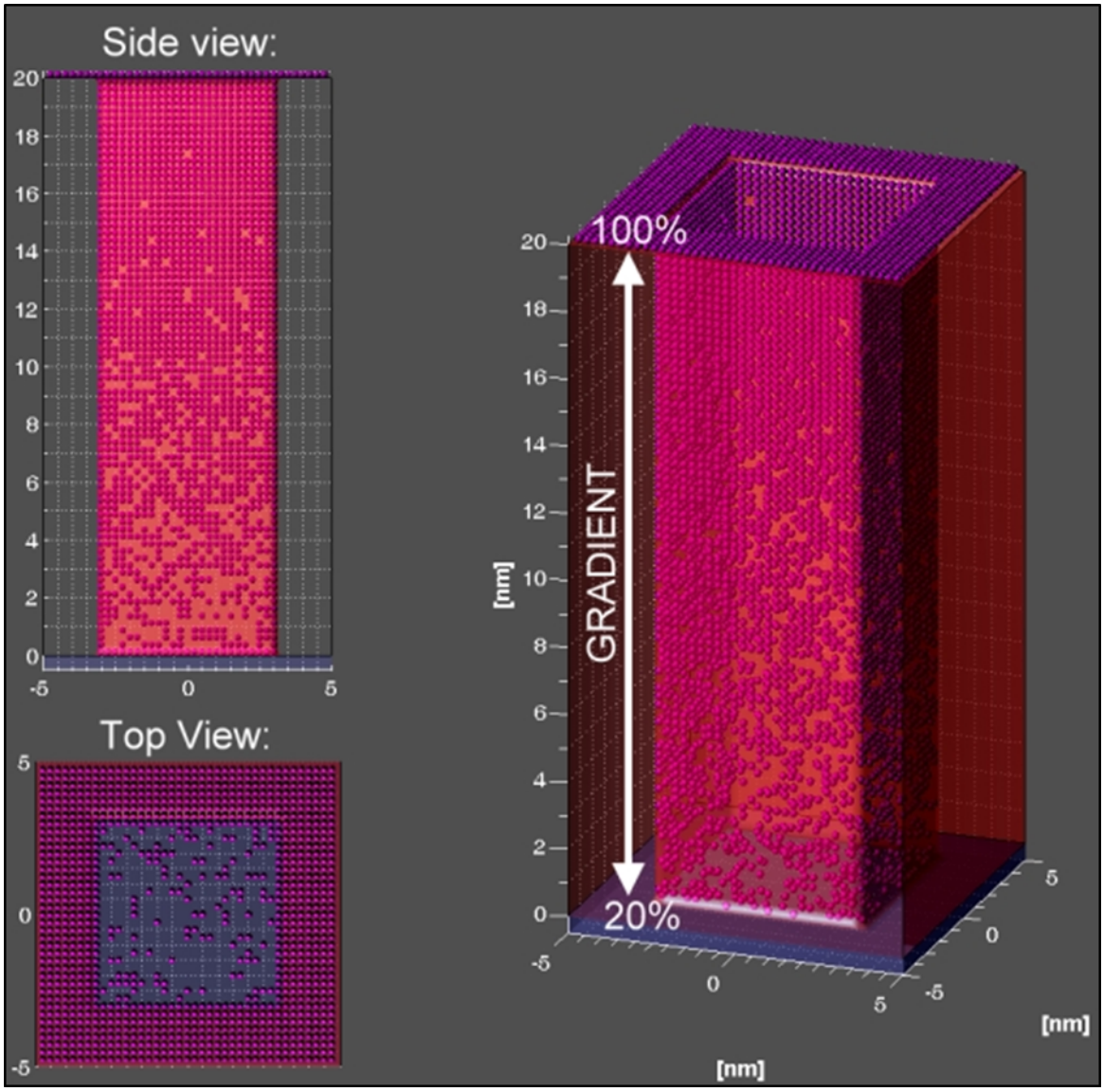


Figure 4-10: Gas Gradient in vias.

Illustration of gas gradient within vias. The gradient was chosen to be linear, ranging from 20% coverage at the bottom of the via to 100% at the aperture surface. The purple spheres are gas molecules.

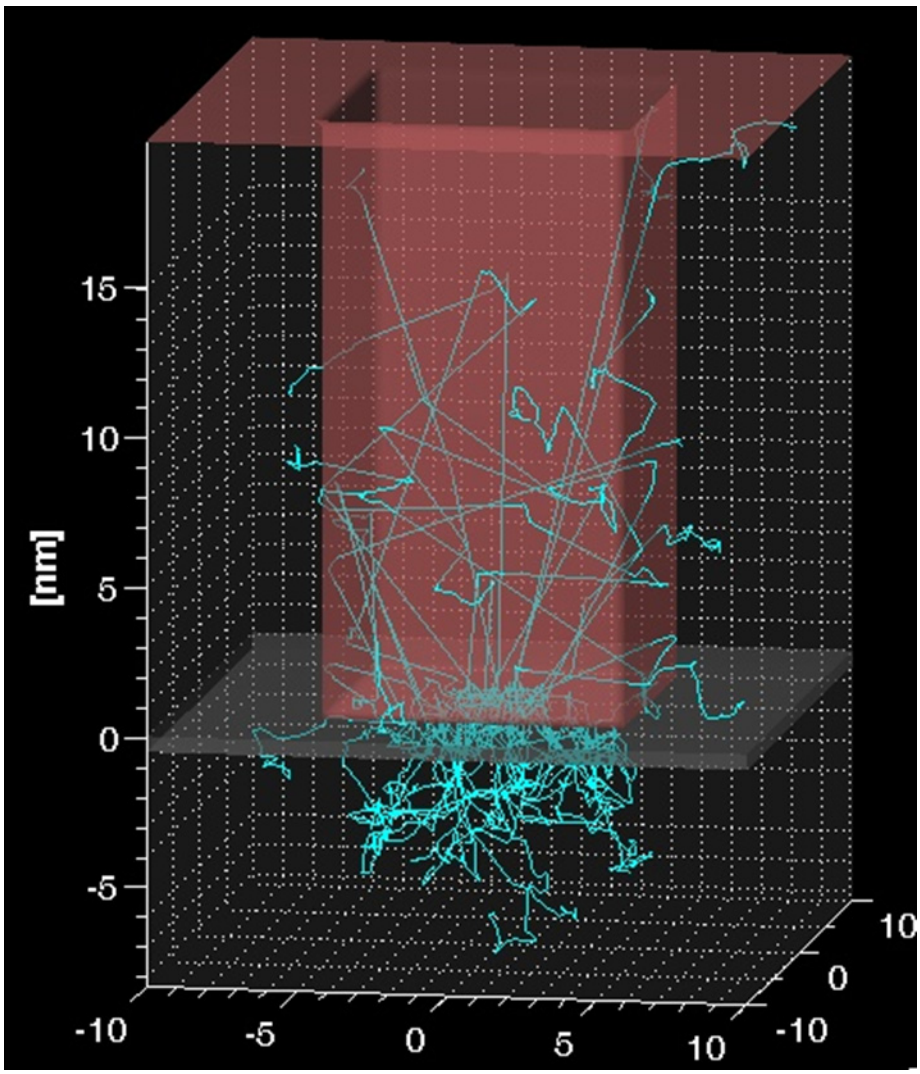


Figure 4-11: Via Monte Carlo Illustration.

Electrons are not confined to the area where the primary beam intersects the sample. Here, 50 electrons are simulated into tungsten at 1keV, showing how BSE's can emerge and travel across the via to create deposition events all along the via sidewalls.

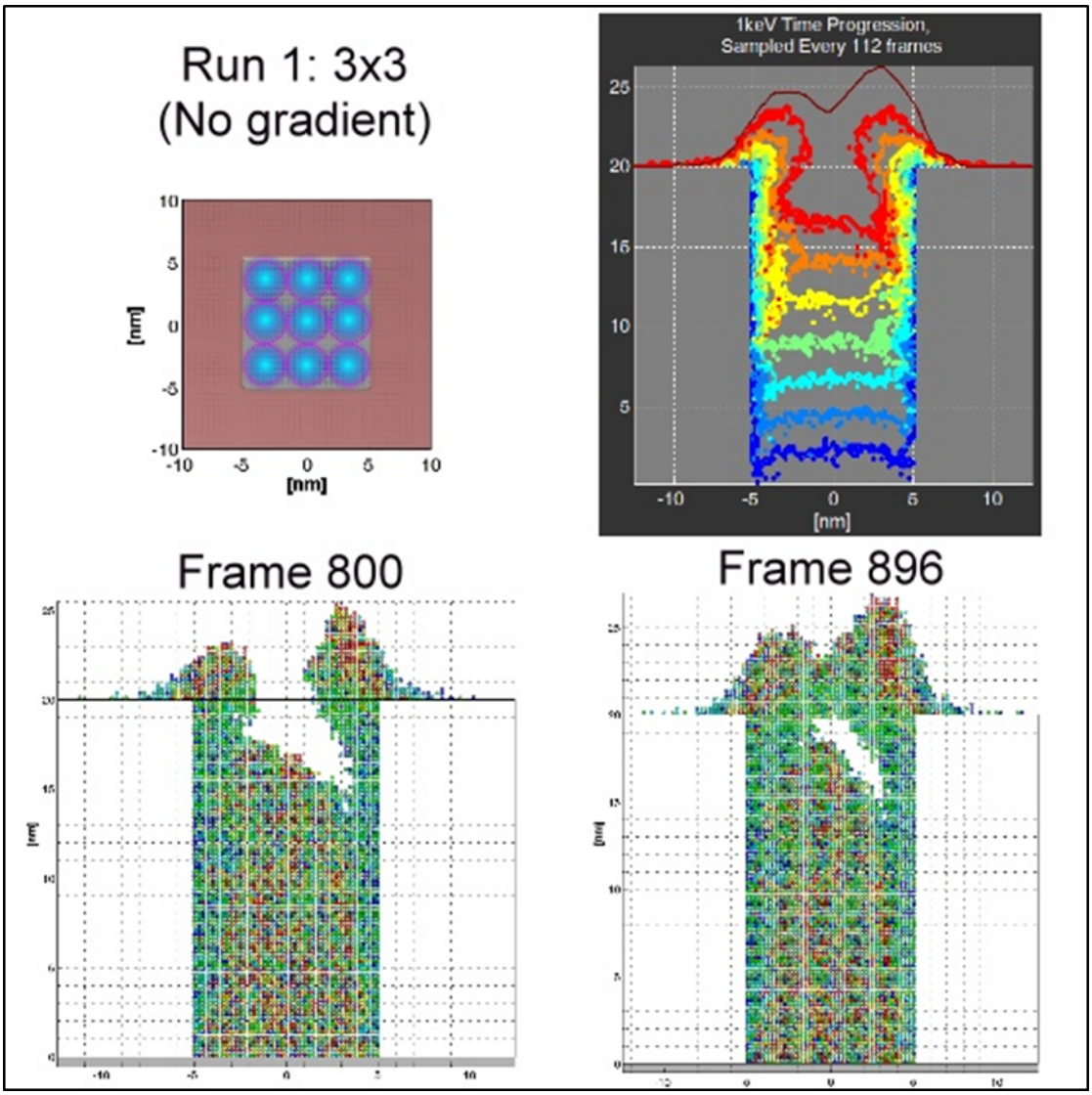


Figure 4-12: Via Run 1 Results.

The 3x3 pixel array (with no gradient) filled the via but left a small void at the top. The time progression shows the shape of the void as it filled, and the slice plane cross sections in the lower views show the fill structure at two stages of growth. The lack of symmetry is due to the randomness of the model.

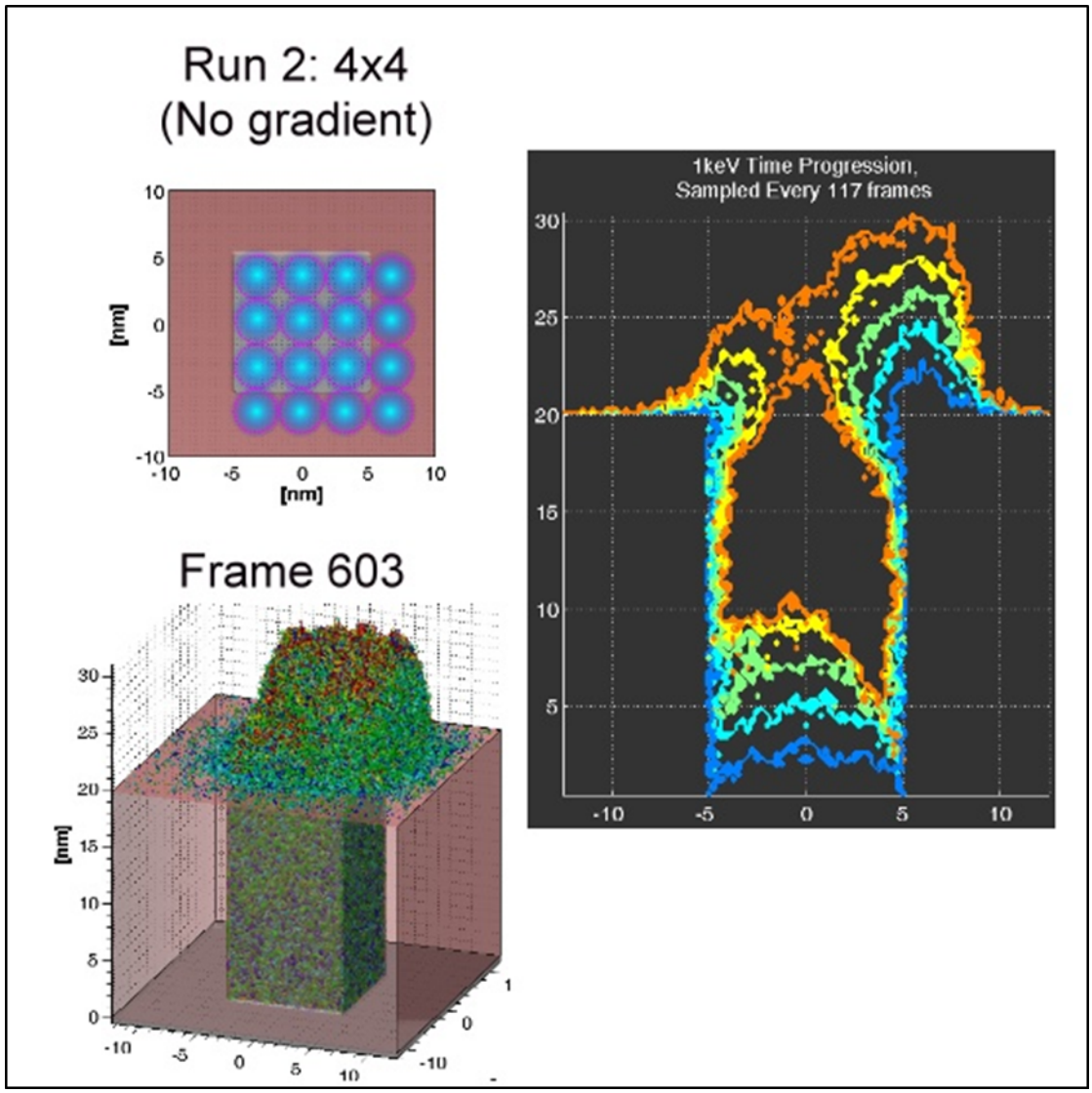


Figure 4-13: Via Run 2 Results.

A 4x4 pixel array shows the effect of overlapping the aperture surface. Electron-solid interactions at the corners of the via cause premature pinch-off and leave a larger void than was seen in Run 1.

array in Run 1. A much larger void was formed, as there was less gas at the bottom of the via to initiate dissociation events. See Figure 4-14 for these results.

Finally, an attempt to illustrate how to properly fill such a via was made in Run 4. Using the same logic that Ray *et al*. used when studying FIB deposition, a small beam (2x2 pixel array) was centered in the via. (Note the linear gas gradient was also applied as in Run 3). Figure 4-15 shows the results of Run 4, where the via filled up nicely. Only a few atomic voids are observed near the bottom of the via.

4.3 The Volcano Effect

Early experiments in EBID by J. Kim *et al.* revealed an unusual structure forming on the substate.[162] Tungsten was being deposited at 5keV, 71pA beam current, when "volcano" shaped structures started to form, as shown in Figure 4-16. The effect was noticed to vary with current, and several structures were documented. It was assumed that the diffusion coefficient of the WF_6 precursor was insufficient to reach the center of the beam spot before being consumed by the beam.

In order to duplicate this effect, the diffusion coefficient had to be back-calculated from the known parameters. For simplicity, the size of the structures in question and were scaled down to allow the simulations to run quickly. The basis for the calculations were as follows: if a 5nm radius homogeneous beam (i.e. a cylindrical or "square" profile) is used, the diffusion coefficient can be calculated from the random walk equation $r^2=4Dt$. In this case, r would be ½ the radius, or 2.5nm. To obtain t, we do some simple calculations based on the electron beam flux.

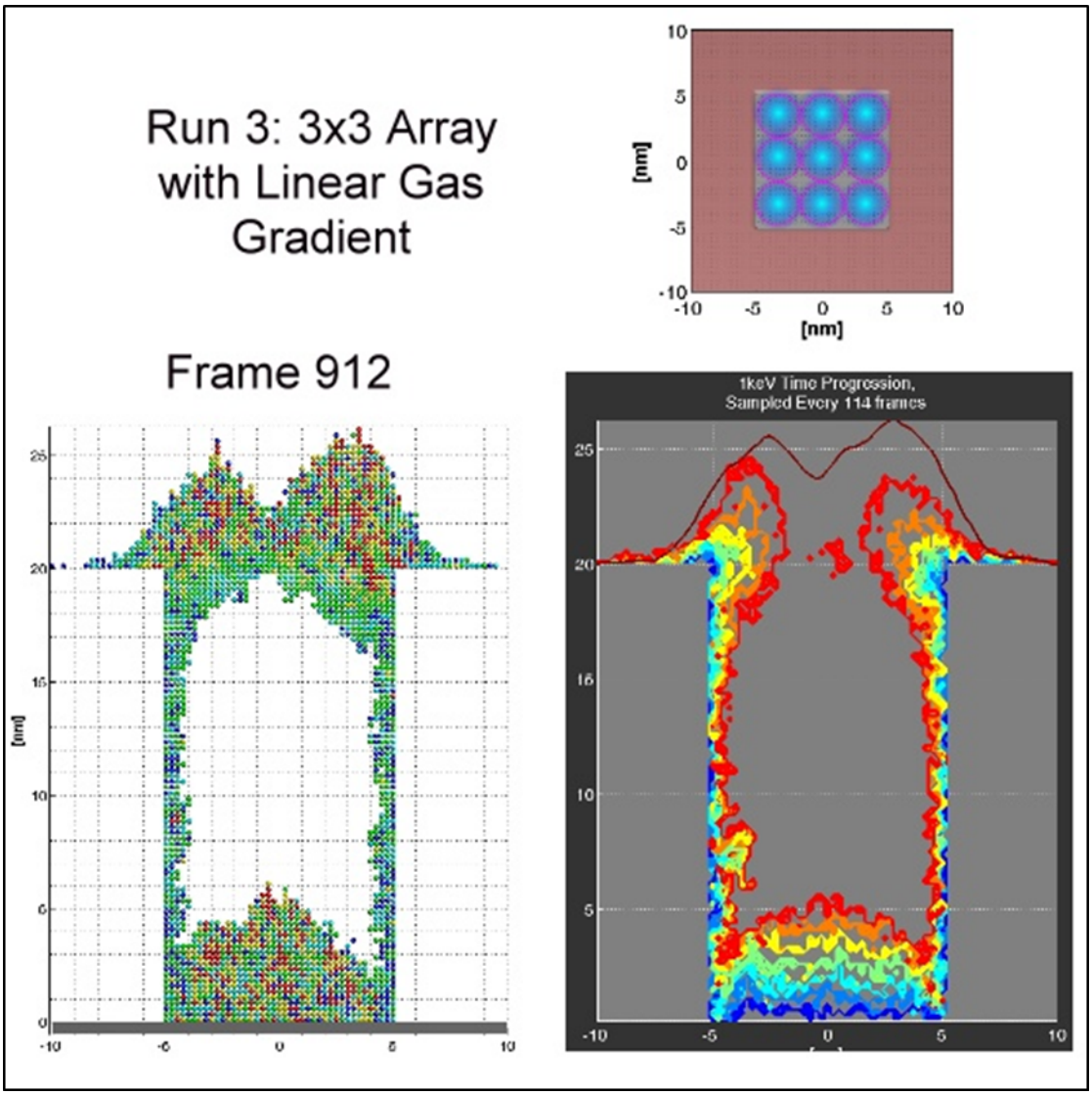


Figure 4-14: Via Run 3 Results.

The effect of applying a linear gas gradient to the via walls shows that a much larger void is formed inside the via.

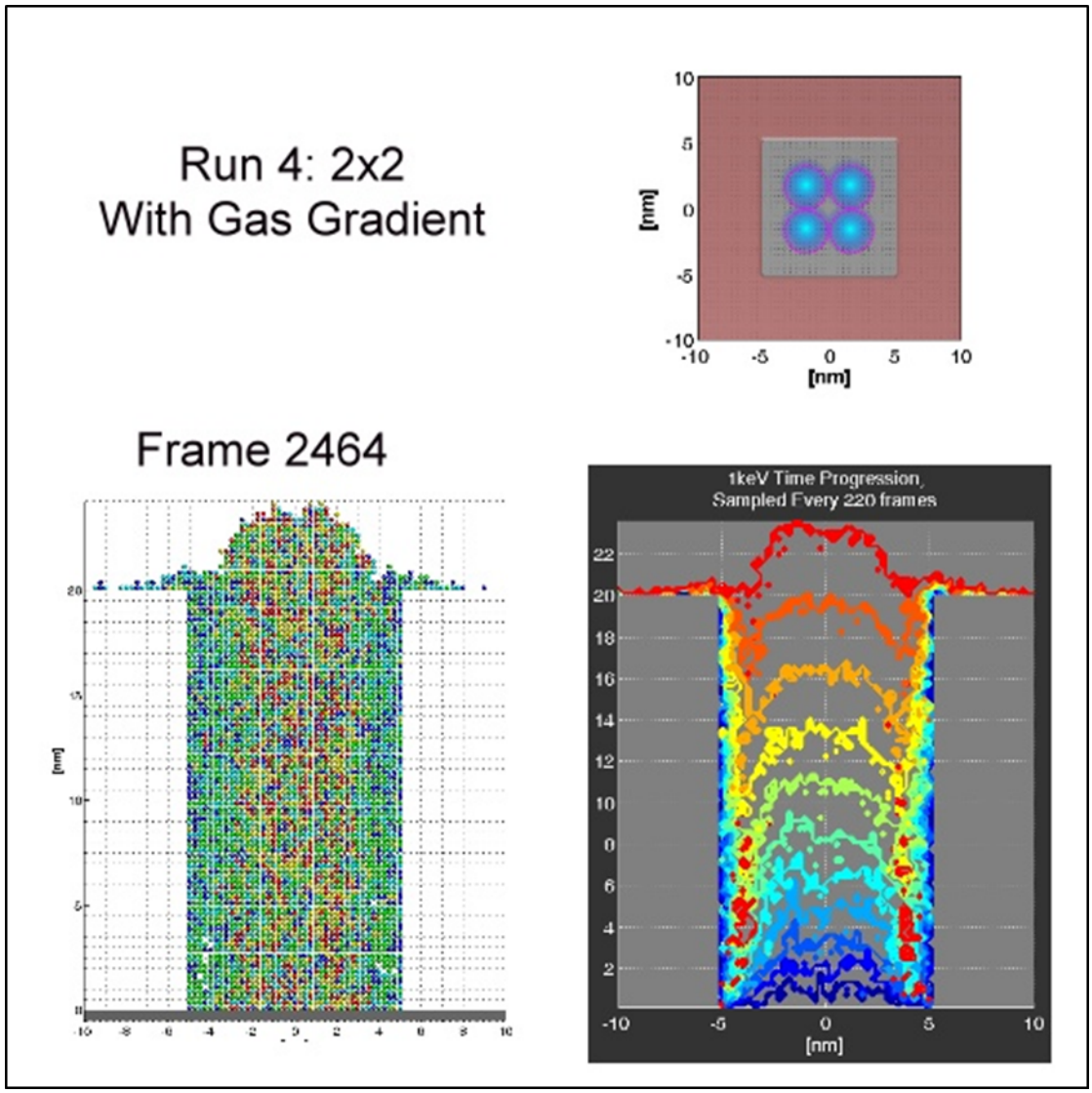


Figure 4-15: Via Run 4 Results.

Using a 2x2 array with no overlap, the via filled nicely. A few atomic voids are seen near the bottom.

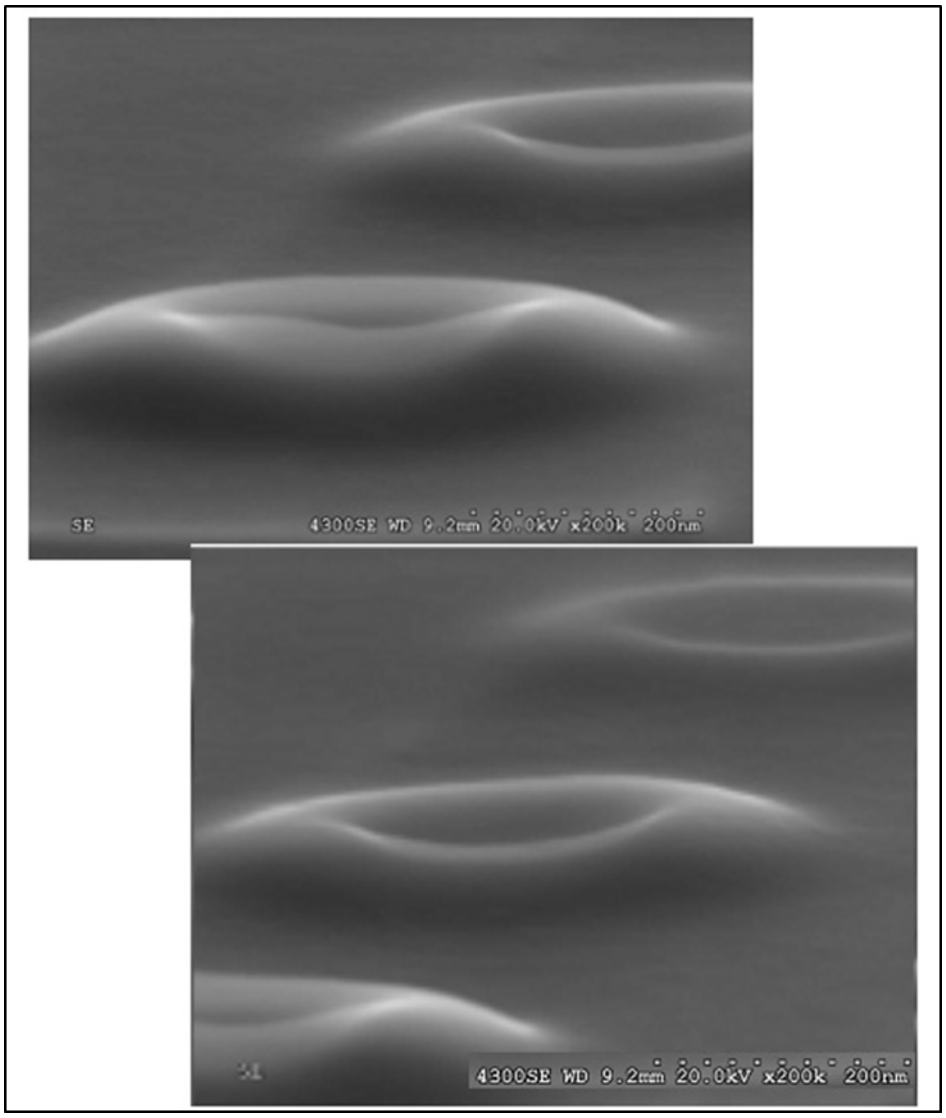


Figure 4-16: Volcano structures grown at UTK by J. Kim.[162]

These structures were grown by depositing tungsten on germanium at 71pA and 5keV.

If we use an arbitrary beam current of 30pA, there are 1.875e+8 electrons entering the sample per second. Therefore, each voxel is irradiated once every 5.3ns on average. The spot size of a 5nm radius beam has an area that is composed of 1257 voxels ($x = y = z = 0.25$nm). Multiplying 1257 voxels by 5.3ns, each pixel will receive an electron every 6.7μs. Using average data from previous runs under MTL conditions, the average probability for dissociation is ~0.05. Each pixel can therefore dissociate every 6.7 μs / 0.05, or 1.34×10^{-4} seconds.

To form a volcano, the gas molecules diffusing from the boundary of the simulation must therefore travel approximately ½ way across the beam radius in t=1.34×10^{-4} seconds. Back calculating D from the random walk equation, this yields a value of 1.165×10^{-10} cm^2/s. Using this value of the diffusion coefficient, a volcano structure similar in shape to the experimentally observed structures was formed as shown in Figure 4-17. Note that the PE deposition events are confined to the interior of the volcano due to the nature of the homogenous beam. Gas molecules diffused from the boundary ½ way into the beam, as anticipated. Figure 4-18 shows a 3D view of the volcano, covered in gas molecules (depicted as purple spheres). For a complete list of inputs and outputs from this simulation, see Appendix J.

In order to see the effect of the diffusion coefficient on the volcano morphology, r was set to the beam radius of 5nm and a new diffusion coefficient, D, was calculated from the random walk equation. For this value of r, D = 4.66×10^{-10} cm^2/s. It was postulated that this would allow the gas molecules to walk farther into the volcano, and dampen the crater effect at the center. Figure 4-19 shows the results of this run (labeled

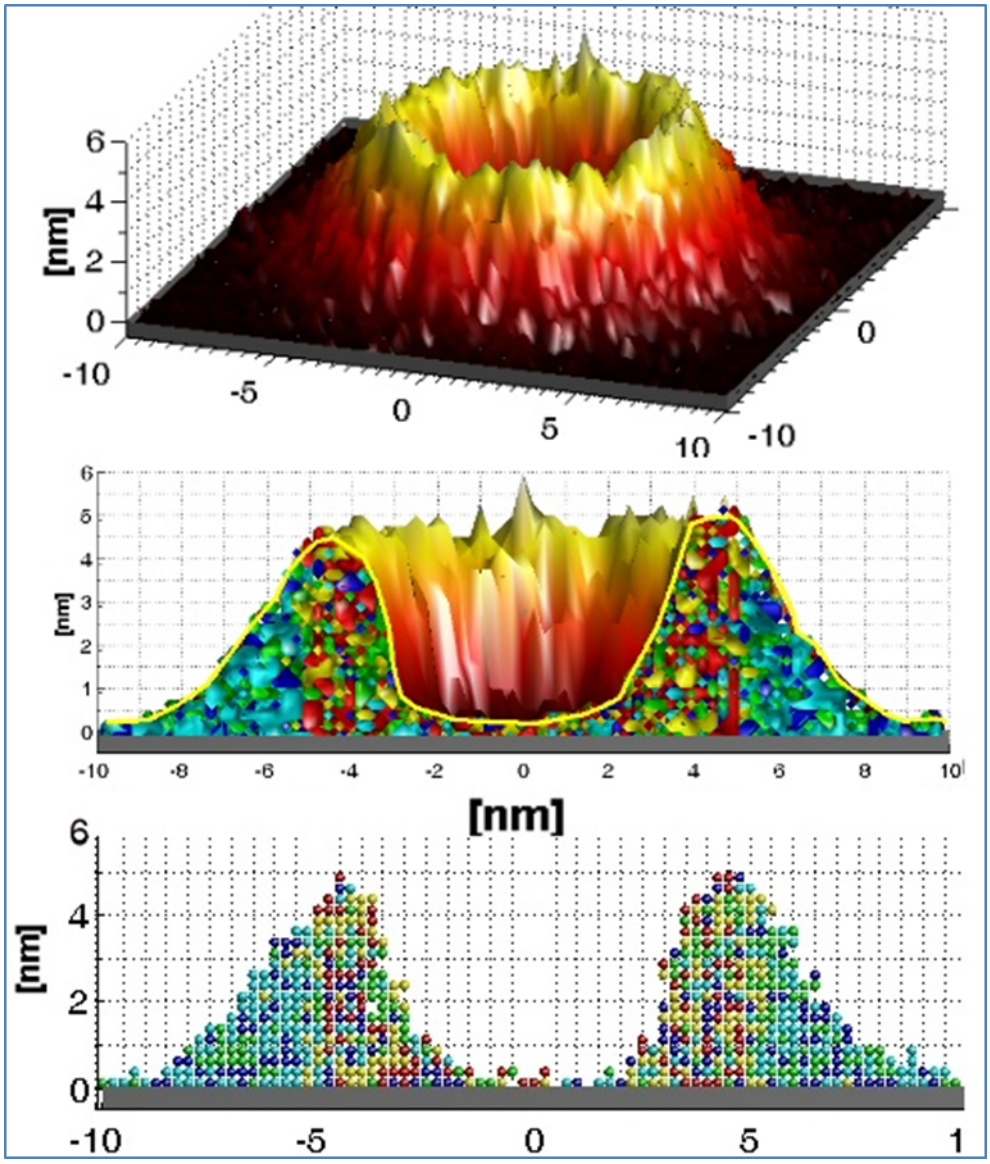


Figure 4-17: Volcano Run 1 Results.

The resultant structure seems to have formed exactly as anticipated. The lack of deposition at the center indicates the gas is not reaching this location.

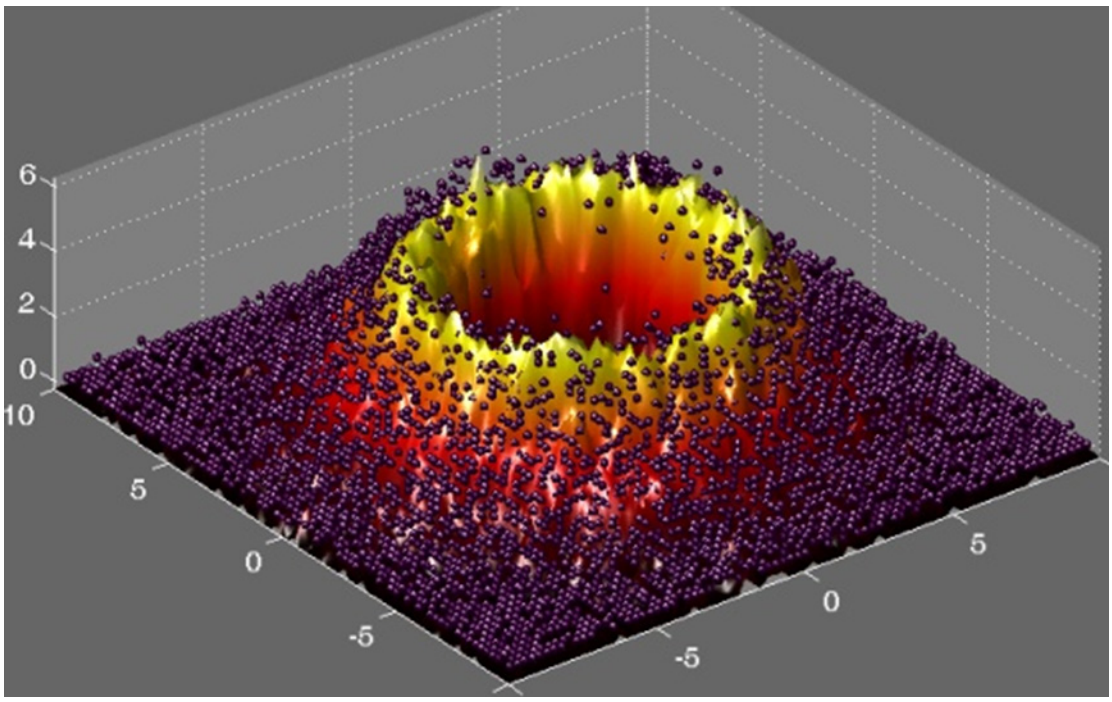


Figure 4-18: Gas surrounding volcano periphery.

Volcano Run 1. Clearly the gas is not traveling far past the rim of the volcano. The volcano was grown under MTL conditions in the WF_6-W system at 1keV. The simulation was ended at 750,000 electrons.

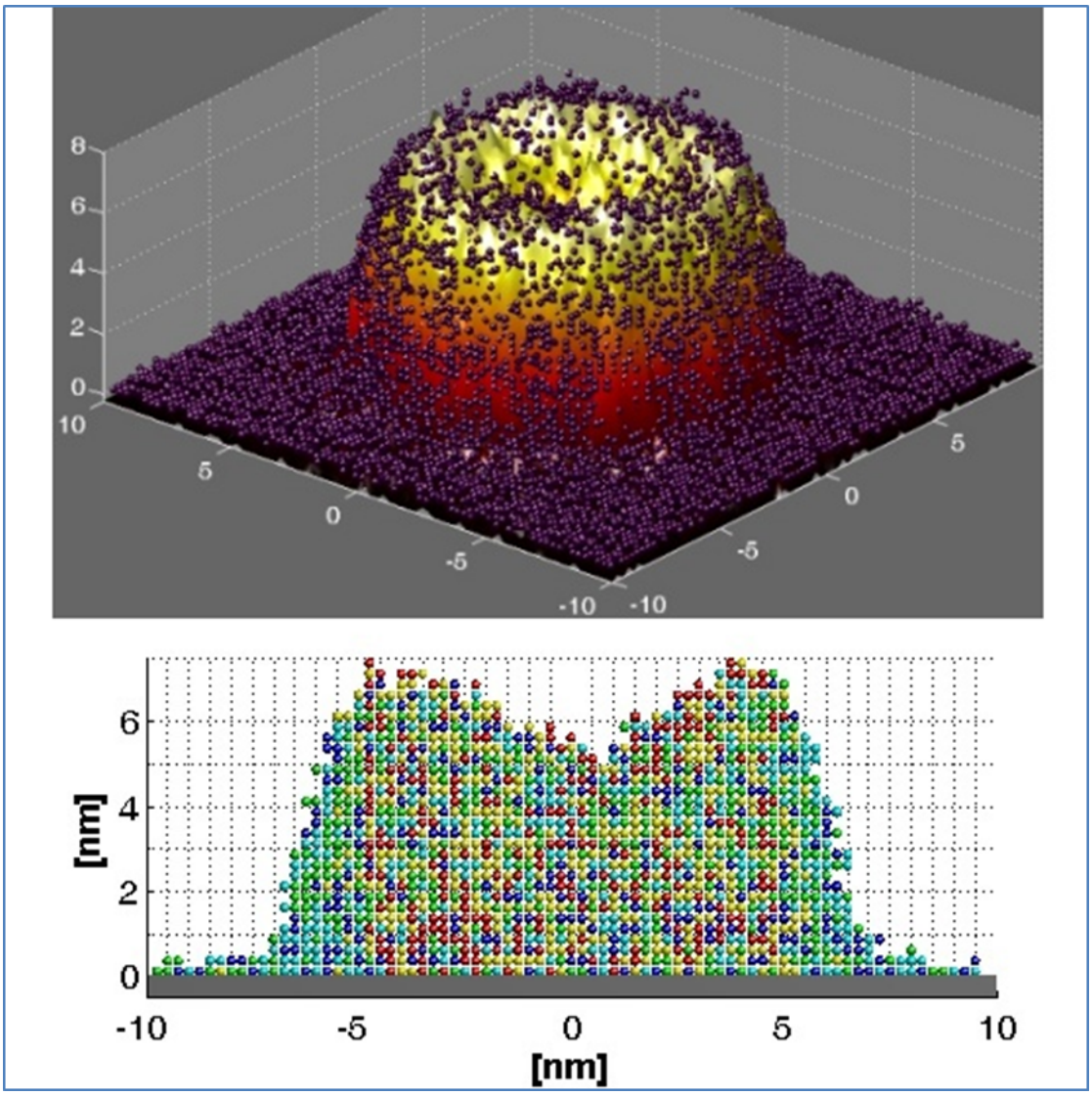


Figure 4-19: Volcano Run 2 Results.

Increasing the diffusion coefficient seemed to dampen the crater effect at the center of the volcano, as more gas atoms could reach the center. This simulation was ended after 500,000 electrons.

"Run 2"). Note that there is still a dimple at the center of the volcano, but since more gas molecules can reach the center, the effect is less pronounced than in the first run.

Chapter 5--Conclusions

As the limits of optical lithography are being pushed in today's highly competitive semiconductor industry, inventive ways of assembling structures on the nanoscopic scale are becoming of increased value. Research in this area is progressing steadily, and it was deemed necessary to develop a comprehensive 3D simulation for the process of EBID which is at the forefront of nanotechnology innovation. The purpose of the simulation was to give insights into the process of EBID, as well as illustrate the usefulness of a 3D simulation in predicting the outcome of experiments with such numerous and complex variables. The simulation, based heavily in algorithms and theories in the field of electron-solid interactions which have been studied for years, was verified by comparing simulated output to many forms of qualitative and quantitative results taken from experiments and literature.

The study of beam energy on EBID pillar growth in the WF_6-tungsten system showed that lower growth rates occurred at higher energies due to lower dissociation cross sections and lower secondary electron yields. An interesting result of this study was that in addition to faster vertical growth rates at lower energies, there was not a loss in lateral resolution. Examination of mass-transport-limited growth vs. a reaction-rate-limited growth regime verified the premise that lateral broadening in these conditions was due primarily to secondary electrons, specifically type II (SE^{II}'s). Furthermore, saturation and steady-state growth were shown to be dependent upon electron stopping power, which is the same in both mass-transport and reaction-rate limited growth conditions. The surface diffusion study revealed how mass-transport-limited growth can be shifted toward a pseudo-reaction-rate-limited regime if the diffusion coefficient was sufficiently high.

The simulation's ability to examine various materials was also verified through analysis of SiO_2 deposition using TEOS as the EBID precursor.

The simulation outputs, including 3D imaging, quantitative plots of sampled deposition events, temporal cross sectioning of pillars throughout the growth process, electron emission tracking, gas surface coverage area plots, etc. all were demonstrated and shown to be useful in gleaning information about the EBID process. Example simulations were performed, to show the simulation's robustness in creating structures with a rastered beam, filling high aspect-ratio vias, and mimicking experimental results.

References

1 Alfonso Velosa, The Bridge, National Academy of Engineering **35** (2005).
2 Mary Bellis, The History of Computers, http://inventors.about.com/library/blcoindex.htm, 2007
3 Intel, Intel Corporation, Moore's Law, http://www.intel.com/technology/mooreslaw/index.htm, 2007
4 Naomasa Shiraishi, Shigeru Hirukawa, Yuichiro Takeuchi, and Nobutaka Magome, Proc. SPIE **1674,** 741-52 (1992).
5 Shinji Okazaki, International Journal of High Speed Electronics and Systems **16,** 375-387 (2006).
6 H. Marchman, D. Taylor, S. Hadisutjipto, S. Mackay, R. Cottle, J. Maltabes, and J. Brown, in *Mask repair technique assessment and development for the 45nm lithographic node*Yokohama, Japan, 2006 (International Society for Optical Engineering, Bellingham WA, WA 98227-0010, United States), p. 628311.
7 Wikibooks, The Opensource Handbook of Nanoscience and Nanotechnology, http://en.wikibooks.org/wiki/Nanotechnology/EBID, 2007
8 R. Lariviere Stewart, Phys. Rev. **45,** 488-490 (1934).
9 C. W. Oatley, Journal of Applied Physics **53,** R1-R13 (1982).
10 K.R. Hart, T.F. Kassner, and J.K. Maurin, Philosophical Magazine **21,** 453 (1970).
11 A. N. Broers, W. W. Molzen, J. J. Cuomo, and N. D. Wittels, Applied Physics Letters **29,** 596-8 (1976).
12 H. Lutz, H. Wiesmann, Y. A. Bashkirov, O. F. Kammerer, M. Strongin, G. Warren, J. Roche, and D. H. Douglass, Ferroelectrics **16,** 259-261 (1975).
13 L. M. Bianchi and S. Shen, in *Electron-beam-deposited overlay coatings*San Diego, CA, USA, 1979, p. 469.
14 N. Silvis-Cividjian, C.W. Hagen, P. Kruit, M.A.J.V.D. Stam, and H.B. Groen, Applied Physics Letters **82,** 3514 (2003).
15 S. Rubel, M. Trochet, E.E. Ehrichs, W.F. Smith, and A.L. de Lozanne, Journal of Vacuum Science & Technology B **12,** 1894 (1994).
16 Y.M. Lau, P.C. Chee, J.T.L. Thong, and V. Ng, Journal of Vacuum Science & Technology A **20,** 1295 (2002).
17 V. Gopal, E.A. Stach, V.R. Radmilovic, and I.A. Mowat, Applied Physics Letters **85,** 49 (2004).
18 I. Utke, B. Dwir, K. Leifer, F. Cicoira, P. Doppelt, P. Hoffmann, and E. Kapon, Microelectronic Engineering **53,** 261 (2000).
19 K. Molhave, D.N. Madsen, A.M. Rasmussen, A. Carlsson, C.C. Appel, M Brorson, C.J.H. Jacobsen, and P Boggild, Nano Letters **3,** 1499 (2003).
20 Z. Q. Liu, K. Mitsuishi, and K. Furuya, J. of Appl. Phys. **96,** 3983-6 (2004).
21 M. Komuro, H. Hiroshima, and A. Takechi, Nanotechnology **9,** 104-7 (1998).
22 M.D. Croitoru, G. Bertsche, and D.P. Kern, in *The 49th International Conference on Electron, Ion, and Photon Beam Technology and Nanofabrication* (Orlando, FL USA, 2005).
23 T. Brintlinger, M.S. Fuhrer, J. Melngailis, I. Utke, T. Bret, A. Perentes, P. Hoffmann, P. Doppelt, and M. Abourida, in *The 49th International Conference on Electron, Ion, and Photon Beam Technology and Nanofabrication* (Orlando, FL USA, 2005).

[24] I. Utke, A. Luisier, P. Hoffmann, D. Laub, and P.A. Buffat, Applied Physics Letters **81,** 3245 (2002).
[25] H.W.P. Koops, J. Kretz, M. Rudolph, and M. Weber, Journal of Vacuum Science & Technology B **11,** 2386 (1993).
[26] H. W. P. Koops, A. Kaya, and M. Weber, J. Vac. Sci. Technol. B **13,** 2400-3 (1996).
[27] K. Ueda and M. Yoshimura, Thin Solid Films **464-465** (2004).
[28] C. H. Jin, J. Y. Wang, Q. Chen, and L.-M. Peng, J. Phys. Chem. B **110,** 5423-5428 (2006).
[29] S. Matsui, T Ichihashi, and M Mito, Journal of Vacuum Science & Technology B **7,** 1182 (1989).
[30] M. A. Guillorn, A. V. Melechko, V. I. Merkulov, E. D. Ellis, M. L. Simpson, D. H. Lowndes, L. R. Baylor, and G. J. Bordonaro, in *Microfabricated field emission devices using carbon nanofibers as cathode elements*Washington, DC, USA, 2001 (AIP for American Vacuum Soc), p. 2598-601.
[31] X. Yang, M. L. Simpson, S. J. Randolph, P. D. Rack, L. R. Baylor, H. Cui, and W. L. Gardner, Appl. Phys. Lett. **86,** 186106 (2005).
[32] K Murakami and M Takai, Journal of Vacuum Science & Technology B **22,** 1266 (2004).
[33] J. Sellmair, K. Edinger, and H. W. P. Koops, Journal of Vacuum Science & Technology B **23,** 781 (2005).
[34] H.W.P. Koops, C. Schossler, A. Kaya, and M. Weber, Journal of Vacuum Science & Technology B **14,** 4105 (1996).
[35] C. Lehrer, L. Frey, S. Petersen, H. Ryssel, M Schafer, and Th. Sulzbach, Journal of Vacuum Science & Technology B **22,** 1402 (2004).
[36] L. R. Baylor, W. L. Gardener, X. Yang, R. J. Kasica, M. A. Guillorn, B. Blalock, H. Cui, D. K. Hensley, S. Islam, D. H. Lowndes, A.V. Melechko, V. I. Merkulov, D. C. Joy, P. D. Rack, M. L. Simpson, and D. K. Thomas, J. Vac. Sci. Technol B **22,** 3021 (2004).
[37] L. R. Baylor, W. L. Gardner, X. Yang, R. J. Kasica, B. Blalock, C. Durisety, J. Fowlkes, D. K. Hensley, S. Islam, D. C. Joy, A. V. Melechko, P. D. Rack, S. J. Randolph, R. Rucker, D. K. Thomas, and M. L. Simpson, in *Progress toward realization of the digital electrostatic e-beam array lithography (DEAL) concept*Oxford, UK, 2005 (IEEE), p. 74-5.
[38] L. R. Baylor, D. H. Lowndes, M. L. Simpson, C. E. Thomas, M. A. Guillorn, V. I. Merkulov, J. H. Whealton, E. D. Ellis, K. Hensley, and A. V. Melechko, J. Vac. Sci. Technol B **20,** 2646 (2002).
[39] E.J. Sanchez, J.T. Krug II, and X.S. Xie, Rev. Sci. Instrum. **73,** 3901 (2002).
[40] T. Liang, A. Stivers, R. Livengood, Yan Pei-Yang, Zhang Guojing, and Lo Fu-Chang, Journal of Vacuum Science & Technology B (Microelectronics and Nanometer Structures) **18,** 3216 (2000).
[41] Ted Liang and Alan Stivers, Proceedings of the SPIE **4688,** 375-83 (2002).
[42] T. Liang, A. Stivers, M. Penn, D. Bald, C. Sethi, V. Boegli, M. Budach, K. Edinger, and P. Spies, Proceedings of the SPIE - The International Society for Optical Engineering **5446,** 291-300 (2004).

[43] T. Liang, D. Bald, B. Lieberman, and A. Stivers, in *The 49th International Conference on Electron, Ion, and Photon Beam Technology and Nanofabrication* (Orlando, FL USA, 2005).
[44] Klaus Edinger, Hans Becht, Johannes Bihr, Volker Boegli, Michael Budach, Thorsten Hofmann, Hans W. P. Koops, Peter Kuschnerus, Jens Oster, Petra Spies, and Bernd Weyrauch, J. Vac. Sci. Technol B **22,** 2902-6 (2004).
[45] W. F. van Dorp, C. W. Hagen, P. A. Crozier, B. van Someren, and P. Kruit, Microelectronic Engineering **83,** 1468-1470 (2006).
[46] S. J. Randolph, J. D. Fowlkes, and P. D. Rack, Critical Reviews in Solid State and Materials Sciences **31,** 55-89 (2006).
[47] L Dong, F Arai, and T Fukuda, Applied Physics Letters **81,** 1919 (2002).
[48] F. Arai, P. Liu, L. Dong, T. Fukuda, T. Noguchi, and K. Tatenuma, in *Pure metal deposit using multi-walled carbon nanotubes decorated with ruthenium dioxide super-nanoparticles*Munich, Germany, 2004 (IEEE), p. 196.
[49] S. Matsui and K. Mori, J. Vac. Sci. Technol B **4,** 299-304 (1986).
[50] P.A. Crozier, J. Tolle, J. Kouvetakis, and C. Ritter, Applied Physics Letters **84,** 3441 (2004).
[51] K. T. Kohlmann-von Platen and W. H. Bruenger, Journal of Vacuum Science & Technology B: Microelectronics Processing and Phenomena **14,** 4262 (1996).
[52] H.W.P. Koops, A. Reinhardt, F. Klabunde, A. Kaya, and R. Plontke, Microelectronic Engineering **57-58,** 909 (2001).
[53] FEI Company, Schottky Emission Cathodes, http://www.feibeamtech.com/pages/schottky.html, 2007
[54] Z. Q. Liu, K. Mitsuishi, and K. Furuya, Nanotechnology **15,** S414-19 (2004).
[55] P. Rai-Choudhury, *Handbook of microlithography, micromachining, and microfabrication* (SPIE Optical Engineering Press ;, Bellingham, Wash., USA, 1997).
[56] F. Cicoira, K. Leifer, P. Hoffmann, I. Utke, B. Dwir, D. Laub, P.A. Buffat, E. Kapon, and P. Doppelt, Journal of Crystal Growth **265,** 619 (2004).
[57] R.R. Kunz, T.E. Allen, and T.M. Mayer, Journal of Vacuum Science & Technology B **5,** 1427 (1987).
[58] S. Wang, Y.-M. Sun, Q Wang, and J.M. White, Journal of Vacuum Science & Technology B **22,** 1803 (2004).
[59] T. J. Stark, T. M. Mayer, D. P. Griffis, and P. E. Russell, J. Vac. Sci. Technol B **10,** 2685-9 (1992).
[60] A. Ishibashi, K. Funato, and Y. Mori, Journal of Vacuum Science & Technology B **9,** 169 (1991).
[61] M. Weber, H.W.P. Koops, M. Rudolph, J. Kretz, and G. Schmidt, Journal of Vacuum Science & Technology B **13,** 1364 (1995).
[62] V. Scheurer, H.W.P. Koops, and T. Tschudi, Microelectronic Engineering **5,** 423 (1986).
[63] N. A. Kislov, I. I. Khodos, E. D. Ivanov, and J. Barthel, Scanning **18,** 114-18 (1996).
[64] T. Takahashi, Y. Arakawa, M. Nishioka, and T. Ikoma, Applied Physics Letters **60,** 68 (1992).
[65] S. Matsui and M. Mito, Applied Physics Letters **53,** 1492 (1988).

[66] B.H. Chin and G Ehrlich, Applied Physics Letters **38,** 253 (1981).
[67] S. Lipp, L. Frey, C. Lehrer, B. Frank, E. Demm, S. Pauthner, and H. Ryssel, Journal of Vacuum Science & Technology B **14,** 3920 (1996).
[68] W.J. Mitchell and E.L. Hu, Journal of Vacuum Science & Technology B **17,** 1622 (1999).
[69] H. W. P. Koops, R. Weiel, D. P. Kern, and T. H. Baum, J. Vac. Sci. Technol B. **6,** 477-81 (1988).
[70] K. Gamo, D. Takehara, Y. Hamamura, M. Tomita, and S. Namba, Microelectronic Engineering **5,** 163 (1986).
[71] H. W. P. Koops, J. Kretz, M. Rudolph, M. Weber, G. Dahm, and K. L. Lee, in *Characterization and application of materials grown by electron-beam-induced deposition*Hsinchu, Taiwan, 1994, p. 7099-107.
[72] P. D. Rack, S. J. Randolph, Y. Deng, J. D. Fowlkes, Y. Choi, and D. C. Joy, Applied Physics Letters **82,** 2326 (2003).
[73] T. Bret, I. Utke, A Bachmann, and P. Hoffmann, Applied Physics Letters **83,** 4005 (2003).
[74] A. Perentes, T. Bret, I. Utke, P. Hoffmann, and M. Vaupel, Journal of Vacuum Science and Technology B: Microelectronics and Nanometer Structures **24,** 587-591 (2006).
[75] T. Djenizian, L Santinacci, and P Schmuki, Journal of the Electrochemical Society **151,** G175 (2004).
[76] M Shimojo, K. Mitsuishi, A Tameike, and K Furuya, Journal of Vacuum Science & Technology B **22,** 742 (2004).
[77] K.T. Kohlmann-von Platen, J. Chlebek, M. Weiss, K. Reimer, H. Oertel, and W. H. Brunger, J. Vac. Sci. Technol B **11,** 2219-23 (1993).
[78] N. Silvis-Cividjian, C. W. Hagen, L. H. Leunissen, and P. Kruit, Microelectron. Eng. **61-62,** 693-9 (2002).
[79] H. Hiroshima and M. Komuro, Nanotechnology **9,** 108-12 (1998).
[80] J. Fujita, M. Ishida, T. Ichihashi, Y. Ochiai, T. Kaito, and S. Matsui, J. Vac. Sci. Technol B **21,** 2990-3 (2003).
[81] T. J. Stark, T. M. Mayer, D. P. Griffis, and P. E. Russell, J. Vac. Sci. Technol B **9,** 3475-8 (1991).
[82] S. J. Randolph, J. D. Fowlkes, and P. D. Rack, Journal of Applied Physics **97,** 124312 (2005).
[83] U. Hübner, R. Plontke, M. Blume, A. Reinhardt, and H.W.P. Koops, Microelectron. Eng. **57-58,** 953-8 (2001).
[84] K.T. Kohlmann-von Platen, L.-M. Buchmann, H.-C. Petzold, and W.H. Brunger, Journal of Vacuum Science & Technology B **10,** 2690 (1992).
[85] T. Bret, I. Utke, and P. Hoffmann, Microelectronic Engineering **78-79,** 307 (2005).
[86] Y. Choi, P. D. Rack, S. Randolph, D. A. Smith, and D. C Joy, Scanning **28,** 311-318 (2006).
[87] D.C. Joy, Scanning Microscopy **5,** 329-337 (1991).
[88] J.D. Fowlkes, S.J. Randolph, and P.D. Rack, in *The 49th International Conference on Electron, Ion, and Photon Beam Technology and Nanofabrication* (Orlando, FL USA, 2005).

[89] T. E. Everhart and M. S. Chung, Journal of Applied Physics **43,** 3707-3711 (1972).

[90] N. Silvis-Cividjian, C.W Hagen, and P. Kruit, J. Appl. Phys **98,** 84905-1-12 (2005).

[91] D. C. Joy, *Monte Carlo Modeling for Electron Microscopy and Microanalysis* (Oxford University Press, New York, 1995).

[92] Z. J. Ding, X. D. Tang, and R. Shimizu, Journal of Applied Physics **89,** 718-26 (2001).

[93] T. Koshikawa and R. Shimizu, Journal of Physics D (Applied Physics) **7,** 1303-15 (1974).

[94] C. Colliex and P. Trebbia, in *Performance and applications of electron energy loss spectroscopy in STEM*Castle Hot Springs, AZ, USA, 1982, p. 259-66.

[95] D. A. Muller and J. Silcox, in *Delocalization in inelastic scattering*Leukerbad, Switzerland, 1995, p. 195-213.

[96] Zhi-Quan Liu, Kazutaka Mitsuishi, and Kazuo Furuya, Japanese Journal of Applied Physics, Part 1: Regular Papers and Short Notes and Review Papers **44,** 5659-5663 (2005).

[97] Zhi-Quan Liu, K. Mitsuishi, and K. Furuya, Nanotechnology **17,** 3832-7 (2006).

[98] K. Mitsuishi, Z. Q. Liu, M. Shimojo, M. Han, and K. Furuya, Ultramicroscopy **103,** 17-22 (2005).

[99] Wikipedia, Monte Carlo Method, http://en.wikipedia.org/wiki/Monte_Carlo_method, 2007

[100] M. Green, Proc. Phys. Soc. **82,** 204 (1963).

[101] Markus Drechsler, Electron Sample Interaction, http://www.mardre.com/homepage/mic/tem/electron_sample_interaction/electron_sample_interaction.html, 2004

[102] James H. Wittke, Effects of Electron Bombardment, http://www4.nau.edu/microanalysis/Microprobe/Interact-Effects.html, 2006

[103] T. E. Everhart, R. F. Herzog, M. S. Chang, and W.J. DeVore, Proc. 6th Intl. Conf. on X-Ray Optics and Microanalysis, 1972 (Univ. Tokyo Press), p. 81.

[104] D. C. Joy and S. Luo, Scanning **11,** 176-80 (1989).

[105] M. Kotera, Journal of Applied Physics **65,** 3991-8 (1989).

[106] Z. J. Ding and R. Shimizu, Scanning **18,** 92-113 (1996).

[107] Li Wen-Zhi, in *A Monte Carlo simulation of range and damage distributions for energetic ions in amorphous solids*Jinan, China, 1989, p. 339-41.

[108] L. Curgenven and P. Duncumb, "Research Report #303," (1971).

[109] Yinghong Lin and D. C. Joy, Surface and Interface Analysis **37,** 895-900 (2005).

[110] D. C. Joy, Luo Suichu, R. Gauvin, P. Hovington, and N. Evans, Scanning Microscopy **10,** 653-66 (1996).

[111] H. J. Hunger and L. Kuchler, Physica Status Solidi A **56,** 45-8 (1979).

[112] G. Love, M. G. C. Cox, and V. D. Scott, Journal of Physics D (Applied Physics) **10,** 7-23 (1977).

[113] M. S. Chung and T. E. Everhart, Journal of Applied Physics **45,** 707-9 (1974).

[114] M. S. Chung and T. E. Everhart, Physical Review B (Solid State) **15,** 4699-715 (1977).

[115] Kenji Murata, David F. Kyser, and Chiu H. Ting, Journal of Applied Physics **52,** 4396-4405 (1981).
[116] D. C Joy, in *Microbeam Analysis*, edited by A. Romig and J. Goldstein (San Francisco Press, San Francisco, 1984), p. 81-86.
[117] Z. J. Ding and R. Shimizu, Surface Science **197,** 539-54 (1988).
[118] S. Luo and D. C. Joy, Scanning Microscopy **2,** 1901-15 (1988).
[119] M. Kotera and T. Kishida, Japanese Journal of Applied Physics, Part 1 (Regular Papers & Short Notes) **28,** 148-9 (1989).
[120] S. Luo and D. C. Joy, Scanning Microsc. Suppl. (USA)**,** 127-46 (1990).
[121] M. Kotera, T. Kishida, and H. Suga, in *Monte Carlo simulation of secondary electrons in solids and its application for scanning electron microscopy*Park City, UT, USA, 1990, p. 111-26.
[122] S. Tanuma, T. Shiratori, T. Kimura, K. Goto, Ichimura, and C. J. Powell, Surface and Interface Analysis **37,** 833-45 (2005).
[123] P. A. Wolff, Physical Review **95,** 56-66 (1954).
[124] J.I. Goldstein, D.E. Newbury, P. Echlin, D.C. Joy, A.D. Romig, C.E. Lyman, C. Fiori, and E. Lifshin, *Scanning Electron Microscopy and X-Ray Microanalysis*, 2 ed. (Plenum Press, New York, 1992).
[125] H. Drescher, L. Reimer, and H. Seidel, Zeitschrift fur Angewandte Physik **29,** 331-6 (1970).
[126] D.C. Joy, J. of Micr. **147,** 51-64 (1987).
[127] *CRC Handbook of Chemistry and Physics*; *Vol.*, edited by David R. Lide (CRC, New York, 2006).
[128] V. Saksena, M. Kushwaha, and S. Khare, Int. J. of Mass Spectrometry and Ion processes **171,** L1-5 (1997).
[129] T. Nakano, H. Toyoda, and H. Sugai, Jpn. J. of Appl. Phys., Part 1 **30,** 2912-15 (1991).
[130] D. A. Alman, D. N. Ruzic, and J. N. Brooks, Physics of Plasmas **7,** 1421-32 (2000).
[131] W. L. Morgan, C. Winstead, and V. McKoy, Journal of Applied Physics **92,** 1663-7 (2002).
[132] J.D. Fowlkes, S.J. Randolph, and P.D. Rack, J. Vac. Sci. Technol. B **23,** 2825-31 (2005).
[133] R. Basner, M. Schmidt, and H. Deutsch, Bull. Am. Soc. Phys. Soc. **38,** 2369 (1993).
[134] S. Kwitnewski, E. Ptasinska-Denga, and C. Szmytkowski, Radiation Physics and Chemistry **68,** 169-74 (2003).
[135] NIST, Electron Impact Cross Sections for Ionization and Excitation, http://physics.nist.gov/PhysRefData/Ionization/intro.html, 2007
[136] S. M. Younger, J. Quant. Spectrosc. Radiat. Transfer **26** (1981).
[137] Y. K. Kim and M. E. Rudd, Phys. Rev. A **50,** 3954 (1994).
[138] N. Silvis-Cividjian, *Electron Beam Induced Nanometer Scale Deposition* (Delft University Press, Amsterdam, Netherlands, 2002).
[139] H. F. Winters and M. Inokuti, Phys. Rev. A **25,** 1420 (1982).
[140] *Perry's Chemical Engineering Handbook, 7th ed.*; *Vol. 1*, edited by R. H. Perry and D.W. Green (McGraw-Hill, New York, 1997).

[141] Tomasz Panczyk and Wladyslaw Rudzinski, J. Non-Equilib. Thermodyn. **28,** 341-397 (2003).
[142] J. H. Seinfeld and S. N. Pandis S. N, *Atmospheric Chemistry and Physics* (John Wiley & Sons, New York, NY, 1998).
[143] Wladyslaw Rudzinski and Tomasz Panczyk, Adsorption **8,** 23-34 (2002).
[144] Milton Ohring, *The materials science of thin films* (Academic Press, Boston, 1992).
[145] J.A. Venables, G.D.T. Spiller, and M. Hanbücken, Rep. Prog. Phys. **47,** 399 (1984).
[146] A. Chambers, B. S. Halliday, NetLibrary Inc., and R. K. Fitch, *Basic vacuum technology*, 2nd ed. (Institute of Physics Pub., Bristol ; Philadelphia, 1998).
[147] R.W. Christy, J. Appl. Phys. **31,** 1680-83 (1960).
[148] I. Utke, "Growth Regimes in FEB and FIB Induced Processing," (2004).
[149] L. Reimer, *Transmission Electron Microscopy* (Springer, New York, NY, 1997).
[150] M. Lieberman and A. Lichtenberg, *Principles of Plasma Discharges and Materials Processing 2nd edn* (Wiley, New York, NY, 1994).
[151] A. Einstein, Annalen der Physik **19,** 371-381 (1906).
[152] Philip Charles Nelson, Marko Radosavljevic, and Sarina Bromberg, *Biological physics : energy, information, life* (W.H. Freeman and Co., New York, 2004).
[153] A. Bowler and E. Hood, J. Chem. Phys. **94** (1991).
[154] K. Kohlmann, M. Thiemann, and W. Brunger, Microelectronic Engineering **13,** 279 (1991).
[155] L. Maissel, *Handbook of Thin Film Technology* (McGraw-Hill Book Company, New York, NY, 1970).
[156] L Reimer and C Tolkamp, Scanning **3,** 35 (1980).
[157] Z. Wang, O. Yaegashi, H. Sakaue, T. Takahagi, and S. Shingubara, Journal of the Electrochemical Society **151,** 781-5 (2004).
[158] Shoso Shingubara, Zengling Wang, Osamu Yaegashi, Ryo Obata, Hiroyuki Sakaue, and Takayuki Takahagi, Electrochemical and Solid-State Letters **7,** 78-80 (2004).
[159] S. N. Mei, T. M. Lu, and S. Robert, Electron Device Letters, IEEE **8,** 503-505 (1987).
[160] M. Wall, M. Fluss, and C. Schaldach, "Dual Beam FIB for Imaging, Nano-Sectioning and Sample Preparation of Sporres: Initial Results," (2004).
[161] V. Ray, N. Antoniou, N. Bassom, A. Krechmer, and A. Saxonis, Journal of Vacuum Science & Technology B: Microelectronics and Nanometer Structures **21,** 2715-2719 (2003).
[162] J. Kim, S. Randolph, J. D. Fowlkes, and P. D. Rack, Unpublished EBID work, University of Tennessee, Knoxville (2004)
[163] C. J. Powell and A. Jablonski, in *Effects of elastic-electron scattering on measurements of silicon dioxide film thicknesses by X-ray photoelectron spectroscopy*Berkeley, CA, USA, 2001 (Elsevier), p. 1139-43.

Appendices

Appendix A: Simulation Inputs

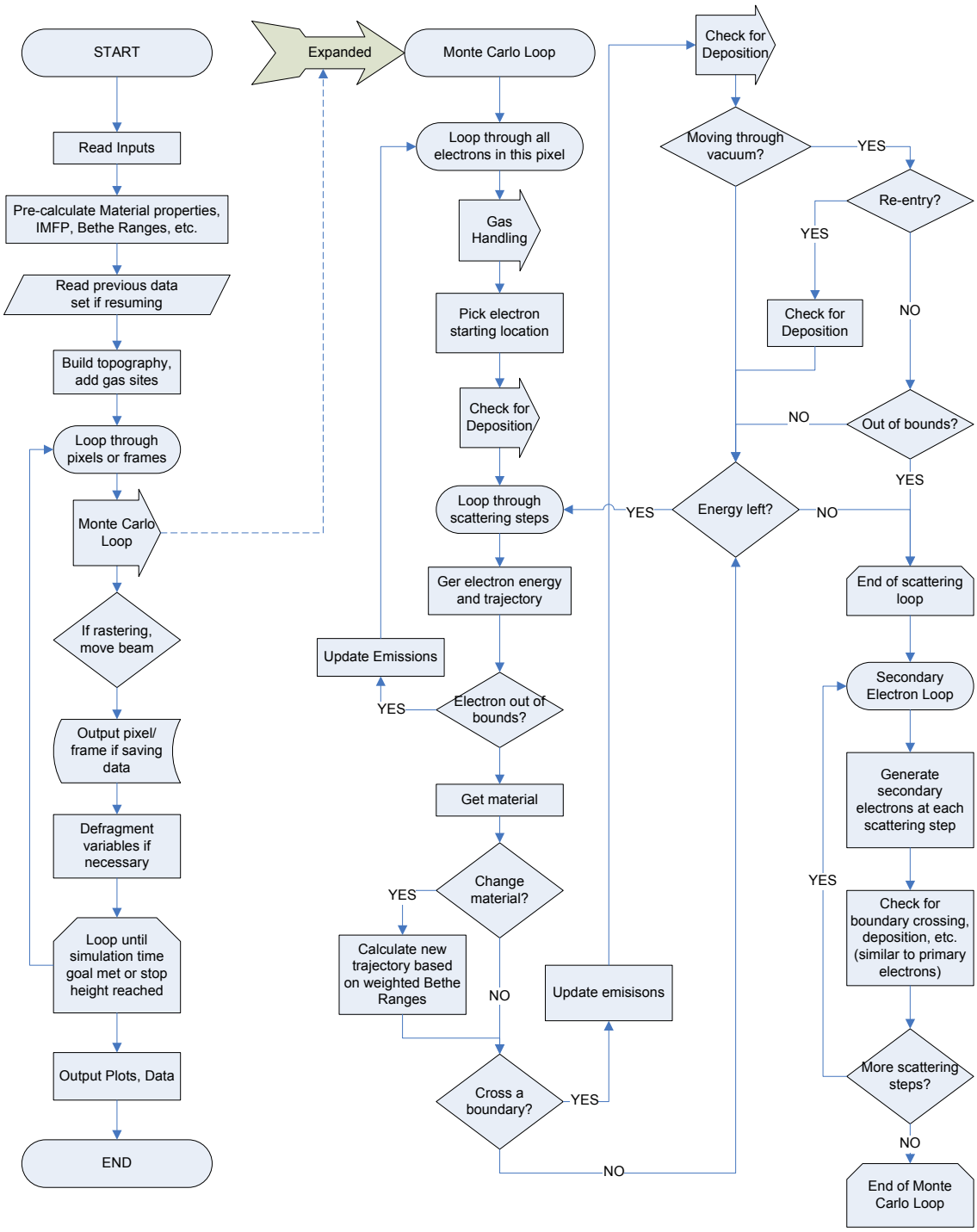
The following variables are required to operate the simulation. Actual variable names have been replaced with more verbose titles for clarity. If a variable is mentioned in the text, its variable name is given.

Title	*Units*	*Comments*
Main Simulation Properties		
Beam Energy, E_o	keV	Operating voltage of beam
Beam Profile	--	Gaussian or Cylinder
Beam Radius, r_{beam}	nm	For Gaussian profile, this is the FWHM
Beam Current, i_{beam}	nA	
Local Pressure, P_{sys}	Torr	Pressure at beam spot
Simulation Time	e^- or s	No. of electrons or seconds to run sim.
Base Size	nm	Size of base (*x* or *y*) along one edge
Process	--	Deposition or Etching
Material Properties		
Substrate material	--	Atomic No. of substrate
Deposited material	--	Atomic No. of deposit
Other materials	--	Atomic Nos. of other pre-existing materials
Molecular weight, MW	g/mol	*These values are taken from a table which is indexed by the material's atomic number (above)*
Density, ρ	g/cm^3	
Fermi Energy, E_F	eV	
Work Function, Φ	eV	
Gas Properties		
Gas MW	g/mol	Molecular Weight of precursor gas
Gas atomic radius	Å	Radius of gas molecule
Cross Section, σ	cm^2	Function for dissociation cross section
Temperature, T	K	Gas temperature
Adsorption Time, τ_a	s	Mean Residence time of gas on surface
Sticking coefficient, s	--	Probability of gas adsorption (0 to 1)
Surface Diffusion	--	Enable random walk of gas on surface (on/off)
Diffusion Coefficient, D_s	cm^2/s	Surface diffusion coefficient
Boundary Source	--	Gas diffusing from boundary? (on/off)
Initial Coverage, θ	--	Fraction gas coverage initially (0 to 1)

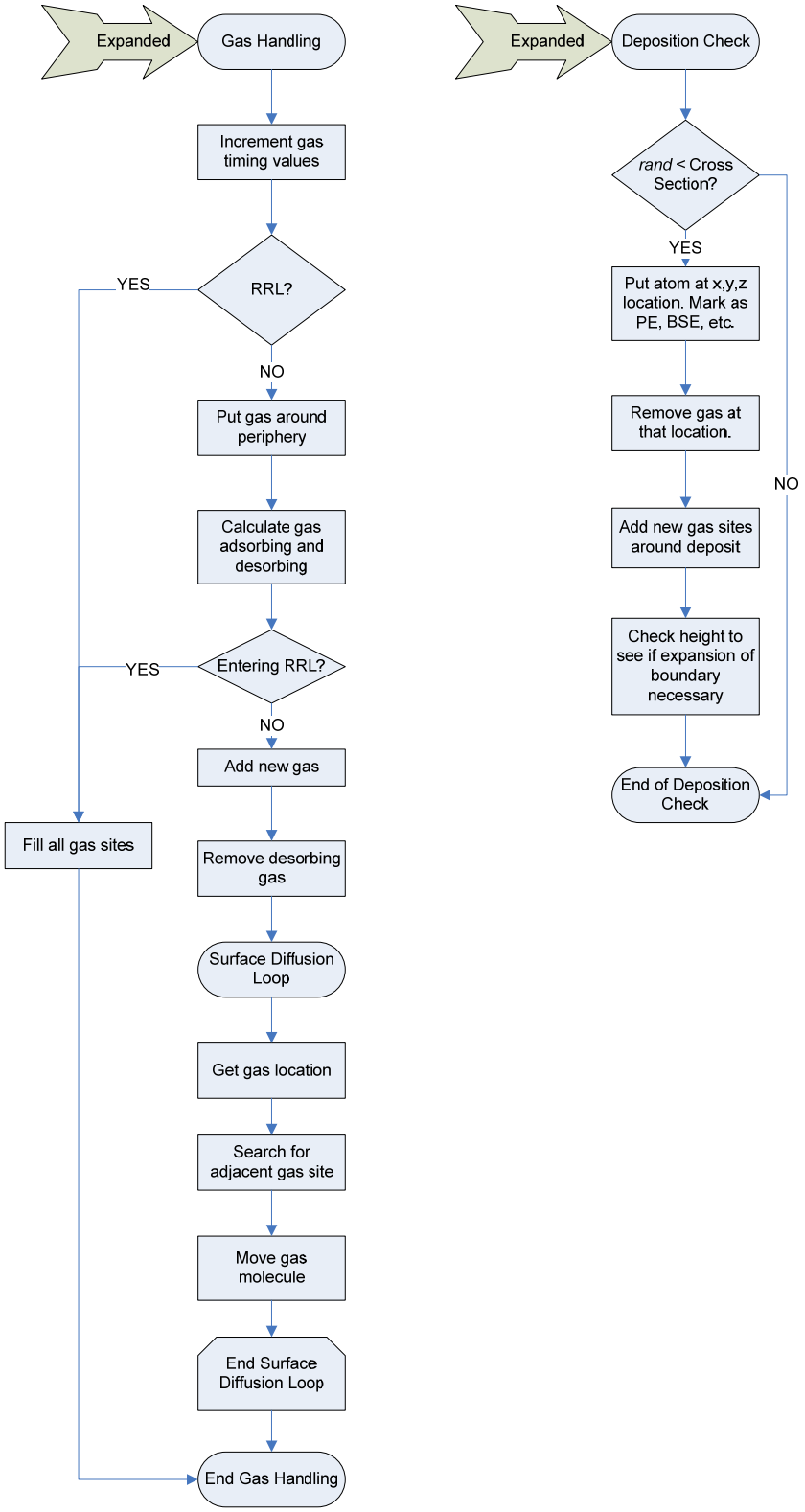
Simulation Input Variables, continued

Title	*Units*	*Comments*
		Raster Setup
Spot or Raster Mode	--	Spot mode or raster scanning?
Pixel Jump	--	Number of pixels to skip between raster spots
Raster area	nm	Top left and bottom right corners of raster area
Dwell Time	s	Time to pause on a pixel
Line Refresh Time	s	Time to pause after a line is complete
Frame Refresh Time	s	Time to pause after a frame is complete
Quick Refresh	--	Fraction of monolayer to add after every frame (0 to 1)
		Secondary Electron Tuning
SEfactor	--	Fraction of SE's to produce (0 to 1)
cascades	--	No of cascade events
		Data Management
Time Divisions	--	Divide the simulation into parts
Save Data	--	Save each part? (y/n)
Save Figures	--	Save output? (y/n)
Suppress Figures	--	Don't plot data? (y/n)
Resume Last	--	Resume from last time division?
Resume multiplier	--	Make simulation continue 2X, 3X, etc.
		Other Misc. / Diagnostic Variables
Stop Height	nm	End simulation if structure reaches certain height
Monte Carlo Steps	--	No. of steps to divide Bethe Range into (50 default)
Enable Gas	--	Turn off gas? (Scattering only- y/n)
Enable Depositions	--	Allow dissociation? (y/n)
Track Monte Carlo	--	Plot Monte Carlo trajectories? (y/n)
Tilt Angle	deg.	Incident beam angle
Pre-existing structure	--	Start with a structure on substrate? (y/n)
Structure dimensions	nm	Size and dimensions of structure
Use prev. structure	--	Start with a previous pillar (data file number)
Inverse	--	Make structure a via? (y/n)
Gradient	--	Gas gradient in via? (y/n)

Appendix B: Simulation Flowchart



Flowchart, continued



Appendix C: Material Properties

Property	*Value*
Tungsten Properties	
Atomic No.	74
Atomic Wt.	183.85 g/mol
Density	19.25 g/cm^3
Fermi Energy, E_F	7.0 eV
Work Function, Φ	4.55 eV
IMFP, λ	Calculated as function of energy (Figure 2-10)
Dissociation Cross Section, σ	Calculated as function of energy (Figure 2-18)
SiO_2 Properties	
Atomic No.	10
Atomic Wt.	60.8 g/mol
Density	2.2 g/cm^3
Fermi Energy, E_F	5.0 eV
Work Function, Φ	5.0 eV
IMFP, λ	3 nm for all energies*
Dissociation Cross Section, σ	From Morgan *et al.*[131]

*Taken from average value in Powell *et al*.[163]

Appendix D: Inputs and Outputs from Energy Study

Run 1: 5keV Reaction-Rate Limited WF_6-tungsten pillar simulation output

```
=======  PRIMARY VARIABLES  ==========
Energy,keV = 5
Beam Current,nA = 9e-006
Beam Profile = GAUSSIAN
Local Pressure, Torr = 7
Initial Theta (gas coverage) = 0
Gas Boundary Source = OFF
Surface Diffusion of Gas = OFF
==========   SIM SETUP   ============
Pixels Ran = 200
Electrons per pixel = 10,000
Total # of electrons = 2,000,000
Beam Radius,nm = 1.5
System Size,nm = 13 X 13
Substrate Z = 74
Pillar Z = 74
# Cascades = 3
SEfac tuner = 0.9
SE1Boost tuner = 3  3  3
========= BSE EMISSIONS =============
Total nu IN THE SYSTEM  = 0.91424
Total nu OUT OF SYSTEM  = 0.037361
Total BSE yield ( nu )  = 0.95161
(Target nu (calculated) = 0.4553)
========== SE EMISSIONS  ============
SE1 yield IN THE SYSTEM    = 0.40456
SE1 yield OUT OF SYSTEM    = 0.00056
SE2 yield IN THE SYSTEM    = 0.14044
SE2 yield OUT OF SYSTEM    = 0.012474
Total SE1 yield IN & OUT   = 0.40512
Total SE2 yield IN & OUT   = 0.15291
Total delta IN THE SYSTEM  = 0.54499
Total delta OUT OF SYSTEM  = 0.013034
Total SE yield ( delta )   = 0.55803
======== RATIOS AND EFFICIENCY ======
Delta2/Delta1 Ratio = 0.37744
(Ratio Target = 1.3659 to 2.2765)
Efficiency (Beta) = 0.829
(Efficiency Target = 3 to 5)
=========   STATISTICS   =============
Total Atoms Deposited = 184496
Deposit Efficiency = 9.2248Percent
PE Atoms Deposited = 29,463
FSE Atoms Deposited = 60,785
BSE Atoms Deposited = 2,601
SE1 Atoms Deposited = 69,483
SE2 Atoms Deposited = 22,164
Structure Height = 168.25nm
Structure FWHM = 5.375nm
```

Run 2: 1keV Reaction-Rate Limited WF_6-tungsten pillar simulation output

```
=======  PRIMARY VARIABLES  ==========
Energy,keV = 1
Beam Current,nA = 9e-006
Beam Profile = GAUSSIAN
Local Pressure, Torr = 7
Initial Theta (gas coverage) = 0
Gas Boundary Source = OFF
Surface Diffusion of Gas = OFF
==========   SIM SETUP   ============
Pixels Ran = 200
Electrons per pixel = 10,000
Total # of electrons = 2,000,000
Beam Radius,nm = 1.5
System Size,nm = 13 X 13
Substrate Z = 74
Pillar Z = 74
# Cascades = 1
SEfac tuner = 0.85
SE1Boost tuner = 6  6  6
========= BSE EMISSIONS =============
Total nu IN THE SYSTEM  = 0.9591
Total nu OUT OF SYSTEM  = 0.001003
Total BSE yield ( nu )  = 0.96011
(Target nu (calculated) = 0.43305)
========== SE EMISSIONS  ============
SE1 yield IN THE SYSTEM    = 0.65521
SE1 yield OUT OF SYSTEM    = 0.0002475
SE2 yield IN THE SYSTEM    = 0.61111
SE2 yield OUT OF SYSTEM    = 0.003021
Total SE1 yield IN & OUT   = 0.65546
Total SE2 yield IN & OUT   = 0.61413
Total delta IN THE SYSTEM  = 1.2663
Total delta OUT OF SYSTEM  = 0.0032685
Total SE yield ( delta )   = 1.2696
======== RATIOS AND EFFICIENCY ======
Delta2/Delta1 Ratio = 0.93695
(Ratio Target = 1.2992 to 2.1653)
Efficiency (Beta) = 2.1636
(Efficiency Target = 3 to 5)
=========   STATISTICS   =============
Total Atoms Deposited = 491,440
Deposit Efficiency = 24.572Percent
PE Atoms Deposited = 88,376
FSE Atoms Deposited = 175,103
BSE Atoms Deposited = 32,806
SE1 Atoms Deposited = 110,726
SE2 Atoms Deposited = 84,429
Structure Height = 446.25nm
Structure FWHM = 5.7917nm
```

Run 2a: 1keV RRL WF_6-Tungsten (same as Run 2, but sampled at 750k electrons)

```
=======  PRIMARY VARIABLES  ==========
Energy,keV = 1
Beam Current,nA = 9e-006
Beam Profile = GAUSSIAN
Local Pressure, Torr = 7
Initial Theta (gas coverage) = 0
Gas Boundary Source = OFF
Surface Diffusion of Gas = OFF
==========   SIM SETUP   ============
Pixels Ran = 75
Electrons per pixel = 10,000
Total # of electrons (ran so far)= 750,000
Beam Radius,nm = 1.5
System Size,nm = 13 X 13
Substrate Z = 74
Pillar Z = 74
# Cascades = 1
SEfac tuner = 0.85
SE1Boost tuner = 6  6  6
========= BSE EMISSIONS =============
Total nu IN THE SYSTEM  = 0.9414
Total nu OUT OF SYSTEM  = 0.0023067
Total BSE yield ( nu )  = 0.94371
(Target nu (calculated) = 0.43305)
========== SE EMISSIONS  ============
SE1 yield IN THE SYSTEM    = 0.65649
SE1 yield OUT OF SYSTEM    = 0.0006
SE2 yield IN THE SYSTEM    = 0.6303
SE2 yield OUT OF SYSTEM    = 0.0071627
Total SE1 yield IN & OUT   = 0.65709
Total SE2 yield IN & OUT   = 0.63746
Total delta IN THE SYSTEM  = 1.2868
Total delta OUT OF SYSTEM  = 0.0077627
Total SE yield ( delta )   = 1.2945
======== RATIOS AND EFFICIENCY ======
Delta2/Delta1 Ratio = 0.97013
(Ratio Target = 1.2992 to 2.1653)
Efficiency (Beta) = 1.028
(Efficiency Target = 2 to 7)
=========   STATISTICS   =============
Total Atoms Deposited = 185707
Deposit Efficiency = 24.7609Percent
PE Atoms Deposited = 33218
FSE Atoms Deposited = 65191
BSE Atoms Deposited = 12895
SE1 Atoms Deposited = 41679
SE2 Atoms Deposited = 32724
Structure Height = 167.25nm
Structure FWHM = 5.3333nm
```

Appendix E: Inputs and Outputs from MTL vs. RRL Study

Run 2b: 1keV RRL WF_6-Tungsten (same as Run 2 but sampled at 50k electrons)

```
=======  PRIMARY VARIABLES  ==========
Energy,keV = 1
Beam Current,nA = 9e-006
Beam Profile = GAUSSIAN
Local Pressure, Torr = 7
Initial Theta (gas coverage) = 0
Gas Boundary Source = OFF
Surface Diffusion of Gas = OFF
==========   SIM SETUP   ============
Pixels Ran = 5
Electrons per pixel = 10,000
Total # of electrons (ran so far)= 50,000
Beam Radius,nm = 1.5
System Size,nm = 13 X 13
Substrate Z = 74
Pillar Z = 74
# Cascades = 1
SEfac tuner = 0.85
SE1Boost tuner = 6  6  6
========= BSE EMISSIONS =============
Total nu IN THE SYSTEM  = 0.70906
Total nu OUT OF SYSTEM  = 0.01592
Total BSE yield ( nu )  = 0.72498
(Target nu (calculated) = 0.43305)
========== SE EMISSIONS  ============
SE1 yield IN THE SYSTEM    = 0.63608
SE1 yield OUT OF SYSTEM    = 0.00562
SE2 yield IN THE SYSTEM    = 0.79466
SE2 yield OUT OF SYSTEM    = 0.05568
Total SE1 yield IN & OUT   = 0.6417
Total SE2 yield IN & OUT   = 0.85034
Total delta IN THE SYSTEM  = 1.4307
Total delta OUT OF SYSTEM  = 0.0613
Total SE yield ( delta )   = 1.492
======== RATIOS AND EFFICIENCY ======
Delta2/Delta1 Ratio = 1.3251
(Ratio Target = 1.2992 to 2.1653)
Efficiency (Beta) = 1.8278
(Efficiency Target = 2 to 7)
=========   STATISTICS   =============
Total Atoms Deposited = 12,415
Deposit Efficiency = 24.83Percent
PE Atoms Deposited = 2,136
FSE Atoms Deposited = 3,676
BSE Atoms Deposited = 1,208
SE1 Atoms Deposited = 2,680
SE2 Atoms Deposited = 2,715
Structure Height = 11.5nm
Structure FWHM = 4.8333nm
```

Run 3: 1keV Mass-Transport Limited WF_6-tungsten pillar simulation output

```
=======  PRIMARY VARIABLES  ==========
Energy,keV = 1
Beam Current,nA = 0.009
Beam Profile = GAUSSIAN
Local Pressure, Torr = 0.007
Initial Theta (gas coverage) = 0
Gas Boundary Source = OFF
Surface Diffusion of Gas = OFF
==========   SIM SETUP   ============
Pixels Ran = 200
Electrons per pixel = 10,000
Total # of electrons = 2,000,000
Beam Radius,nm = 1.5
System Size,nm = 13 X 13
Substrate Z = 74
Pillar Z = 74
# Cascades = 1
SEfac tuner = 0.85
SE1Boost tuner = 6  6  6
========= BSE EMISSIONS =============
Total nu IN THE SYSTEM  = 0.62518
Total nu OUT OF SYSTEM  = 0.0031515
Total BSE yield ( nu )  = 0.62833
(Target nu (calculated) = 0.43305)
========== SE EMISSIONS  ============
SE1 yield IN THE SYSTEM    = 0.60284
SE1 yield OUT OF SYSTEM    = 0.0048485
SE2 yield IN THE SYSTEM    = 0.96435
SE2 yield OUT OF SYSTEM    = 0.027398
Total SE1 yield IN & OUT   = 0.60769
Total SE2 yield IN & OUT   = 0.99175
Total delta IN THE SYSTEM  = 1.5672
Total delta OUT OF SYSTEM  = 0.032246
Total SE yield ( delta )   = 1.5994
======== RATIOS AND EFFICIENCY ======
Delta2/Delta1 Ratio = 1.632
(Ratio Target = 1.2992 to 2.1653)
Efficiency (Beta) = 3.7686
(Efficiency Target = 3 to 5)
=========   STATISTICS   =============
Total Atoms Deposited = 47097
Deposit Efficiency = 2.3548Percent
PE Atoms Deposited = 2922
FSE Atoms Deposited = 14294
BSE Atoms Deposited = 8264
SE1 Atoms Deposited = 4810
SE2 Atoms Deposited = 16807
Structure Height = 11.5nm
Structure FWHM = 9.7083nm
```

Appendix F: Inputs and Outputs from Surface Diffusion Study

Run 4: 1keV MTL Tungsten, With Monolayer Added

```
=======  PRIMARY VARIABLES  ==========
Energy,keV = 1
Beam Current,nA = 0.009
Beam Profile = GAUSSIAN
Local Pressure, Torr = 0.007
Initial Theta (gas coverage) = 1
Gas Boundary Source = OFF
Surface Diffusion of Gas = OFF
==========   SIM SETUP   ============
Pixels Ran = 200
Electrons per pixel = 10,000
Total # of electrons = 2,000,000
Beam Radius,nm = 1.5
System Size,nm = 13 X 13
Substrate Z = 74
Pillar Z = 74
# Cascades = 1
SEfac tuner = 0.85
SE1Boost tuner = 6  6  6
========= BSE EMISSIONS =============
Total nu IN THE SYSTEM  = 0.69472
Total nu OUT OF SYSTEM  = 0.0033535
Total BSE yield ( nu )  = 0.69807
(Target nu (calculated) = 0.43305)
========== SE EMISSIONS  ============
SE1 yield IN THE SYSTEM    = 0.63152
SE1 yield OUT OF SYSTEM    = 0.0029285
SE2 yield IN THE SYSTEM    = 0.93401
SE2 yield OUT OF SYSTEM    = 0.021396
Total SE1 yield IN & OUT   = 0.63445
Total SE2 yield IN & OUT   = 0.9554
Total delta IN THE SYSTEM  = 1.5655
Total delta OUT OF SYSTEM  = 0.024325
Total SE yield ( delta )   = 1.5899
======== RATIOS AND EFFICIENCY ======
Delta2/Delta1 Ratio = 1.5059
(Ratio Target = 1.2992 to 2.1653)
Efficiency (Beta) = 3.4774
(Efficiency Target = 3 to 5)
=========   STATISTICS   =============
Total Atoms Deposited = 49,129
Deposit Efficiency = 2.4564Percent
PE Atoms Deposited = 3,116
FSE Atoms Deposited = 16,106
BSE Atoms Deposited = 7,897
SE1 Atoms Deposited = 5,317
SE2 Atoms Deposited = 16,693
Structure Height = 13.5nm
Structure FWHM = 8.875nm
```

Run 5: 1keV MTL Tungsten, With Surface Diffusion Enabled

```
=======  PRIMARY VARIABLES  ==========
Energy,keV = 1
Beam Current,nA = 0.009
Beam Profile = GAUSSIAN
Local Pressure, Torr = 0.007
Initial Theta (gas coverage) = 0
Gas Boundary Source = OFF
Surface Diffusion of Gas = ON
Diffusion Coefficient, cm^2/s = 1e-009
==========   SIM SETUP   ============
Pixels Ran = 200
Electrons per pixel = 10,000
Total # of electrons = 2,000,000
Beam Radius,nm = 1.5
System Size,nm = 13 X 13
Substrate Z = 74
Pillar Z = 74
# Cascades = 1
SEfac tuner = 0.85
SE1Boost tuner = 6  6  6
========= BSE EMISSIONS =============
Total nu IN THE SYSTEM  = 0.87298
Total nu OUT OF SYSTEM  = 0.005346
Total BSE yield ( nu )  = 0.87833
(Target nu (calculated) = 0.43305)
========== SE EMISSIONS  ============
SE1 yield IN THE SYSTEM    = 0.66305
SE1 yield OUT OF SYSTEM    = 0.002259
SE2 yield IN THE SYSTEM    = 0.77413
SE2 yield OUT OF SYSTEM    = 0.017902
Total SE1 yield IN & OUT   = 0.66531
Total SE2 yield IN & OUT   = 0.79204
Total delta IN THE SYSTEM  = 1.4372
Total delta OUT OF SYSTEM  = 0.020161
Total SE yield ( delta )   = 1.4573
======== RATIOS AND EFFICIENCY ======
Delta2/Delta1 Ratio = 1.1905
(Ratio Target = 1.2992 to 2.1653)
Efficiency (Beta) = 2.749
(Efficiency Target = 3 to 5)
=========   STATISTICS   =============
Total Atoms Deposited = 96,120
Deposit Efficiency = 4.806Percent
PE Atoms Deposited = 14,861
FSE Atoms Deposited = 34,141
BSE Atoms Deposited = 8,128
SE1 Atoms Deposited = 19,066
SE2 Atoms Deposited = 19,924
Structure Height = 61.75nm
Structure FWHM = 5.9167nm
```

Run 6: 1keV MTL Tungsten, With Surface Diffusion and Boundary Source

```
=======  PRIMARY VARIABLES  ==========
Energy,keV = 1
Beam Current,nA = 0.009
Beam Profile = GAUSSIAN
Local Pressure, Torr = 0.007
Initial Theta (gas coverage) = 0
Gas Boundary Source = ON
Surface Diffusion of Gas = ON
Diffusion Coefficient, cm^2/s = 1e-009
==========   SIM SETUP   ============
Pixels Ran = 200
Electrons per pixel = 10,000
Total # of electrons = 2,000,000
Beam Radius,nm = 1.5
System Size,nm = 13 X 13
Substrate Z = 74
Pillar Z = 74
# Cascades = 1
SEfac tuner = 0.85
SE1Boost tuner = 6  6  6
========= BSE EMISSIONS =============
Total nu IN THE SYSTEM  = 0.93605
Total nu OUT OF SYSTEM  = 0.00119
Total BSE yield ( nu )  = 0.93724
(Target nu (calculated) = 0.43305)
========== SE EMISSIONS  ============
SE1 yield IN THE SYSTEM    = 0.66949
SE1 yield OUT OF SYSTEM    = 0.0003075
SE2 yield IN THE SYSTEM    = 0.74381
SE2 yield OUT OF SYSTEM    = 0.003588
Total SE1 yield IN & OUT   = 0.66979
Total SE2 yield IN & OUT   = 0.7474
Total delta IN THE SYSTEM  = 1.4133
Total delta OUT OF SYSTEM  = 0.0038955
Total SE yield ( delta )   = 1.4172
======== RATIOS AND EFFICIENCY ======
Delta2/Delta1 Ratio = 1.1159
(Ratio Target = 1.2992 to 2.1653)
Efficiency (Beta) = 2.5767
(Efficiency Target = 3 to 5)
=========   STATISTICS   =============
Total Atoms Deposited = 167,183
Deposit Efficiency = 8.3591Percent
PE Atoms Deposited = 26,746
FSE Atoms Deposited = 60,006
BSE Atoms Deposited = 13,374
SE1 Atoms Deposited = 33,432
SE2 Atoms Deposited = 33,625
Structure Height = 110.5nm
Structure FWHM = 6.25nm
```

Appendix G: Inputs and Outputs from TEOS Study

Run 1: 5keV Reaction-Rate-Limited TEOS-SiO_2 Pillar Simulation Output

```
=======  PRIMARY VARIABLES  ==========
Energy,keV = 5
Beam Current,nA = 9e-006
Beam Profile = GAUSSIAN
Local Pressure, Torr = 7
Initial Theta (gas coverage) = 0
Gas Boundary Source = OFF
Surface Diffusion of Gas = OFF
==========   SIM SETUP   ============
Pixels Ran = 200
Electrons per pixel = 10,000
Total # of electrons = 2,000,000
Beam Radius,nm = 1.5
System Size,nm = 19 X 19
Substrate Z = 10
Pillar Z = 10
# Cascades = 4
SEfac tuner = 1
SE1Boost tuner = 2  2  2
========= BSE EMISSIONS =============
Total nu IN THE SYSTEM  = 0.47222
Total nu OUT OF SYSTEM  = 0.4697
Total BSE yield ( nu )  = 0.94192
(Target nu (calculated) = 0.13972)
========== SE EMISSIONS  ============
SE1 yield IN THE SYSTEM    = 0.41257
SE1 yield OUT OF SYSTEM    = 0.000153
SE2 yield IN THE SYSTEM    = 0.47644
SE2 yield OUT OF SYSTEM    = 0.0016005
Total SE1 yield IN & OUT   = 0.41273
Total SE2 yield IN & OUT   = 0.47804
Total delta IN THE SYSTEM  = 0.88901
Total delta OUT OF SYSTEM  = 0.0017535
Total SE yield ( delta )   = 0.89077
======== RATIOS AND EFFICIENCY ======
Delta2/Delta1 Ratio = 1.1583
(Ratio Target = 0.41916 to 0.69861)
Efficiency (Beta) = 8.2898
(Efficiency Target = 3 to 5)
=========   STATISTICS   =============
Total Atoms Deposited = 387,119
Deposit Efficiency = 19.356Percent
PE Atoms Deposited = 84,707
FSE Atoms Deposited = 77,935
BSE Atoms Deposited = 16
SE1 Atoms Deposited = 102,384
SE2 Atoms Deposited = 122,077
Structure Height = 903.24nm
Structure FWHM = 5.94nm
```

Run 2: 1keV Reaction-Rate-Limited TEOS-SiO_2 Pillar Simulation Output

```
=======  PRIMARY VARIABLES  ==========
Energy,keV = 1
Beam Current,nA = 9e-006
Beam Profile = GAUSSIAN
Local Pressure, Torr = 7
Initial Theta (gas coverage) = 0
Gas Boundary Source = OFF
Surface Diffusion of Gas = OFF
==========   SIM SETUP   ============
Pixels Ran = 200
Electrons per pixel = 10,000
Total # of electrons = 2,000,000
Beam Radius,nm = 1.5
System Size,nm = 19 X 19
Substrate Z = 10
Pillar Z = 10
# Cascades = 4
SEfac tuner = 1
SE1Boost tuner = 2  2  2
========= BSE EMISSIONS =============
Total nu IN THE SYSTEM  = 0.98723
Total nu OUT OF SYSTEM  = 0.002241
Total BSE yield ( nu )  = 0.98947
(Target nu (calculated) = 0.17876)
========== SE EMISSIONS  ============
SE1 yield IN THE SYSTEM    = 0.4296
SE1 yield OUT OF SYSTEM    = 2.35e-005
SE2 yield IN THE SYSTEM    = 0.83158
SE2 yield OUT OF SYSTEM    = 0.004882
Total SE1 yield IN & OUT   = 0.42963
Total SE2 yield IN & OUT   = 0.83647
Total delta IN THE SYSTEM  = 1.2612
Total delta OUT OF SYSTEM  = 0.0049055
Total SE yield ( delta )   = 1.2661
======== RATIOS AND EFFICIENCY ======
Delta2/Delta1 Ratio = 1.947
(Ratio Target = 0.53627 to 0.89378)
Efficiency (Beta) = 10.8918
(Efficiency Target = 3 to 5)
=========   STATISTICS   =============
Total Atoms Deposited = 1,220,599
Deposit Efficiency = 61.0299Percent
PE Atoms Deposited = 261,296
FSE Atoms Deposited = 621,437
BSE Atoms Deposited = 6,312
SE1 Atoms Deposited = 108,236
SE2 Atoms Deposited = 223,318
Structure Height = 2,465.64nm
Structure FWHM = 6.3nm
```

Run 3: 1keV Mass Transport-Limited TEOS-SiO_2 Pillar Simulation Output

```
=======  PRIMARY VARIABLES  ==========
Energy,keV = 1
Beam Current,nA = 0.009
Beam Profile = GAUSSIAN
Local Pressure, Torr = 0.007
Initial Theta (gas coverage) = 0
Gas Boundary Source = OFF
Surface Diffusion of Gas = OFF
==========   SIM SETUP   ============
Pixels Ran = 200
Electrons per pixel = 10,000
Total # of electrons = 2,000,000
Beam Radius,nm = 1.5
System Size,nm = 39 X 39
Substrate Z = 10
Pillar Z = 10
# Cascades = 4
SEfac tuner = 1
SE1Boost tuner = 2  2  2
========= BSE EMISSIONS =============
Total nu IN THE SYSTEM  = 0.31684
Total nu OUT OF SYSTEM  = 0.11259
Total BSE yield ( nu )  = 0.42943
(Target nu (calculated) = 0.17876)
========== SE EMISSIONS  ============
SE1 yield IN THE SYSTEM    = 0.43091
SE1 yield OUT OF SYSTEM    = 1.55e-005
SE2 yield IN THE SYSTEM    = 1.1916
SE2 yield OUT OF SYSTEM    = 0.18514
Total SE1 yield IN & OUT   = 0.43093
Total SE2 yield IN & OUT   = 1.3767
Total delta IN THE SYSTEM  = 1.6225
Total delta OUT OF SYSTEM  = 0.18515
Total SE yield ( delta )   = 1.8076
======== RATIOS AND EFFICIENCY ======
Delta2/Delta1 Ratio = 3.1948
(Ratio Target = 0.53627 to 0.89378)
Efficiency (Beta) = 7.4395
(Efficiency Target = 2 to 7)
=========   STATISTICS   =============
Total Atoms Deposited = 268,176
Deposit Efficiency = 13.4088Percent
PE Atoms Deposited = 7,438
FSE Atoms Deposited = 89,565
BSE Atoms Deposited = 18,052
SE1 Atoms Deposited = 11,508
SE2 Atoms Deposited = 141,613
Structure Height = 38.88nm
Structure FWHM = 17.82nm
```

Run 4: 1keV Mass Transport-Limited TEOS-SiO_2 With Initial Monolayer

```
=======  PRIMARY VARIABLES  ==========
Energy,keV = 1
Beam Current,nA = 0.009
Beam Profile = GAUSSIAN
Local Pressure, Torr = 0.007
Initial Theta (gas coverage) = 1
Gas Boundary Source = OFF
Surface Diffusion of Gas = OFF
==========   SIM SETUP   ============
Pixels Ran = 200
Electrons per pixel = 10,000
Total # of electrons = 2,000,000
Beam Radius,nm = 1.5
System Size,nm = 39 X 39
Substrate Z = 10
Pillar Z = 10
# Cascades = 4
SEfac tuner = 1
SE1Boost tuner = 2  2  2
========= BSE EMISSIONS =============
Total nu IN THE SYSTEM  = 0.35872
Total nu OUT OF SYSTEM  = 0.10793
Total BSE yield ( nu )  = 0.46665
(Target nu (calculated) = 0.17876)
========== SE EMISSIONS  ============
SE1 yield IN THE SYSTEM    = 0.43415
SE1 yield OUT OF SYSTEM    = 2.95e-005
SE2 yield IN THE SYSTEM    = 1.2656
SE2 yield OUT OF SYSTEM    = 0.18043
Total SE1 yield IN & OUT   = 0.43418
Total SE2 yield IN & OUT   = 1.4461
Total delta IN THE SYSTEM  = 1.6998
Total delta OUT OF SYSTEM  = 0.18046
Total SE yield ( delta )   = 1.8803
======== RATIOS AND EFFICIENCY ======
Delta2/Delta1 Ratio = 3.3306
(Ratio Target = 0.53627 to 0.89378)
Efficiency (Beta) = 18.632
(Efficiency Target = 3 to 5)
=========   STATISTICS   =============
Total Atoms Deposited = 291,370
Deposit Efficiency = 14.5685Percent
PE Atoms Deposited = 7,599
FSE Atoms Deposited = 105,982
BSE Atoms Deposited = 18,034
SE1 Atoms Deposited = 11,211
SE2 Atoms Deposited = 148,544
Structure Height = 41.04nm
Structure FWHM = 18.36nm
```

Run 5: 1keV Mass Transport-Limited TEOS-SiO_2 With Surface Diffusion Enabled

```
=======  PRIMARY VARIABLES  ==========
Energy,keV = 1
Beam Current,nA = 0.009
Beam Profile = GAUSSIAN
Local Pressure, Torr = 0.007
Initial Theta (gas coverage) = 0
Gas Boundary Source = OFF
Surface Diffusion of Gas = ON
Diffusion Coefficient, cm^2/s = 1e-009
==========   SIM SETUP   ============
Pixels Ran = 200
Electrons per pixel = 10,000
Total # of electrons = 2,000,000
Beam Radius,nm = 1.5
System Size,nm = 39 X 39
Substrate Z = 10
Pillar Z = 10
# Cascades = 4
SEfac tuner = 1
SE1Boost tuner = 2  2  2
========= BSE EMISSIONS =============
Total nu IN THE SYSTEM  = 0.74625
Total nu OUT OF SYSTEM  = 0.04096
Total BSE yield ( nu )  = 0.78721
(Target nu (calculated) = 0.17876)
========== SE EMISSIONS  ============
SE1 yield IN THE SYSTEM    = 0.43772
SE1 yield OUT OF SYSTEM    = 6.85e-005
SE2 yield IN THE SYSTEM    = 1.4023
SE2 yield OUT OF SYSTEM    = 0.084117
Total SE1 yield IN & OUT   = 0.43779
Total SE2 yield IN & OUT   = 1.4864
Total delta IN THE SYSTEM  = 1.84
Total delta OUT OF SYSTEM  = 0.084186
Total SE yield ( delta )   = 1.9242
======== RATIOS AND EFFICIENCY ======
Delta2/Delta1 Ratio = 3.3952
(Ratio Target = 0.53627 to 0.89378)
Efficiency (Beta) = 18.9936
(Efficiency Target = 3 to 5)
=========   STATISTICS   =============
Total Atoms Deposited = 355,405
Deposit Efficiency = 17.7703Percent
PE Atoms Deposited = 19,453
FSE Atoms Deposited = 193,426
BSE Atoms Deposited = 8,957
SE1 Atoms Deposited = 10,343
SE2 Atoms Deposited = 123,226
Structure Height = 101.52nm
Structure FWHM = 15.72nm
```

Run 6: 1keV MTL TEOS-SiO_2 With Surface Diffusion and Boundary Source

```
=======  PRIMARY VARIABLES  ==========
Energy,keV = 1
Beam Current,nA = 0.009
Beam Profile = GAUSSIAN
Local Pressure, Torr = 0.007
Initial Theta (gas coverage) = 0
Gas Boundary Source = ON
Surface Diffusion of Gas = ON
Diffusion Coefficient, cm^2/s = 1e-009
==========   SIM SETUP   ============
Pixels Ran = 200
Electrons per pixel = 10,000
Total # of electrons = 2,000,000
Beam Radius,nm = 1.5
System Size,nm = 39 X 39
Substrate Z = 10
Pillar Z = 10
# Cascades = 4
SEfac tuner = 1
SE1Boost tuner = 2  2  2
========= BSE EMISSIONS =============
Total nu IN THE SYSTEM  = 0.82033
Total nu OUT OF SYSTEM  = 0.030293
Total BSE yield ( nu )  = 0.85062
(Target nu (calculated) = 0.17876)
========== SE EMISSIONS  ============
SE1 yield IN THE SYSTEM    = 0.43827
SE1 yield OUT OF SYSTEM    = 4.25e-005
SE2 yield IN THE SYSTEM    = 1.4238
SE2 yield OUT OF SYSTEM    = 0.063893
Total SE1 yield IN & OUT   = 0.43832
Total SE2 yield IN & OUT   = 1.4877
Total delta IN THE SYSTEM  = 1.8621
Total delta OUT OF SYSTEM  = 0.063935
Total SE yield ( delta )   = 1.926
======== RATIOS AND EFFICIENCY ======
Delta2/Delta1 Ratio = 3.3942
(Ratio Target = 0.53627 to 0.89378)
Efficiency (Beta) = 18.9878
(Efficiency Target = 3 to 5)
=========   STATISTICS   =============
Total Atoms Deposited = 405,773
Deposit Efficiency = 20.2887Percent
PE Atoms Deposited = 20,211
FSE Atoms Deposited = 222,653
BSE Atoms Deposited = 10,728
SE1 Atoms Deposited = 10,816
SE2 Atoms Deposited = 141,365
Structure Height = 103.68nm
Structure FWHM = 16.5nm
```

Appendix H: Raster Run Results

Run 1: 1keV MTL WF_6-Tungsten 3x3 Adjacent Pixels, 1ML after each frame.

```
=======  PRIMARY VARIABLES  ==========
Energy,keV = 1
Beam Current,nA = 0.009
Beam Profile = GAUSSIAN
Local Pressure, Torr = 0.007
Initial Theta (gas coverage) = 1
Gas Boundary Source = OFF
Surface Diffusion of Gas = OFF
==========   SIM SETUP   ============
Pixels Ran = 17,856; Electrons per pixel = 56
Total # of electrons = 999,936
Beam Radius,nm = 1.5
System Size,nm = 19 X 19
Substrate Z = 74; Pillar Z = 74
SEfac tuner = 0.85; # Cascades = 1
SE1Boost tuner = 6  6  6
=========   RASTER SETUP   ==========
Frames Ran = 1,985
Raster Size: 3x3
Pixel Spacing, nm = 3
Pixel Dwell Time, us = 1
Line Refresh Time, us = 0
Frame Refresh Time, us = 1000
Quick Monolayer after frame =1
========= BSE EMISSIONS =============
Total nu IN THE SYSTEM  = 0.6709
Total nu OUT OF SYSTEM  = 0.0027582
Total BSE yield ( nu )  = 0.67366 (Target nu (calculated) = 0.43305)
========== SE EMISSIONS  ============
SE1 yield IN THE SYSTEM    = 0.58673
SE1 yield OUT OF SYSTEM    = 0.00035802
SE2 yield IN THE SYSTEM    = 0.89964
SE2 yield OUT OF SYSTEM    = 0.0074445
Total SE1 yield IN & OUT   = 0.58709
Total SE2 yield IN & OUT   = 0.90708
Total delta IN THE SYSTEM  = 1.4864
Total delta OUT OF SYSTEM  = 0.0078025
Total SE yield ( delta )   = 1.4942
======== RATIOS AND EFFICIENCY ======
Delta2/Delta1 Ratio = 1.545 (Ratio Target = 1.2992 to 2.1653)
Efficiency (Beta) = 3.5678 (Efficiency Target = 3 to 5)
=========   STATISTICS   =============
Total Atoms Deposited = 240,432
Deposit Efficiency = 24.0447Percent
PE Atoms Deposited = 43,692
FSE Atoms Deposited = 66,194
BSE Atoms Deposited = 27,046
SE1 Atoms Deposited = 49,809
SE2 Atoms Deposited = 53,691
Structure Height = 36.5nm
Structure FWHM = 11.7917nm
```

Run 2: 1keV MTL WF_6-Tungsten 3x3 Adjacent Pixels, No ML after each frame.

```
=======  PRIMARY VARIABLES  ==========
Energy,keV = 1
Beam Current,nA = 0.009
Beam Profile = GAUSSIAN
Local Pressure, Torr = 0.007
Initial Theta (gas coverage) = 0
Gas Boundary Source = OFF
Surface Diffusion of Gas = OFF
==========   SIM SETUP   ============
Pixels Ran = 17,856
Electrons per pixel = 56
Total # of electrons = 999,936
Beam Radius,nm = 1.5
System Size,nm = 19 X 19
Substrate Z = 74; Pillar Z = 74
SEfac tuner = 0.85; # Cascades = 1
SE1Boost tuner = 6  6  6
=========   RASTER SETUP   ==========
Frames Ran = 1985
Raster Size: 3x3
Pixel Spacing, nm = 3
Pixel Dwell Time, us = 1
Line Refresh Time, us = 0
Frame Refresh Time, us = 1000
Quick Monolayer after frame = NO
========= BSE EMISSIONS =============
Total nu IN THE SYSTEM  = 0.46352
Total nu OUT OF SYSTEM  = 0.0019041
Total BSE yield ( nu )  = 0.46543; (Target nu (calculated) = 0.43305)
========== SE EMISSIONS  ============
SE1 yield IN THE SYSTEM    = 0.55116
SE1 yield OUT OF SYSTEM    = 0.00061004
SE2 yield IN THE SYSTEM    = 0.88581
SE2 yield OUT OF SYSTEM    = 0.012073
Total SE1 yield IN & OUT   = 0.55177
Total SE2 yield IN & OUT   = 0.89788
Total delta IN THE SYSTEM  = 1.437
Total delta OUT OF SYSTEM  = 0.012683
Total SE yield ( delta )   = 1.4497
======== RATIOS AND EFFICIENCY ======
Delta2/Delta1 Ratio = 1.6273; (Ratio Target = 1.2992 to 2.1653)
Efficiency (Beta) = 3.7577; (Efficiency Target = 3 to 5)
=========   STATISTICS   =============
Total Atoms Deposited = 35,231
Deposit Efficiency = 3.5233Percent
PE Atoms Deposited = 4,983
FSE Atoms Deposited = 7,634
BSE Atoms Deposited = 6,000
SE1 Atoms Deposited = 6,140
SE2 Atoms Deposited = 10,474
Structure Height = 5nm
Structure FWHM = 12nm
```

Run 3: 1keV MTL WF_6-Tungsten 3x3, 2 FWHM Pixels, ML after each frame.

```
=======  PRIMARY VARIABLES  ==========
Energy,keV = 1
Beam Current,nA = 0.009
Beam Profile = GAUSSIAN
Local Pressure, Torr = 0.007
Initial Theta (gas coverage) = 1
Gas Boundary Source = OFF
Surface Diffusion of Gas = OFF
==========   SIM SETUP   ============
Pixels Ran = 17,856
Electrons per pixel = 56
Total # of electrons = 999,936
Beam Radius,nm = 1.5
System Size,nm = 25 X 25
Substrate Z = 74; Pillar Z = 74
SEfac tuner = 0.85; # Cascades = 1
SE1Boost tuner = 6  6  6
=========   RASTER SETUP   ==========
Frames Ran = 1985
Raster Size = 3x3
Pixel Spacing, nm = 6
Pixel Dwell Time, us = 1
Line Refresh Time, us = 0
Frame Refresh Time, us = 1000
Quick Monolayer after frame =1
========= BSE EMISSIONS =============
Total nu IN THE SYSTEM  = 0.70718
Total nu OUT OF SYSTEM  = 0.0046103
Total BSE yield ( nu )  = 0.71179; (Target nu (calculated) = 0.43305)
========== SE EMISSIONS  ============
SE1 yield IN THE SYSTEM    = 0.66591
SE1 yield OUT OF SYSTEM    = 0.00058604
SE2 yield IN THE SYSTEM    = 1.1404
SE2 yield OUT OF SYSTEM    = 0.011589
Total SE1 yield IN & OUT   = 0.6665
Total SE2 yield IN & OUT   = 1.152
Total delta IN THE SYSTEM  = 1.8063
Total delta OUT OF SYSTEM  = 0.012175
Total SE yield ( delta )   = 1.8185
======== RATIOS AND EFFICIENCY ======
Delta2/Delta1 Ratio = 1.7284; (Ratio Target = 1.2992 to 2.1653)
Efficiency (Beta) = 3.9912; (Efficiency Target = 3 to 5)
=========   STATISTICS   =============
Total Atoms Deposited = 353,967
Deposit Efficiency = 35.399Percent
PE Atoms Deposited = 43,722
FSE Atoms Deposited = 132,304
BSE Atoms Deposited = 40,004
SE1 Atoms Deposited = 57,095
SE2 Atoms Deposited = 80,842
Structure Height = 28.25nm
Structure FWHM = 17.5833nm
```

Run 4: 1keV MTL WF_6-Tungsten 3x3, ½ FWHM Pixels, ML after each frame.

```
=======  PRIMARY VARIABLES  ==========
Energy,keV = 1
Beam Current,nA = 0.009
Beam Profile = GAUSSIAN
Local Pressure, Torr = 0.007
Initial Theta (gas coverage) = 1
Gas Boundary Source = OFF
Surface Diffusion of Gas = OFF
==========   SIM SETUP   ============
Pixels Ran = 17,856
Electrons per pixel = 56
Total # of electrons = 999,936
Beam Radius,nm = 1.5
System Size,nm = 13 X 13
Substrate Z = 74; Pillar Z = 74
SEfac tuner = 0.85; # Cascades = 1
SE1Boost tuner = 6  6  6
=========   RASTER SETUP   ==========
Frames Ran = 1985
Raster Size = 3x3
Pixel Spacing, nm = 1.5
Pixel Dwell Time, us = 1
Line Refresh Time, us = 0
Frame Refresh Time, us = 1000
Quick Monolayer after frame =1
========= BSE EMISSIONS =============
Total nu IN THE SYSTEM  = 0.84061
Total nu OUT OF SYSTEM  = 0.0031732
Total BSE yield ( nu )  = 0.84378; (Target nu (calculated) = 0.43305)
========== SE EMISSIONS  ============
SE1 yield IN THE SYSTEM    = 0.61622
SE1 yield OUT OF SYSTEM    = 0.00056904
SE2 yield IN THE SYSTEM    = 0.80423
SE2 yield OUT OF SYSTEM    = 0.0085115
Total SE1 yield IN & OUT   = 0.61679
Total SE2 yield IN & OUT   = 0.81274
Total delta IN THE SYSTEM  = 1.4205
Total delta OUT OF SYSTEM  = 0.0090806
Total SE yield ( delta )   = 1.4295
======== RATIOS AND EFFICIENCY ======
Delta2/Delta1 Ratio = 1.3177; (Ratio Target = 1.2992 to 2.1653)
Efficiency (Beta) = 3.0428; (Efficiency Target = 3 to 5)
=========   STATISTICS   =============
Total Atoms Deposited = 242,731
Deposit Efficiency = 24.2747Percent
PE Atoms Deposited = 43,196
FSE Atoms Deposited = 77,049
BSE Atoms Deposited = 21,700
SE1 Atoms Deposited = 51,212
SE2 Atoms Deposited = 49,574
Structure Height = 92nm
Structure FWHM = 8.2083nm
```

Appendix I: Via Simulation Results

Run 1: 1keV MTL WF_6-Tungsten 3x3, No Overlap, No Gradient

```
=======  PRIMARY VARIABLES  ==========
Energy,keV = 1
Beam Current,nA = 0.009
Beam Profile = GAUSSIAN
Local Pressure, Torr = 0.007
Initial Theta (gas coverage) = 1
Gas Boundary Source = OFF
Surface Diffusion of Gas = OFF
==========   SIM SETUP   ============
Pixels Ran = 200
Electrons per pixel = 56
Total # of electrons (ran so far)= 11,200
Beam Radius,nm = 1.5
System Size,nm = 25 X 25
Substrate Z = 74; Pillar Z = 74
SEfac tuner = 0.85; # Cascades = 1
SE1Boost tuner = 6  6  6
=========   RASTER SETUP   ==========
Frames Ran = 896
Raster Size = 3x3
Via Size = 10x10nm
Pixel Spacing, nm = 3
Pixel Dwell Time, us = 1
Line Refresh Time, us = 0
Frame Refresh Time, us = 1000
Quick Monolayer after frame =1
========= BSE EMISSIONS =============
Total nu IN THE SYSTEM  = 0.22473
Total nu OUT OF SYSTEM  = 0.0023052
Total BSE yield ( nu )  = 0.22704; (Target nu (calculated) = 0.43305)
========== SE EMISSIONS  ============
SE1 yield IN THE SYSTEM    = 0.56924
SE1 yield OUT OF SYSTEM    = 4.4289e-006
SE2 yield IN THE SYSTEM    = 1.1368
SE2 yield OUT OF SYSTEM    = 0.00025909
Total SE1 yield IN & OUT   = 0.56925
Total SE2 yield IN & OUT   = 1.1371
Total delta IN THE SYSTEM  = 1.7061
Total delta OUT OF SYSTEM  = 0.00026352
Total SE yield ( delta )   = 1.7063
======== RATIOS AND EFFICIENCY ======
Delta2/Delta1 Ratio = 1.9975; (Ratio Target = 1.2992 to 2.1653)
Efficiency (Beta) = 8.7982; (Efficiency Target = 2 to 7)
=========   STATISTICS   =============
Total Atoms Deposited = 166,227
Deposit Efficiency = 36.8098Percent
PE Atoms Deposited = 19,717
FSE Atoms Deposited = 57,931
BSE Atoms Deposited = 27,368
SE1 Atoms Deposited = 23,535
SE2 Atoms Deposited = 37,676
```

Run 2: 1keV MTL WF_6-Tungsten 4x4, Overlapped Aperture, No Gradient

```
=======  PRIMARY VARIABLES  ==========
Energy,keV = 1
Beam Current,nA = 0.009
Beam Profile = GAUSSIAN
Local Pressure, Torr = 0.007
Initial Theta (gas coverage) = 1
Gas Boundary Source = OFF
Surface Diffusion of Gas = OFF
==========   SIM SETUP   ============
Pixels Ran = 200
Electrons per pixel = 56
Total # of electrons (ran so far)= 11,200
Beam Radius,nm = 1.5
System Size,nm = 25 X 25
Substrate Z = 74; Pillar Z = 74
SEfac tuner = 0.85; # Cascades = 1
SE1Boost tuner = 6  6  6
=========   RASTER SETUP   ==========
Frames Ran = 603
Raster Size = 4x4
Via Size = 10x10nm
Pixel Spacing, nm = 3
Pixel Dwell Time, us = 1
Line Refresh Time, us = 0
Frame Refresh Time, us = 1000
Quick Monolayer after frame =1
========= BSE EMISSIONS =============
Total nu IN THE SYSTEM  = 0.4125
Total nu OUT OF SYSTEM  = 0.0087879
Total BSE yield ( nu )  = 0.42129; (Target nu (calculated) = 0.43305)
========== SE EMISSIONS  ============
SE1 yield IN THE SYSTEM    = 0.58895
SE1 yield OUT OF SYSTEM    = 3.7017e-006
SE2 yield IN THE SYSTEM    = 1.1339
SE2 yield OUT OF SYSTEM    = 0.00016843
Total SE1 yield IN & OUT   = 0.58896
Total SE2 yield IN & OUT   = 1.1341
Total delta IN THE SYSTEM  = 1.7229
Total delta OUT OF SYSTEM  = 0.00017213
Total SE yield ( delta )   = 1.723
======== RATIOS AND EFFICIENCY ======
Delta2/Delta1 Ratio = 1.9256; (Ratio Target = 1.2992 to 2.1653)
Efficiency (Beta) = 4.5707; (Efficiency Target = 2 to 7)
=========   STATISTICS   =============
Total Atoms Deposited = 175,356
Deposit Efficiency = 32.456Percent
PE Atoms Deposited = 23,421
FSE Atoms Deposited = 58,211
BSE Atoms Deposited = 25,150
SE1 Atoms Deposited = 27,605
SE2 Atoms Deposited = 40,969
```

Run 3: 1keV MTL WF_6-Tungsten 3x3, No overlap, Linear Gradient

```
=======  PRIMARY VARIABLES  ==========
Energy,keV = 1
Beam Current,nA = 0.009
Beam Profile = GAUSSIAN
Local Pressure, Torr = 0.007
Initial Theta (gas coverage) = 0
Gas Boundary Source = OFF
Surface Diffusion of Gas = OFF
==========   SIM SETUP   ============
Pixels Ran = 8,208
Electrons per pixel = 56
Total # of electrons (ran so far)= 459,648
Beam Radius,nm = 1.5
System Size,nm = 20 X 20
Substrate Z = 74; Pillar Z = 74
SEfac tuner = 0.85; # Cascades = 1
SE1Boost tuner = 6  6  6
=========   RASTER SETUP   ==========
Frames Ran = 912
Raster Size = 3x3
Via Size = 10x10nm
Pixel Spacing, nm = 3
Pixel Dwell Time, us = 1
Line Refresh Time, us = 0
Frame Refresh Time, us = 1000
Quick Monolayer after frame =1
========= BSE EMISSIONS =============
Total nu IN THE SYSTEM  = 0.20054
Total nu OUT OF SYSTEM  = 0.020139
Total BSE yield ( nu )  = 0.22068; (Target nu (calculated) = 0.43305)
========== SE EMISSIONS  ============
SE1 yield IN THE SYSTEM    = 0.56765
SE1 yield OUT OF SYSTEM    = 0.00010878
SE2 yield IN THE SYSTEM    = 1.2129
SE2 yield OUT OF SYSTEM    = 0.0052301
Total SE1 yield IN & OUT   = 0.56776
Total SE2 yield IN & OUT   = 1.2181
Total delta IN THE SYSTEM  = 1.7805
Total delta OUT OF SYSTEM  = 0.0053389
Total SE yield ( delta )   = 1.7859
======== RATIOS AND EFFICIENCY ======
Delta2/Delta1 Ratio = 2.1455; (Ratio Target = 1.2992 to 2.1653)
Efficiency (Beta) = 9.7221; (Efficiency Target = 2 to 7)
=========   STATISTICS   =============
Total Atoms Deposited = 96,039
Deposit Efficiency = 20.894Percent
PE Atoms Deposited = 11,207
FSE Atoms Deposited = 33,532
BSE Atoms Deposited = 15,767
SE1 Atoms Deposited = 13,493
SE2 Atoms Deposited = 22,040
```

Run 4: 1keV MTL WF_6-Tungsten 2x2, No overlap, Linear Gradient

```
=======  PRIMARY VARIABLES  ==========
Energy,keV = 1
Beam Current,nA = 0.009
Beam Profile = GAUSSIAN
Local Pressure, Torr = 0.007
Initial Theta (gas coverage) = 0
Gas Boundary Source = OFF
Surface Diffusion of Gas = OFF
==========   SIM SETUP   ============
Pixels Ran = 8,208
Electrons per pixel = 56
Total # of electrons (ran so far)= 459,648
Beam Radius,nm = 1.5
System Size,nm = 20 X 20
Substrate Z = 74; Pillar Z = 74
SEfac tuner = 0.85; # Cascades = 1
SE1Boost tuner = 6  6  6
=========   RASTER SETUP   ==========
Frames Ran = 2,464
Raster Size = 2x2
Via Size = 10x10nm
Pixel Spacing, nm = 3
Pixel Dwell Time, us = 1
Line Refresh Time, us = 0
Frame Refresh Time, us = 1000
Quick Monolayer after frame =1
========= BSE EMISSIONS =============
Total nu IN THE SYSTEM  = 0.15814
Total nu OUT OF SYSTEM  = 0.018053
Total BSE yield ( nu )  = 0.17619; (Target nu (calculated) = 0.43305)
========== SE EMISSIONS  ============
SE1 yield IN THE SYSTEM    = 0.58764
SE1 yield OUT OF SYSTEM    = 2.7177e-005
SE2 yield IN THE SYSTEM    = 1.3858
SE2 yield OUT OF SYSTEM    = 0.0033971
Total SE1 yield IN & OUT   = 0.58766
Total SE2 yield IN & OUT   = 1.3892
Total delta IN THE SYSTEM  = 1.9734
Total delta OUT OF SYSTEM  = 0.0034243
Total SE yield ( delta )   = 1.9769
======== RATIOS AND EFFICIENCY ======
Delta2/Delta1 Ratio = 2.3639; (Ratio Target = 1.2992 to 2.1653)
Efficiency (Beta) = 13.417; (Efficiency Target = 2 to 7)
=========   STATISTICS   =============
Total Atoms Deposited = 133,148
Deposit Efficiency = 24.1238Percent
PE Atoms Deposited = 13,857
FSE Atoms Deposited = 46,968
BSE Atoms Deposited = 23,908
SE1 Atoms Deposited = 16,781
SE2 Atoms Deposited = 31,634
```

Appendix J: Volcano Run Results

Run 1: 1keV WF_6-Tungsten, Gas walks ½ across beam radius (2.5nm)

```
=======  PRIMARY VARIABLES  ==========
Energy,keV = 1
Beam Current,nA = 0.03
Beam Profile = SQUARE
Local Pressure, Torr = 0
Initial Theta (gas coverage) = 0
Gas Boundary Source = ON
Surface Diffusion of Gas = ON
Diffusion Coefficient, cm^2/s = 1.1653e-010
==========   SIM SETUP   ============
Pixels Ran = 77
Electrons per pixel = 10,000
Total # of electrons (ran so far)= 770,000
Beam Radius,nm = 5
System Size,nm = 20 X 20
Substrate Z = 74; Pillar Z = 74
SEfac tuner = 0.85; # Cascades = 1
SE1Boost tuner = 6  6  6
========= BSE EMISSIONS =============
Total nu IN THE SYSTEM  = 0.4562
Total nu OUT OF SYSTEM  = 0.0020098
Total BSE yield ( nu )  = 0.45821
(Target nu (calculated) = 0.43305)
========== SE EMISSIONS  ============
SE1 yield IN THE SYSTEM    = 0.55964
SE1 yield OUT OF SYSTEM    = 0.011308
SE2 yield IN THE SYSTEM    = 0.92072
SE2 yield OUT OF SYSTEM    = 0.032242
Total SE1 yield IN & OUT   = 0.57095
Total SE2 yield IN & OUT   = 0.95296
Total delta IN THE SYSTEM  = 1.4804
Total delta OUT OF SYSTEM  = 0.043549
Total SE yield ( delta )   = 1.5239
======== RATIOS AND EFFICIENCY ======
Delta2/Delta1 Ratio = 1.6691
(Ratio Target = 1.2992 to 2.1653)
Efficiency (Beta) = 3.6426
(Efficiency Target = 2 to 7)
=========   STATISTICS   =============
Total Atoms Deposited = 33,216
Deposit Efficiency = 4.2876Percent
PE Atoms Deposited = 4,004
FSE Atoms Deposited = 7,695
BSE Atoms Deposited = 5,928
SE1 Atoms Deposited = 4,911
SE2 Atoms Deposited = 10,678
Structure Height = 6.5nm
Structure FWHM = 12.625nm
```

Run 2: 1keV WF_6-Tungsten, Gas walks to center of beam (5nm)

```
=======  PRIMARY VARIABLES  ==========
Energy,keV = 1
Beam Current,nA = 0.03
Beam Profile = SQUARE
Local Pressure, Torr = 7e-030
Initial Theta (gas coverage) = 0
Gas Boundary Source = ON
Surface Diffusion of Gas = ON
Diffusion Coefficient, cm^2/s = 4.6614e-010
==========   SIM SETUP   ============
Pixels Ran = 56
Electrons per pixel = 10,000
Total # of electrons (ran so far)= 560,000
Beam Radius,nm = 5
System Size,nm = 20 X 20
Substrate Z = 74
Pillar Z = 74
# Cascades = 1
SEfac tuner = 0.85
SE1Boost tuner = 6  6  6
========= BSE EMISSIONS =============
Total nu IN THE SYSTEM  = 0.5548
Total nu OUT OF SYSTEM  = 0.0039886
Total BSE yield ( nu )  = 0.55879
(Target nu (calculated) = 0.43305)
========== SE EMISSIONS  ============
SE1 yield IN THE SYSTEM    = 0.58936
SE1 yield OUT OF SYSTEM    = 0.0057484
SE2 yield IN THE SYSTEM    = 1.0873
SE2 yield OUT OF SYSTEM    = 0.024321
Total SE1 yield IN & OUT   = 0.59511
Total SE2 yield IN & OUT   = 1.1116
Total delta IN THE SYSTEM  = 1.6767
Total delta OUT OF SYSTEM  = 0.03007
Total SE yield ( delta )   = 1.7067
======== RATIOS AND EFFICIENCY ======
Delta2/Delta1 Ratio = 1.8679
(Ratio Target = 1.2992 to 2.1653)
Efficiency (Beta) = 3.3428
(Efficiency Target = 2 to 7)
=========   STATISTICS   =============
Total Atoms Deposited = 58,426
Deposit Efficiency = 10.3023Percent
PE Atoms Deposited = 9,461
FSE Atoms Deposited = 14,066
BSE Atoms Deposited = 8,343
SE1 Atoms Deposited = 10,978
SE2 Atoms Deposited = 15,578
Structure Height = 8.5nm
Structure FWHM = 13nm
```

Vita

Daryl A. Smith was born on June 28, 1971 in Knoxville, Tennessee. He graduated from Farragut High School in 1989 with a 3.8 GPA. Daryl earned a second degree black belt while studying and teaching martial arts in high school, then went on to earn a Bachelor of Science degree from the University of Tennessee, Knoxville in 1993. During college, he interned at CTI, Inc. where he learned to design Positron Emission Tomograph (PET) scanners. He graduated Cum Laude from UTK with a major in Materials Science & Engineering, having earned three scholarships and chairing the Tau Beta Pi Engineering Honor Society. He then worked for TVA in Chattanooga, Tennessee for several years as a Metallurgical Engineer, before returning to the University of Tennessee to pursue his Masters degree which he earned in 2004 with a 3.94 GPA. After earning this degree, he continued to work at the university in pursuit of a Ph.D. in Materials Science & Engineering. He interned at Intel, Inc. during 2005 to expand his horizons, and then returned to Knoxville to finish the work toward his degree.